



UNIVERSITÀ DEGLI STUDI
DI GENOVA

UNIVERSITÀ DEGLI STUDI DI GENOVA

DITEN - DIPARTIMENTO DI INGEGNERIA NAVALE, ELETTRICA,
ELETTRONICA E DELLE TELECOMUNICAZIONI

Human-Machine Interfaces using Distributed Sensing and Stimulation Systems

Author:

Yahya Abbass

Supervisor:

Prof. Maurizio Valle

Cordinator of the PhD course: Prof. Maurizio Valle

This dissertation is submitted for the degree of

Doctor of Philosophy

in

Science and Technology for Electronic and Telecommunication Engineering

Cycle XXXIV (2018-2021)

COSMIC Lab - DITEN

Declaration

I hereby declare that except where specific reference is made to the work of others, the contents of this dissertation are original and have not been submitted in whole for consideration for any other degree or qualification in this, or any other universities. This dissertation is my own work and contains nothing which is the outcome of work done in collaboration with others, except as specified in the text and Acknowledgements. This dissertation contains fewer than 65,000 words including bibliography, footnotes, tables and equations and has fewer than 150 figures.

January 2022

Acknowledgements

This thesis wouldn't have been possible without the presence of certain people around me. It is my pleasure to acknowledge their efforts and contributions through my journey to earn my Ph.D.

I would like to express my deepest thanks and sincere appreciation to Prof. Maurizio Valle, Dr. Lucia Seminara and Prof. Strahinja Dosen for all the guidance and encouragement. Their dedication and keen interest above all their overwhelming attitude to help me had been solely and mainly responsible for completing my work.

Furthermore, I appreciate the support I received from the University of Genova in Italy. All the staff showed the highest level of dedication to foster a positive working environment for me.

I am extremely thankful to my friends for enlightening me the first glance of research. Their mentoring and encourgment have been especially valuable, and their early insights launched the greater part of this dissertation.

Last but not the least, I would like to thank my family: my parents for supporting me spiritually throughout my life.

Yahya Abbass

Abstract

As the technology moves towards more natural human-machine interfaces (e.g. bionic limbs, teleoperation, virtual reality), it is necessary to develop a sensory feedback system in order to foster embodiment and achieve better immersion in the control system. Contemporary feedback interfaces presented in research use few sensors and stimulation units to feedback at most two discrete feedback variables (e.g. grasping force and aperture), whereas the human sense of touch relies on a distributed network of mechanoreceptors providing a wide bandwidth of information. To provide this type of feedback, it is necessary to develop a distributed sensing system that could extract a wide range of information during the interaction between the robot and the environment. In addition, a distributed feedback interface is needed to deliver such information to the user. This thesis proposes the development of a distributed sensing system (e-skin) to acquire tactile sensation, a first integration of distributed sensing system on a robotic hand, the development of a sensory feedback system that compromises the distributed sensing system and a distributed stimulation system, and finally the implementation of deep learning methods for the classification of tactile data. It's core focus addresses the development and testing of a sensory feedback system, based on the latest distributed sensing and stimulation techniques. To this end, the thesis is comprised of two introductory chapters that describe the state of art in the field, the objectives, and the used methodology and contributions; as well as six studies that tackled the development of human-machine interfaces.

The first study presents the realization of a novel, flexible, screen-printed e-skin based on P(VDF-TrFE) piezoelectric polymers. A complete set of sensing arrays was designed and fabricated to sensorize a robotic hand (particularly the Michelangelo hand by Ottobock). Moreover, it represents the first step toward the development of skin patches to be used in different scenarios (e.g., prosthetic hand). Particularly, it presents a validation methodology to examine the behavior of the sensors. The characterization results showed compatibility between the modeled behavior of the sensors to the measured mechanical force at the skin surface, which in turn proves that both the fabrication and assembly processes were successful. This paves the way to define a practical, simplified and reproducible characterization protocol for e-skin patches and the development of the skin patch.

The second study presents the experimental assessment and characterization of an interface electronic system for piezoelectric tactile sensors. The system is based on a low-power arm-microcontroller and a DDC232 device. The sensing arrays developed and tested in the first study were used to validate the interface electronics. Electrical and electromechanical setups have been implemented to assess the response of the interface electronic with the PVDF-based sensors we developed and are part of the first study, described in Chapter 3. The results of electrical and electromechanical tests validate the correct functionality of the proposed system. This study represents the second step toward the development and integration of a sensory feedback system in various applications.

The third study represents a further assessment of the sensing system that is based on the PVDF sensors and the interface electronics described in Chapter 3 and Chapter 4 respectively. In particular, first, it presents the development of a skin patch (multi-layer structure) that could be used to sensorize a robotic hand or develop sensorized glove. Second, it shows the characterization of the developed skin patch. Third, it validates the sensing system. Moreover, the study aims at developing methods for noise

filtering and detection of a touch. The experimental assessment demonstrated that the developed skin patch and the interface electronics indeed can detect different touch patterns and stimulus waveforms. Moreover, the results of the experiments defined the frequency range of interest and the response of the system to realistic interactions with the electronic skin.

The fourth study describes the development of a novel embedded electrotactile feedback system for hand prostheses using matrix electrodes and electronic skin. The system was developed for tactile feedback integrating advanced distributed sensing (e-skin) and stimulation (matrix electrodes). Specifically, the study presents a new approach of integrating the e-skin (described in Chapter 3) onto the curved surfaces of a prosthetic finger. Next, a method to process the tactile data and extract contact information from the e-skin. The data processing method, as well as a communication protocol to transmit the processed data to the stimulation unit, were implemented within the embedded electronic system (described in Chapter 4). Finally, an experimental assessment was conducted to demonstrate that the developed components properly work together. The experimental assessment demonstrated that the developed system indeed delivered the desired functionality i.e., a timely distributed electrotactile feedback on the static and dynamic contact patterns, which was easily perceived and interpreted by the subjects.

The fifth study describes the development of a novel electrotactile feedback system for teleoperation using distributed electronic skin and distributed feedback interface. Specifically, the study presents the integration of the complete set of sensing arrays presented in the first study onto a mockup of the Michelangelo prosthetic hand. The system comprises six flexible sensing arrays (described in Chapter 3) integrated on the fingers and palm of a robotic hand, embedded electronics (described in Chapter 4), a multichannel stimulator, and seven flexible electrodes placed on the volar side of the subject's hand. The data processing method, as well as a communication protocol

to transmit the processed data to the stimulation system, were implemented in this study. Finally, an experimental assessment was conducted to demonstrate that the developed system is working properly. The experimental assessment demonstrated that the developed system indeed delivered a timely distributed electrotactile feedback, which was easily interpreted by the subjects.

The sixth study proposed a novel touch modality classification framework using Recurrent Neural Networks. In particular, it explores the potential of such networks for touch modality classification. For this purpose, the study proposes two methods that are based on two separate networks to capture long-term dependence from tactile data. Moreover, the study proposes a case-specific approach to dataset organization to address the peculiarities of tactile data within the aforementioned networks. the proposed methods have been experimentally validated with a real dataset and compared to the state-of-the-art achievements. The experimental results demonstrate that the proposed approach achieves a reduction in the number of FLOPs i.e., in-memory storage compared to the same problem in the state of the art. the proposed methods achieved high accuracy on a 3-class touch modality dataset. This study opens interesting perspectives for near-sensor processing with critical constraints.

In conclusion, by adopting innovative methodologies in sensing, processing, and stimulation methods, this thesis advances the overall development of a sensory feedback for human-machine interface. Moreover, this research could lead to high-bandwidth and high-fidelity transmission of tactile information in human-machine applications that could improve the end-user experience and facilitate embodiment.

Keywords: Sensory Feedback Systems, Sensory Substitution, Electronic Skin, Sense of Touch, Distributed Tactile Sensing, Distributed Electrotactile Stimulation, Myoelectric Prosthesis, Teleoperation, Deep Learning, Recurrent Neural Network, Tactile Data classification

Contents

Acknowledgements	v
Abstract	vii
List of Figures	xix
List of Tables	xxxi
1 Introduction	1
1.1 Motivation	6
1.2 Contributions	7
1.2.1 Distributed tactile sensing system	7
1.2.2 Sensory feedback system	7
1.2.3 Tactile Data processing and classification	8
1.3 Thesis Outline	8
2 Feedback Systems for Sense of Touch	11
2.1 Introduction	11
2.2 Tactile Sensing Systems	12
2.2.1 Tactile sensing techniques	13
2.2.1.1 Piezoelectric sensors	15
2.2.1.2 Resistive sensors	16

2.2.1.3	Capacitive sensors	16
2.2.1.4	Optical sensors	17
2.2.2	Robot hands equipped with tactile sensors	17
2.2.3	Tactile sensors on prosthetic hands	20
2.3	Interface electronics system	21
2.4	Signal processing and classification	22
2.5	Feedback techniques	24
2.5.1	Vibrotactile feedback	24
2.5.2	Electrotactile Feedback	24
2.5.3	Mechanotactile feedback	25
2.5.4	Kinesthetic feedback	25
2.6	High-bandwidth feedback system	26
3	Development and Validation of Screen-printed Electronic Skin Based on Piezoelectric Polymer Sensors	29
3.1	Introduction	29
3.2	Materials and Methods	32
3.2.1	Electronic Skin Design	32
3.2.2	Experimental Setup	36
3.2.3	Reference Skin Structure and Model	39
3.3	Results	43
3.3.1	Morphology of the sensing arrays: Issues	43
3.3.2	Experimental tests	45
3.3.2.1	Frequency Range Selection	46
3.3.2.2	Systematic sensor validation	47
3.4	Discussion	55
3.5	Conclusion and Future Work	61

4	Experimental Assessment of the Interface Electronic System for PVDF-Based Piezoelectric Tactile Sensors	65
4.1	Introduction	65
4.2	Background	66
4.3	Tactile Sensing System	68
4.3.1	Piezoelectric Tactile Sensor	68
4.3.2	Piezoelectric Tactile Sensor Model	68
4.3.3	The Interface Electronic System	70
4.3.3.1	Requirements and Specifications	70
4.3.3.2	Block Diagram and Circuit Design	70
4.4	Experimental Setup and Methods	72
4.5	Experimental Results	75
4.5.1	Electrical Measurements Results	75
4.5.2	Electromechanical Measurement Results	76
4.6	Signal to Noise Ratio Analysis	79
4.7	Conclusion	80
5	Development of a Skin Patch based on P(VDF-TrFE) sensors and assessment of the sensing system	83
5.1	Introduction	83
5.2	Skin Patch	85
5.3	Systematic skin patch validation	87
5.3.1	Experimental setup	89
5.3.2	Response to different stimulus waveforms	89
5.3.3	Repeatability and Linearity	94
5.4	Touch pattern detection	97
5.5	Implementation of tactile signal processing	103
5.5.1	Filtering using Finite Impulse Response method	103

5.5.2	Filtering by Moving Average Filter	104
5.6	Conclusion	106
6	Embedded Electrotactile Feedback System for Hand Prostheses using Matrix Electrode and Electronic Skin	109
6.1	Introduction	109
6.2	Materials and Methods	115
6.2.1	System Architecture	115
6.2.1.1	Tactile sensors Arrays	115
6.2.1.2	Interface Electronics	119
6.2.1.3	Electrotactile Stimulator	120
6.2.1.4	Electrodes	121
6.2.2	Signal processing to detect contact events	121
6.2.3	Online feedback	122
6.3	Experimental Assessment	123
6.3.1	Experiments	123
6.3.2	Setup and Protocol	125
6.3.3	Data Analysis	129
6.4	Results	130
6.5	Discussion and Conclusion	133
7	Full-hand electrotactile feedback using electronic skin and matrix electrodes for high-bandwidth human-machine interfacing	141
7.1	Introduction	141
7.2	Materials and Methods	144
7.2.1	System Description	144
7.2.1.1	Sensorized mockup of the Michelangelo hand	146
7.2.1.2	Embedded Electronics	147

7.2.1.3	Feedback System	149
7.2.2	Mapping Sensors to Pads	150
7.3	Sensing System Validation	153
7.4	Psychometric assessment	155
7.4.1	Experiments	155
7.4.1.1	(Static pattern experiment (SPE)	155
7.4.1.2	(Dynamic pattern experiment (DPE)	156
7.4.2	Setup and Protocol	157
7.4.3	Data Analysis	158
7.5	Results	160
7.6	Discussion and Conclusion	162
8	Touch Modality Classification Using Recursive Neural Networks	167
8.1	Introduction	167
8.2	Background	169
8.3	Methodology	174
8.3.1	LSTM network	174
8.3.2	GRU network	175
8.3.3	CNN-LSTM network	176
8.3.4	ConvLSTM network	176
8.4	Experimental Setup	177
8.4.1	Dataset Organisation	178
8.4.2	Implementation	180
8.4.2.1	LSTM network	181
8.4.2.2	GRU network	181
8.4.2.3	CNN-LSTM network	181
8.4.2.4	ConvLSTM network	182
8.4.3	Training	182

8.5 Results and Discussion	184
8.6 Conclusion	188
9 Conclusion and Future work	191
Bibliography	195

List of Figures

1.1	Proposed Sensory feedback system using electronic skin and electrotactile stimulation	5
3.1	Illustration of the manufacturing process flow of printed ferroelectric sensor arrays based on polyvinylidene fluoride-trifluoroethylene P(VDF-TrFE) repeated units (reprinted with permission from JOANNEUM RESEARCH (JNR)). (a) Substrate; (b) Bottom Electrodes; (c) Active sensors based on P(VDF-TrFE) film + Top electrodes (1); (d) Top electrodes (2); (e) Connecting lines.	33
3.2	(a) Cross sectional view of a single sensor unit: Indicative thicknesses of the various layers have been extracted from scanning electron microscopy (SEM) pictures sent in private communications; (b) Sketch of the sensing patch; (c) Picture of a real sample.	34

3.3	Design of different sensing patches. (a) Sensing array for right hand tactile glove: Palm 1 two 4×2 arrays 16 taxels, taxel diameter = 2 mm, center-to-center pitch = 0.9 cm. Palm 2 - 4×2 array = 8 taxels, taxel diameter = 2 mm, center-to-center pitch = 1 cm. Index, Middle, Ring, Little, and Thumb - 8 taxels, taxel diameter = 1 mm, center-to-center pitch = 1 cm. (b) Sensing array for left hand tactile glove. (c) Sensing array for Michelangelo prosthetic hand: M.Middle 13 taxels, taxel diameter = 1 mm. M.Index 16 taxels, taxel diameter = 1 mm. M.Palm 12 taxels, taxel diameter = 2 mm. M.Little and M.Ring - 4 taxels, taxel diameter = 1 mm. M.Thumb - 15 taxels, taxel diameter = 1 mm.	35
3.4	Experimental setup. Top: Block Diagram, Bottom: Pictures of the setup. The blue dotted line shows the alignment of the testing elements.	37
3.5	The applied coupling scenario.	38
3.6	Sketch of the general working mechanism of the P(VDF-TrFE) sensor: The Hertzian input force (with contact radius a) is transmitted to the sensor (with radius r_T) through the elastomer layer of thickness h . With the presupposition that the sensor works solely in compressive mode, it directly converts the received normal stress T_3 into electrical displacement D_3 , through a characterizing piezoelectric coefficient, namely the d_{33} (1). A charge amplifier is used to convert the total sensor charge into voltage	39

3.7	Results for the numerical COMSOL simulations for the finite case. The proportionality coefficient σ between average normal stress r_T on the sensor and overall (Hertzian) contact force F_3 (2) is plotted versus the imprint radius a (contact size) scaled by the elastomer thickness h . Note that the applied force is centered on the sensor. The two curves are associated to two different sensor sizes: $r_T = 1$ mm (sensors on the palm), $r_T = 0.5$ mm (sensors on the fingertip).	40
3.8	(a) Normal sensor, (b) Fault in the sensor top electrode (pole), (c) Cut in the sensor tracks, due to short circuits during the poling procedure, (d) Shortcuts between sensor tracks.	43
3.9	The heat map of the fabrication substrate (DIN A3) prone to shrinkage. .	44
3.10	Example of the frequency behavior of both the real (white curve) and imaginary (red curve) part of the d_{33} piezoelectric coefficient. The scale for the Im ($d'' = D_{33}$) is on the right y-axis.	46
3.11	Compared categories (CAT1, CAT2, CAT3 and CAT 4) and heat map on the A3 fabrication substrate.(a) Heat map of the fabrication and the selected categories for testing, (b) Zoom in view for each category's location.	49
3.12	(a) Cloud distribution of working palm sensors. (b) Working palm sensors(c) Category 1 (palm left 2). (d) Category 2 (palm right 2). (e) Category 3 (palm right 1). (f) Category 4 (M.palm). Statistical study: One-way analysis of variasnce (ANOVA) ($p < 0.05$), average d_{33} vs preload.	50
3.13	Average d_{33} vs. patches at PL = 1 N, 2 N, and 3 N, arranged respectively as (a), (b) and (c). The four categories and all corresponding patches can be distinguished on the x-axis.	51

3.14 (a) Average d_{33} vs. preload. Sensors belonging to categories 1 and 4, only. To avoid dot superposition, values associated with the same preload are plotted such that dots do not lie on the same vertical line .Average d_{33} for each sensor at PL = 1 N (top), 2 N (middle) and 3 N (bottom). (b) Average d_{33} for each sensor at PL = 1 N, (c) Average d_{33} for each sensor at PL = 2 N (d) Average d_{33} for each sensor at PL = 3 N	52
3.15 Average d_{33} vs. preload for the three analyzed patches belonging to category 1: (a) Palm left 2.2., (b) Palm left 2.3 and (c) Palm left 2.4 (bottom).	53
3.16 Finger sensors (Michelangelo Little, ML) located in the sweet spot on the heat map of the A3 fabrication substrate. Bottom: Average d_{33} vs. preload for the two samples of Michelangelo little: ML.1 and ML.2. Statistical study: one-Way ANOVA ($p < 0.05$)	56
3.17 Sensor electrodes have been severely damaged after coupling with adhesive tape all over the skin patch. (a) An overall adhesive tape coupled sensor, (b) Impaired top electrode of sensor after removing the adhesive tape.	59
3.18 Illustration of different coupling methods.	61
4.1 Interface electronic printed board circuit (left) and block diagram of the DDC232 (right)	71
4.2 Block diagram of the electrical setup; equivalent circuit of sensor (left) connected to interface electronics; generated signals are reconstructed by the interface electronics (IE) and sent to the PC.	73
4.3 Experimental setup. Top: Block Diagram, Bottom: Pictures of the setup.	74

4.4	(a) The theoretical fit-line is calculated from $Q_{\text{theoretical}} = C_p V_p \sin(2\pi f T_{\text{INT}})$ derived from the equations presented in [1]; (b) shows the output of the IE relative to input signals generated from the source generator.	75
4.5	(a) IE output measurements with real sensors; (b) conditioner output measurements with real sensors.	77
4.6	(a) Sensitivity as a function of frequency; (b) measured charges at the minimum detectable force (0.01 N).	77
4.7	Example of an input signal at 100 Hz of frequency in time and frequency domains.	78
4.8	SINAD and ENOB variation with respect to applied forces.	79
5.1	Skin patch development process. The sensing array is shielded using conductive tapes and a thin protective layer is used to protect the sensing areas.	86
5.2	Experimental setup. Top: Pictures of the setup, Bottom: Block Diagram. The blue dotted line shows the alignment of the testing elements. . . .	88
5.3	Response of a single sensor to swept sine stimulus with the PCB conditioner. The amplitude of the signal was increased or decreased automatically by the host PC.	90
5.4	The Fast Fourier Transformation of the swept sine stimulus and the response of the sensor using the conditioner.	91
5.5	Response of a single sensor to swept sine stimulus with the PCB conditioner. The amplitude of the signal was increased or decreased automatically by the host PC.	92
5.6	Response of a single sensor using the conditioner to rectangular (Top) and triangular (bottom) stimuli.	93

5.7	An example of a sequence of forces and the corresponding charge response at preload of 0.6 N (left) and 3 N (right)	95
5.8	Average charge response vs force at four preloads.	96
5.9	Experimental setup. Top: Pictures of the setup, Bottom: Block Diagram. The blue dotted line shows the alignment of the testing elements.	98
5.10	Response of the single sensor to tapping (left) and press-hold-release (right) touch patterns.	99
5.11	Response of single sensor to a continuous touch pattern (Top) and the correlation between the applied stimulus and the sensor response (Middle). Bottom: continuous wavelet transform (CWT) of the applied stimulus and the sensor response.	100
5.12	The Output of inverting the continuous wavelet transform over three frequency ranges (< 50 Hz, < 30 Hz, and < 10 Hz) Bottom: Specification of a low-pass IIR filter that could be used to reduce the noise level and the output signal.	101
5.13	The output of the FIR filter after being implemented in the firmware of the interface electronics. Left: response of the sensor to Press-Hold-Release touch pattern. Right: continuous wavelet transform (CWT) of the sensor response.	103
5.14	The output of the moving average filter after being implemented in the firmware of the interface electronics. Top: response of the sensor to the Tapping, Press-Hold-Release, and continuous touch patterns. Bottom: continuous wavelet transform (CWT) of the force stimulus and the sensor response.	105

- 6.1 System Architecture. The system comprises an e-skin with 16 sensors, interface electronics for signal acquisition, and a multichannel stimulator with flexible matrix electrodes integrating 24 electrode pads to deliver the electrotactile stimulation to the subject. The system therefore translates the tactile data recorded by the e-skin into stimulation profiles that are delivered online to the skin of the subject. 114
- 6.2 (a) Single sensors structure, a P(VDF-TrFE) layer sandwiched between two electrodes. (b) Layout and dimension of the sensing array dimensioned to cover the index finger of the Michelangelo hand prosthesis. (c) The sensing array is composed of three sensing areas and a tracks area. (d) Skin patch development process. The sensing array is shielded using conductive tapes and a thin protective layer is used to protect the sensing areas. 116
- 6.3 Sensing system integrated on the Michelangelo hand mockup. (a) The sensing array with 16 sensors attached to the index finger (b) Sensing array connected to a PCB placed inside a shielding box and attached to the back of the hand. (c) A shielded flat cable connects the PCB on the back to the interface electronics, and the interface electronics with Bluetooth module were placed inside a shielding box. 117
- 6.4 Interface electronics printed board circuit (left) and its block diagram (right). The module can sample 32 tactile signals, process and transmit them wirelessly with a remote host via a Bluetooth connection. The module also implements the encoding scheme mapping the tactile signals into stimulation profiles and a command protocol to set the stimulation parameters of an electrotactile stimulator. 119

- 6.5 The online processing pipeline of the embedded feedback system. The left panel shows an electrical response (sensor signals) due to a contact applied to the e-skin by an experimenter using a pen tip (press-hold-release). The exponential moving average filter was applied and then the signal was thresholded to detect press and release (middle panel). Finally, the interface electronics sent stimulation commands to the stimulator to activate or deactivate stimulation at the corresponding channel, thereby eliciting tactile sensations (right panel) over the subject’s forearm. . . . 122
- 6.6 (a) Sensor distribution within the electronic skin placed on the index finger of the Michelangelo mockup. The sensors are numbered and each sensor is associated to a stimulation pad on a matrix electrode placed on the subject’s forearm as shown in (c). The sensor and pads were also grouped into six corresponding groups (G1-6, boxes in (b) and (c)) where G1 corresponds to Group 1 and G6 corresponds to Group 6. (b) Three experiments were conducted to assess the subject’s ability to perceive and interpret the feedback: 1- touch on a group of sensors (low spatial resolution), 2- touch on individual sensors (full spatial resolution), and 3- dynamic touch (i.e. sliding across medial, lateral, distal, middle, and proximal lines in two directions). 126

6.7 Experimental setup. (a) Experimenter interacting with the sensing system, (b) Subject received electrotactile feedback through a matrix electrode placed on the right forearm and covered with a medical bandage. The subject received visual feedback shown on the computer screen only during the familiarization phase. (c) In an additional experiment, the setup was used to measure the acceptable touch-stimulation delay. In this test, the subjects received the tactile feedback while looking at the experimenter touching the hand, and they were asked to report when the delay (intentionally added in the system) between tactile and visual feedback became noticeable. 129

6.8 Confusion matrices for the G2G (Top left) and S2P (Bottom) and SLP experiments (Top right). The results demonstrate a good recognition of 6 classes in G2G experiment, 16 classes in S2P experiment, and 5 classes in SLP experiment (well-focused diagonal line. The confusion matrix of S2P experiment demonstrates the superior performance in recognizing pads on the borders. 131

6.9 The overall success rate of recognizing tactile patterns: (a) sensor group in experiment S2P, (b) sliding movements in experiment SLP. 132

- 7.1 Top: System structure. The system comprises an e-skin including 57 sensors, embedded electronics for signal acquisition, processing and communication, and a multichannel electrotactile stimulator with flexible matrix electrodes (32 electrode pads). Bottom: The online operation of the feedback system. The black signal (left) corresponds to a sensor output due to a specific type of contact (“long press”). The embedded electronics uses two thresholds to detect press and release, and based on that generate the event signal (red signal) and send it to the host PC. The PC sends commands to the stimulator and the train of stimulation pulses (blue signal) is delivered through the corresponding electrode pad as tactile feedback to the subject’s hand. 145
- 7.2 (a) Layout of the sensing arrays for the fingers and palm of the Michelangelo robotic hand. (b) Sensor distribution over the hand. (c) Skin patch. (d) Sensing system integrated on the mockup of the Michelangelo hand (front and back views). 146
- 7.3 (a) Top and Bottom view of the printed circuit board of the embedded electronics. (b) Block diagram. (c) Sensing system integrated on the mockup of the Michelangelo hand. Individual sensors are marked as red dots. 148
- 7.4 Flexible electrodes for the electrotactile stimulation of the hand. (a) Layout of the pad arrays to cover the fingers and palm. (b) Volar and dorsal view of a human hand covered with the electrode arrays. Stimulation pads are indicated as black dots (volar) and rectangles (later index). 150

7.5 E-skin (left) and Electrode Arrays (right): Cathode and anode distributions within the electrode arrays (subject hand). The numbers on the e-skin and electrode array indicate the mapping of sensor sets to corresponding groups of pads connected to a single stimulation channel. Two anode configurations were considered: a) a distributed anode comprised of a subset of pads (DAC), and b) a single dedicated electrode placed on the dorsal side of the hand (SAC). 151

7.6 Illustrative data showing sensor outputs. Signals from six sensors are shown during touch interactions. The legend attributes colours to each specific sensor output. Indentation tests: (a) long press on two sensors located on the palm; (b) long press on the three phalanges of the index finger starting from the proximal phalange; (c) long press on two sensors (on the palm) at the same time. Shear tests: (d) sliding movement starting from the palm and moving toward the tip of the index finger. . . 154

7.7 Left: Sensor distribution within the electronic skin placed on the fingers and palm of the mockup of the Michelangelo hand. The sensors were grouped into fourteen groups (G1-14, boxes). Right: Two psychometric experiments were conducted: 1- SPE – skin indentation aligned on specific sensors (*Static* pattern) and 2- DPE - shear tests (*Dynamic* pattern), i.e. sliding across M, IV, PTh, IL, PF and FT lines in two directions). . . . 156

7.8	Experimental setup. (a) The subject received electrotactile feedback through electrode arrays placed on the right hand and covered with a medical bandage. The electrodes were connected to a small PCB routing 64 pads to 32 stimulation channels. The PCB includes a small jumper that was used to switch between the anode configurations, i.e., SAC and DAC. (b) Example of the experimenter interacting with the sensors: (bottom) the experimenter applies single touch on a set of sensors on the palm and (top) the experimenter touches the index and middle fingers simultaneously.	157
7.9	The overall success rate (SR) of recognizing sliding lines in experiment DPE for DAC (left) and groups of sensors in SPE experiment for SAC and DAC (right). Asterisks indicates the statistically significant difference in mean SR for the different anode configurations. (*, $p < 0.05$).	159
7.10	Confusion matrix for SPE experiment.	160
7.11	Confusion matrix for DPE experiment.	161
8.1	LSTM / GRU	173
8.2	Scheme of touch modalities, tactile acquisition system and dataset properties.	177
8.3	Dataset Organisation	179
8.4	CNN-LSTM Structure.	181
8.5	Accuracy Summary	183
8.6	LSTM Accuracy / Folds	185
8.7	Model Scalability	186

List of Tables

2.1	Design requirements for tactile sensing system	13
2.2	Characteristics of different tactile sensing techniques used for e-skin fabrication	14
3.1	Palm patches categories (Data set 1, palm sensors)	48
3.2	Summary of results.	57
6.1	Summary of Performed Experiments	125
6.2	Summary Results (Mean \pm Stand Dev) of Experiments	130
7.1	System features	152
7.2	Summary of experiments	155
8.1	Comparison of accuracy, number of parameters, and FLOPs	184

Chapter 1

Introduction

Human-machine interfaces (HMIs), as a window of communication between the user and the equipment, robot, or virtual world, are the key elements for achieving effective, intuitive, and seamless manipulation to complete the tasks. As these interactions become more complex there is a keen interest in developing technologies that enrich the interaction between humans and robots. Industry experts are predicting substantial growth for the HMI market. According to one report, the market is set to grow at a 9% compound annual growth rate up through 2019. Driving this growth is an increased demand for automation and efficiency in the workplace, both of which are tasks accomplished by an HMI. With the aid of advanced technology, HMI evolves from conventional control terminals to more diversified and creative alternatives. As a result, more realistic interactions between users and machines eventually satisfy the additional needs beyond the simple controlling of objects. An ideal HMI should provide bilateral communication between the user and the machine [2]. The ideal goal is to enable the user to not only control the machine but also perceive it as if it were being touched directly. Conventional HMIs have been widely applied in robotic systems, such as rehabilitation robots [3, 4], motion gesture monitoring [5], and biological health monitoring [6]. However, most of the conventional HMI solutions are still a long way from

improving utility and promoting the feeling of embodiment, as well as, establishing an immersed experience by enabling users to sense virtual objects. Mostly, this is related to the absence of sensory feedback systems in most of the conventional HMI. For example, although there is an impressive development of prosthesis technology, the insufficient sensory feedback still makes many amputees reluctant to use these products [7, 8]. According to statistics, 88% of respondents believe that sensory feedback is necessary for the control of prosthetic hands [9]. Besides, many studies have also indicated the significance of sensory feedback in hand prostheses [10, 11]. Similarly, realistic and transparent sensory feedback is expected to improve the performance and the dexterity in executing telemanipulation tasks [12]. Therefore, developing a bidirectional HMI with reliable control and rich perception capabilities improve the motor control of the machine.

Currently, most robotic hands merely focus on improving the mechanical structure and control strategies to obtain better performance, However none of it (i.e., commercial or research hands) could ensure comprehensive feedback. For example, taking top commercial myoelectric hands such as Bebionic by Steeper [13] and Michelangelo hand by OttoBock [14], and i-limb Ultra-revolution by Ossur [15], enables users to perform basic daily tasks, yet none of them could provide tactile information without visual feedback. Apart, only VINCENT evolution 3, provide tactile feedback, the grasping force applied by the prosthesis is translated into vibration profiles [16] and still, no reports confirmed its effectiveness. Clinically wise, SensorHand [14] contains a three-dimensional force sensor, which measures the shear force to automatically change the grip force to prevent slipping of grasped objects.

The human skin and afferent nerves provide the central nervous system with various sensory information, which is essential for perceiving the environment that surrounds us. The skin of the human hand is innervated by many types of mechanoreceptors, which are responsible for perceiving pain, thermal, kinesthetic, and tactile (e.g.,

texture, skin's motion, pressure) sensations [17]. A wide range of application scenarios, haptic information is required to enrich interaction fidelity of user's awareness [18]. For example, These haptic information is considered crucial for facilitating an effective human-machine/computer interaction [19, 20]

The implementation of sensory feedback is a long-standing challenge [21]. To this aim, the information from tactile sensors is transmitted to the user using different kinds of feedback interfaces. The last few decades have witnessed tremendous progress in the development of electronic skins (e-skins) for robot sensing. Research into developing soft tactile sensors that are constructed from soft, thin, flexible, stretchable, and lightweight materials is nowadays also beginning to attract increasing attention. These soft sensors represent an emerging class of technologies [22] that have the potential to improve the ability of robots to possess the physical properties and somatosensory functionalities of natural human tissue. The characteristics of such technologies make them ideally suited as artificial skin with adequate elasticity to conform to multiple surfaces and sufficient mechanical compliance to make them safe and comfortable for physical human-robot interaction [23]. While there have been promising developments in tactile sensor technologies over recent years [24–26], many of these are rigid or bulky and do not meet the desired mechanical characteristics of artificial skin.

Knowing that afferent nerves can be stimulated by electric, mechanical, and thermal stimuli, several haptic interfaces have been developed to deliver tactile information captured by the tactile sensors [18]. At present, developing a haptic interface has both invasive and non-invasive solutions. Although the invasive HMI has high spatial resolution and preferable precision, its cost and risk are also high, making it still stay in the experimental stage. On the other hand, the non-invasive HMI is favored in research and the market due to its low cost, high safety, and ease of use. The most common non-invasive methods employed to elicit sensory feedback are kinesthetic feedback and

sensory substitutions methods that rely on vibrotactile, mechanotactile, electrotactile stimulation, etc. [27].

The human sense of touch relies on the dense network of mechanoreceptors to provide spatially distributed information (e.g., pressure distribution). To provide high-resolution tactile information mimicking the human sense of touch, this information first needs to be measured by adequate artificial systems integrating a high-density network of sensing units. For transmitting the tactile information coming from distributed sensing system to the user, a homologous spatial distribution of tactile stimulators is needed. Endowing a robot with a distributed sensing system combined with distributed feedback interface would enable high-bandwidth bilateral communication between the user and the robot. Despite the tremendous progress in the development of e-skin and effective feedback interfaces, few examples of distributed sensing and stimulation systems have been used in human-machine interfacing (e.g., prosthetics, teleoperation). In some cases, multichannel interfaces have been used to encode up to two discrete variables (e.g., grasping force and aperture) [28]. There have been many investigations on the nature of these artificial sensory feedback systems, yet all the developed systems have been limited by a small information transfer bandwidth [29].

While distributed sensing system technologies are now available in the autonomous robotic domain, only a few examples of these systems integrated into human-machine interfacing for robotic hands have been reported [30–32]. In this context, this thesis presents the development of a sensory feedback system for bilateral HMI. Figure 1.1 presents a close-up image of the proposed system. The proposed system would comprise:

- Electronic skin: An electronic skin (e-skin) to mimic the tactile receptors and cover the robotic hand. The realization of the screen-printed e-skin and characterization is considered the first basic corner of this thesis's achievements and contributions.

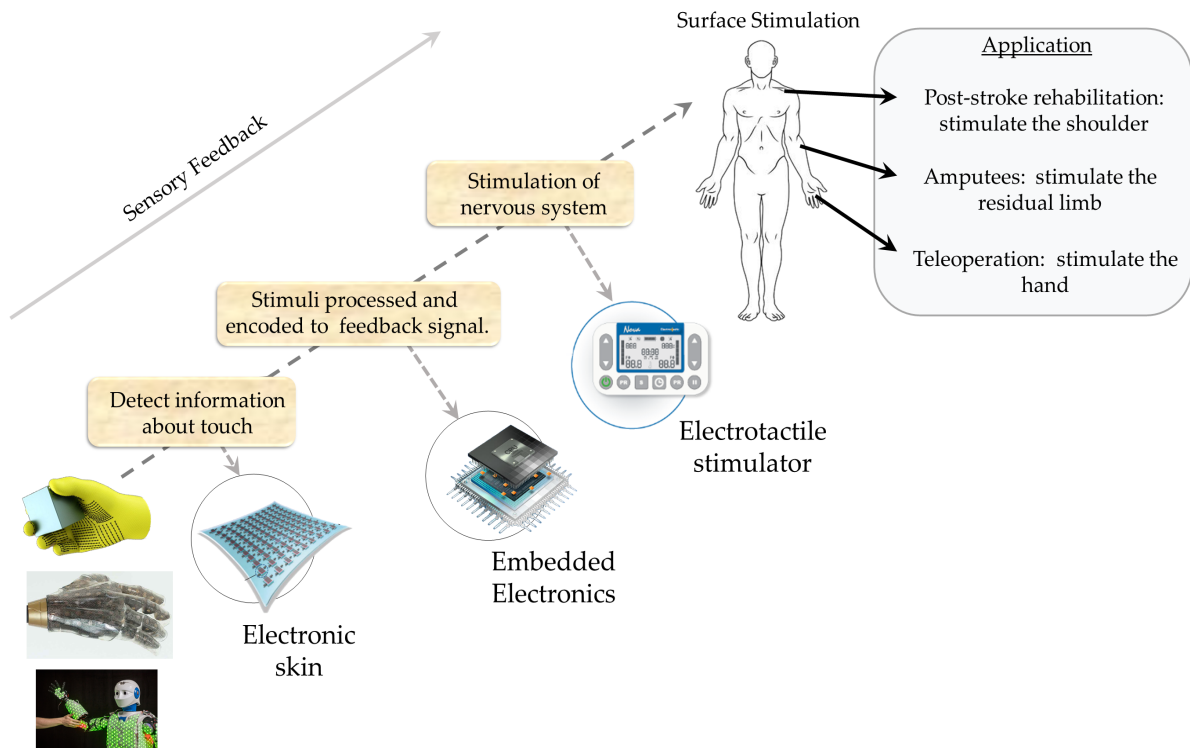


Figure 1.1 Proposed Sensory feedback system using electronic skin and electro-tactile stimulation

- **Processing unit:** An embedded electronic system integrating signal conditioning, data acquisition, and tactile data processing. The assessment of the embedded electronics is the second basic corner of this thesis's achievements and contributions. In addition to the development of new processing, methods to reduce system noise and extract contact information were developed.
- **Feedback interface:** A non-invasive electro-tactile based stimulation system is used to deliver the captured information into feedback signals through surface electrodes attached to the skin of the user. Several methods have been developed to interpret tactile data in real-time and efficiently deliver artificial tactile information (recorded by artificial skin) to the user through a multichannel electro-tactile stimulation.

1.1 Motivation

With the advancement of the technologies for high-density tactile sensing and electrotactile stimulation, the goal of developing bilateral HMI becomes reachable. Remarkable research efforts had been done to develop a high-bandwidth HMI; however, it is still not achieved. Our pivotal goal is a feedback system that is compromised of a dense network of tactile sensors and stimulators to provide the feeling of touch over the whole surface of the robotic hand. Such a system would provide a completely new experience to the user, improving utility and facilitating the feeling of embodiment to the level that is far beyond the conventional systems based on discrete sensing and stimulation.

The main objective of this thesis is to develop a high-bandwidth sensory feedback system that would provide the user with the sense of touch. The system compromises a piezoelectric polymer sensory array acting as an artificial skin to measure tactile information and an electrotactile stimulation interface to convey the acquired tactile information to the users (e.g., amputees, robot operators, virtual reality, etc.). This thesis proposed the idea of integrating an artificial distributed tactile sensing and stimulation systems into a robotic hand (Michelangelo prosthetic hand [14]) to provide high-fidelity and high-bandwidth tactile feedback to the users. This idea has been established on one hand by developing artificial tactile sensing arrays (e-skin) for the hand that mimic human skin features, testing its reliability and efficient functionality, and developing a novel method for e-skin integration on the robotic hand. On the other hand, by developing optimized methods/tools (such as coding, electrode configuration) for the transmission of sensory feedback acquired from the artificial skin through non-invasive multichannel electrotactile stimulation and test its effectiveness in delivering tactile information to the user.

1.2 Contributions

The following thesis merely focuses on the tactile feedback system, and its principal contributions fall into three main parts of the application: the sensing system, tactile data processing and classification, and the feedback interface.

1.2.1 Distributed tactile sensing system

In the follow-up procedure of realizing a distributed tactile sensing system, the first three studies were conducted to validate the functionality of the different parts of the sensing system (i.e., e-skin and electronics).

- In the first study, we developed a testing methodology to validate the functionality of the novel screen-printed PVDF-based sensory arrays while being embedded into an elastic protective layer and working in thickness mode.
- In the second study, an embedded electronics used for signal acquisition and data processing has been experimentally assessed.
- The third study presents the realization of the skin patch and the experimental testing of the sensing system i.e., embedded electronics and skin patch.

1.2.2 Sensory feedback system

In the follow-up procedure of developing a bilateral HMI, two feedback systems were developed to provide tactile feedback. Two studies were conducted aiming to prove the feasibility of two feedback systems in providing high-bandwidth tactile information through distributed sensing and simulation interfaces.

- The fourth study presents a novel system for tactile feedback for prosthetic hand integrating the sensing system and a multipoint stimulation. The sensing

system was integrated into the mockup of the Michelangelo prosthetic hand. To demonstrate the feasibility, the system was tested in healthy subjects who were asked to recognize touch patterns presented on the electronic skin. Such systems would allow mimicking spatially distributed natural feedback, thereby facilitating the control and embodiment of the artificial device into the user body scheme.

- The fifth study describes a novel technology that relies on distributed sensing and stimulation to convey comprehensive tactile feedback to the user of a robotic end-effector. The system comprises the sensing system which covers the full robotic hand (fingertips and palm), an embedded electronics, a multichannel stimulator, and seven flexible electrodes placed on the volar side of the subject's hand. The system was tested in healthy subjects who were asked to recognize touch patterns applied on the electronic skin. The proposed system is an important step towards the development of a high-density human-machine interfacing between the user and a robotic hand.

1.2.3 Tactile Data processing and classification

The sixth study presents the implementation of small-size (memory), low-latency, low-complexity tactile data classification model based on shared-weights Recurrent Neural Networks (RNN) models e.g., LSTM and GRU. This work has reduced more than 99% of FLOPs, and more than 98% of model size with respect to the adopted models in the literature. This study opens the opportunities to implement this solution on embedded hardware in the future work.

1.3 Thesis Outline

Chapter 2 introduces an inter-comparison between sensing and feedback techniques, addressing their features, advantages, and disadvantages. Finally, it introduces the

motivation of our approach of using distributed sensing system and non-invasive electrotactile distributed stimulation interfaces to extract and deliver high bandwidth tactile information.

Chapter 3 presents the first study conducted on the tactile sensing part. It presents the validation of a fully screen-printed tactile sensing arrays based on P(VDF-TrFE) piezoelectric polymers. This chapter describes the experimental setup and procedures used for the characterization of sensors behavior while being embedded by the protective layer. Several coupling scenarios were developed which led to a new methodology of testing e-skin patches (i.e., validation protocol for e-skin).

Chapter 4 describes the second study conducted to test the sensing part. It presents the experimental assessment of an embedded electronic system for piezoelectric tactile sensors. Electrical and electromechanical setups have been implemented to assess the response of the interface electronic with the sensing arrays developed and tested in the first study. The study was the second step toward the development and integration of the sensing system in various applications.

Chapter 5 presents the development and characterization of a skin patch (multi-layer structure) to be used to sensorize a robotic hand. The chapter presents the experimental assessment of the skin patch and the response of the sensing system to different type of stimulus. Moreover, the study aims at defining the frequency range of interest and developing signal processing methods for noise cancellation and touch detection.

Chapter 6 presents a novel method for integrating skin patches onto the Michelangelo prosthetic hand. A skin patch was used to sensorize the index finger of the mockup of the Michelangelo prosthetic hand. In addition, the chapter presents the development of an electrotactile feedback system for prosthetic hands using a single skin patch and a single matrix electrode. The feasibility of the developed system and the processing

methods was demonstrated by conducting experiments to test the ability of the system to deliver tactile information to the users.

Chapter 7 presents the development of a high bandwidth electrotactile feedback system for teleoperation using electronic skin and matrix electrodes. The chapter presents the integration of the complete set of skin patches presented in the third chapter onto a mockup of the Michelangelo prosthetic hand. Moreover, it describes the tactile data processing method implemented to extract tactile information, as well as a communication protocol to transmit the extracted information to the user's hand. The feasibility of the developed system and methods was demonstrated by conducting experiments on healthy subjects.

Chapter 8 describes the deployment of RNN for tactile data classification. Tactile data of real dynamic touch modalities were processed as time series data using two RNNs. The study proposes a data organization methodology as well.

Chapter 9 summarizes the thesis in a general outlook. It discusses the impact of the methods used in this thesis that would pave the way for the development of an efficient bilateral HMI. Finally, recommendations and future work are reported.

Chapter 2

Feedback Systems for Sense of Touch

2.1 Introduction

The parallel advances across neuroscience, neuroengineering, electronics, and robotics in recent years have led to the development of advanced robotic hands. Nevertheless, real-time, accurate, and reliable control of robotic hands remains to be effectively achieved [33]. Users of conventional robotic hands lose the ability to feel when or how an object is being grasped and thus cannot adequately modulate the hand movements. There is still an unmet need to develop more realistic and sophisticated sensory feedback systems to provide a sense of utility, immersion, or embodiment of robotic hands, which is one of the main focuses of scientists presently. The development of a sensory feedback loop mimicking the natural sensory feedback loop starts with sensors that can detect various stimuli from the surrounding environment and physical world. From the use of basic piezoresistive elements to advanced biomimetic implementations, scientists have been exploring how to best mimic and replace subdermal receptors for improved grasping control in robotic hands (e.g., prostheses).

Technology of current tactile sensors increased pressure sensitivity and high-fidelity signal resolution which allow the classification and discrimination of many surface

properties. This is done through digital signal and waveform processing as well as statistical and machine learning techniques. To reiterate, such techniques are used to process the sensors signals and extract tactile information that will be processed and delivered to the user through feedback interfaces. Implanted electrodes can interface directly with intact afferent neurons, mimicking stimuli that would be perceived as sensory stimulations from the robotic hand. Non-invasive extra-dermal systems have also been developed to provide sensory feedback [34]. In addition, surface electrode systems have been used to stimulate different parts of the user's skin depending on the application (e.g., residual limb of amputees, shoulder of post-stroke patients, or hand for teleoperation). This chapter aims to provide a comprehensive review of current technologies and new developments of tactile sensing systems, tactile data processing and classification, and feedback strategies that have been used to deliver tactile information to the users. The review will focus mainly on sensing and feedback methods developed for prosthesis and teleoperation. Finally, it provides the motivation of our approach of using distributed sensing system and non-invasive electrotactile distributed stimulation interfaces to deliver high bandwidth tactile information and to obtain comprehensive feedback.

2.2 Tactile Sensing Systems

Sensors for robotic hands transduce various modalities of tactile stimuli aiming at recreating naturalistic perception. Today's tactile sensing systems encounter many challenges that limit their integration in robotic hand systems (e.g., prosthetic systems) such as designs issues, spatial distribution, low signal to noise ratio (SNR), cross talk, wireless communication, and the lack of signal processing and machine learning methods to encode the acquired data from tactile sensors [35]. The main design requirements are summarized in Table 2.1. It is expected that artificial tactile sensors

Table 2.1 Design requirements for tactile sensing system

Design criteria	Character guideline
Detectable force range (Dynamic range)	0.01N-10N
Spatial resolution	$\geq 1\text{mm}$ for small sensing areas (e.g. fingertips) $\geq 5\text{mm}$ for large sensing arrays (e.g. limbs, torso, etc.)
Sensor frequency bandwidth (sensor response time)	0.1 Hz -1kHz , About 1kHz (1ms)
Mechanical sensing detection capability	Normal and shear forces; vibrations
Sensor System characteristics	<u>Mechanical:</u> Flexible, stretchable, conformable and soft, robust and durable. <u>Electrical:</u> Low power, minimal wiring and cross talk, electrically and magnetically minimal sensitivity.
Sensor response	Monotonic, not necessarily linear, low hysteresis, stable and repeatable
Temporal variation	Both dynamic and static

demonstrate small spatial resolution ($\geq 1\text{mm}$ for fingertips, 5 mm for hand palm), high sensitivity varying from 0.01 to 10 N, which extend along with the tactile frequency range ($<1\text{Hz}$ - 1 kHz), low hysteresis, fast and linear response (less than 1 ms), wide dynamic range and high reliability. Furthermore, it needs to exhibit high electro-mechanical bandwidth to detect fast events (e.g., incipient slip) and customizable shape of e-skin patches and sensor number. Additionally, low cost, low power consumption, and scalability are major factors for the robotic application.

2.2.1 Tactile sensing techniques

Enabling tactile sensation particularly in upper limb prostheses is still not as mature as that in other fields (such as robotics, touch screens, etc.), yet the achievements could be adopted into this field. Given that grasping is one of the major functions of hands, most

Table 2.2 Characteristics of different tactile sensing techniques used for e-skin fabrication

Tactile sensors	Working principle	Advantages	Disadvantages
Piezoresistive	Its resistance varies with the deformation caused by applied force.	Simple electronics; High sensitivity; Resistant to interference	Hysteresis; Temperature Sensitivity; Fragile and Rigid; High power consumption
Capacitive	Its capacitance varies with the deformation caused by applied force.	Sensitivity of small force change; Reliability; Dynamic and static force measurement; Low temperature sensitivity; Low power consumption.	Limited spatial resolution; Noise sensitivity; Complex electronics; Cross-talk between elements; Hysteresis
Piezoelectric	An electric voltage will be produced when a force applied to it.	No need for power supply; High reliability; Fast dynamic response; High sensitivity; High accuracy	Low spatial resolution High temperature sensitivity Inability to sense static value.
Optical	The intensity or the spectrum of light varies with the applied force.	Immune to electromagnetic fields; High spatial resolution; Wide sensing range; Good reliability	Fragile and rigid; Large size;

studies of tactile sensing focus on grasp force or pressure to prevent slip and achieve a stable grasp. The measured characteristics of touch, however, can be not only force and pressure, but also stiffness, texture, or shape. Thus, different sensing techniques are desired to be synthesized to realize a human-like tactile sensing system [36].

The following is a review of the available tactile sensing techniques which have the potential to be applied in robotic hands and specifically in prosthetic hands, namely, resistive sensors (such as strain gauges and piezoresistive), capacitive sensors, piezo-

electric sensors, and optical sensors. Table 2.2 summarizes the advantages and disadvantages of each of the aforementioned sensing techniques.

2.2.1.1 Piezoelectric sensors

Piezoelectric materials transfer mechanical stress into an electrical potential. Piezoelectric sensing is one of the few sensing techniques that do not require a power supply, which is considered an outstanding advantage. Besides, it also exhibits high sensitivity, reliability, and fast dynamic response. Its wide response range of 0 to 1 kHz makes it a good choice for vibrations measurement [37].

Various piezoelectric materials can be used for constructing piezoelectric tactile sensors. The most widely used one is polyvinylidene fluoride (PVDF). PVDF has many advantages like mechanical flexibility, dimensional stability, high piezoelectric coefficients, formability into very thin sheets ($5\ \mu m$), and relatively low price. Moreover, it has a fast and accurate response to high-frequency vibrations. Polymers such as PDMS have been used in mesa micro-structures to achieve flexible and sensitive sensors [38]. Another promising piezoelectric material is zinc oxide (ZnO) nanotransducer because of its high flexibility and biocompatibility [39, 40]. ZnO is proposed to be a good candidate material for pressure and temperature sensor to be applied to prosthetic limbs.

During the past years, piezoelectric sensors have been used for the detection of slip [39], texture [41, 42], roughness [43] and stiffness [44]. Thus, many surface characteristics can be completely determined using piezoelectric sensors. However, piezoelectric tactile sensors also have inherent drawbacks, the greatest one of which is the inability to measure static contact forces. Moreover, robustness and sensitivity to temperature are lacking.

2.2.1.2 Resistive sensors

Resistive sensors measure internal changes in resistance due to an externally applied force. Resistive sensors have been used to detect the normal force, shear force, lateral strain, and bending strain through the conversion of such mechanical changes into an electrical resistance [45, 46].

Certainly, sensors that are more useful for robotic hands are those which are more sensitive to a range of low-impact forces that would typically be experienced at the fingertips. Jorgovanovic et al. presented the static and dynamic characterization of piezoresistive sensors used for detecting the positions of prosthetic finger joints [47]. Kane et al. [48] proposed a piezoresistive stress sensor array with high spatial resolution comparable to the human dermis. It exhibited a high potential for dexterous manipulation applications. Various applications with piezoresistive tactile sensors can also be found in stress and force measurement [48], stiffness of soft tissues detection [49], and for fingertip sensing [50] etc.

2.2.1.3 Capacitive sensors

Generally, a capacitive sensor consists of a dielectric material sandwiched between two parallel conductive layers. The capacitance between the two layers varies with the deformation of the dielectric material as a result of the force applied to the sensor. The capacitive sensor is considered the most sensitive sensor for detecting small force changes. Moreover, it exhibits high sensitivity, robust performance, a large dynamic range, temperature sensitivity, and low power consumption [51]. It can be used for both dynamic and static force measurement. Additionally, their sensitivity to noise leads to relatively complex electronics for noise filtration. Many designs for pressure detection, shear force sensing, and texture recognition were proposed in the literature [52]. The capacitive touch sensor array was integrated into a prosthetic hand thumb finger in [53]. Capacitive sensors have been also deployed for multi-axis force measurement for

gripping and object manipulation, texture recognition [51], shear sensing [54], and touch screen application [55], etc. Another capacitive tactile sensor was presented for gripping force measurement with a sensor range of 0-3000 mN [53].

2.2.1.4 Optical sensors

Optical sensors have been used for tactile signal transduction, measuring optical variations across semitransparent media due to physical deformation upon contact and pressure [56]. Optical sensors maintain high sensitivity and resolution while being immune to electromagnetic interference from nearby sources [54]. These sensors are subject to less hysteresis and time response than other types of devices due to the immediate response of light intensity to strain in the device. Recently, a prosthetic finger was developed using a sensor with a looped optical waveguide [57].

2.2.2 Robot hands equipped with tactile sensors

The human tactile sense is excellent for extracting significant tactile information about the object nature [58, 59]. Most information can be obtained through the vision in autonomous manipulation of a robot hand, but when the object is obscured by the robot hand and fingertips, accurate estimation of the pose is disturbed, and accuracy is limited [60]. At this time, it needs tactile sensors that can provide accurate information. Many robotics researchers have focused on achieving human tactile sensation by deploying different tactile sensing techniques [61]. Below is an overview of sensorized artificial robotic hands, developed in the framework of research projects in autonomous manipulation and tactile sensing applications.

Mounting tactile sensors on the palm with flat surfaces is relatively straightforward, one of the simplest ways involving using double side tape. However, attaching tactile sensors on fingers and fingertips is a complex process as curved surfaces with a small radius of curvature must be considered. Many robot hands are equipped with tactile

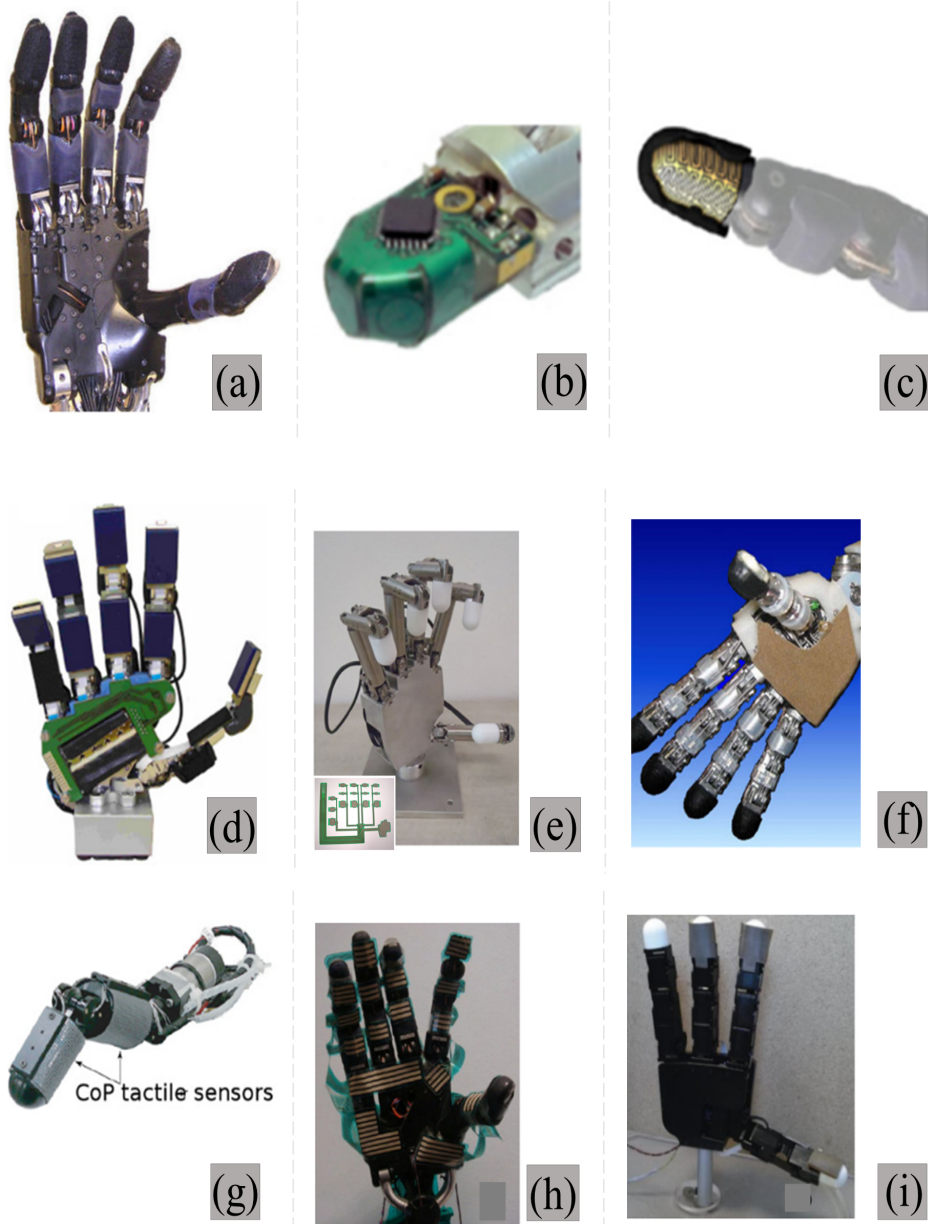


Figure 2.1 (a) Shadow Dexterous Hand that has been covered with a tactile skin [62], (b) the BioTac multimodal tactile sensor installed on the Shadow robot hand by replacing two last links of the finger [63], (c) a 3D-shaped rigid tactile sensing array with 12 sensing elements attached to the fingertip of the Shadow robot hand [50], (d) the fluidic robot hand with combined piezoelectric and piezoresistive tactile sensors that can sense high-frequency vibrations due to the absence of electric motors [64], (e) the SKKU robot hand [65], (f) the robot hand of the iCub humanoid robot with tactile sensors on the fingertips and the palm [66], (g) a finger with tactile sensor of the 3-fingered high-speed robot hand [67], (h) the Tekscan tactile sensing system consisting of 349 taxels with the Shadow robot hand [68], (i) the Allegro robot hand with PPS RoboTouch capacitive arrays [69].

sensors, especially at the fingertips [61, 70, 71, 29, 72], An example of a robot hand with tactile sensors on the fingertips, phalanges, and palm [62] can be seen in Figure 2.1.a. Tactile sensors should be either: (a) flexible and appropriately shaped to envelop a given surface, as in iCub tactile fingertip sensors (see Figure 2.1.b [73]); (b) rigid and shaped as an attachment part, e.g. [50] or [74] where a 3D-shaped tactile sensing array and an ellipsoid F/T sensor replace the fingertips of the Shadow robot hand as shown in Figure 2.1.c [75]. The Universal robot hand has 102 taxels on fingertips and 70 taxels on the rest of the links [76]. An optical tactile array of 41 taxels with the ability to measure normal and tangential forces has been placed on the tips of a two-fingered robot system [56]. Figure 2.1.d shows the Fluidic hand [77] with modified version of the Weiss sensors [78]. The dexterous Gifu III robot hand (Figure 2.1.e) has a sensing array of 859 piezoresistive taxels [79]. The robot hand of the iCub humanoid robot [80] has sensors on the fingertips and palm, but not on the middle and proximal phalanges (see Figure 2.1.f). Outstanding in speed performance, the Lightweight High-Speed Multi-fingered Hand System [67] integrates Center-of-Pressure (CoP) sensor for the force measurements and PVDF based high sensitive tactile sensor for slip detection, as shown in Figure 2.1.g [81]. Figure 2.1.h shows the Shadow Hand equipped with the Tekscan tactile sensing system (Model 4256E), which was used for contact shape recognition [68]. In another manipulating setup, off-the-shelf capacitive arrays have been installed on the fingertips of the four-fingered “Allegro” robot hand (Figure 2.1.i) [69].

In addition to the sensing system described above, some sensing systems were developed for robotic grippers. The Robotiq adaptive gripper was covered by capacitive pressure sensing arrays, which were used for the recognition of the type of the slip [82]. In [60] an 8×8 tactile array based on piezoresistive rubber has been attached onto the grippers of the 3-fingered Schunk SDH hand for classifying deformable objects.

The Seashell effect sensors [83], which also provide proximity information, have been installed on the PR2 robot grippers.

In addition to the sensing techniques explained in section 2.2.1, a wide variety of commercial sensor systems have been developed for robotic hands. The most relevant for tactile sensing are BioTac [84], Weiss [85], TekscanTM [86], Peratech [87], and DigiTacts [88]. Although these technologies are very advanced, they also present limitations. Among main issues:

- Narrow applicability (e.g., BioTac only available for fingertips)
- High power consumption (Weiss 250 mW)
- Large sensor array size and/or thickness (Peratech: large size, e.g. 15×36 cm², Weiss: large thickness, i.e. 2cm for fingertips),
- Low framerate (Weiss 400 f/s, TekscanTM 200 f/s, DigiTacts 100 f/s),
- Low resolution (DigiTacts, 22 taxels), 6) difficult system integration (TekscanTM complex wiring), and high price (e.g. BioTac).

These drawbacks limit system applicability in situations that require compact, robust, flexible, and power-efficient solutions, as for prosthetic applications.

2.2.3 Tactile sensors on prosthetic hands

Conventional sensorized prosthetic hands possess two kinds of sensors: position sensors, for providing hands with proprioceptive information, and force sensors, for estimating mechanical interactions with the environment. However, the measured characteristics cannot be limited to force or position only; ideally, they should also include stiffness, texture, shape, etc. Osborn et al. have used them in the development of a closed-loop upper limb prosthetic system that measures contact force to detect object slippage and

reduce grip strength to prevent breaking of the objects [89]. Other tactile sensors use piezoelectricity, and they are usually employed to measure dynamic forces/pressures. Southampton hand used two different types of sensors on the fingertips to restore tactile information: piezoelectric sensors based on PZT for slippage detection and FSR sensors for measuring force [90]. Finally, looking at the commercial prosthetics hands, only the Senor Hand from Otto Bock is provided with a slippage detecting system (i.e. SUVA sensor system) while the recent models such as i-Limb, the Bebionic are not yet provided with force or tactile feedback [91, 92].

2.3 Interface electronics system

The interface electronics system takes as input the tactile signals from the sensors and processes them to extract meaningful information to be conveyed to the user through the feedback interface. It includes the interface, acquisition system, tactile data processing, and decoding system. This section presents an overview of the electronic circuits dedicated to interface different types of tactile sensors (capacitive, resistive, and piezoelectric).

Many researchers have worked on developing interface electronics dedicated to acquiring and process electrical signals from tactile sensors [93, 94]. For example, Rossi et al. [95] proposed a design that could be integrated between the prosthetic limb and the patient body. The design is based on a CC3200 Texas Instruments Launchpad board and a signal conditioning circuit composed of a charge amplifier. The four input sensors signals were acquired, sampled, and then sent through Wi-Fi to the PC in continuous mode at an average 111 mA current consumption. Handling many sensors to provide high-resolution tactile information was also considered in the literature. For instance, a tactile sensor suite in [96] can handle more than 32 taxels mounted in the palm and fingers. Each finger pad carries sensors connected directly to FPGA, and all pads are

connected through an SPI interface. The tactile sensors are scanned, and the data are preprocessed in the palm unit with a power consumption of around 1.175 mW (235 mA at 5V). Schmitz et al. [66] proposed a PCB of sensors and charge to voltage converter AD7147. The AD7147 handles up to 13 inputs channels through a switch matrix and provides an I2C serial bus for communication. This allows building a chain of sensor PCBs with an I2C connection in between and a microcontroller master board connected to one of the sensor PCBs for acquiring data. Authors in [97] proposed NI-sbRIO-9632 mainboard connected to DDC112 to provide high-resolution measurements for the gas concentration of the two photo detectors inputs.

Most of the recent interface electronics are based on charge amplifier and data acquisition (DAQ) boards [98]. Despite the developments of tactile sensors and their interface electronic units presented in the literature, the developed interface electronic units were not wearable devices especially from the hardware size and energy consumption point of view. Wearable devices must be capable of performing the requested tasks with minimal time latency and minimum energy consumption, therefore, powered by a small battery size [99].

2.4 Signal processing and classification

In the robotics literature, tactile feedback has been widely used for telemanipulation, haptic devices, and prosthetic hands [72]. The use of tactile information for object exploration and recognition, material classification, and slip prediction has recently become rather popular as it is reflected in [61, 71, 29, 72]. Signal processing and feature extraction algorithms are crucial to properly decode and translate tactile sensor signals into useable tactile information. General statistical algorithms and machine learning techniques have been applied to the problem of extracting tactile information.

The Fast Fourier Transform (FFT) and Discrete Wavelet Transform (DWT) are leading techniques for preprocessing and simplifying signal output from sensors. The FFT is most used for temporal signals from sensors. For example, it characterizes surface features by correlating the frequency of pressure changes across a tactile sensor [100, 101]. The FFT captures the different frequencies of pressure changes, which can be directly used as a subset of features in machine learning strategies [102, 103]. DWT is often used only when FFT results fail to produce satisfactory features of the touched object (e.g. surface characteristic) [104]. Like FFT, DWT can also be used for feature extraction for machine learning strategies. Wavelet filters can also be applied for the processing of raw signals, DWT can be used for creating high-pass and low-pass filters that can construct the original frequency and the temporal information. Classical statistical features of the raw signal have also been used to provide engineered features for machine learning algorithms. Classical statistical features include variance, standard deviation, power, kurtosis, mean, median, max, mode, and range [105]. A combination of features from FFT, DWT, statistical measures, and raw temporal signals provides a more comprehensive description of the surrounding. Statistical and learning algorithms including decision trees (DT), support vector machines (SVM), extreme learning machines (ELM), gradient boosting machines (GBM), maximum likelihood estimations (MLE), k-means clustering (KM), and k nearest neighbors (KNN) are used to categorize and identify many properties of the touched object. Finally, Supervised machine learning algorithms with labeled training data (DT, SVM, ELM, GBM) have dominated the literature [72].

Advances in computational resources and applied algorithms have allowed for the high sampling rates and real-time processing needed for responsive feedback systems. For example, using processed signals from the sensorized hand allows for a secondary closed-loop system within the hand itself to modulate hand positions and grasping forces [106].

2.5 Feedback techniques

In this section, we will preview the different methods deployed to provide non-invasive sensory feedback as an HMI. The review will focus on the usage of such methods for restoration of the sense of touch in prosthetics and provide tactile feedback in teleoperation.

2.5.1 Vibrotactile feedback

Vibrotactile stimulation is provoked by mechanical vibration normal or transverse to the skin surface. Mechanical vibration conveys tactile information by modulating vibration frequency, amplitude, duration, timber, or spatial location [107]. The quality of vibrotactile stimulus perception depends on the frequency of the vibration ($\sim 10\text{Hz}$ to 500 Hz , which corresponds to the bandwidth of the human tactile sense) [108], the body position, and age of the subject [109]. Vibrotactile devices delivering variable pressure on the skin have been employed [110], for instance, it has been implemented to establish proprioceptive communication between the user and the robotic hand. For example, It is suitable for myoelectric prostheses and EEG- based prostheses (e.g. i-Limb myoelectric prostheses Ottobock [14], MANUS [111], Fluid [112] and Smart hands [113]) since no interference with electrical signals.

2.5.2 Electrotactile Feedback

Electrotactile (or electrocutaneous) stimulation elicits tactile sensations within the skin by passing low current to stimulate afferent nerve endings in the PNS [108]. Tactile information is delivered through electrotactile stimulation by modulating the electrical components of the pulse waveform i.e. current amplitude ($1\text{-}20\text{ mA}$), pulse waveform (monophasic/biphasic, rectangular/sinusoidal), frequency, pulse width, duration of pulse bursts, electrode properties i.e. size(small/large), conducting material and

location [114, 27]. The variety in the stimulation parameters leads to delivering high bandwidth of tactile information to the user. Electrotactile stimulation can elicit a range of sensations like tingling, itch, vibration, buzz, touch, pressure, pinch, and sharp or burning pain [115] depending on the stimulation parameter and the location. Since there are no moving mechanical parts, the electrotactile systems consume less power, have low weight, produce less noise, and respond faster compared to other tactile feedback systems. Several electrotactile displays have been developed as sensory aids for hearing [116] and vision [117] and can also be used to create perceptual illusions of surface changes [118].

2.5.3 Mechanotactile feedback

Mechanotactile feedback is modality-matched sensory feedback. It involves the use of physical pressure or tangential stretch mechanisms that elicit the sensation of applied force [119]. It has a high user acceptance despite its large weight, bulky size, and high-energy consumption since it can provide the user with a natural feeling of force and pressure unlike electrotactile and vibrotactile stimulation methods [27, 28].

2.5.4 Kinesthetic feedback

Unlike tactile feedback, force feedback relates to the kinesthetic sense, it involves positions, velocities, and forces sensed through muscles and tendons [110]. It can provide information about hand position and strength applied. Devices that provide kinesthetic feedback are usually grounded, since the display of the force or motion is delivered through a tool, such as PHANToM [120] or Omega [121]. For example, haptic clinical devices, such as robotic systems have notably been used to guide the movements of paralyzed limbs of patients [122].

2.6 High-bandwidth feedback system

In the initial years of robotics, there were very few developments of artificial skin [123]. Perhaps the earliest example of e-skin realization is from the 1970s when an artificial hand covered with skin was explored to detect grip strength, slip, and certain properties of a held object such as texture and hardness [124]. In the late 1980s, the use of infrared sensors on a large area of the robotic arm was shown to avoid contact [125]. Nowadays, robots are expected to be involved in tasks requiring physical interaction with the environment, objects, or humans. As a result, there is an increased focus on developing artificial skins with tactile capabilities [59, 126] and safe physical contact [127, 128]. Cutaneous skin-like devices have also found applications in wearable systems as the second skin or tattoolike skin to measure various physiological parameters to monitor health conditions [129–131]. In all these cases, it is important to consider the sensor distribution, the readout, and a suitable integration strategy [132]. Distributed sensing embedded in robotic systems enhances human-robot interaction and is important for safety reasons. However, a large area of tactile skin and the concomitant increase in the number of taxels present challenges with regards to optimal data acquisition and wiring. The number of sensing taxels should be easily changeable for arbitrary surfaces to enhance the performance of the system.

Endowing a robotic hand with many sensors will present a challenge in processing data and delivering tactile information to the user. The increase in the number of integrated sensors must be followed by distributed feedback channels to provide the user with high bandwidth of information about the touched object. Distributed stimulation interfaces comprise a matrix of stimulation units that are placed on the skin surface. Due to many stimulation channels with independently controllable parameters, such an interface can deliver rich stimulation patterns that are modulated in space and time, thereby providing a high-bandwidth communication channel between the

human and the machine. Matrix interfaces have been presented and tested in the past for sensory substitution [27, 133–136].

In summary, with the availability of the technology for high-density tactile sensing and electrotactile stimulation, the important goal of providing comprehensive feedback from the robotic hand to the user comes within reach. Significant research efforts had been done however still required to address the challenges. The ultimate goal is a robotic hand covered with a dense network of tactile sensors to develop the feeling of touch over the whole surface of the hand. Such a robotic hand would provide a whole new experience to the user, improving utility and facilitating the feeling of embodiment to the level that is far beyond the conventional systems based on discrete sensing and stimulation.

Chapter 3

Development and Validation of Screen-printed Electronic Skin Based on Piezoelectric Polymer Sensors

3.1 Introduction

Electronic skin (e-skin) is a touch-sensitive, electronic system that incorporates functional and structural materials coupled to a suitable electronic interface for sensor signal acquisition. Tactile data processing algorithms might provide information about contact properties (e.g., contact force [137] or contact shape [138]), given properties of the contact object (such as surface texture [139], object shape [140]), or contact events (e.g., discrimination between touch modalities [141]), to cite some examples. Artificial skin systems are implemented in a wide range of applications, such as robotics, prosthetics and teleoperation systems [61, 37, 142].

As the functional properties of the electronic skin mostly depend on the sensor type, it is worth focusing on the sensor itself. Various tactile sensors have been developed, like piezoelectric, piezoresistive, capacitive, optical, electromagnetic, ultrasonic, etc.

[61]. The development of tactile sensors based on piezoelectric polymers has been extensively investigated in recent years due to their interesting features. They exhibit high sensitivity, fast dynamic response and a large operating frequency range (from <1 Hz to 1 kHz), covering the whole frequency bandwidth of human skin mechanoreceptors [37]. Drawbacks of these materials are their poor temperature stability and their inability to measure static forces [142].

Different piezoelectric materials, such as quartz single crystals, ceramics and polymers, have been used to fabricate piezoelectric tactile sensors. Polymer materials, especially polyvinylidene fluoride (PVDF) and its (TrFE) Trifluoroethylene copolymers, exhibit ultra-sensitivity, flexibility and piezo, pyro and ferroelectric stability. Moreover, they have been proven to be good candidates for flexible tactile sensors, suitable for dynamic tactile sensing, and to be integrated into artificial electronic skin [37]. Regtien et al. [143] presented the advantages of P(VDF-TrFE) as tactile sensors, and Khan et al. [144] demonstrated fully screen-printed tactile P(VDF-TrFE) sensor arrays for robotic applications. Hsu et al. proved the strain sensitivity of PVDF-arrays on flexible substrates [145], and Tien et al. exploited the sensing multimodality with P(VDF-TrFE) gated OFETs for the simultaneous detection of pressure and temperature [146]. In general, the cross-sensitivity between temperature and pressure sensing in ferroelectrics (therefore also in PVDF) can become an issue; hence, a separation of the piezo- and pyroelectric effects may be advantageous [147].

PVDF is a semi-crystalline polymer synthesized by the polymerization of the $H_2C=CF_2$ monomer. Its copolymer, Poly (vinylidene fluoride trifluoroethylene) or P(VDF-TrFE), is a ferroelectric material that does not need to undergo the mechanical stretching of the molecular chains along one of the transversal axes, leading to easier fabrication. Different fabrication technologies have been reported for P(VDF-TrFE)-based sensors, such as spin coating, electrospinning, sol-gel, chemical vapor deposition, micromachined mold transfer and inkjet printing [148]. The frequently used techniques, such

as spin coating and inkjet printing, have limitations of process speed and overlay registration accuracy in multilayered structures. Despite the high lateral resolution, the patterning of large areas through ink-jet printing requires the repeated deposition of droplets, which often results in a nonuniform layer thickness and edges. In addition, the patterning of P(VDF-TrFE) after spin coating requires photolithography, which leads to an increased complexity of the manufacturing process. The cost-effectiveness and faster fabrication of sensors over large areas indeed make screen- printing a very attractive technique [149].

Hoda et al. recently developed fully screen-printed tactile sensing arrays (in the following: sensing patches) based on P(VDF-TrFE) piezoelectric polymers for prosthetic applications [150], where arrays of piezoelectric polymer sensors provided of their metal contacts have been screen-printed on a transparent, plastic foil. The same fabrication process has been used to design and fabricate ad-hoc sensing patches to be mounted over two different systems, i.e., an assistive sensorized glove and the Michelangelo prosthetic Hand by Ottobock [14].

The focus of this study is the validation of the manufacturing technology, i.e., ascertaining that these printed sensors are working as expected. Characterizing sensor behavior directly would be a quite complex, lengthy, risky and hardly reproducible process. In addition, direct contact of the indenter with the sensor would have various shortcomings: (1) the contact would hardly be uniformly distributed, as both the indenter and sensor surfaces have natural roughness; (2) the contact surface could then not be precisely determined; (3) the direct indenter contact leads to sensor damage. Therefore, an indirect procedure is proposed here: it requires the integration of a protective layer on top of the sensing patch, giving rise to what we call the skin patch. As sensors are embedded into the mechanical structure of the skin, a model is needed to relate the applied force to sensor charge response, accounting for stress transmission through the cover layer. The reference for this approach is a validated model of

analogous skin structure based on a rigid substrate, PVDF piezoelectric polymer sensors and the same (elastic) protective layer [151].

In particular, the study presented in this chapter reports the experimental setup and procedures which allow for a fast characterization of piezoelectric sensors embedded into an elastic layer and working in thickness mode (i.e., pure compression mode). For that, direct compression tests have been replaced by indentation tests over the skin surface, performed continuously over the whole frequency range of interest for tactile applications (<1 Hz–1 kHz). The model cited in the previous paragraph [151] has thus been used to estimate the d_{33} piezoelectric coefficient of each sensor from the measure of both a basic mechanical action at the skin surface and sensor charge, meaning P(VDF-TrFE) sensor electromechanical characterization. Finding d_{33} values aligned with expected values from the literature in turn validates each sensor and the skin fabrication technology. Finally, a protocol for quick e-skin validation is provided.

This chapter presents the analyzed results related to P(VDF-TrFE) electromechanical characterization and sensor validation by comparing the d_{33} piezoelectric coefficient with values found in the literature. It is organized as follows: Section 3.2 presents the materials and methods, briefly illustrating the e-skin design and technology, the reference skin model and the experimental setup. The results related to the validation of screen printed sensor arrays are reported in Section 3.3. Finally, discussion and conclusive remarks are given in Section 3.4 and 4.7. The content of this chapter is presented in [152].

3.2 Materials and Methods

3.2.1 Electronic Skin Design

Fully screen-printed, flexible sensing patches based on P(VDF-TrFE) piezoelectric polymer sensors have been fabricated by JOANNEUM RESEARCH [153] (in the following,

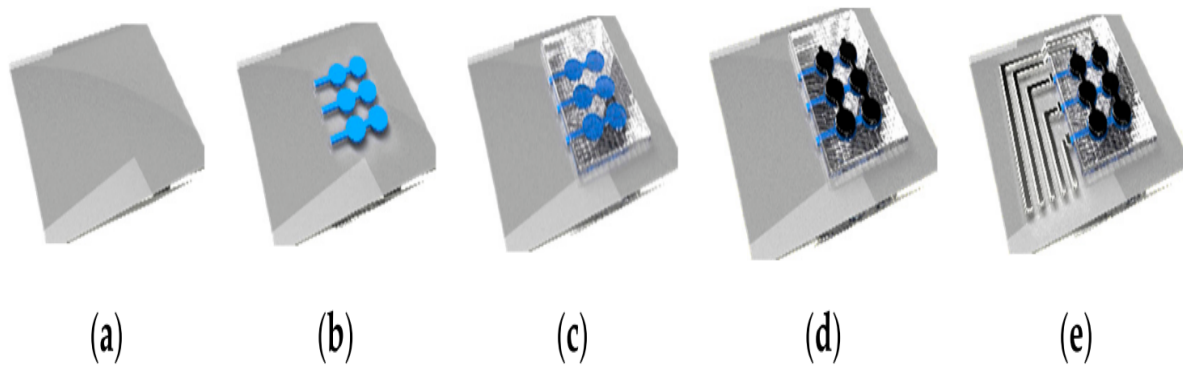


Figure 3.1 Illustration of the manufacturing process flow of printed ferroelectric sensor arrays based on polyvinylidene fluoride-trifluoroethylene P(VDF-TrFE) repeated units (reprinted with permission from JOANNEUM RESEARCH (JNR)). (a) Substrate; (b) Bottom Electrodes; (c) Active sensors based on P(VDF-TrFE) film + Top electrodes (1); (d) Top electrodes (2); (e) Connecting lines.

JNR). They patented a low-temperature, sol-gel based synthesis for P(VDF-TrFE) inks [154]. The main steps of the overall manufacturing process used by JNR to print ferroelectric sensor arrays based on P(VDF-TrFE) repeated units is illustrated in Figure 3.1. The fabrication of these sensing patches is done by screen- printing at a Thieme LAB 1000. A transparent and flexible ($175\ \mu\text{m}$ thick) DIN A4 plastic foil (Melinex® ST 725 from DuPont Teijin films, USA) is used as the substrate; it ensures high flexibility and good adhesion of the functional materials applied during the screen-printing process (Figure 3.1.a). First, the circular bottom electrodes of the P(VDF-TrFE) are screen-printed (Figure 3.1.b). In the second step, the ferroelectric polymer P(VDF-TrFE) is screen-printed onto the bottom electrodes, followed by a short curing step at $110\ ^\circ\text{C}$. The curing step supports the formation of the crystalline piezo- and pyroelectric -phase and accelerates evaporation of the solvent. Figure 3.1.c also includes the third step of screen-printing the top electrodes. Either PEDOT: PSS or silver or carbon have been used as these top electrodes [155]: it is worth noting that the carbon layer (Figure 3.1.d) is alternative to the usage of PEDOT:PSS or silver (Figure 3.1.c). Conductive silver ink has been used for electrical interconnections (Figure 3.1.e).

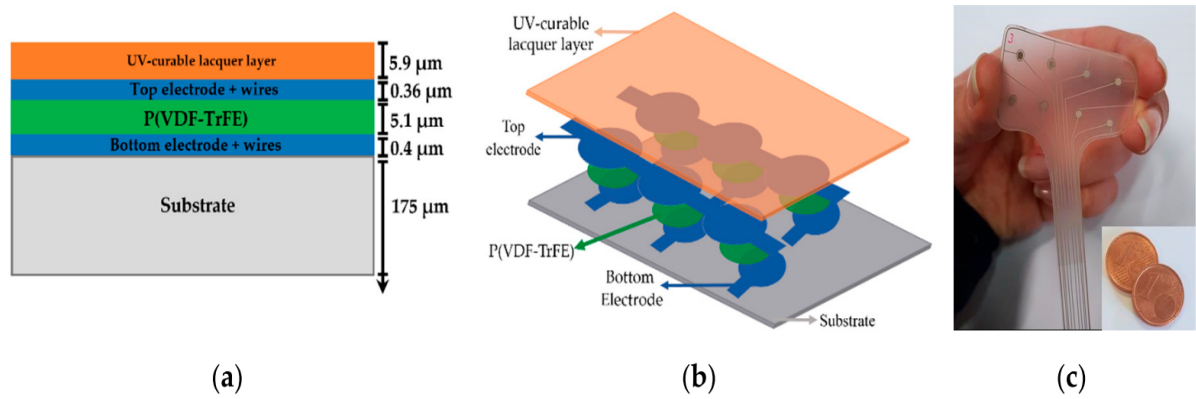


Figure 3.2 (a) Cross sectional view of a single sensor unit: Indicative thicknesses of the various layers have been extracted from scanning electron microscopy (SEM) pictures sent in private communications; (b) Sketch of the sensing patch; (c) Picture of a real sample.

A final UV-curable lacquer layer is deposited on top for overall sensor protection. The poling procedure then aligns in the thickness direction randomly oriented dipoles contained in P(VDF-TrFE) crystallites. This has been achieved by hysteresis poling of each sensor with an alternating electric field at a frequency between 2 and 10 Hz and a magnitude of 100 MV/m, corresponding to twice the coercive field strength. Final geometries of sensor array patches have been obtained through cutting the manufactured foil with a Trotec Speedy 300 laser. The full deposition process has been thoroughly presented in [142, 155], to which the reader is referred for further details. Figure 3.2 depicts (a) the cross-sectional view of a single sensor unit and (b) the structure of a sensing patch built on a sensor array and (c) a photo of Two sets of sensing patches that have been designed and manufactured. The former is intended for a textile glove with sensorized fingertips and palm, while the latter includes skin patches for the fingers and palm of the prosthetic Michelangelo Hand designed by Ottobock [14]. Sensor densities of the fingertips and of the palm have been oriented by psychophysical measurements of the spatial acuity of the human skin [59]. Usually to define the point-localization threshold, a stimulus is presented to the skin, followed in time by a second stimulus that may or may not be applied to the same site. Observers are required to say whether the two stimuli occur at the same or different locations.

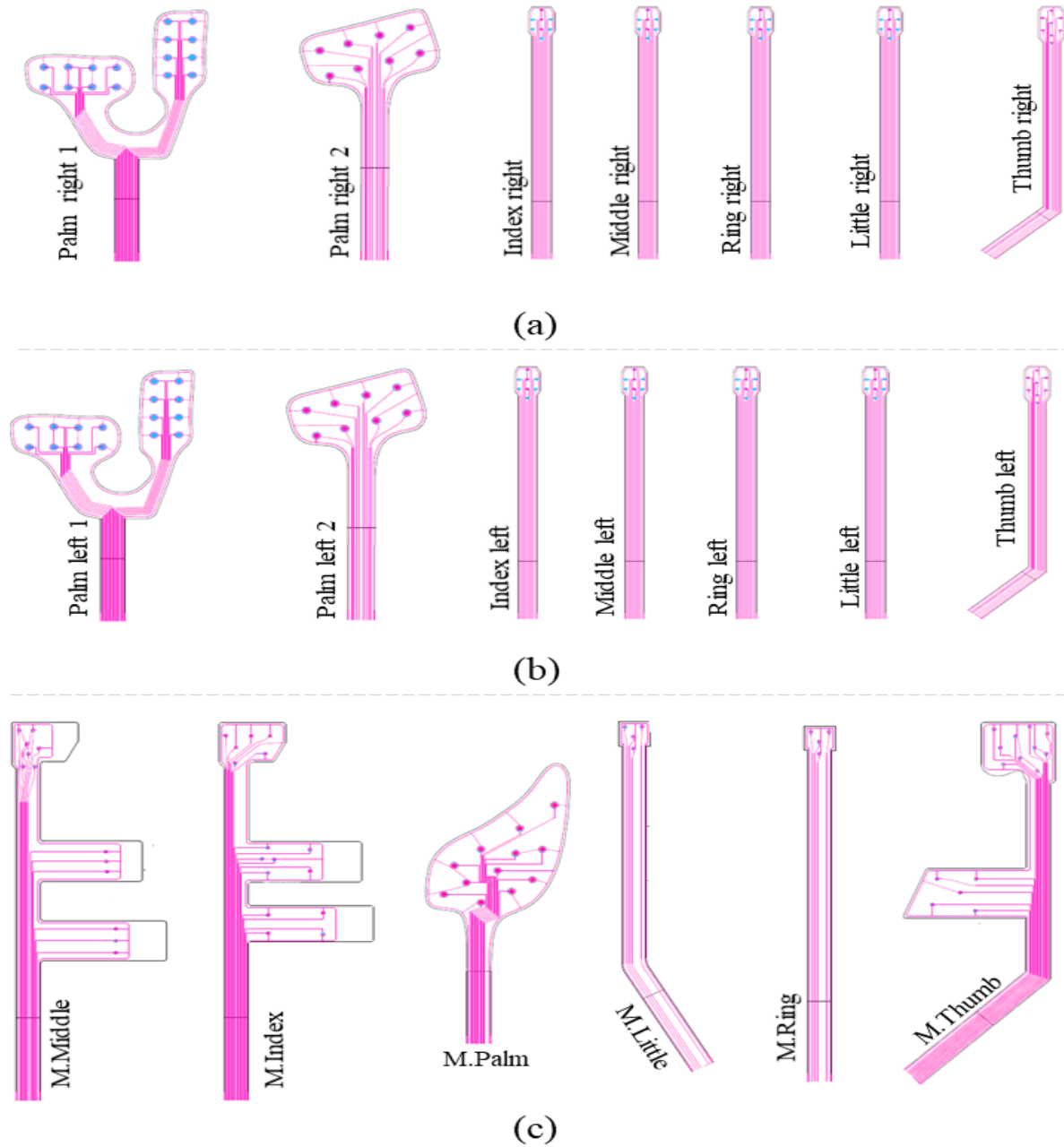


Figure 3.3 Design of different sensing patches. (a) Sensing array for right hand tactile glove: Palm 1 two 4×2 arrays 16 taxels, taxel diameter = 2 mm, center-to-center pitch = 0.9 cm. Palm 2 - 4×2 array = 8 taxels, taxel diameter = 2 mm, center-to-center pitch = 1 cm. Index, Middle, Ring, Little, and Thumb - 8 taxels, taxel diameter = 1 mm, center-to-center pitch = 1 cm. (b) Sensing array for left hand tactile glove. (c) Sensing array for Michelangelo prosthetic hand: M.Middle 13 taxels, taxel diameter = 1 mm. M.Index 16 taxels, taxel diameter = 1 mm. M.Palm 12 taxels, taxel diameter = 2 mm. M.Little and M.Ring - 4 taxels, taxel diameter = 1 mm. M.Thumb - 15 taxels, taxel diameter = 1 mm.

The point localization threshold is 1–2 mm on the fingertip and around 1 cm on the palm. These values are only for reference, as the spatial acuity of the artificial skin is strongly dependent upon the thickness and on the material of the protective layer, as demonstrated in [151]. In particular, we refer to the proportionality coefficient γ plotted in [151], which gives a measure of the skin spatial acuity through the sensor receptive field, i.e., the spatial concentration of the mechanical stress information around a single sensor. The γ coefficient depends on the thickness of the elastic cover layer, and vanishes at a distance between the point force and the sensor axis, that marks the transition to the region where the force does no longer affect the given sensor. Five different patch geometries have been experimentally characterized, and the correspondent results are presented in the current chapter. The patch layouts are shown in Figure 3.3.

3.2.2 Experimental Setup

Twelve skin patches of five categories (the A, B, C, D and E samples, as shown in Figure 3.3) were tested using the mechanical chain shown in Figure 3.5 and described in [151]. Each sensing patch was integrated on a rigid substrate and covered by an elastic protective layer, thus building a skin patch (see the bottom part of Figure 3.5). In particular, the same elastomer material has been used for stress transmission as in [151]. Building a skin structure that mimics, as close as possible, the conditions imposed by the model presented in [151] has two implications. On the one hand, we would like to enable sensors to work in a pure compressive mode. This would require that the coupling does not lead to the development of normal stresses T_1 and T_2 in the sensors which are comparable to T_3 . Operationally, in order to be able to keep the sensing patch intact for use after the validation stage, we have simply laid it over a rigid substrate with no further mechanical constraints (for better clarity, see Figure 3.6). This implies that the boundary conditions at the contact sensing patch, the rigid

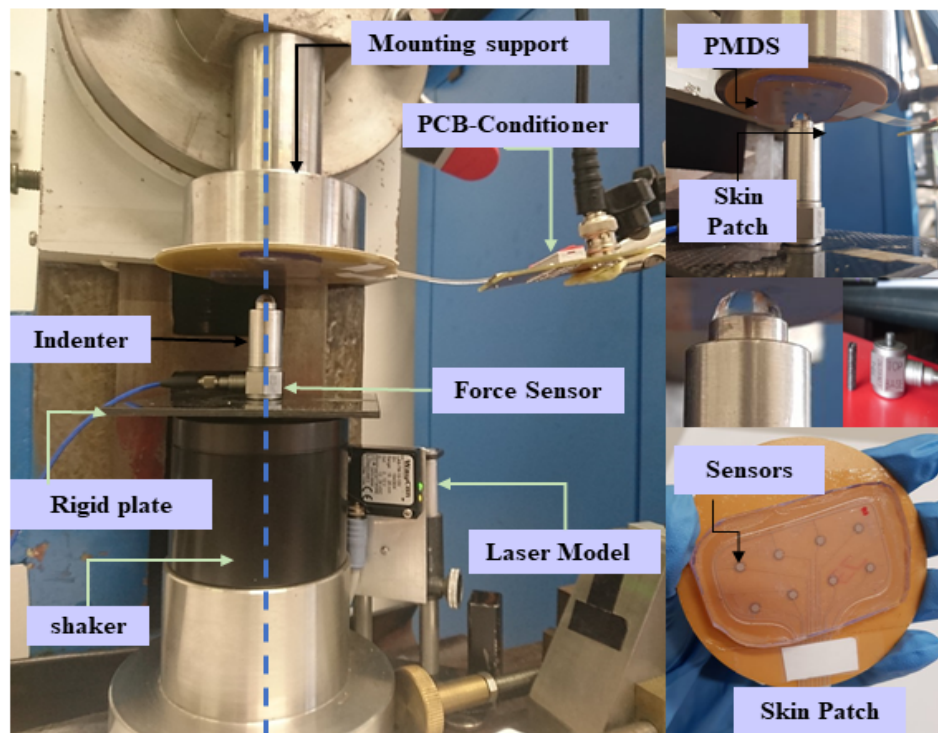
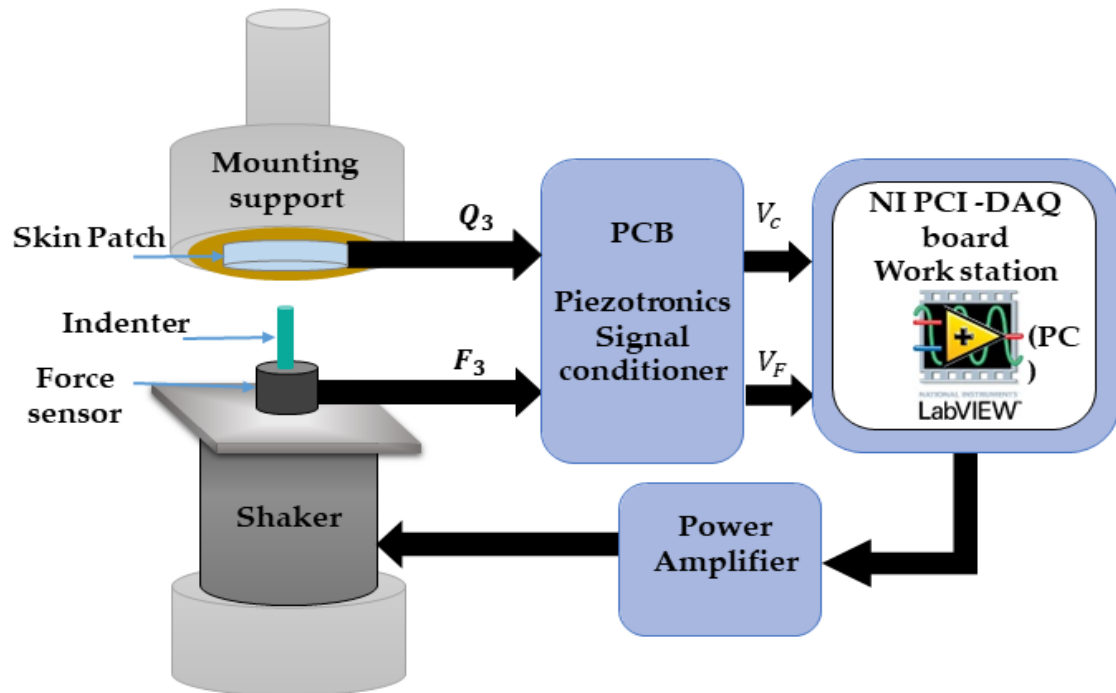


Figure 3.4 Experimental setup. Top: Block Diagram, Bottom: Pictures of the setup. The blue dotted line shows the alignment of the testing elements.

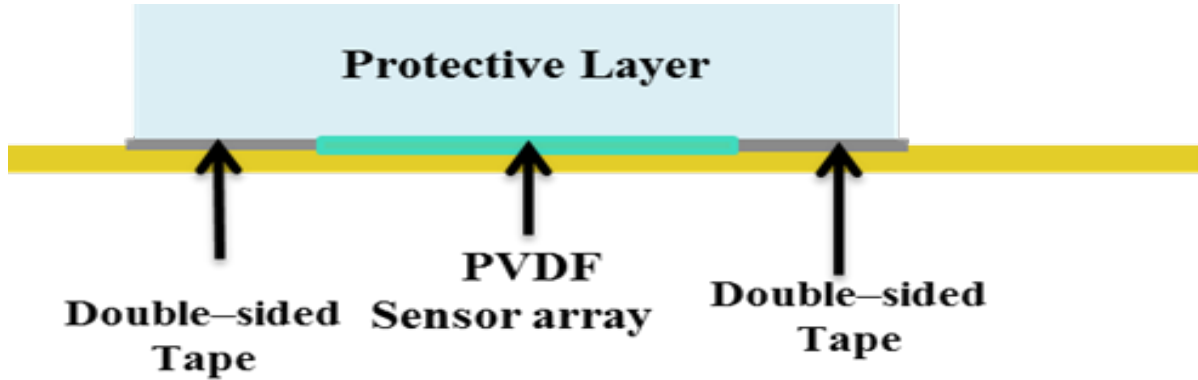


Figure 3.5 The applied coupling scenario.

substrate, would be a simple roller. On the other hand, the upper protective layer is kept in contact with the substrate, constraining the lateral boundary of its bottom surface with double-sided adhesive tape (Model 3M300L, 3M). This scheme allows one to assume a roller type boundary condition at the elastomer at the bottom with constrained boundaries. The applied coupling scenario is illustrated in Figure 3.6. A rigid plate was fixed on the moving head of an electromechanical shaker (Brüel and Kjaer, Minishaker Type 4810 from HBK company, Germany). A rigid spherical indenter ($R = 4 \text{ mm}$) and a piezoelectric force transducer (Model 208C01, PCB Piezotronics, MTS system, were coupled on the upper head of the rigid frame. The skin patch assembled on the rigid circular plate was then mounted on a fixed support and faced down side. During the tests, we applied a mechanical input (force) and measured the electrical output (charge). A preload was first applied to guarantee indenter-PDMS contact during the whole mechanical stimulation. The value of the preload has been controlled by a laser (Waycon LAS TM10), allowing us to fix the displacement of the rigid plate at a certain value for a certain preload, through displacement–force calibration curves. A swept sine signal was provided to an electromechanical shaker by a graphical user interface (GUI) developed with NI LabVIEW on a host PC and NI DAQ data acquisition board. The signal was amplified using a Power Amplifier (Type 2706). All of these elements have been accurately aligned before any test. Forces in

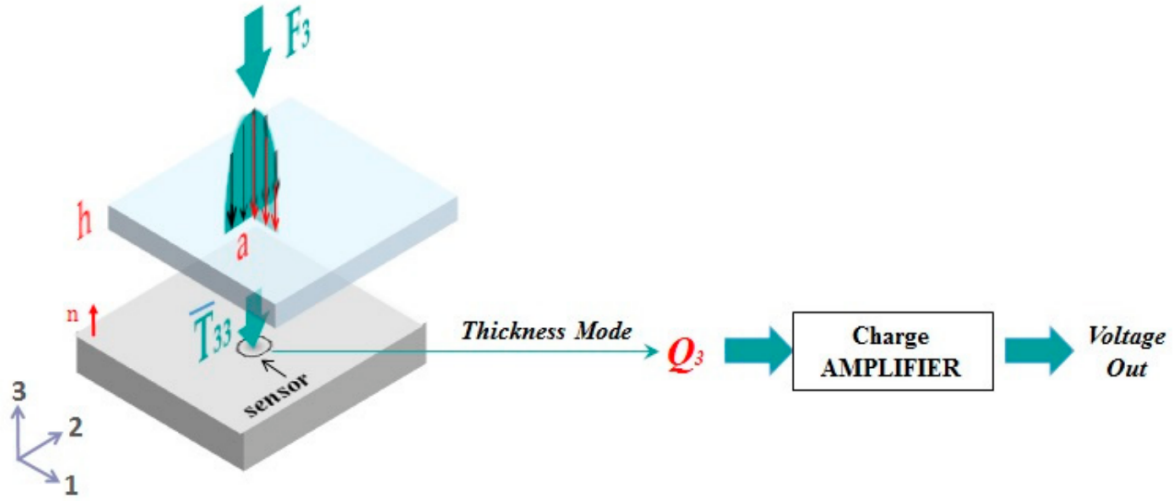


Figure 3.6 Sketch of the general working mechanism of the P(VDF-TrFE) sensor: The Hertzian input force (with contact radius a) is transmitted to the sensor (with radius r_T) through the elastomer layer of thickness h . With the presupposition that the sensor works solely in compressive mode, it directly converts the received normal stress T_3 into electrical displacement D_3 , through a characterizing piezoelectric coefficient, namely the d_{33} (1). A charge amplifier is used to convert the total sensor charge into voltage

the frequency range of (0.5–1 kHz) have been applied through the spherical indenter shown in Figure 3.5 and coupled to the electromechanical shaker. The force transducer (stimulus) and the charge developed by the sensor (response) were conditioned by PCB Sensor Signal Conditioner (482C54) and processed in frequency to give the System Response Function (FRF) at each frequency step. We recall that FRF corresponds to the ratio between the Fourier transform of the output charge and that of the input force.

3.2.3 Reference Skin Structure and Model

As mentioned in the introduction, in order to validate sensor behavior without damaging the sensors themselves, the sensing patches need to be integrated into a rigid substrate and covered by an elastomer. Hence, the indenter force is applied to the surface of the protective layer and transmitted to the sensors, working in thickness mode. In order to derive the stress acting on the sensor, our previous model [155] has been used, and is

briefly summarized below (Figure 3.7). The ultimate use of the model is to estimate the electrical sensor output (i.e., charge) from a measure of a basic mechanical action at the skin surface. In other words, using the constitutive relationship of the sensors working in thickness-mode (purely compressive), one might write:

$$Q_3 = \pi r_T^2 d_{33} \bar{T}_3 \quad (3.1)$$

where Q_3 is the total sensor charge measured by the charge amplifier [156], r_T is the sensor radius, d_{33} is the P(VDF-TrFE) piezoelectric coefficient and \bar{T}_3 is the normal stress component T_3 averaged over a single sensor. The application of the model leads to the following relationship between the charge and the applied force F_3 :

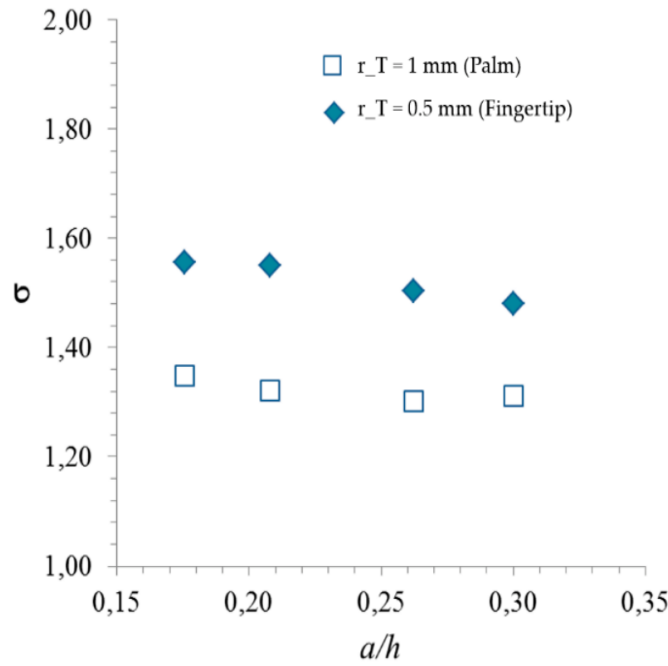


Figure 3.7 Results for the numerical COMSOL simulations for the finite case. The proportionality coefficient σ between average normal stress r_T on the sensor and overall (Hertzian) contact force F_3 (2) is plotted versus the imprint radius a (contact size) scaled by the elastomer thickness h . Note that the applied force is centered on the sensor. The two curves are associated to two different sensor sizes: $r_T = 1$ mm (sensors on the palm), $r_T = 0.5$ mm (sensors on the fingertip).

$$Q_3 = -d_{33} \frac{2}{3} \left(\frac{r_T}{h} \right)^2 \sigma \left(\frac{a}{h}, \frac{r_T}{h} \right) F_3 \quad (3.2)$$

where h is the elastomer thickness, a is the contact radius and σ is an output function of the theory, expressed as a double integral to be solved numerically, for each chosen value of $\frac{r_T}{h}$ and $\frac{a}{h}$

The radius a of the imprint is related to the applied load F_3 by the equation:

$$a^3 = -\frac{3F_3 R}{4E} (1 - \nu^2) \quad (3.3)$$

where R is the indenter radius, and E and ν are Young's modulus and the Poisson ratio of the elastic protective layer, respectively. Note that the given preload affects the contact radius a 3.3, while the amplitude of the dynamic swept sine force determines the PVDF charge. On the contrary, the dynamic component does not affect the computation of the contact radius, as the dynamic signal amplitude is negligible with respect to the preload.

For a given skin geometry, associated with a specific $\frac{r_T}{h}$, (3.2) allows one to estimate the effective piezoelectric coefficient d_{33} of each P(VDF-TrFE) sensor, once the charge Q_3 and the (normal) applied force F_3 centered on that specific sensor have been measured. Comparison with the expected value of d_{33} [142, 155] helps validating sensor functioning.

The effect of the finite thickness of the elastomer layer has been expressed by the value of σ for the given skin geometry presented in this chapter and calculated numerically through FEM simulations, as discussed in [151]. In particular, we considered an elastic, virtually incompressible, medium (Poisson ratio sufficiently close to 0.5) consisting of a layer of finite thickness $h = 2.5$ mm, length $l = 40$ mm and width $b = 20$ mm. Length and width of the layer have been chosen arbitrarily, with the sole requirement of the distance between the elastomer side and the sensor center being

much larger than the sensor radius, such as to justify the assumption that the lateral boundaries do not significantly affect the stress field acting on the sensor. The elastomer surface is presumed to be subjected to an external Hertzian pressure distribution, the contact radius a being dependent from R , F_3 , E and ν , as for (3.3). The indenter radius R is 4 mm in all the present study, the employed value for the elastomer modulus E is the result of the experimental characterization of the elastic layer reported in [151] and corresponds to 16 MPa (slope of the linear portion of the stress–strain curve), while ν is assumed to equal 0.5. As said above, the contact radius is mainly a function of the given preload, as the dynamic signal amplitude is negligible with respect to the preload itself. As discussed in the previous section, a roller type boundary condition was assumed at the lower boundary, while the perimeter is constrained. The proportionality coefficient σ , which allows to estimate the d_{33} value of each sensor (3.2), based on the measured ratio between Q_3 and F_3 , is reported in Figure 3.4. The value of the contact radius a changes with the following preload values: $PL = 0.6, 1, 2$ and 3 N. It is worth pointing out that the present results are consistent with those found in Seminara’s work [151]. As well, note that values of σ obtained for palm sensors differ slightly from the fingertip ones, as σ depends on the ratio $\frac{r_T}{h}$ (recall (3.2)). In addition, we have verified the consistency of the experimental setup for the sensing patch with the pure compressive mode assumption. Then, we have performed a series of simulations aiming to evaluate the stress tensor in the sensing patch as a function of the preload, subject to a roller type boundary condition at the bottom and free lateral boundaries. These simulations show that the normal stresses T_1 and T_2 keep at least an order of magnitude smaller than T_3 within the sensing patch. Recalling the complete constitutive relationship [37]:

$$D_3 = d_{31}T_1 + d_{32}T_2 + d_{33}T_3 \quad (3.4)$$

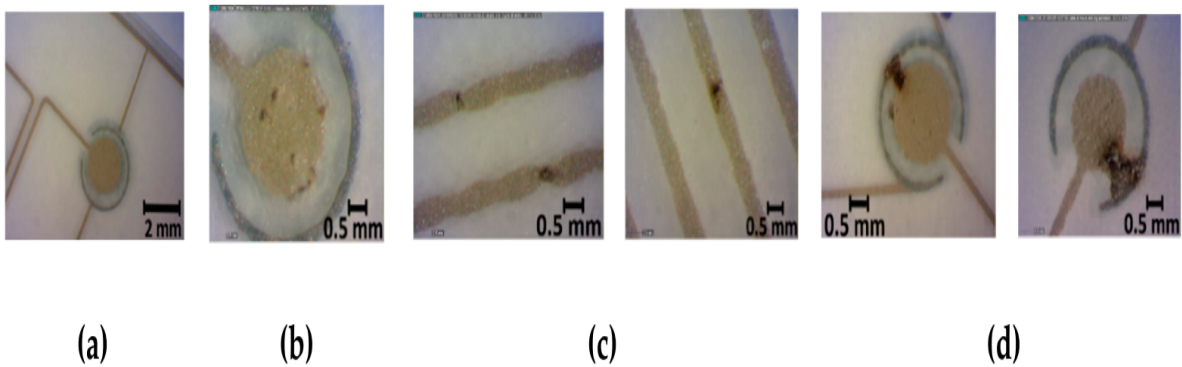


Figure 3.8 (a) Normal sensor, (b) Fault in the sensor top electrode (pole), (c) Cut in the sensor tracks, due to short circuits during the poling procedure, (d) Shortcuts between sensor tracks.

and noting that d_{31} and d_{32} are smaller than d_{33} [37], we end up concluding that the assumption of pure compressive mode was sufficiently adequate for the experimental setting.

3.3 Results

3.3.1 Morphology of the sensing arrays: Issues

All sensing patches have been visually inspected using first a photo scanner (EPSON perfection V800 photo) and then an optical microscope (Nikon eclipse LV100 and Wild M32). Some fabrication defects have been detected (see Figure 3.8). They are listed below:

- Faults in the top sensor electrode. The choice of silver ink for the top electrode has been the result of a compromise between resolution, conductivity and top-electrode performance. Using silver, the printing resolution was very good and the conductivity was very high at the 100 °C temperature treatment. At a careful examination, small defects were detected, due to solvents in the ink (Figure 3.8.b). However, this does not heavily compromise sensor behavior.

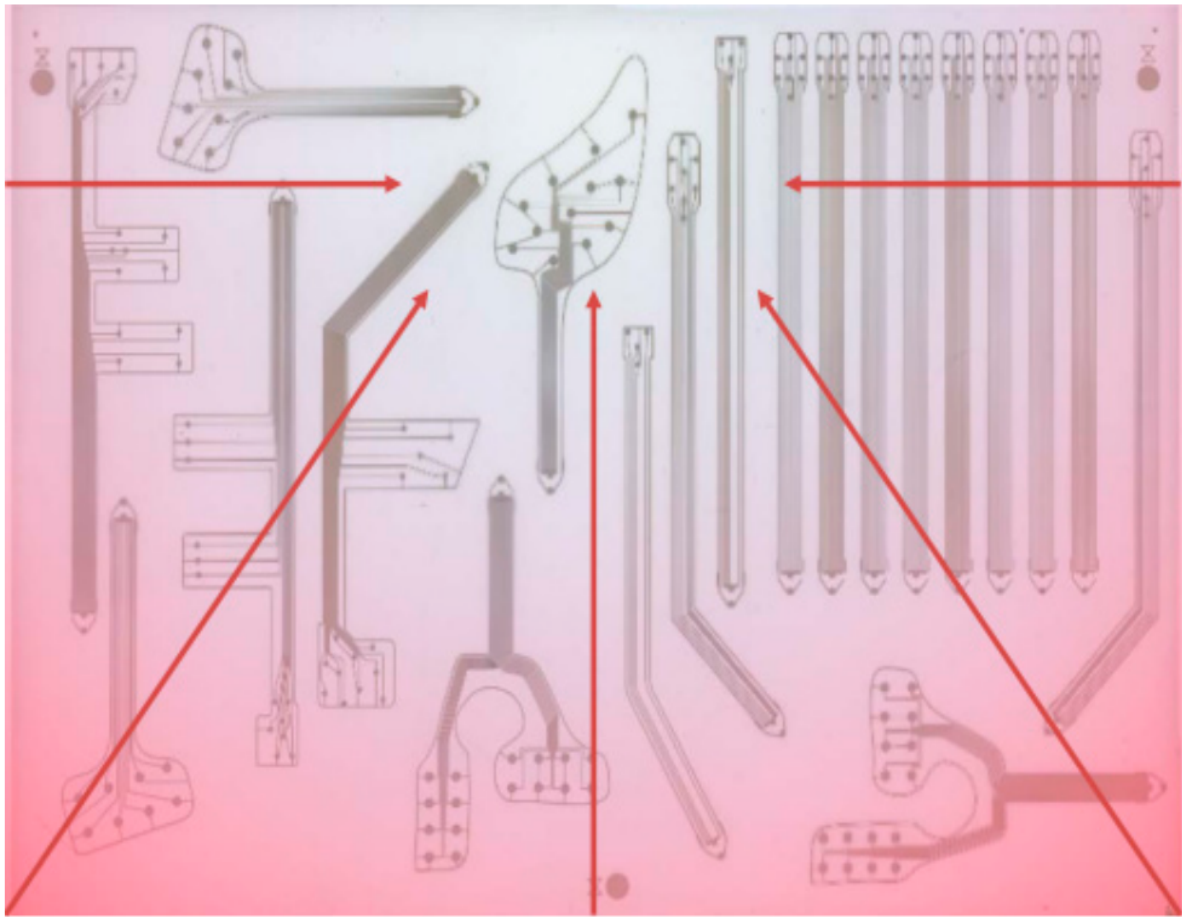


Figure 3.9 The heat map of the fabrication substrate (DIN A3) prone to shrinkage.

- Interrupted tracks (Figure 3.8.c). During high-voltage hysteresis poling, sensor lines burned for current exceeding a given threshold due to short circuits between top and bottom electrodes (caused by their too small distance).
- Short circuits. They occurred between sensor lines or due to the misalignment between top and bottom electrodes (Figure 3.8.d). The high spatial resolution led to too small distances between lines and top/bottom electrodes, causing short-circuits due to the shrinkage of the whole DIN A3 fabrication substrate during high temperature treatment. Figure 3.9 shows the heat map of the substrate prone to shrinkage. We observed that certain sensing patches (such as M.Palm) lie on the blue sweet spot, corresponding to less shrinkage. This guarantees a

larger number of working sensors. Other samples (such as palm right 2) are on the red zones, associated with high shrinkage. This causes higher number of short circuits, which in turn leads to less working sensors than expected.

In summary, the required high resolution (i.e., small sensor size, short distance between the top and bottom electrodes, short distance between the sensor tracks) is challenging. In particular, such fine structures cannot be distributed over such a large area (DIN A3) if the substrate is not dimensionally stable during all process steps (including sensor polarization). How these fabrication defects affected sensor behavior is illustrated in this Section.

3.3.2 Experimental tests

A series of experiments were conducted to extract the sensor behavior, i.e., ultimately their d_{33} values, from indentation tests on the skin surface, by using the model illustrated in Section 3.2.3. Before running each test, a preload has been applied to guarantee indenter-skin contact during the entire mechanical stimulation. As specified in Section 3.2.3, the preload is responsible for determining the contact radius a (3.3), as for all tests the amplitude of the dynamic oscillation is maintained low enough ($F_{dyn} = 0.09$ N) not to significantly affect the contact area. Different P(VDF-TrFE) sensing patches have been tested as described in Section 3.2.2. We applied a swept sine signal from 0.5 Hz up to 1000 Hz by the electromechanical shaker at each sensor epicenter on the e-skin outer surface, causing e-skin indentation aligned with each sensor center. We recorded the sensor frequency-response function one-shot over the whole frequency range. The numerical model described in Section 3.2.3 has been integrated into the LabVIEW software, directly giving the frequency behavior of the d_{33} piezoelectric modulus (both real and imaginary parts) of each solicited sensor, calculated from the sensor frequency response function as for (3.2). Sigma values have been extracted from Figure 3.4, each time in accordance with the specific preload and sensor radius.

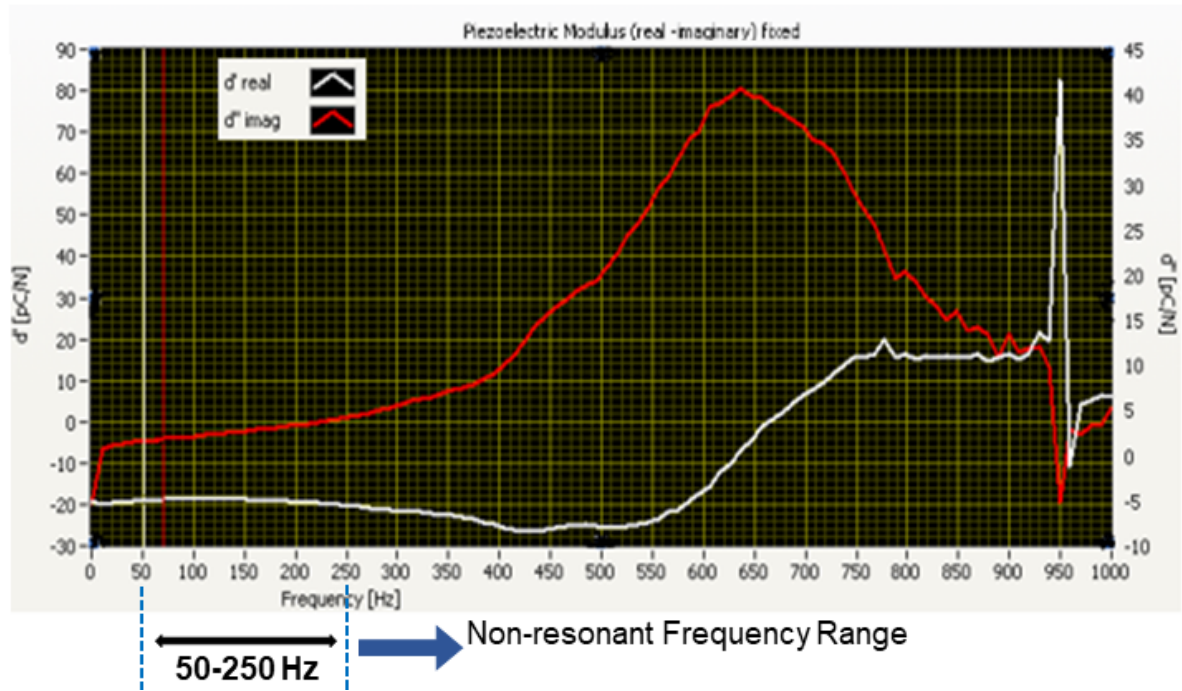


Figure 3.10 Example of the frequency behavior of both the real (white curve) and imaginary (red curve) part of the d_{33} piezoelectric coefficient. The scale for the Im ($d'' = D_{33}$) is on the right y-axis.

3.3.2.1 Frequency Range Selection

In a preliminary stage, we investigated the minimal value of the applied preload that ensured a stable behavior of d_{33} . Multiple tests at preloads less than 1 N have been run over the whole frequency range (0.5 Hz–1000 Hz), especially at preload 0.6 N. Main observation is that this low value for the preload does not ensure a stable contact during oscillations of the indenter over the skin patch, due to the dynamic amplitude of the indenter oscillation being not enough smaller than the preload itself. This causes noisy behavior for the d_{33} . For that reason, in the rest of the study, the results at this preload are not reported. Then, tests have been done at preloads 1, 2 and 3 N. It turned out that resonances do exist, and their characteristic frequencies depend upon the preload. In the 300–750 Hz range, a systematic preload-dependent resonance peak is responsible for sign flipping of the real part of the d_{33} coefficient. At low preloads (i.e., PL = 1 N) the resonance falls in the 300–500 Hz range, while at higher preloads (i.e., PL = 2, 3 N)

the resonance shifts to the 500–750 Hz frequency range. Around 950 Hz, a mechanical resonance appears due to high vibrations from the shaker system while stopping. As reported in Seminara’s work [151], resonances may derive from a variety of causes (e.g., movable contacts, contact surface asperities, motor-induced vibrations), which cannot be reliably controlled. The model can only be applied with dynamic contacts with forcing frequencies that fall outside the range of any notable resonance [151]. Therefore, a non-resonant 50–250 Hz frequency range has been identified, where the frequency response function is systematically quite flat. In particular, the imaginary part of the d_{33} piezoelectric coefficient, which accounts for any viscoelastic component of the response, is systematically roughly an order of magnitude smaller than the real (elastic) part. The aforementioned statements are clarified in the representative example reported in Figure 3.10, where both the real and imaginary parts of d_{33} are expressed as a function of frequency, and the non-resonant.

Based on these results, hereafter the imaginary part of the d_{33} coefficient will be ignored and “Re” will be removed from the notation. In other words, the system is treated as purely elastic. Moreover, each run has been performed, stimulating the skin over the whole frequency range, yet the corresponding d_{33} response is averaged over the non-resonant range only.

3.3.2.2 Systematic sensor validation

Each sensing patch has been tested by stimulating the e-skin surface with the same indenter ($R = 4$ mm) aligned with the epicenter of each selected sensor. As mentioned in Section 3.3.2.1, each run has been performed at small force amplitude ($F_{dyn} = 0.09$ N), and the corresponding d_{33} response has been averaged over the non-resonant range to get a single value of that coefficient for each sensor. Two sets of data have been obtained. The former data set (96 sensors in total, 10 different samples, four categories of patches) focuses on Palm sensors (i.e., sensors with diameter = 2 mm, belonging to

Table 3.1 Palm patches categories (Data set 1, palm sensors)

Category	Category name	Number of tested patches	Number of sensors\patch
Category 1	Palm left 2	3	8
Category 2	Palm right 2	4	8
Category 3	Palm right 1	1	16
Category 4	M.Palm	2	12

arrays designed to cover the palm), all tested at different preloads (Figure 3.11). On the other hand, the second data set (eight sensors, two samples, Michelangelo little) focuses on finger sensors (i.e., sensors with diameter = 1 mm, belonging to arrays designed to cover the fingertips). One-way analysis of variance (ANOVA) and Tukey–Kramer’s honestly significant difference (HSD) test, for the post-hoc pairwise comparison, were used to test the statistically significant difference in the mean performance among the tested conditions.

- **First Analysis: Palm Sensors** We selected four palm patch designs that vary in their positions and sensor number. These designs have been classified into four categories as reported in the Table 3.1 below. Figure 3.11 illustrates how these categories are distributed over the A3 substrate used for patch fabrication. A comparative study has been performed to examine whether the shape and position over the A3 fabrication substrate affected the sensor behavior at different preloads.

Sixty seven sensors out of the whole set (96 sensors) have been selected, eliminating sensors that did not work due to fabrication failures (see Section 3.3.1) and few sensors that gave physically unacceptable values for d_{33} . Note that the number of malfunctioning sensors was quite high for this first fabrication batch, due to those issues discussed in Section 3.3.1. Figure 3.12 shows the cloud distribution of the averaged d_{33} values for the palm sensors.

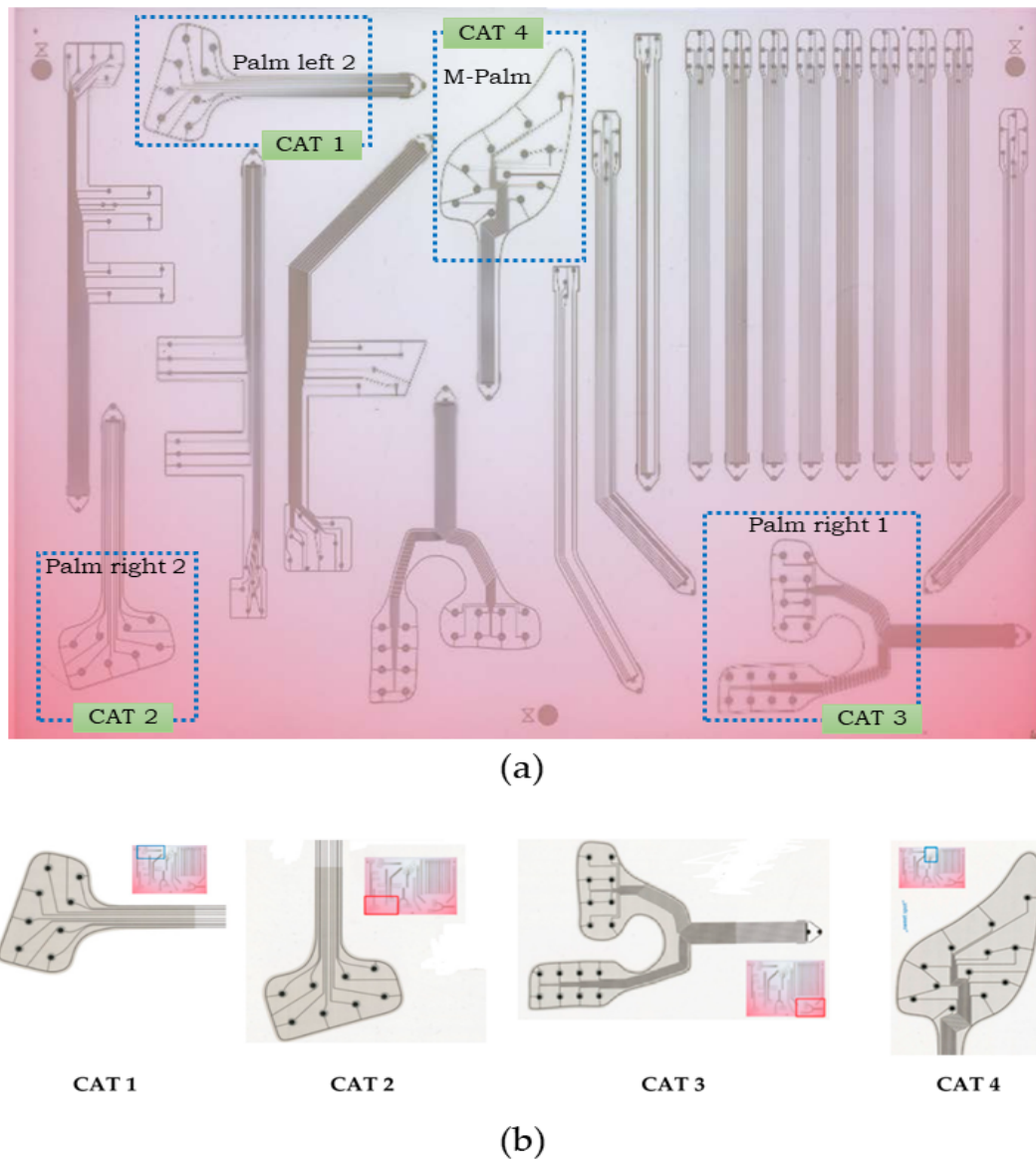


Figure 3.11 Compared categories (CAT1, CAT2, CAT3 and CAT 4) and heat map on the A3 fabrication substrate. (a) Heat map of the fabrication and the selected categories for testing, (b) Zoom in view for each category's location.

All categories have been analyzed in order to check whether any dependence of the patch behavior on the specific category existed. This was needed to understand if a specific patch position affected sensor behavior, e.g., due to not uniform polarization or other unwanted effects related to the shrinkage of the substrate during the fabrication process. The results presented in Figure 3.12

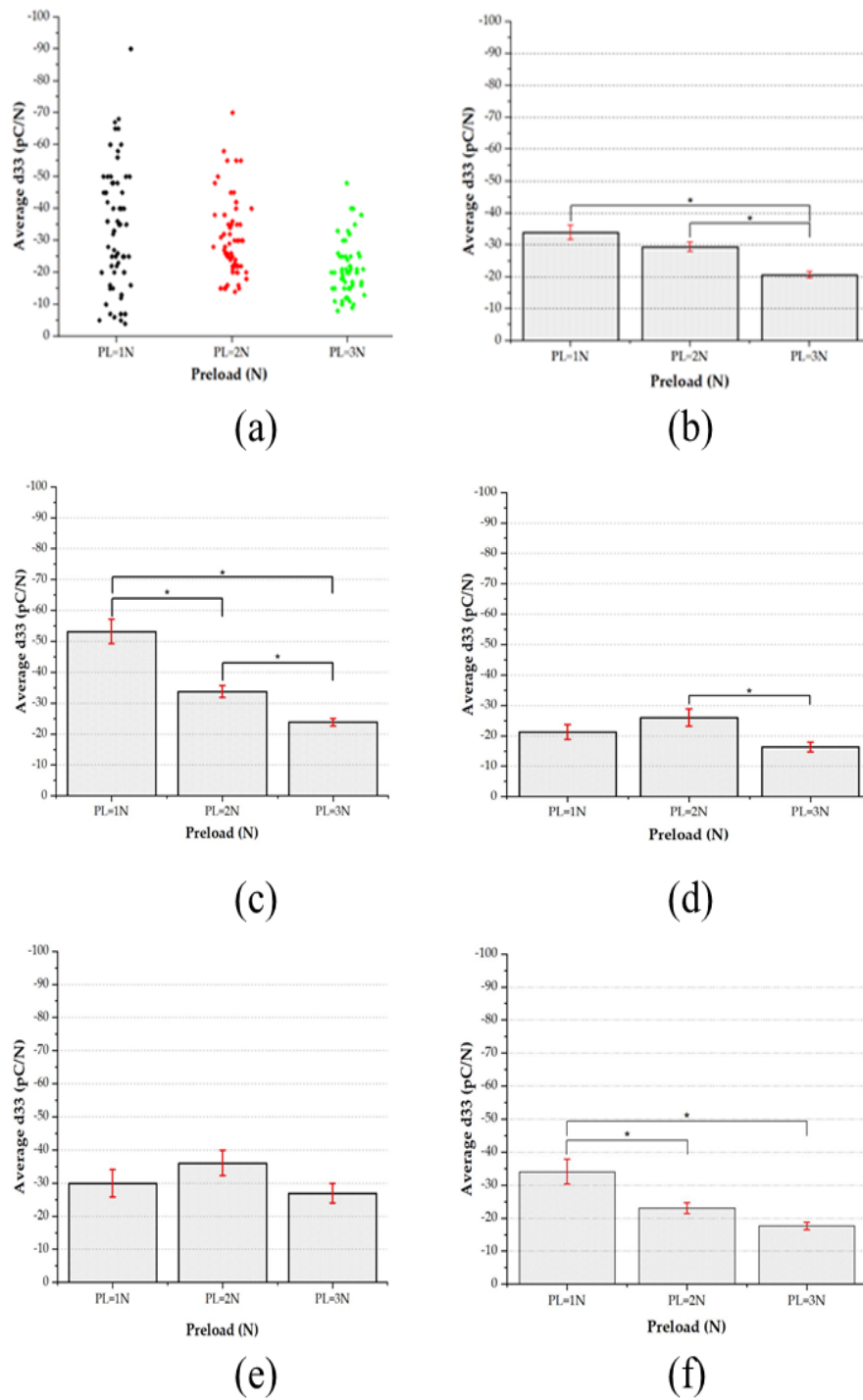


Figure 3.12 (a) Cloud distribution of working palm sensors. (b) Working palm sensors (c) Category 1 (palm left 2). (d) Category 2 (palm right 2). (e) Category 3 (palm right 1). (f) Category 4 (M.palm). Statistical study: One-way analysis of variance (ANOVA) ($p < 0.05$), average d_{33} vs preload.

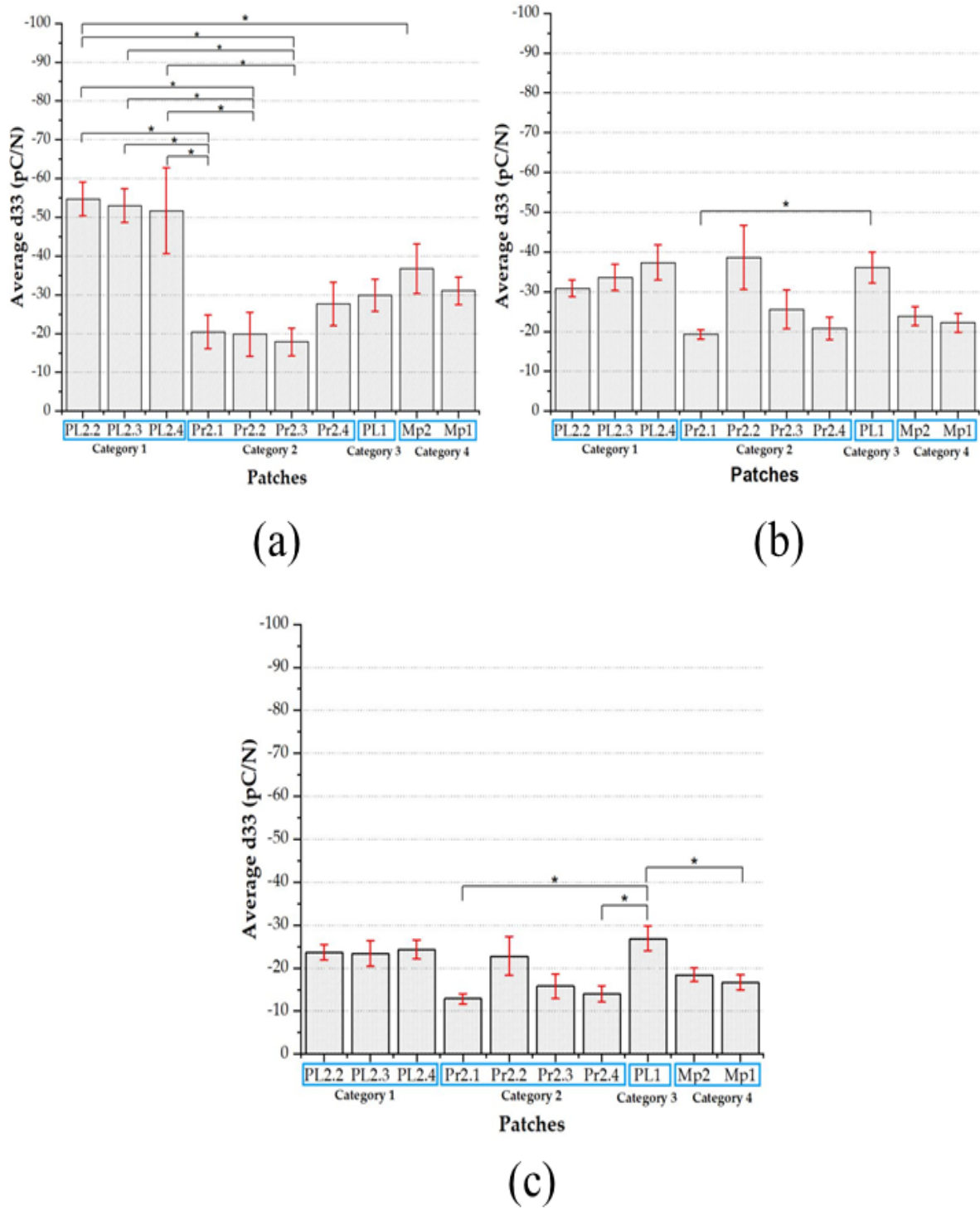


Figure 3.13 Average d_{33} vs. patches at PL = 1 N, 2 N, and 3 N, arranged respectively as (a), (b) and (c). The four categories and all corresponding patches can be distinguished on the x-axis.

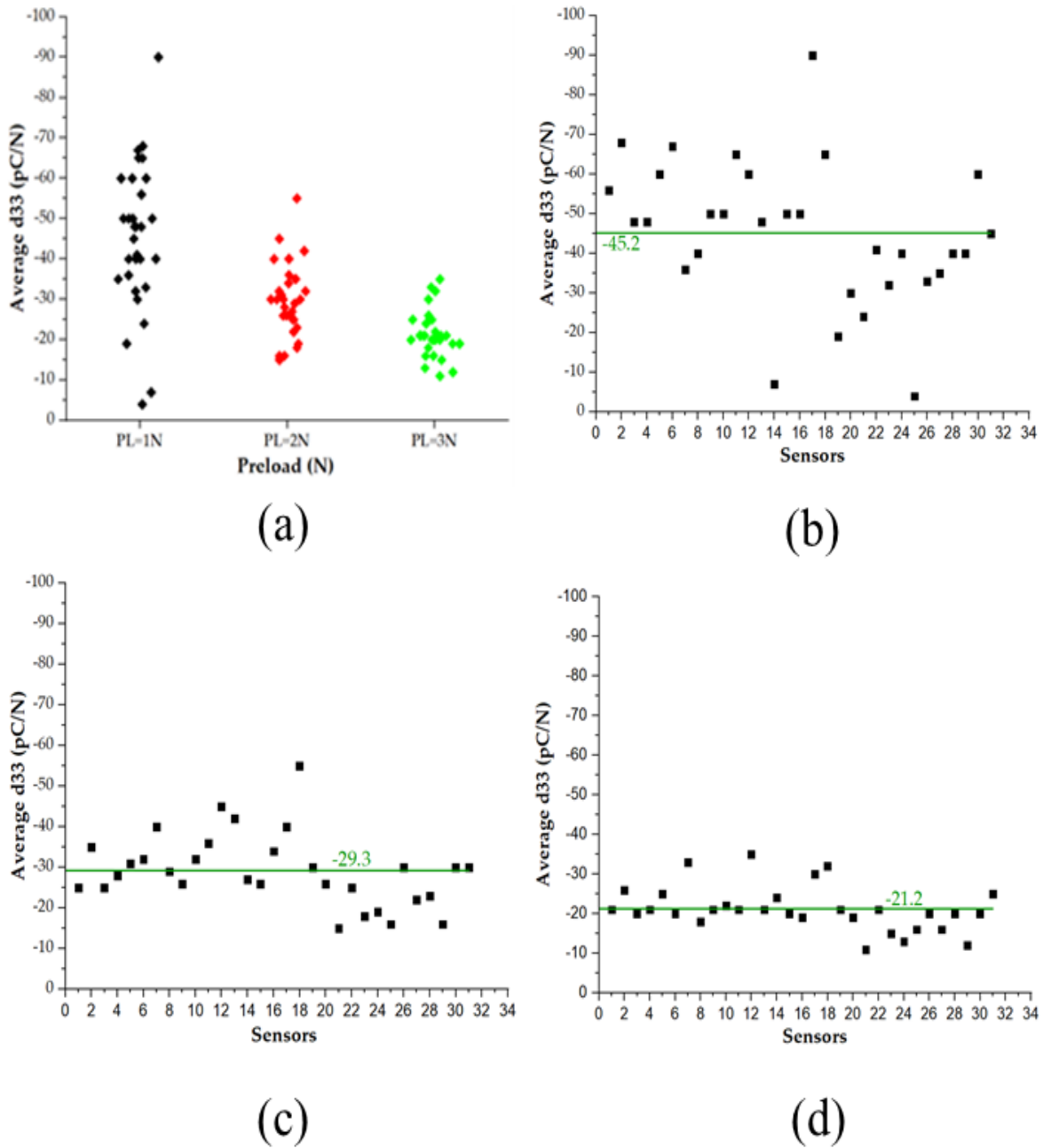


Figure 3.14 (a) Average d_{33} vs. preload. Sensors belonging to categories 1 and 4, only. To avoid dot superposition, values associated with the same preload are plotted such that dots do not lie on the same vertical line. Average d_{33} for each sensor at PL = 1 N (top), 2 N (middle) and 3 N (bottom). (b) Average d_{33} for each sensor at PL = 1 N, (c) Average d_{33} for each sensor at PL = 2 N (d) Average d_{33} for each sensor at PL = 3 N

show that indeed sensor response to preload does significantly depend on the category, which is associated to a specific position on the substrate. In particular,

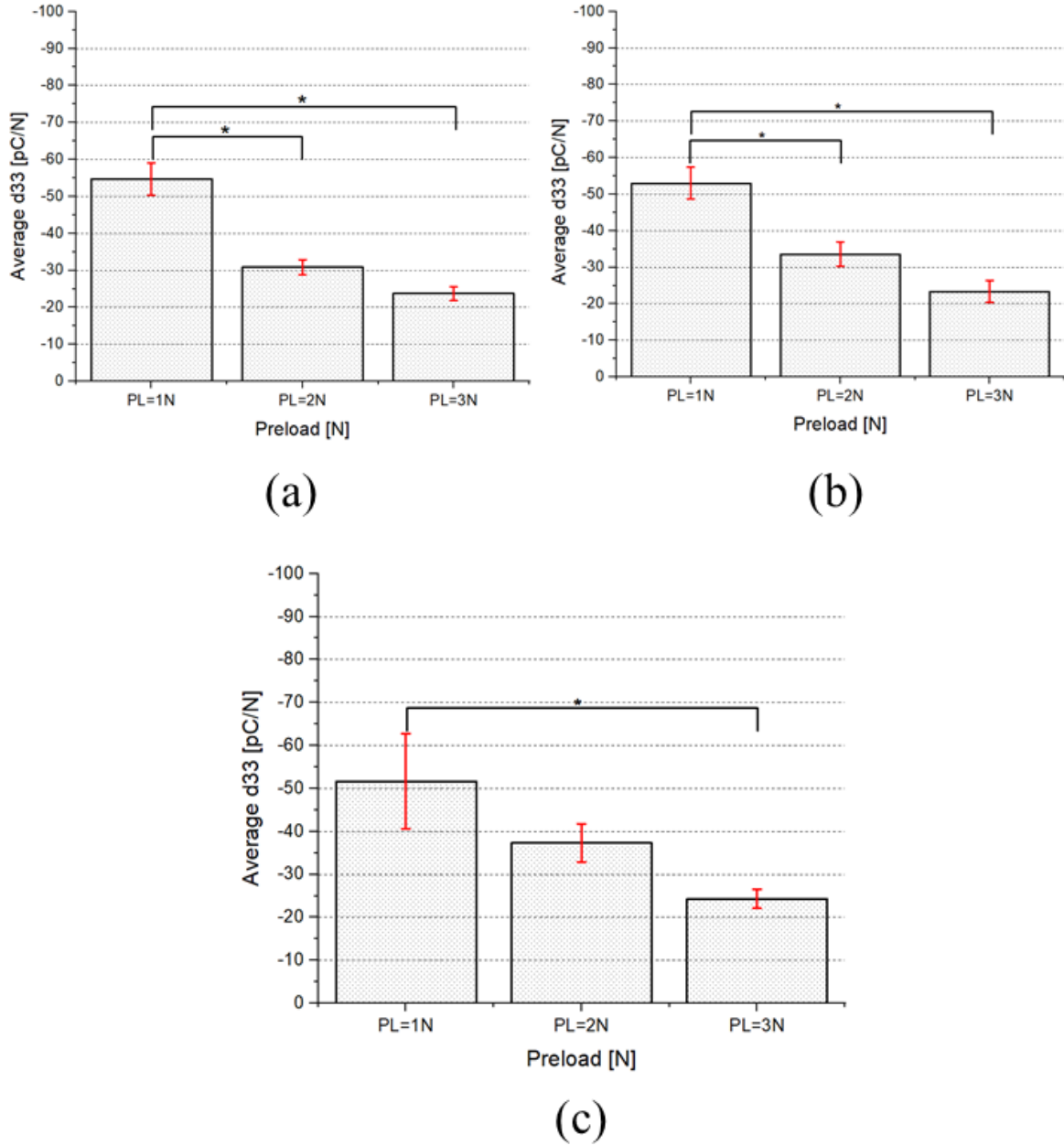


Figure 3.15 Average d_{33} vs. preload for the three analyzed patches belonging to category 1: (a) Palm left 2.2., (b) Palm left 2.3 and (c) Palm left 2.4 (bottom).

note that results for categories 2 (Figure 3.12.b) and 3 (Figure 3.12c) show a dependence of d_{33} on the preload, which turns out not to be statistically significant. It is worth pointing out that categories 2 and 3 are those located in the red zone of the heat map, where strong substrate shrinkage occurred. In order to check the effectiveness of the sensor fabrication technology, we have then decided to

discard results referring to categories 2 and 3. On the other hand, it is reassuring to note that, as shown in Figure 3.13, patches belonging to the same category (including those in the red zone) are statistically equivalent among themselves, a result which does suggest the reproducibility of the fabrication process for each patch. Results for all sensors belonging to the two categories located in the sweet spot associated with low shrinkage (i.e., categories 1 and 4) are plotted in the Figures 3.14 and 3.14. They show d_{33} values mostly compatible with the state of the art [142]. It turns out that as the preload increases, the average d_{33} decreases, and values for different sensors exhibit a lower dispersion. In Figure 3.14, a best-fit line is used to compute the average of the d_{33} values associated with all sensors. Data related to the highest preload (=3 N) are well fitted using a d_{33} value equal to approximately 22 pC/N, while data corresponding to the lower preload (=1 N) yield a d_{33} value of approximately -46 pC/N. To conclude results on the first batch, we have performed a more detailed analysis of results obtained for category 1, analyzing the behavior of each patch belonging to that category. Results are plotted in Figure 3.15, which shows a statistically significant systematic decrease of the d_{33} coefficient with a preload for all three patches.

- **Second Analysis (Preliminary): Finger Sensors** A complementary case study has been performed in order to check whether the proposed method could be extended to sensors with lower diameter (i.e., finger sensors) or not. To this aim, a second data set only including finger sensors was analyzed. It is worth remarking that the alignment procedure was particularly critical in this case: the small sensor size would require an alignment system to more precisely align the indenter with the sensor center for reliable sensor characterization using the current model. This is the reason why this analysis has been only performed on a low number of sensing patches. Two samples of Michelangelo little finger located on the sweet spot (see Figure 3.16-Top) were tested using the experimental setup

and method reported above. Each sample has four taxels with 1 mm diameter each. Figure 3.16 shows the analyzed results after applying one- Way ANOVA using Tukey–Kramer’s HSD test. As for the palm, the results indicate a significant statistical difference of d_{33} at different applied preloads and a systematic decrease of d_{33} at increasing preload.

3.4 Discussion

Table 3.2 shows a conclusive summary of the findings which emerged from the different experimental studies performed. A broad outcome of the performed tests is that both palm and finger sensors share the same statistically significant systematic decrease of d_{33} with preload. In the first analysis, for all categories, the patches are statistically equivalent among themselves when belonging to the same category, which proves the reproducibility of the whole deposition process. Excluding categories located in the red zone (i.e., CAT 2 and CAT 3) of the heat map, which is associated with high shrinkage, the single sensors belonging to the other two categories (CAT 1 and CAT 4) show a piezoelectric behavior (i.e., d_{33} values), which is quite compatible with the current state of the art [145]. On the other hand, the behavior of the d_{33} versus preload for CAT 2 and CAT 3 in the red zone shows no alignment with the decreasing behavior observed for patches located in the sweet spot. This result is a hint at the need of employing smaller fabrication substrates in future e-skin manufacturing, in order to considerably reduce red zones, which are not compliant to the expected sensing behavior.

Focusing on categories located in the sweet spot, all analyzed patches belonging to categories 1 and 4 have quite systematic decreasing behavior for d_{33} vs. PL. This has been checked using one-way ANOVA for statistical analysis and Tukey–Kramer’s HSD test for the post-hoc pairwise comparison. Systematically, average d_{33} behavior at PL = 1 N is statistically different from that at PL = 3 N, both for the two categories

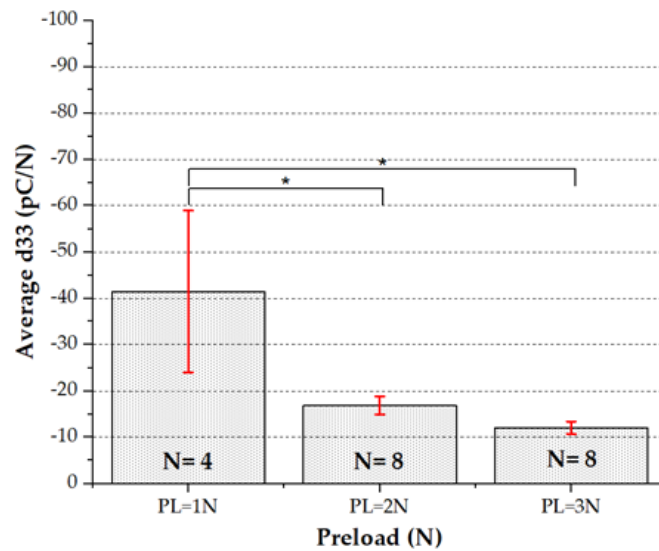
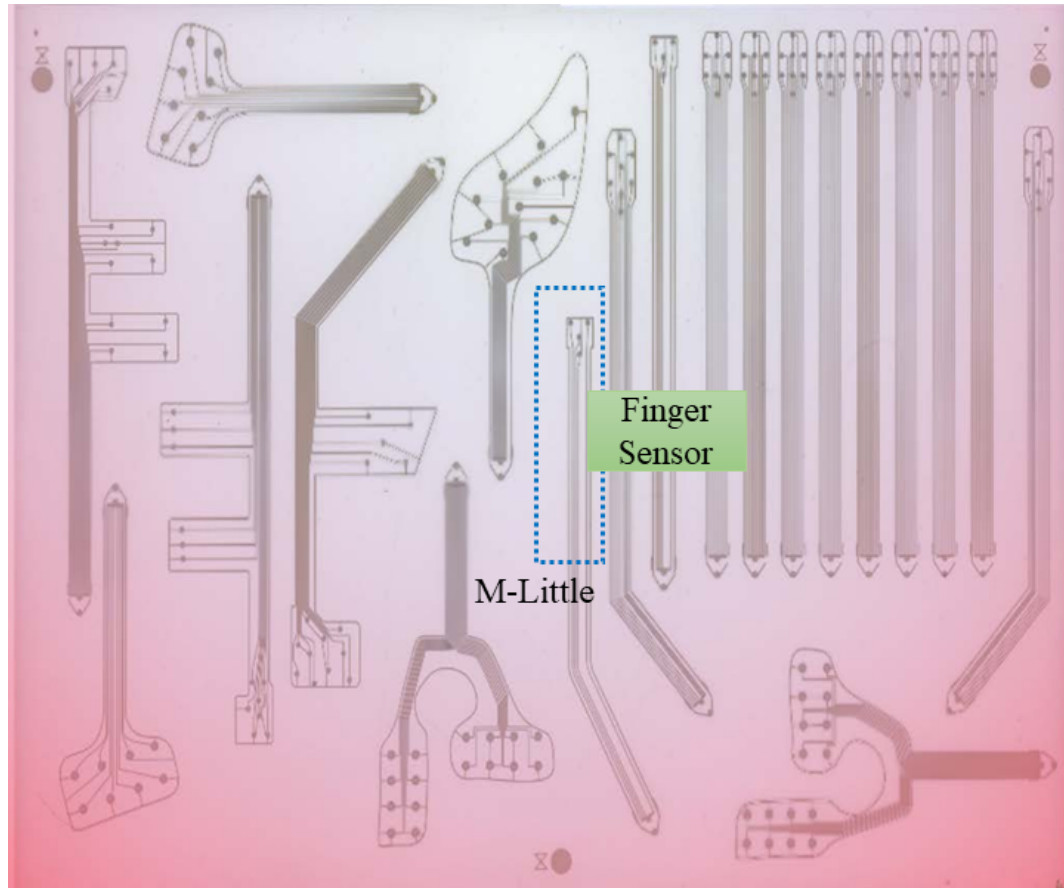


Figure 3.16 Finger sensors (Michelangelo Little, ML) located in the sweet spot on the heat map of the A3 fabrication substrate. Bottom: Average d_{33} vs. preload for the two samples of Michelangelo little: ML.1 and ML.2. Statistical study: one-Way ANOVA ($p < 0.05$)

Table 3.2 Summary of results.

Sensor location	Study	Number of patches	Preload	working sensors	Average d_{33}	Standard Error
Palm	All sensors	10	PL = 1 N	67	-34.014	2.29
			PL = 2 N		-29.49	1.47
			PL = 3 N		-20.65	1
	Category 1	3	PL = 1 N	18	-53.22	3.98
			PL = 2 N		-33.77	1.91
			PL = 3 N		-23.88	1.23
	Category 2 (red zone)	4	PL = 1 N	23	-21.26	2.39
			PL = 2 N		-26.04	2.83
			PL = 3 N		-16.34	1.58
	Category 3 (red zone)	1	PL = 1 N	23	-29.92	4.13
			PL = 2 N		-36.07	3.84
			PL = 3 N		-26.92	2.89
	Category 4	2	PL = 1 N	13	-34.07	3.75
			PL = 2 N		-23.07	3.75
			PL = 3 N		-17.61	1.14
Finger	All sensors	2	PL = 1 N	4	-41.5	1.14
			PL = 2 N	8	-16.87	1.95
			PL = 3 N	8	-12.06	1.35

(Figure 3.12.a,d) and for single patches from category 1 (Figure 3.14). This would be compatible with a non-linearity of d_{33} with respect to the preload, and with some nonlinearity in the stress–strain curve observed for this elastomer layer around 2 MPa [154]. In the second analysis, similar results were obtained for the finger sensors, despite the high distribution error, which emerges from the low number of sensors tested.

The dispersed behavior of d_{33} (i.e., sensor response) does depend on both the fabrication process (including deposition and assembly) and on the alignment of the indenter with the sensor center. A laser-like positioning system could be used in the future to align the indenter precisely, thus avoiding errors due to wrong positioning. As for the fabrication process, these errors are the results of different factors including different point-to-point values for the sensor radius and/or for the local layer thickness and inhomogeneity in PVDF film polarization. These combined factors are considered intrinsic in the whole fabrication process, and could not be decoupled in the proposed tests.

In Section 3.2.3, we described how we coupled the sensing patch to the substrate and to the protective layer, to be able to test sensor behavior without damaging the sensors themselves. Applying double-sided adhesive tape all over the sensors in the validation stage is not feasible unless the cover layer is the final layer, because sensors would be damaged during tape removal (Figure 3.17).

It would be also better to avoid the adhesive tape between the substrate and the sensors themselves, as damages may occur during tape removal.

Therefore, the choice of the coupling procedure is somehow obliged in the validation stage. Operationally, as described in Section 3.2.3, we placed double-sided adhesive tape around the sensing patch (Figure 3.18, solution1), to rigidly couple to the substrate the protective layer on its boundaries, thus keeping in place the sensing patch itself. We also proved through simulations that this configuration leads to negligible normal stresses other than T_{33} , thus confirming that sensors work in thickness model, as required by the model.

However, this coupling procedure can only be used in the validation stage, as discussed in the following. In real applications shear contact forces on the skin surface will be possible, which requires using a real rigid coupling between the sensing patch and both the cover layer and the substrate (Figure 3.18, solution 2), to avoid any sliding

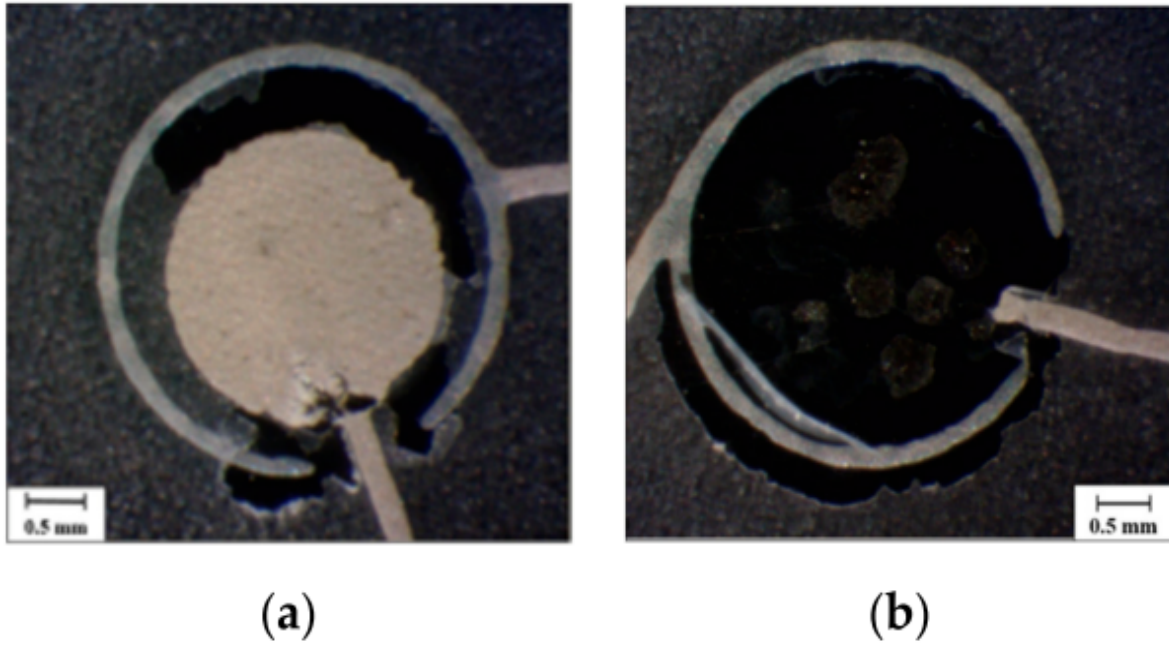


Figure 3.17 Sensor electrodes have been severely damaged after coupling with adhesive tape all over the skin patch. (a) An overall adhesive tape coupled sensor, (b) Impaired top electrode of sensor after removing the adhesive tape.

due to shear forces. This is achieved in practice by using an adhesive layer below and all-over the sensing patch itself. Care would only be needed during tape integration as non-uniform stress transmission and sensor bending can be naturally induced by the inclusion of air bubbles into the coupling adhesive layer. An underestimation of the d_{33} value is expected due to the addition of deformable adhesive layers between the sensor and both the substrate and the cover, which are not accounted for in the model. This leads not to be perfectly compliant with the model, as normal stresses other than T_3 may contribute to the measured charge: preliminary simulations confirmed this prediction and hint at a contribution of normal T_1 and T_2 stresses, which is not negligible with respect to the normal T_3 component. New models and more extensive simulations will be thus needed to describe the real application system.

A time-saving protocol for future sensing patch validation can be extracted as an outcome of the analysis presented in this chapter. It could be summarized as

follows. As a first step, the sensing patch is to be coupled to the rigid substrate by only applying double-sided adhesive tape around the patch perimeter (Figure 3.18, solution 1). As shown in Figure 3.18 solution 1, the protective layer can then be applied on top of the sensing patch, being rigidly coupled to the substrate through the double-sided adhesive layer. After mounting the skin patch built as such along the mechanical chain illustrated in Figure 3.5, the indenter is to be aligned with a reference sensor. A laser positioning system would facilitate such a procedure, thus reducing the dispersion of sensor behavior. Avoiding complete systematic measures at different preloads, which are not needed if the scope is a check of the sensor manufacturing process, an indentation test over the non-resonant frequency range (50–250 Hz) can be quickly run at an average preload (i.e., =2 N). This procedure lasts no more than a few seconds. The indenter is then released and moved over a distant sensor, to avoid artifacts due to the relaxation of the protective layer after indenter release. The same procedure as before is performed, consisting of applying the given preload, running the indentation test, releasing the indenter and moving the indenter over a distant sensor. The same scheme is applied on all sensors belonging to the sensing patch. The result of the whole procedure is a single value of the d_{33} piezoelectric coefficient for each sensor, averaged over the non-resonant frequency range. An error signal can be set up to notify if any of the sensors has a value of d_{33} which differs from the expected value by more than a previously defined tolerance. It is important to note that, except for the initial coupling procedure and first indenter centering, the rest of the procedure can be automatized, reducing to a few minutes the validation of a sensing patch built of 15–20 sensor units.

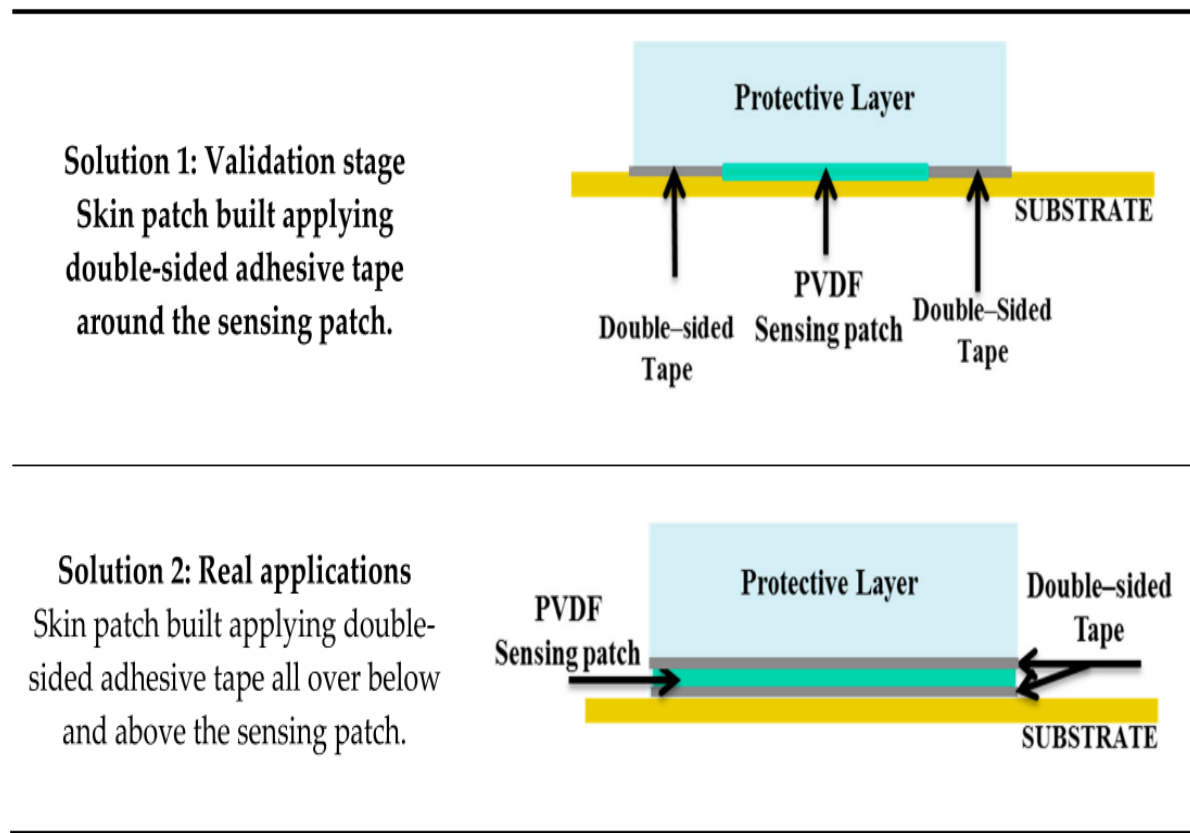


Figure 3.18 Illustration of different coupling methods.

3.5 Conclusion and Future Work

This study tackled some of the challenges related to employing electronic skin systems in real applications. In particular, this mainly requires validating the building blocks of the e-skin system, i.e., the sensing patches, and finding adequate ways to integrate these sensing patches into an electronic skin structure which also includes structural elements. Both these steps are preliminary to include the e-skin system into the target system, e.g., a glove or a prosthetic hand.

First, a set of tools is thus needed for the validation of the fabrication technology of the sensing patches. Throughout this study, a non-invasive method to validate the deposition technique of piezoelectric polymer sensors working in thickness mode has been defined and demonstrated. In particular, this chapter reports the validation of

the fabrication technology of flexible screen-printed sensing patches based on P(VDF-TrFE) piezoelectric polymers. This method is independent of the specific deposition technique and can cover a large number of applications requiring the employment of artificial tactile sensing through e-skin based on piezoelectric polymer sensor such as P(VDF-TrFE).

Extensive preliminary tests with an electromechanical setup have been performed on four different patch geometries/categories for the palm and one patch geometry for the fingertips. In particular, twelve sensing patches have been characterized (10 palm patches and two fingertip patches), 104 sensors in total (96 palm sensors and 8 fingertip sensors). P(VDF-TrFE) sensors worked in thickness-mode and a protective layer has been integrated on top of the sensing patch for stress transmission and sensor protection. Dynamic skin indentation with normal force centered on each sensor has been performed, with three different preloads (1, 2 and 3 N). An average value of the d_{33} coefficient over a non-resonant frequency range has been extracted for each sensor, without damaging the sensor itself. Obtaining expected (modeled) behavior of the electrical response of each sensor to measured mechanical (normal) force at the skin surface proves that the combination of both fabrication and assembly processes was successful.

Throughout the study course, several issues were observed such as substrate shrinkage that occurred during the fabrication process, leading to shortcuts. The proposed validation and characterization provided us with cues to optimize the fabrication of the next-line batches such as choosing smaller fabrication substrates (and smaller masks, accordingly).

The study demonstrated that for every sensing category (i.e., CAT1, CAT 2, CAT 3 and CAT 4), the sensing patches are statistically equivalent among themselves, which proves fabrication reproducibility, one of the main requirements when fabricating large volumes.

More specifically, after excluding the sensing categories that fall in the red zone of the heat map, i.e., that have been prone to high substrate shrinkage, the remnant sensors show d_{33} values which are quite compatible with the state of art. All the sensing patches that lie in categories 1 and 4 have a systematic declining behavior for d_{33} versus preload. This in turn is compatible with the nonlinearity of d_{33} with respect to the preload and with the few nonlinearities in the stress–strain curve observed for the PDMS protective layer [151]. The same behavior was observed from tested fingertips sensors, belonging to patches that were specifically chosen as lying in the sweet spot on the heat map.

The chapter presented an effective, repeatable and simple characterization protocol to validate the skin patches. A laser positioning system would be useful to align the indenter with the sensor center, therefore reducing errors arising from indenter misalignment, especially when testing fingertip sensors characterized by small radius. Future studies should take this into account. A critical limitation of the developed model is the inability to predict the behavior of artificial sensors in real applications, since this would require another sensor integration procedure, including double-sided adhesive layers on both sensing patch surfaces to avoid sliding. This could be done in a future work.

The usage of e-skin patches in real scenarios (e.g., biomedical applications requiring sensorized gloves or robotics) would likely lead to film degradation and consequent P(VDF-TrFE) aging and fatigue. Estimating the piezoelectric d_{33} coefficient from the overall system response function is a practical tool to measure the reliability of e-skin degradation, whenever embedded sensors are not accessible anymore for a direct characterization. The model presented in this chapter could be adapted to take into account the coupling procedure required to avoid sliding, including the deformable adhesive layers. However, measuring how the film degrades over time implies differentially

comparing the current value of d_{33} to an initial value, with no influence of the wrong estimation of that absolute initial value.

Chapter 4

Experimental Assessment of the Interface Electronic System for PVDF-Based Piezoelectric Tactile Sensors

4.1 Introduction

Recent advances in electronic systems are playing a key role in enabling tactile sensing systems to be used for important and critical applications, such as restoring the sense of touch in prosthetics [150]. These applications interact with the surrounding environment through tactile sensors using different transducing methods, such as capacitive [157], piezo-resistive [158], and piezoelectric [159]. Piezoelectric tactile sensors are able to detect contacts and slip, and provide the possibility to estimate applied forces. To meet the application requirements, suitable interface electronic system are needed to amplify and measure the electrical response generated from the tactile sensors.

When aiming for the reconstruction of accurate contact/touch, such as shape and texture, large numbers of tactile sensors should be deployed. These sensors have to provide high sensitivity, flexibility, and a wide frequency range e.g., polyvinylidene fluoride (PVDF) based piezoelectric sensors [36]. Finally, the frequency of interest for the dynamic interaction range from 0 up to 1 kHz [37]. Unfortunately, few researchers had focused on developing dedicated IE for tactile sensors considering the above mentioned requirements dealing with portable interface electronic systems. Taking into consideration the described requirements, an interface electronic system integrated with the tactile sensor array has been developed [160]. The system is introduced as a wearable tactile sensing system that can be employed in HMI. The IE design is based on low power ARM-microcontroller and low-current input analog-to-digital converters that features multiple input channels (i.e., 32 sensors) [160].

In this chapter, the experimental characterization of the interface electronics with the piezoelectric PVDF-based tactile sensors is presented. Section 4.2 reports the state of the art showing the recent developments in IE systems for tactile sensing. In Section 4.3, the tactile sensing system blocks, along with its implementation, are described. The experimental setup and method for the characterization of the interface electronics with the piezoelectric PVDF-based sensors are illustrated in Section 4.4. Then, the experimental results are presented in Section 4.5. After that, the signal to noise and distortion and the effective number of bits of the system are analyzed in Section 4.6 followed by conclusions in Section 4.7. The content of this chapter is presented in [161].

4.2 Background

Interfacing tactile sensors have been given particular importance in research works in the last years. Studies have targeted sensor characterization where the proposed

electronics are responsible for collecting sensor signals for analyses and to examine the behavior/response of the sensor [162], [163]. Dedicated interface electronics have been designed for integration purposes in specific applications [160], [156], [1], i.e., robotics.

The characterization of PVDF-based piezoelectric sensors has been done by studying their sensitivity with or without protective layers with the variation of the contact force. In particular, when used for acquiring the electrical signals of piezoelectric sensors, the IE was mainly composed of a charge amplifier and a DAQ device for digitizing and filtering the signals. In [162], a prototype of a sensor array, 4×2 of a ceramic type, was characterized. The output of the sensors is conditioned using TLV2772 operational amplifier and then sampled through a DAQ device (National instrument, USB-6009). Similarly, the DH5862 device was used in [163] to measure signals of one tactile unit (4 sensors) of a patch with 3×2 tactile units (24 sensors). Signals are result of applying three-axis contact forces where normal and shear forces are loaded on the surface of the tactile unit. The output signals, resulting from applying sinusoidal normal force using a shaker in the frequency range 4–500 Hz with variable amplitude in the range of 0–1.5 N, were then collected by an NI-DAQ device (USB-6343). A dedicated IE system was proposed in [163], where the authors presented a design methodology to define the metrics required in assessing the developed IE prototype. The prototype design depends on the sensor charge value that should be detected. So, tests were performed to check the prototype behavior when coupled to integrated PVDF sensors. The IE is composed of an op-amp (OPA348) and a low pass filter. Results reported a sensitivity of about 5.7 pC/N after the PVDF sample had been stimulated with a shaker with fixed frequency (i.e., 230 Hz) at variable force amplitude (i.e., 0.2–0.6 N). Moreover, the IE circuit in [1] adopts a dual-channel analog to digital converter DDC112U and an FPGA Xilinx Spartan®-6. The results demonstrated the feasibility of the proposed circuit with 0.6 pC/kPa average sensitivity in the frequency range from 10 Hz to 250 Hz.

Furthermore, the functionality of the interface electronics system developed in [1] has been assessed and its implementation was experimentally characterized in [164]. In [160], we proposed a wearable IE system aimed at providing tactile sensory feedback in prosthetic applications. The design provides the possibility to interface 32 piezoelectric tactile sensors with a low power budget maintaining real-time operation.

4.3 Tactile Sensing System

4.3.1 Piezoelectric Tactile Sensor

The study presented in chapter 3 validated the technology of the piezoelectric sensors and demonstrated the functionality in terms of the piezoelectric coefficient. Since the sensors and the coupling methodology were validated in that study, in this study we used the same sensors and the same methodology (Soulution 1, see Figure 3.18). Moreover, the interface electronics has been developed to interface such sensors. Therefore, in order to validate the interface electronics, one sensing array was selected from the two sets presented in Section 3.2.1.

4.3.2 Piezoelectric Tactile Sensor Model

The behavior of the piezoelectric sensor is a function of the reaction of piezoelectric transducer layers under an applied contact stress, see Figure 3.6. Accordingly, the amount of generated charges from the sensor are a function of the amplitude of the applied force. Thus, to estimate such an amount, it is important to have an electromechanical model that shows a relation between the sensor charge and the contact stress. For that, the mathematical mechanical model described in [1] has been adopted. The derived model finds the relationship between the applied mechanical stimulus and the corresponding charge that will be measured by the IE. Equation

(4.1) represents the open-circuit voltage generated by the piezoelectric sensor when a constant vertical stress (T_3) is applied:

$$V_{OC} = -\frac{q_{sensor}}{C_p} = -\frac{d_{33}A_{piezo}}{C_p}T_3 \quad (4.1)$$

where q_{sensor} is the amount of charge generated upon T_3 stress, d_{33} is the longitudinal piezoelectric charge coefficient, (T_3) is the mechanical stress, (C_p) is the equivalent capacitance between the electrodes of the piezoelectric film, and (A_{piezo}) is the loaded piezoelectric area. Since the sensor is covered with a protective layer of thickness (h), the direct applied stress is not (T_3).

According to Equation (4.1), the authors in [1] defined an electrical circuit consisting of a voltage source (V_{OC}) connected in series with a capacitor (C_p). This represents an equivalent electrical model of the piezoelectric sensor. Thus, the output charge (q_{sensor}) of the electrical model—equivalent to the output of the real sensors is calculated in Equation (4.2) [1]. Furthermore, Equation (4.2) will be used to calculate the charge generated from the model at the input of the analog-to-digital converter of the IE.

$$q_{sensor} = C_p V_p \sin 2\pi f T_{INT} \quad (4.2)$$

where (f) is the frequency of the input signal, converted from current-to-voltage every (T_{INT}) by internal integrators provided by the analog to digital converter (DDC232): Equation (4.2) will be used as a reference point for the electrical validation of the IE in Section 4.5.

4.3.3 The Interface Electronic System

4.3.3.1 Requirements and Specifications

The development of an interface electronic system necessitates possessing quantitative information about the application requirements, such as defining the contact stress/-force range and the electrical response of the piezoelectric sensor. These dynamics have been quantified in [165] and can be used as a reference point for defining electronic design specifications. Based on their estimations, the application range goes from 50 Pa to 5 MPa (over 5 orders of magnitude) resulting in a charge response ranging from 0.01 pC to 1 nC. However, the range of interest according to [166] is to cover stresses of the order 10,100 kPa for normal manipulation tasks and those lower than 10 kPa correspond to gentle touches. Given the considerations above and based on the frequency range of interest for the electronic skin application mentioned in [37], the designed interface electronics should be able to measure an input charge up to hundreds of pC with a large frequency bandwidth up to 1 kHz. Thus, the sampling rate must satisfy the Nyquist condition (above 2 kSps). Moreover, the design must take into consideration a large number of input sensors that will be integrated into the prosthetic glove attached to the amputee's forearm.

4.3.3.2 Block Diagram and Circuit Design

This section describes the block diagram and the implementation process for the IE shown in Figure 4.1, which has been proposed in [160]. The IE comprises two main components: (1) the DDC232 and (2) the BL600. The DDC232 is a 32-channel analog-to-digital converter (DDC232), interfaced at the side of the sensors (32 sensors) with a current offset circuit. The offset circuit is necessary to handle the bipolar charge-output of the sensor that generates both positive and negative charges when stimulated. This can be done by connecting voltage reference equal to $(V_{ref}/2)$ at the input of the

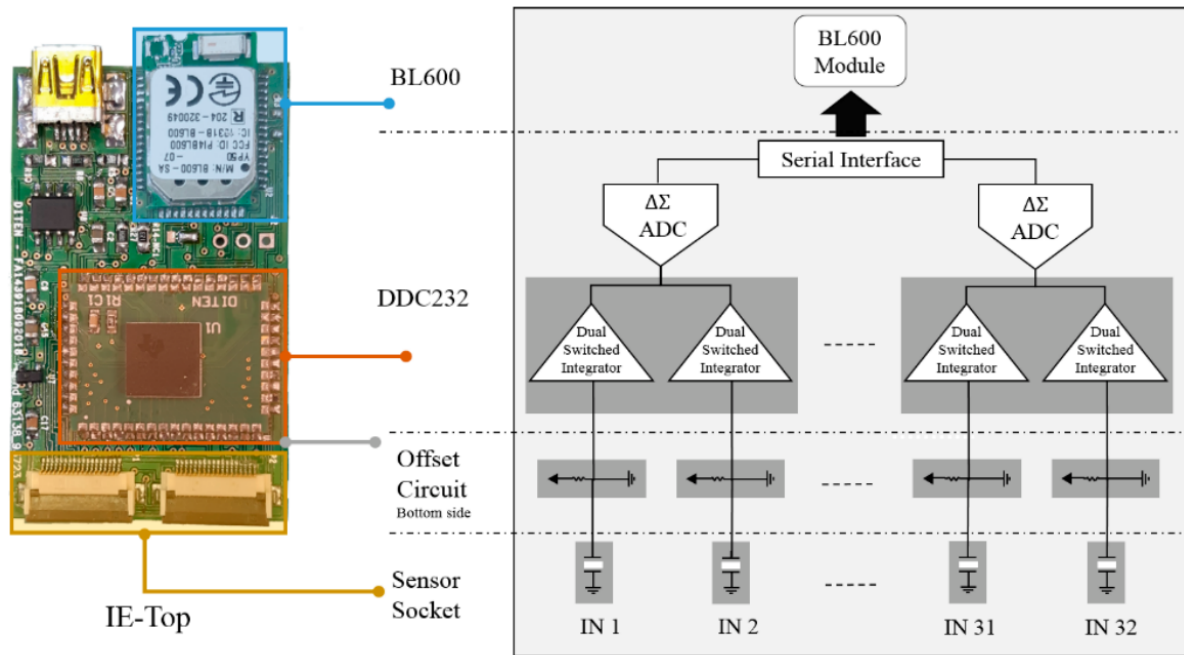


Figure 4.1 Interface electronic printed board circuit (left) and block diagram of the DDC232 (right)

DDC232 converter. The 32 sensors are connected to the 32 available integrators in the DDC232 so that the current-to-voltage integration can be continuous in time. For the 32 inputs, the output of the 64 integrators are switched to 16 delta-sigma converters via multiplexers where the first 32 integrators are digitized while the other 32 are in the integration mode. The second component is the BL600 module, a low-power ARM-Cortex M0 based microcontroller. It is connected to the ADC using a synchronous serial interface to configure the conversion rate and control the reading process of the converted data [167]. The conversion process is controlled by a CLK pin (configured at frequency 10 MHz) connected to the system clock of the microcontroller. The results of each conversion are stored in a shift register. The output signal (DVALID) goes low to indicate that data are valid and it triggers the controller to start the retrieving process. The retrieved data format can be configured to be either 20 bits or 16 bits. This is done by writing to the 12-bit onboard configuration register the corresponding format value.

Three pins DIN-CFG, CLK-CFG, and RESET pins of the ADC are used to write to this register and set the feedback capacitance of the integrators.

The SPI peripheral of the microcontroller has been enabled for controlling the conversion and data retrieval process using the Keil-ARM IDE. The ADC is initialized to convert data with a 16-bit resolution and configured to cover the maximum input charge response by selecting the maximum value of the integrator feedback capacitance, $C_f = 87.5 \text{ pF}$; the BL600 module begins the write operation to the register by holding CONV to control the switching between integrators and setting the RESET signal. After that, the configuration process starts by shifting in the configuration data on the configuration register data input (DIN-CFG) on the falling edge of the CLK-CFG (the configuration register clock input). After the configuration is done, a clock signal CLK at a frequency of 10 MHz is generated by the BL600 to operate the ADC. Then, a CONV signal of 1 kHz frequency is generated to convert data of 32 channels at 2 kSps. Sampled data are retrieved by the microcontroller and shifted out on the falling edge of the serial data clock (DCLK) generated at 4 MHz frequency. Finally, data are sent to the PC via UART-to-USB port at a baud rate of 115,200 bits per second (bps) to be collected in the MATLAB tool and further analyzed.

4.4 Experimental Setup and Methods

After design implementation, two experimental tests were performed: electrical and electromechanical. In the electrical test, the equivalent sensor model was implemented by connecting a function generator in series with a capacitor and followed by the interface electronic, as shown in Figure 4.2. The interface electronics acquire and sample the sinusoidal waveforms produced by the source generator. Then, the sampled data are sent to the PC to reconstruct the original signal where results were verified in Section 4.5, according to Equation (4.2).

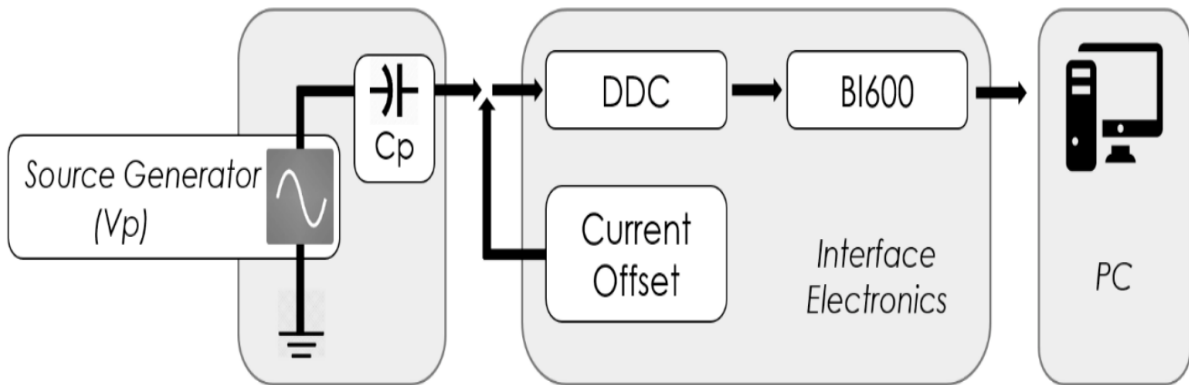


Figure 4.2 Block diagram of the electrical setup; equivalent circuit of sensor (left) connected to interface electronics; generated signals are reconstructed by the interface electronics (IE) and sent to the PC.

After the electrical validation of the design, an electromechanical setup was performed to study the functionality of the IE with real sensors. In the electromechanical test, the frequency of the stimulus applied on the sensor has been fixed while the stimulus amplitude was changing by controlling the shaker through a source generator, see Figure 4.3 (Top). The IE connected to the sensor patch measures the generated charges and sends the recorded data to the LabVIEW software. LabVIEW receives the measured applied force from the PCB Piezotronics conditioner as well. In particular, the shaker was controlled to apply 1.2 N as the maximum force with the maximum shaking frequency at 400 Hz.

The mechanical chain used for measurements is shown in Figure 4.3 (Bottom) and it is described in Section 3.2.2. Before running each test, a preload was applied to guarantee indenter-PDMS contact during the whole test. Two tests were done on the same sensors and under the same conditions (same coupling and indenter positioning). In the first test, the charge generated by the sensor was conditioned and processed by the PCB Sensor Signal Conditioner (482C54), while in the second test, the generated charge was processed by the interface electronics. In the two tests, the electromechanical stimulus measured by the piezoelectric force transducer was conditioned and processed by the PCB Sensor Signal Conditioner (482C54). A graphical

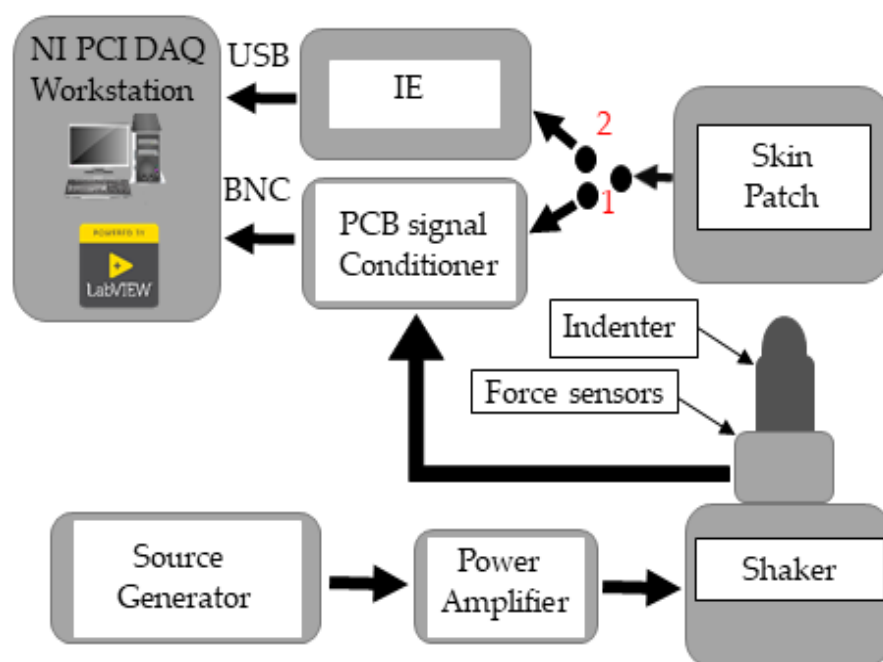


Figure 4.3 Experimental setup. Top: Block Diagram, Bottom: Pictures of the setup.

user interface (GUI) developed with NI LabVIEW on a host PC and NI PCI-4461 DAQ data acquisition board was used to collect and visualize both the force transducer (stimulus) and the generated charge.

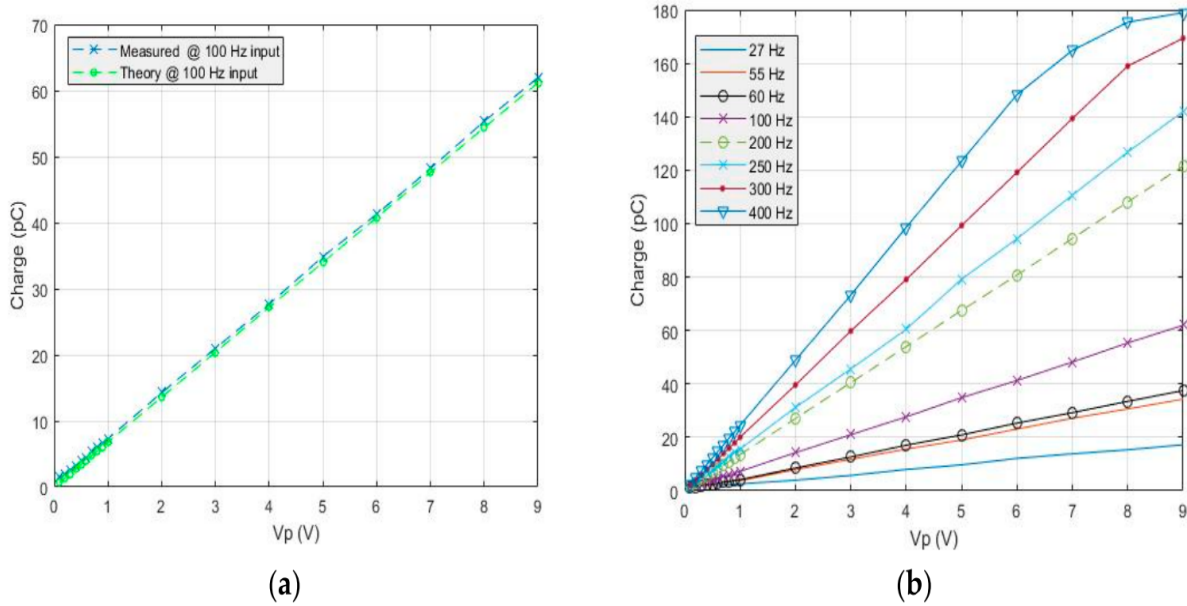


Figure 4.4 (a) The theoretical fit-line is calculated from $Q_{\text{theoretical}} = C_p V_p \sin(2\pi f T_{\text{INT}})$ derived from the equations presented in [1]; (b) shows the output of the IE relative to input signals generated from the source generator.

4.5 Experimental Results

This section presents the experimental results obtained from both electrical and electromechanical tests.

4.5.1 Electrical Measurements Results

The electrical setup illustrated in Figure 4.2 was used to validate the interface electronics. An equivalent piezoelectric sensor model, composed of the source generator connected in series with a capacitor of 22 pF, is connected to the IE. The IE was configured to acquire data sampled at 2 kSps. The sampled data was sent to the PC where it was analyzed using MATLAB. The test was done by generating a sine waveform, from the source generator, of a specific frequency at which the IE measures the specified signal at different amplitudes (from 100 mV up to 9 V). The same scenario was repeated at different frequencies within the targeted bandwidth (i.e., 1 Hz–1 kHz). Figure 4.4.a

shows that the charge measured with a 100 Hz input sine wave as a function of the amplitude is close to the theoretical results computed from Equation ((4.2). The same test was performed for several frequencies and the results illustrated in Figure 4.4.b verify, according to Equation (4.2) ($Q_{theoretical} = C_p V_p \sin(2\pi f T_{INT})$), that the amount of charge becomes larger as the input frequency increases. Moreover, the non-linearity error was estimated using the best-fit method, where 2.3% for the average error was recorded. Therefore, the results validate the correct functionality of IE in measuring charges, which are close to the theoretical results.

The frequency response of the DDC232 depends on its integrators and the 3-dB bandwidth location is affected according to the integration time. Since the DDC232 is converting data at 2 kSps (means $T_{integration} = 500 \mu s$), then according to [167], around 900 Hz bandwidth is within a 3 dB gain. This offers a wide range of frequencies (up to 1 kHz) that can be set for testing. According to datasheet [167] and based on the fact that the DDC is a current-input analog to digital converter, the maximum input current that can be acquired is around $216 \mu A$. Thus, at the maximum current, the signal is at the digital full-scale and any further increase in signal amplitude results in an error. For this reason, the error was realized when the injected signals of high frequencies (above 400 Hz) reached amplitudes above 6 V. Therefore, DDC will reconstruct signals up to 1 kHz frequency at amplitudes up to approximately 3 V. So, high-frequency signals at high amplitudes were not included in the test.

4.5.2 Electromechanical Measurement Results

Figure 4.5.a shows the behavior of the IE in detecting and measuring the change of charges as a function of force. Although the obtained results meet the concept expressed in Equation ((4.2) that as force increases charge increases, the conditioner was included in the test to be a reference point for evaluating the behavior of the IE. In addition to force conditioning, the conditioner features charge conditioning from

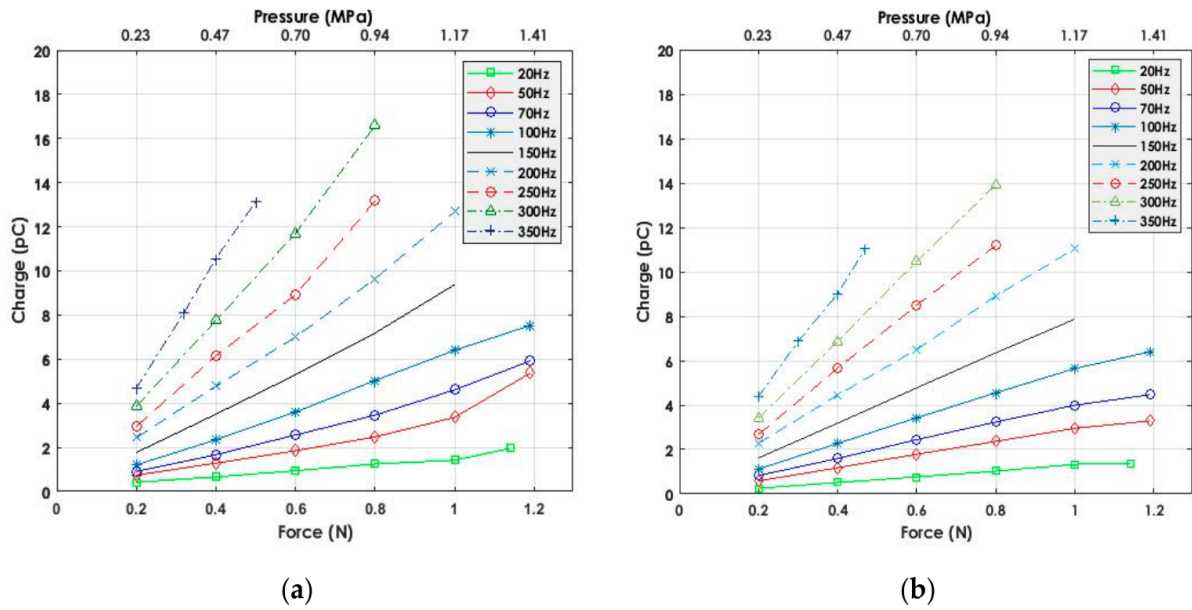


Figure 4.5 (a) IE output measurements with real sensors; (b) conditioner output measurements with real sensors.

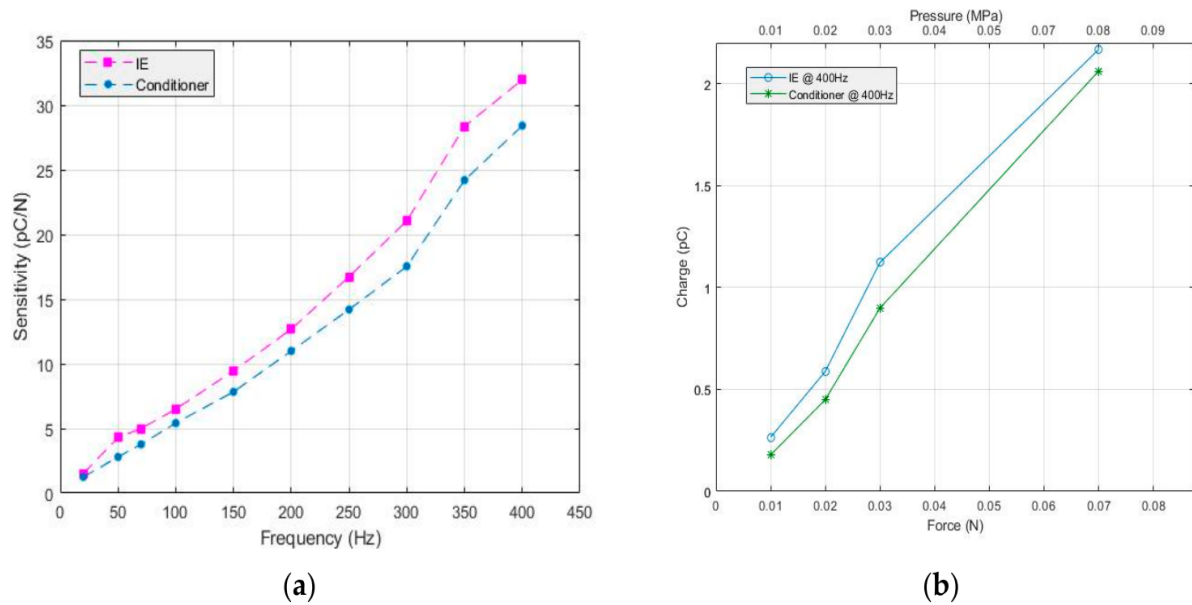


Figure 4.6 (a) Sensitivity as a function of frequency; (b) measured charges at the minimum detectable force (0.01 N).

piezoelectric sensors. Then, the IE was disconnected from the sensors and replaced by a conditioner. The test was repeated under the same conditions (sensor coupling and positioning) and the corresponding force and charge measurements were recorded. It

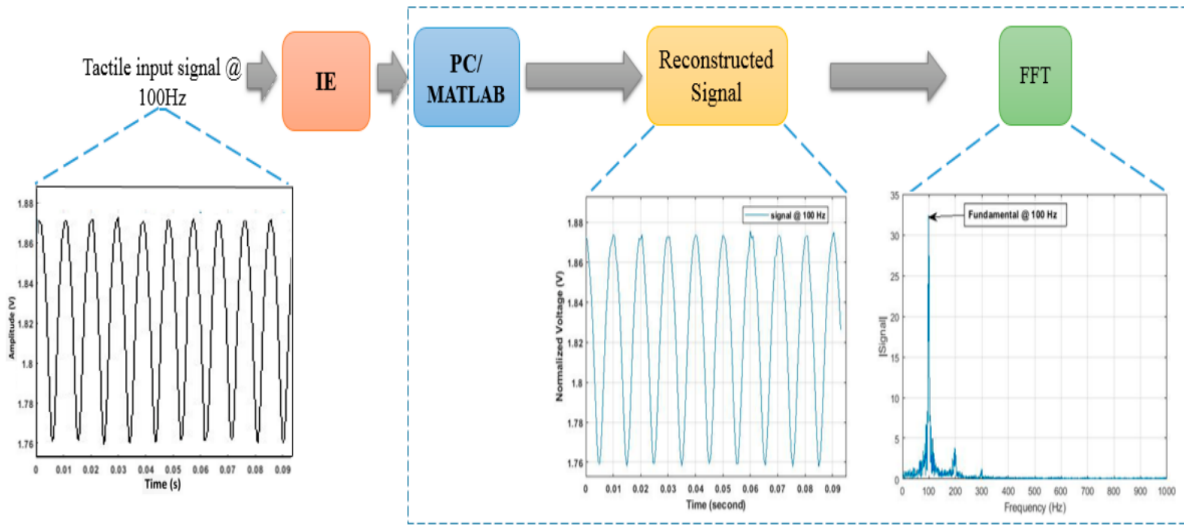


Figure 4.7 Example of an input signal at 100 Hz of frequency in time and frequency domains.

is noticed, as expected from Figure 3.7.b, that when increasing the force, an increase of the amount of charge is observed. We can deduct from Figure 4.5 that the IE is able to detect and measure the linear change of input charges within the given frequency and force ranges, 20–350 Hz and 0.2–1.2 N, respectively, with slight differences in charge values. The difference in charge values between IE and conditioner can be observed from the sensitivity curve reported in Figure 4.6.a. The plot demonstrates the increase in sensitivity (1.5–31.96 pC/N) as a function of frequency. The sensitivities have been estimated by calculating the slopes of the measured charge versus force within the frequency range 20–400 Hz. By analyzing the figure, it seems that the difference between the IE and the conditioner is almost constant and, thus, it is possible to apply setup calibration to find the empirical difference value. Moreover, in order to demonstrate the ability of the IE in acquiring data at higher frequencies, a test was done by fixing the frequency at 400 Hz and adjusting the amplitude—controlling the shaker—to reach the minimum force value. Results presented in Figure 4.6.b show that the IE is able to measure charges obtained under minimum applied force (0.01 N).

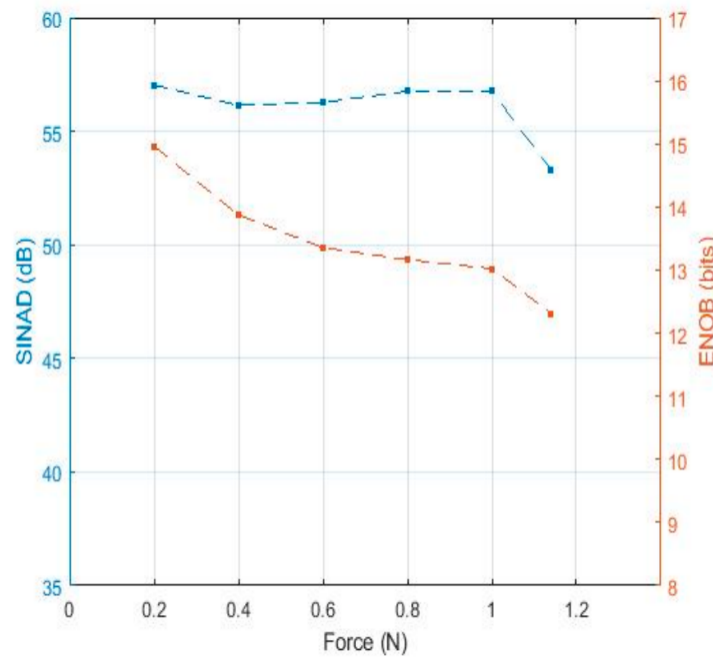


Figure 4.8 SINAD and ENOB variation with respect to applied forces.

4.6 Signal to Noise Ratio Analysis

This section presents the analysis carried out to study the measured signal with respect to noise by using methods as adopted in [164]. The noise may be a result of harmonic distortion added to the input signal or at the output of the IE circuits described above as we are analyzing the signal output of the whole system, i.e., sensors and interface electronics. Such noise contributes directly to the signal-to-noise ratio of the design. IEEE in [168] has defined test methods for analog to digital converters, i.e., the signal to noise and distortion ratio (SINAD) and the effective number of bits (ENOB). In particular, SINAD is used to measure the degradation of the signal by unwanted signals in noise and distortion. It is the ratio of total signal power level to the noise and distortion power. Also, SINAD provides the basis for calculating the ENOB, which specifies the number of bits of the signal that is above the noise floor. Figure 4.8 illustrates the SINAD and ENOB curve versus frequency where SINAD was computed by calculating the ratio of the root-mean-square (rms) of the fundamental signal to

the root-mean-square of noise and distortion. After normalizing the input data to scale between 0 and 4.09 V (ADC reference voltage), FFT has been applied to distinguish the fundamental signal from other harmonics and noise existing in the spectrum. Finally, the amplitude of the signals in the spectrum have been measured and substituted in the equation below to calculate the SINAD:

$$SINAD = 20 \log \frac{rms(A_s)}{rms(n + k)} \quad (4.3)$$

where A_s is the amplitude of fundamental signal and $(n + k)$ is the amplitude of noise and distortion. Moreover, we used Equation (4.4), derived in [169], to compute the ENOB after applying a fast Fourier transformation (FFT) to the data recorded in the previous test. Figure 4.7 shows an example of an input signal at 100 Hz: (a) original signal in the time domain, (b) reconstructed signal after ADC conversion, and (c) the FFT of the signal demonstrating the fundamental signal at 100 Hz of frequency.

$$ENOB = \frac{SINAD - 1.76 \text{ dB} + 20 \log \left(\frac{\text{full scale amplitude}}{\text{input amplitude}} \right)}{6.02} \quad (4.4)$$

Figure 4.8 shows consistent behavior of the IE over a frequency where around 14 bits out of 16 of the digitized signal are above the noise floor. So, this will be an advantage to retain more accurate data and, thus, acquiring tactile data with a high resolution.

4.7 Conclusion

This chapter presented an experimental assessment of new wearable interface electronics proposed for interfacing PVDF-based piezoelectric tactile sensors for prosthetic application. Interface electronics is composed of a low-power ARM-Cortex M0 microcontroller and a DDC232 analog-to-digital converter to interface 32-input tactile sensors.

The system has been experimentally evaluated by electrical and electromechanical tests where results demonstrate charge estimation within the force range 0.01 to 1.2 N (10 kPa–1.4 MPa) with approximately 0.2 pC charge value readable by the IE at 0.01 N, lowest input force. Results validate the proper functionality of the interface electronics in measuring the dynamic range of charges estimated within the force range of interest to cover normal manipulation tasks and stresses of orders up to 100 kPa. An average signal-to-noise and distortion ratio of about 56 dB was measured for applied forces from 0.2 to 1.2 N. Therefore, the results demonstrate the suitability of the proposed system for acquiring tactile bipolar signals with high-resolution after achieving 14 bits of ENOB.

Chapter 5

Development of a Skin Patch based on P(VDF-TrFE) sensors and assessment of the sensing system

5.1 Introduction

The studies presented in Chapter 3 and 4 focused on the validation and experimental assessment of the PVDF-based sensing arrays and the interface electronics respectively. Chapter 3 presented the validation of the newly developed sensor technology. The sensors were tested in a controlled environment where the stimulus parameters are controlled (contact area, applied force, waveform, etc.). The response of the sensors was examined in the frequency domain and within a limited range of frequency (50 Hz -250 Hz). The response of the sensors was further examined in Chapter 4 while assessing experimentally the behavior of the interface electronics. Results in Chapter 4 demonstrated that the sensing system i.e. sensors and interface electronics are capable of detecting different levels of forces within the frequency range of 20- 450 Hz. Furthermore, a linear relationship between the charge response and the force stimulus

was found. However, the experimental assessment of the interface electronics was done also in a controlled environment using an electromechanical setup. Both studies were limited in the frequency range of the stimulus. In addition, in both studies, we didn't examine the response of the sensors to a stimulus with low-frequency content < 30 Hz. Moreover, still, the sensing system wasn't tested in a non-controlled environment where the contact parameters are not controlled. Finally, all the tests done so far were implemented on the sensing array with the PDMS layer as a protective layer and with no shielding. This makes the sensing system still not applicable for usage in a more realistic scenario where none of the aforementioned parameters (e.g., contact parameters) are controlled. Characterizing the sensor behavior directly would be a quite complex, lengthy, risky, and hardly reproducible process. Direct objects contact leads to sensor damage. To use the sensing array in the different applications requires integration of the shielding layer to the sensing arrays from all sides and requires the integration of a protective layer on top of the sensing patch, giving rise to what we call the skin patch. This chapter focuses on the development and demonstration of a novel skin patch that has been developed using the sensing arrays presented in Chapter 3. Moreover, it presents the assessment of the developed skin patch in a controlled and non-controlled environment for which we developed two experimental setups. The skin patch was tested using a PCB piezoelectric conditioner and later using the interface electronics. Moreover, the ability of the skin patch to detect different touch patterns was evaluated. Finally, this chapter presents the implementation of signal processing methods for noise cancellation. The methods were implemented in the firmware of the interface electronics and tested using the skin patch in a non-controlled environment.

The chapter is organized as follows: Section 5.2 describes the developed skin patch. Section 5.3 presents the validation of the skin patch in a controlled environment whereas Section 5.4 describes the ability of the sensing system to detect touch patterns applied in a non-controlled environment. Section 5.5 presented the implementation of

signal processing methods in the interface electronics. Finally, our conclusive remarks are given in Section 5.6.

5.2 Skin Patch

The embedded sensing system raises several issues: it must be compliant with the e-skin structure, that is, flexible, it must be robust against electrical noise and mechanical damages, and must be resilient [35]. Adding an element of protection from damage to the sensing arrays is essential when integrating it into the robotic hand that will be used in daily life activities. All such demanding requirements are challenging especially when considering integrating the sensing system on the robotic hand. In addition to the mentioned noises, the sensing system might be exposed to external charge especially when the arrangement of the sensing system is based on piezoelectric sensor and charge amplifiers. Such an issue can be resolved by integrating a shielding layer, which guarantees a minimum sensitivity to noise. In addition to shielding, adding a thin protective layer on the contact side of the sensing array would protect the sensors from any damage and increase the lifetime of the integrated sensing system. This section describes the fabrication of the skin patch that fulfill the aforementioned requirements of the sensing system. Chapter 3 studied the piezoelectric coefficient of the sensors and demonstrated the relation between the preload and the piezoelectric coefficient. It was found that the sensing arrays located in the white spot of the heat map (see Figure 3.11), have the most reasonable behavior in terms of the piezoelectric coefficient. Based on that, in this study, we chose to develop a skin patch using the Michelangelo Palm patch (category 4) which is located on the white spot.

To prepare a skin that could be applied on different surfaces, a novel multi-layer skin patch was invented. The target is to protect the e-skin electrically and mechanically while allowing it to conform to different shapes (e.g., fingers). Figure 5.1

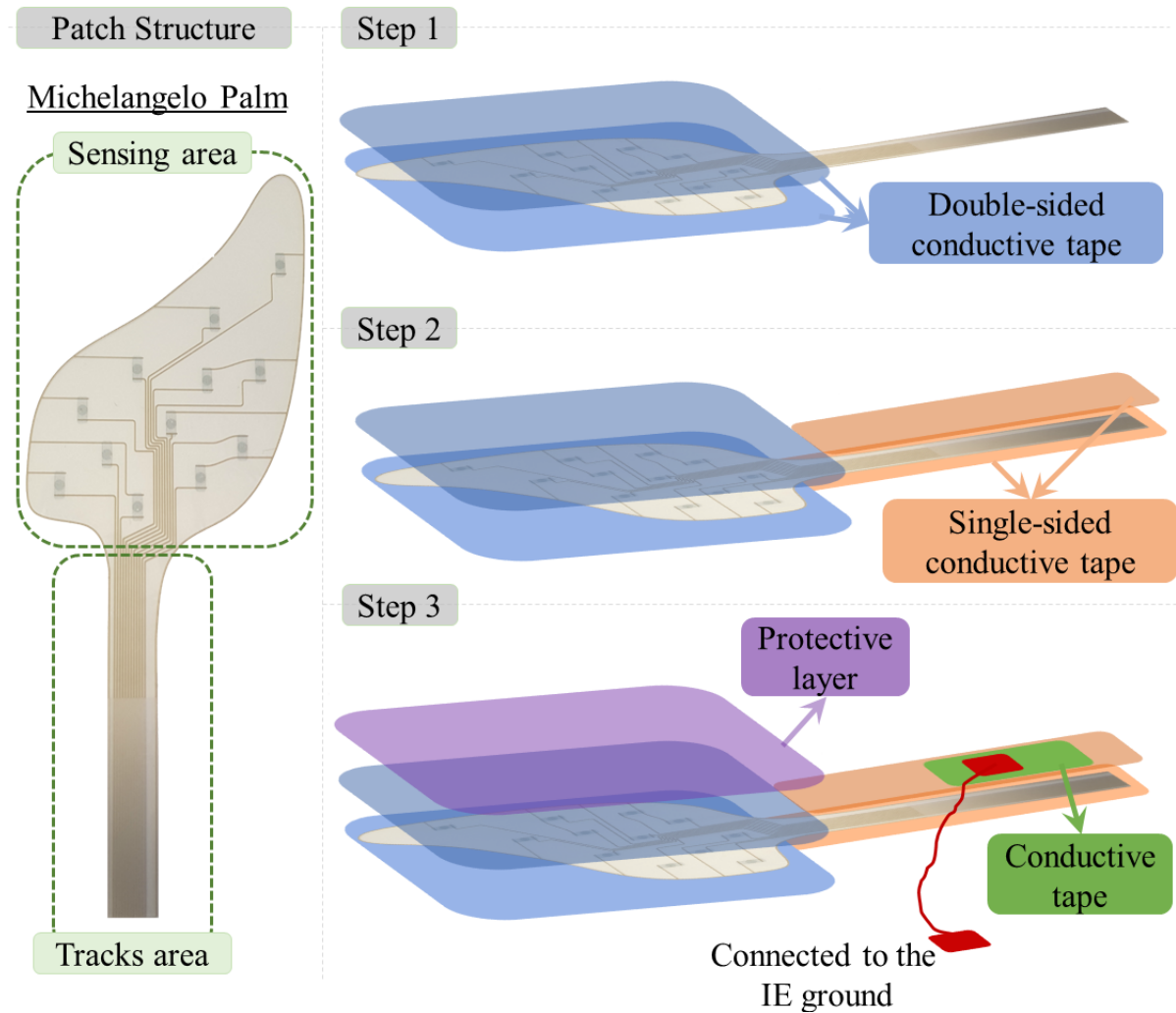


Figure 5.1 Skin patch development process. The sensing array is shielded using conductive tapes and a thin protective layer is used to protect the sensing areas.

(left) shows the structure of a single sensing array. The sensing arrays are composed of single or triple sensing arrays and each has its tracks area (see Figure 3.3). The fabrication process of the skin patch is shown in Figure 5.1 (right). The integration process was done in three main steps. Since the sensing system might be exposed to external charge especially when the arrangement is based on piezoelectric sensor and charge amplifiers, the sensing areas were first sandwiched between two double-sided electrically conductive tapes (Model tesa 60262, tesa). The conductive tape was used as a shielding layer, which guarantees a minimum sensitivity to noise. Since the tracks

must be connected to the interface electronics, the tracks area is not covered with the UV-curable lacquer layer during the fabrication of the sensing arrays (see section 3.2.1). For that reason, an insulating coating (Model PLASTIK 70, KONTAKT CHEMIE) was applied to the unprotected part of the tracks area to protect and insulate the sensor tracks. The tracks area was shielded using single-sided electrically conductive tape (Model tesa 60234, tesa). Both conductive tapes (single-sided and double-sided) are conductive from both sides and hence they were electrically connected once they were coupled to each other. The shielding layers were connected to the ground of the interface electronics using a self-adhesive copper foil tape and a wire. Finally, a thin flexible cylindrical shape protective layer (Art. 5500 Dream, Framisitalia) was added on the top of the sensing area to protect the sensors from damage and increase the lifetime of the integrated sensing system, forming the skin patch. When used on different surfaces, the skin patch was coupled from the bottom side with a flexible cylindrical shape substrate (PVC of 0.25 mm thickness) using a double-sided adhesive tape (Model 3M 9485, 3M) to avoid bending and protect the skin patch from the bottom side.

5.3 Systematic skin patch validation

Chapter 3 and 4 proved that the sensing system has a linear response to the applied force stimulus. Such a result was found using the sensing arrays coupled to the PDMS protective layer which is not the structure to be used in the application because of its thickness and rigidity. It is important to test the response of the sensors after being integrated into a multi-layer structure i.e., skin patch. Moreover, such testing must be done using the interface electronics and then compared to the response of commercial sensors and readout circuits. For that reason, we conducted new experiments to test the response of the skin patch to different stimulus waveforms, and check if repeatability and linearity in the response are achieved. To accomplish such a task, we modified

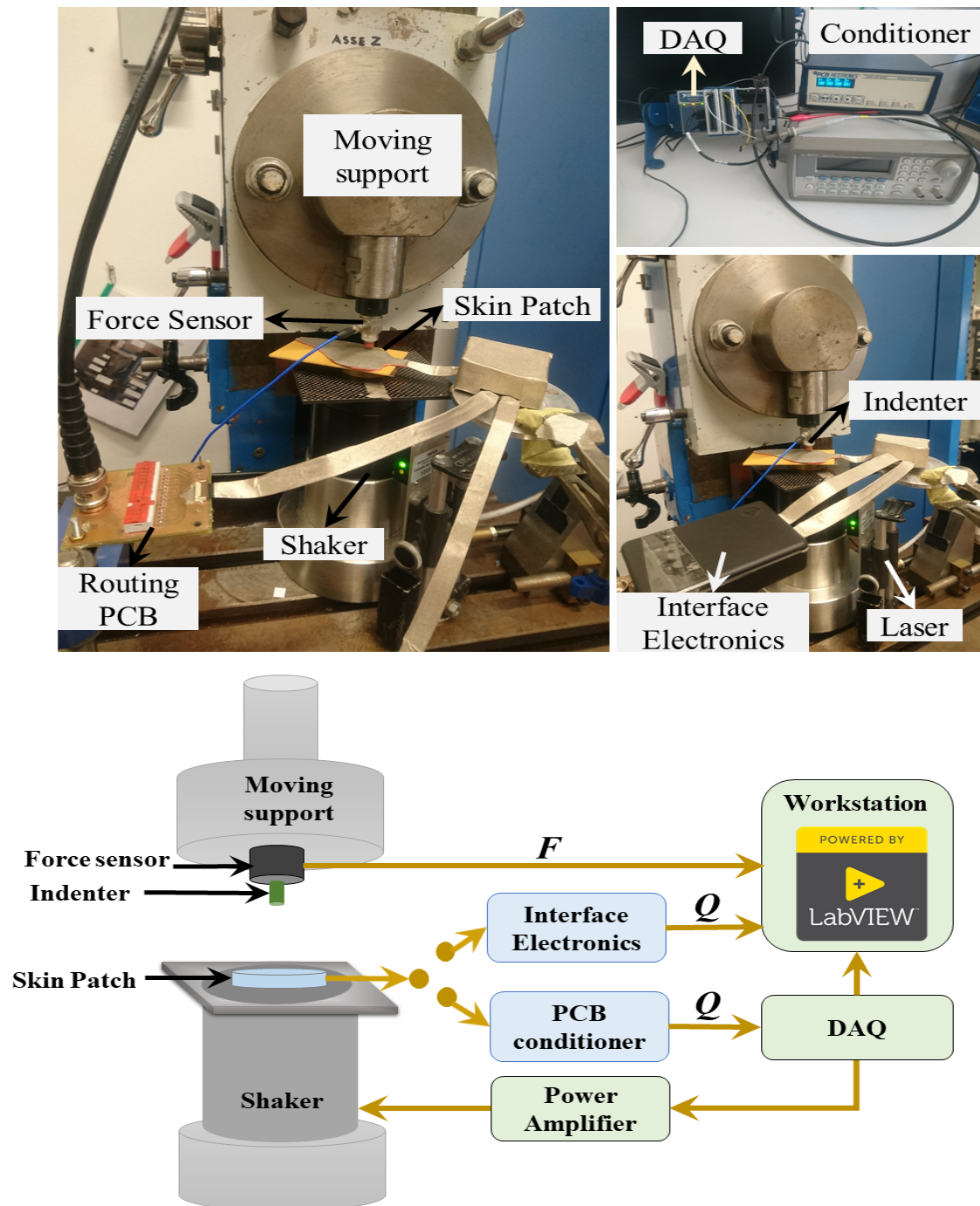


Figure 5.2 Experimental setup. Top: Pictures of the setup, Bottom: Block Diagram. The blue dotted line shows the alignment of the testing elements.

the electromechanical setup used in Chapter 3 so that it mimics the touches in a real scenario (e.g. passive touch).

5.3.1 Experimental setup

Figure 5.2 shows the electromechanical setup. The skin patch was then coupled to a rigid plate which was fixed on the moving head of an electromechanical shaker (Bruel and Kjaer, Minishaker Type 4810 from HBM company, Germany). A soft spherical indenter ($R = 2 \text{ mm}$) and a piezoelectric force transducer (Model 208C01, PCB Piezotronics, MTS system), were coupled on the lower head of the moving support. In all the experiments done in this study, the test started by activating the electromechanical shaker with a specific waveform (sine, rectangular, or triangular) and at a specific force (amplitude of the signal). A preload was then applied to guarantee indenter-patch contact during the whole mechanical stimulation. The value of the preload has been controlled by a laser (Waycon LAS TM10), allowing us to fix the displacement of the rigid plate at a certain value for a certain preload, through displacement–force calibration curves. Three different signals (see next section) were provided to an electromechanical shaker by a graphical user interface (GUI) developed with NI LabVIEW on a host PC and NI DAQ data acquisition board. The signal was amplified using a Power Amplifier (Type 2706). The force transducer (stimulus) was conditioned by a PCB Sensor Signal Conditioner (482C54) while the charge developed by the sensor (response) was conditioned either by the conditioner or by the interface electronics as illustrated in Figure 5.2.

5.3.2 Response to different stimulus waveforms

In Chapter 3, the response of the sensors to a swept sine signal was examined. Forces in the frequency range of (0.5–1 kHz) have been applied through the spherical rigid indenter. The force and the charge developed by the sensor (response) were processed in frequency to give the System Response Function (FRF) at each frequency step. We recall that FRF corresponds to the ratio between the Fourier transform of the output charge and that of the input force. However, in the study presented in Chapter 3 we

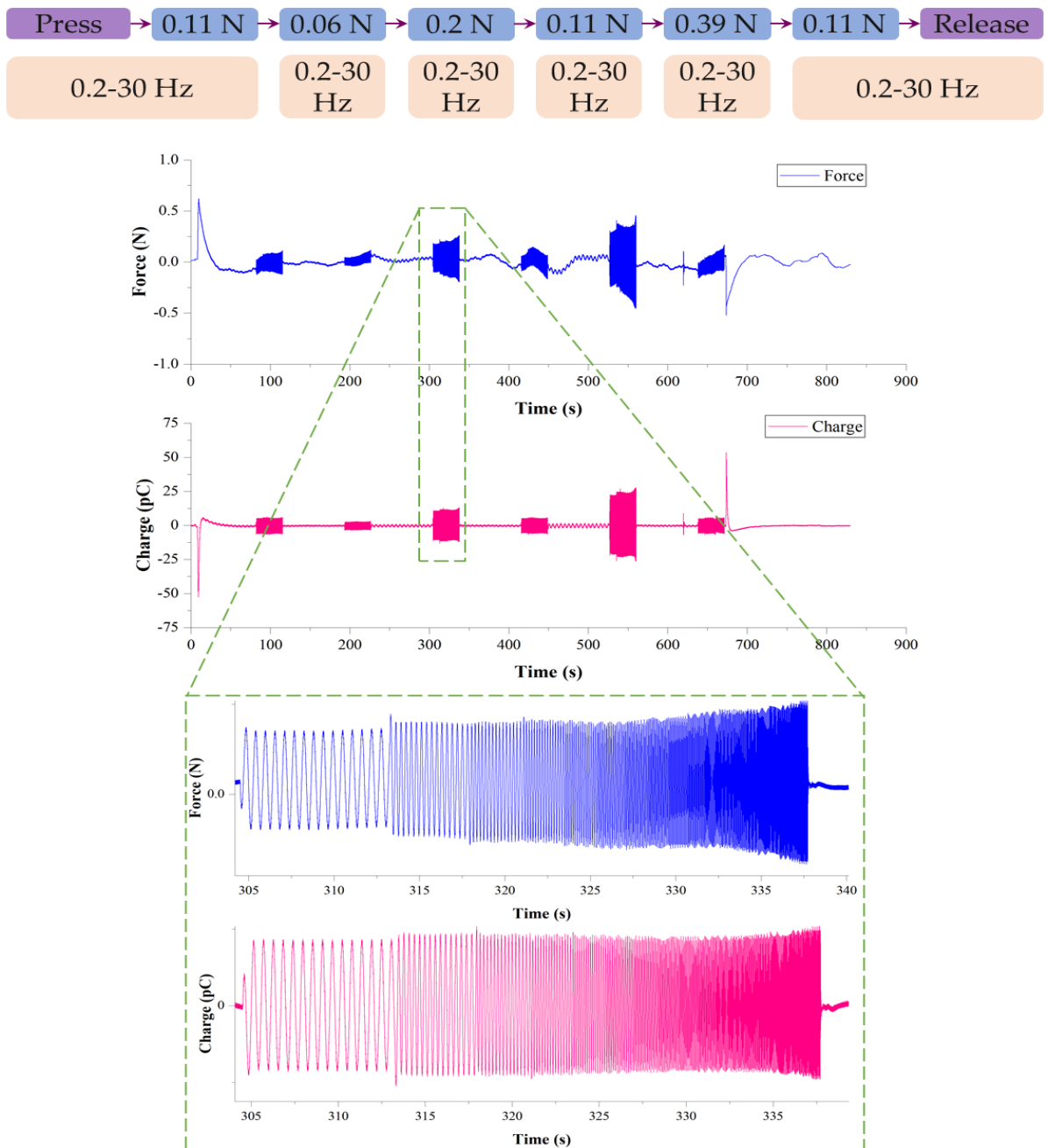


Figure 5.3 Response of a single sensor to swept sine stimulus with the PCB conditioner. The amplitude of the signal was increased or decreased automatically by the host PC.

didn't examine the response of the sensors in the time domain and the response to different waveforms, for example, the triangular and rectangular signals. Recalling that the frequency range selected in the study of Chapter 3 was 50-250 Hz, hereby in this

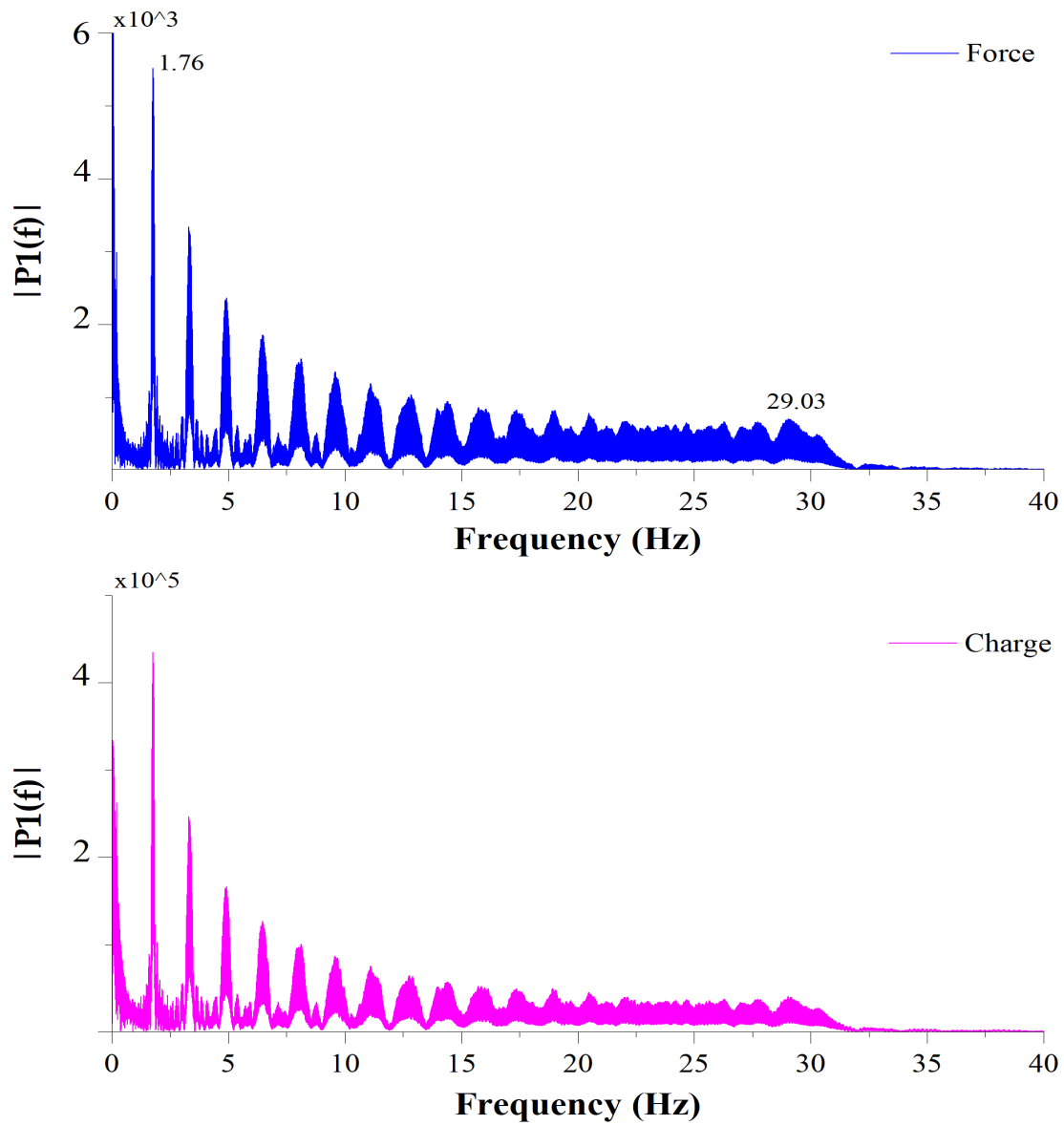


Figure 5.4 The Fast Fourier Transformation of the swept sine stimulus and the response of the sensor using the conditioner.

chapter we examine the response of the developed skin patch to forces in the frequency range below 30 Hz and especially in the very low frequencies ~ 0.5 Hz.

Figure 5.3 shows the response of the skin patch to a sweep sine signal of frequency range 0.2-30 Hz with a step frequency of 1.49 Hz. The amplitude of the swept sine signal was changed automatically by the host PC during the experiment. This was

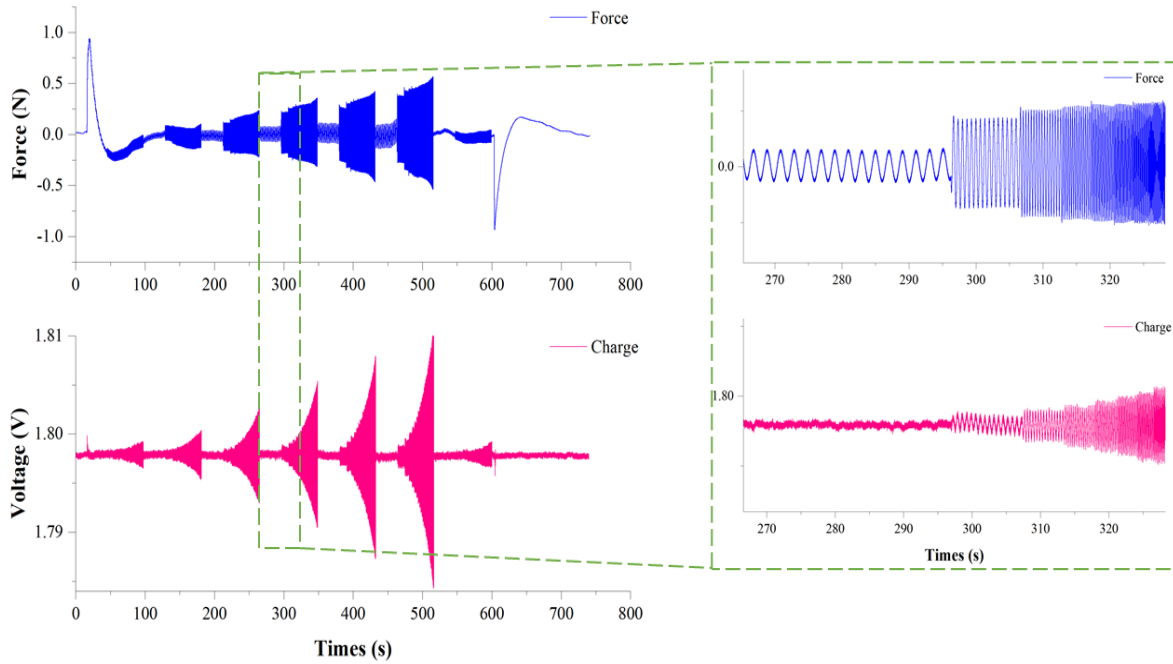


Figure 5.5 Response of a single sensor to swept sine stimulus with the PCB conditioner. The amplitude of the signal was increased or decreased automatically by the host PC.

done to ensure that the sensors respond to all the frequencies regardless of the signal amplitude. Moreover, it is important to note the applied force depends first on the amplitude of the signal and second on the behavior of the electromechanical shaker which increases the force as the frequency increases. The sensor response was measured by the PCB conditioner.

The plots shown in Figure 5.3 prove the following, first the sensor responds to the press and release of the soft indenter, which refers to applying and releasing the preload respectively. Second, the figure shows that the response of the force transducer and the sensor are aligned where the sensor responds to the increase/decrease in the force and the increase in the frequency. This is more illustrated in Figure 5.4 where the Fast Fourier Transformation (FFT) was applied to the swept sine stimulus measured by the force transducer and the to the response of the PVDF sensors (skin patch). The figure shows that the sensor responds to all the frequencies applied within the range.

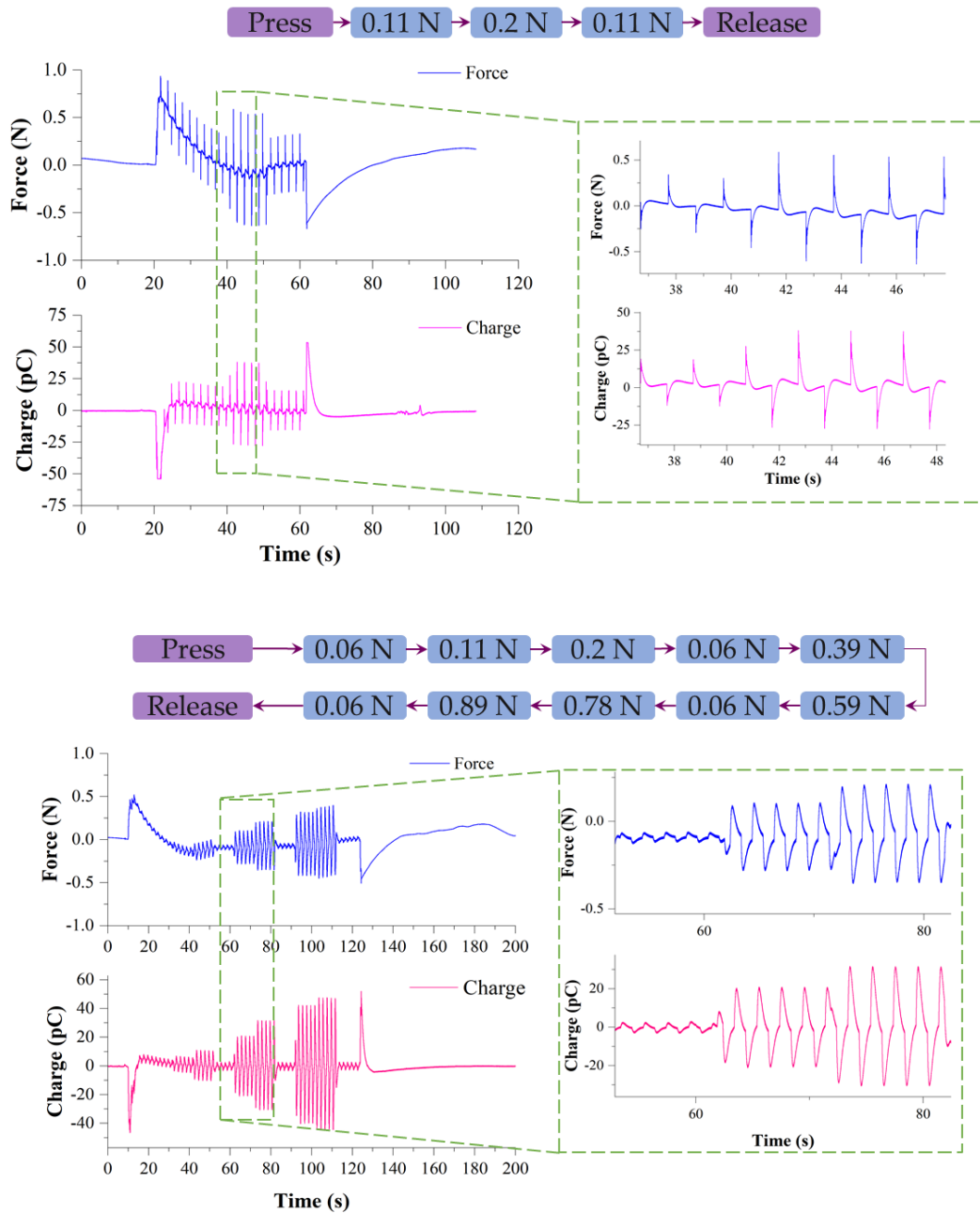


Figure 5.6 Response of a single sensor using the conditioner to rectangular (Top) and triangular (bottom) stimuli.

The same experiment was repeated, however, the PCB conditioner was replaced by the interface electronics. Figure 5.5 shows the swept sine stimulus and the response of the sensing system (i.e., skin patch and interface electronics). The figure shows that the sensing system can easily detect the change in the frequency and the force level.

However, the systems encounter a high noise level which might affect detecting very low frequencies. This is discussed and solved in section 5.5.

The response of the sensor to triangular and rectangular stimulus signals was examined as well. Figure 5.6 (Top) shows the rectangular stimulus and the corresponding sensor response. In addition, Figure 5.6 (Bottom) shows the triangular stimulus and the corresponding sensor response. In both tests, a series of forces were randomly applied. Considering the response of the force transducer as the reference signal, both figures show that the sensors respond perfectly to the change in the different stimuli and the change in the force level.

5.3.3 Repeatability and Linearity

The study conducted in Chapter 4 demonstrated that the interface electronics is capable of reading and processing the sensor signal and has been compared to the conditioner. Moreover, it demonstrated the linear relation between the force stimulus and the charge response. However, we never tested how could such relation be affected by the applied forces and their order. Moreover, this section check if the response of the sensors is repeatable. To tackle such problems, we used the electromechanical setup presented in Figure 5.2 to study the response of the skin patch to a sequence of forces. Since the focus is on the response of the sensors, we used the conditioner to acquire the sensor's signal.

A series of forces was applied to extract the sensor behavior to a change in the order of the force levels, i.e., ultimately their charge response, from indentation tests on the skin patch surface. A set of force sequences were predefined on the host PC where the force levels were randomly ordered to exclude the impact of the force order on the response of the sensor. The force level was modulated by changing the amplitude of the sine signal fed to the electromechanical shaker. The frequency of the sine signal (force stimulus) was fixed to 0.5 Hz, which is the minimum frequency that guarantees

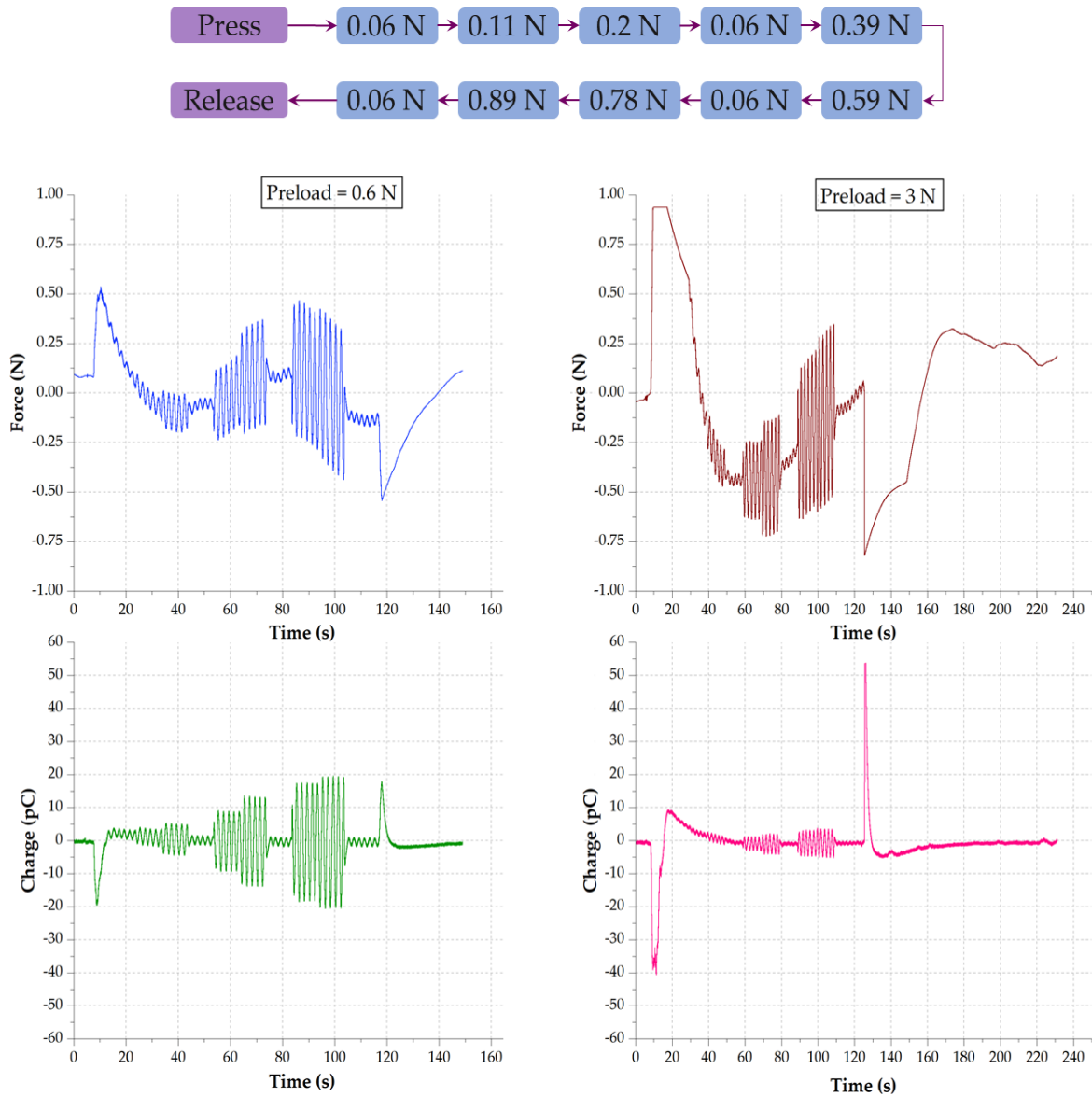


Figure 5.7 An example of a sequence of forces and the corresponding charge response at preload of 0.6 N (left) and 3 N (right)

a normal behavior from the shaker. Moreover, the force range and levels were selected based on the specification of the shaker where higher forces might damage the shaker. Therefore, it is important to note that the force range is limited by the setup, not by the response of the sensors. Before running each sequence, a preload has been applied to guarantee indenter-skin contact during the entire mechanical stimulation. Then, each sequence has been repeated for each of the following preloads 0.6, 1, 2, and 3

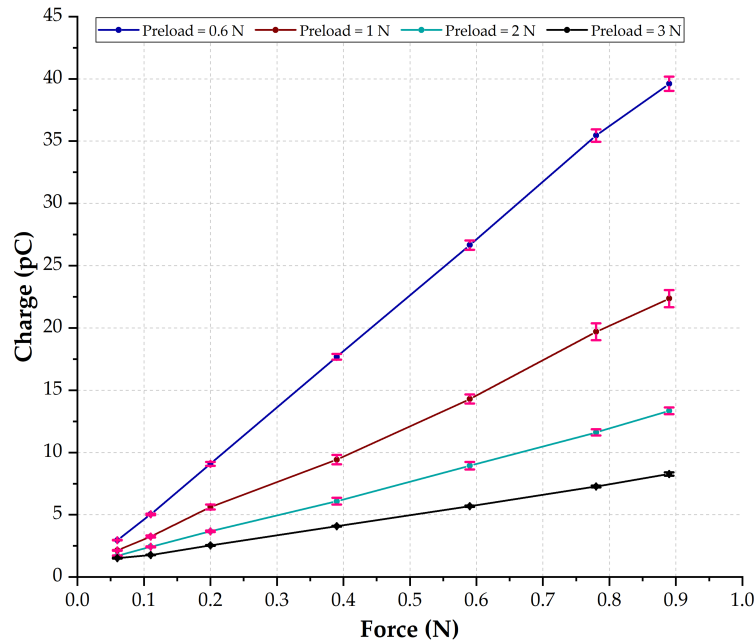


Figure 5.8 Average charge response vs force at four preloads.

N. Figure 5.7 shows an example of a sequence of forces applied on a single sensor. The figure illustrates the applied stimulus and the corresponding charge response at two preloads (0.6 N and 3 N). As shown in the figure, in each sequence there is one force level that was repeated four times to check the repeatability in the response of the sensor. Therefore, In each sequence, there is a force level repeated four times and it has a specific force order. This was repeated for all the selected force levels, therefore, resulting in six sequences of forces, and each sequence was repeated 4 times (4 preloads).

For each sequence, the charge response at each force level was computed as the peak-to-peak amplitude and then averaged over time. Therefore, the output of each sequence is a single charge value for each force level. For example, the sequence shown in Figure 5.7 results in four charge values for the 0.06 N force and one charge value for each of the remaining forces. This was repeated for all six sequences. To plot charge response vs the force level, the charge values (for each force level) from all the sequences were averaged and then we computed the standard deviation as an

indication of the repeatability in the sensor response. Figure 5.8 shows a linear behavior between the charge response and the force applied on the surface of the skin patch. The obtained results meet the results obtained in Chapter 5 where a linear relationship between the charge response and the force stimulus was detected. The results presented in Figure 5.8 show that indeed sensor response to force does significantly depend on the preload. It turns out that as the preload increases, the average charge response decreases, and values from different trials exhibit a lower dispersion (lower standard deviation). Such result is aligned with the findings of the study presented in Chapter 3, where it was found that as the preload increases, the average d_{33} decreases, and values for different sensors exhibit a lower dispersion. The results shown in Figure 5.8 illustrate that the response of the sensors is repeatable where the standard deviation at each force level is very low compared to the charge value.

5.4 Touch pattern detection

The experiments done so far use a quasi-ideal experimental setup where testing parameters have been pre-defined (i.e. touch alignments, pre-programmed force, and frequency). Although the results verify and validate the good response of the sensing system and especially the skin patch, however, the system should be further tested in a more realistic scenario. The aim is to study the response of the sensing system to different touch patterns that might be incorporated while the skin patch interacts with objects. Moreover, we would like to study the correlation between a stimulus applied at the surface of the skin patch and the charge response. For this purpose, we have arranged a new experimental setup. Figure 5.9 shows the developed setup, The skin patch was placed on the top of a strain gauge load cell (Tedea Huntleigh, Model 1042) and faced upside. The load cell was used to measure the force applied on its surface where the skin patch is placed. The force stimulus was conditioned by a PXIe-4330

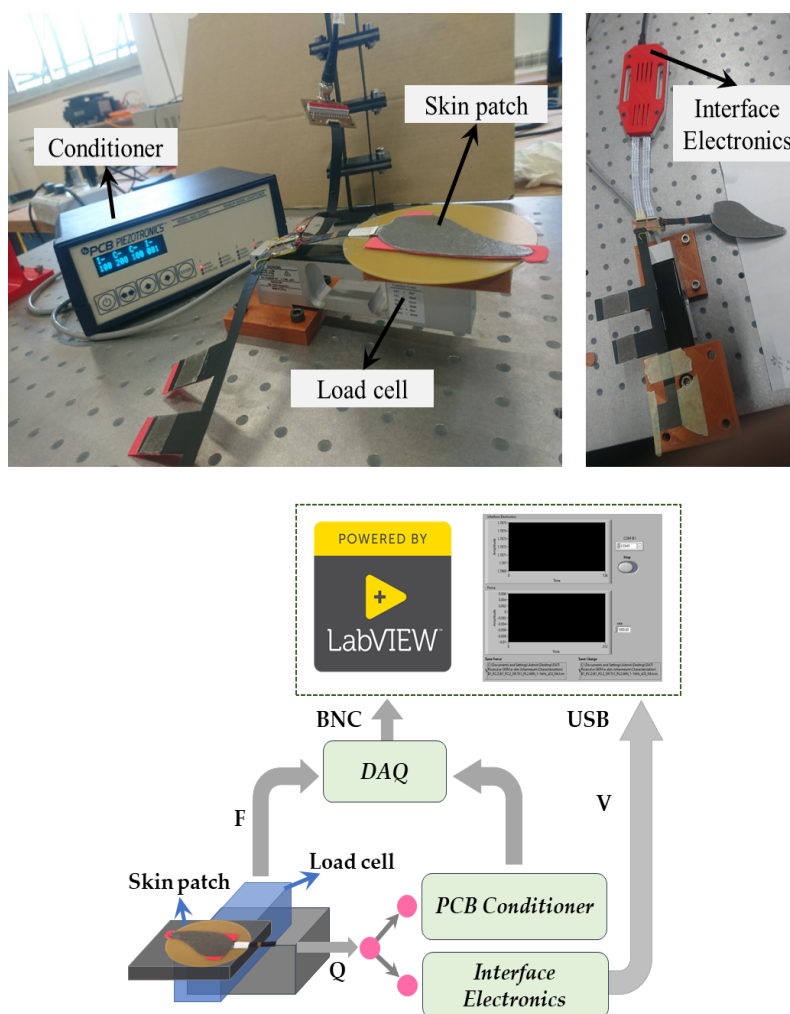


Figure 5.9 Experimental setup. Top: Pictures of the setup, Bottom: Block Diagram. The blue dotted line shows the alignment of the testing elements.

(NI, US) conditioning board while the charge developed by the sensor (response) was conditioned either by the PCB Sensor Signal Conditioner (482C54) or by the interface electronics as illustrated in Figure 5.9. A LabVIEW software developed on a National Instruments PXI system was used to collect, visualize, and save the force stimulus and the charge response.

Three touch patterns were selected, tapping, Press-Hold-Release, and continuous touch. We believe that these touch patterns are the most used during daily life activity, for example, tapping might be used for detecting the stiffness of the object. During

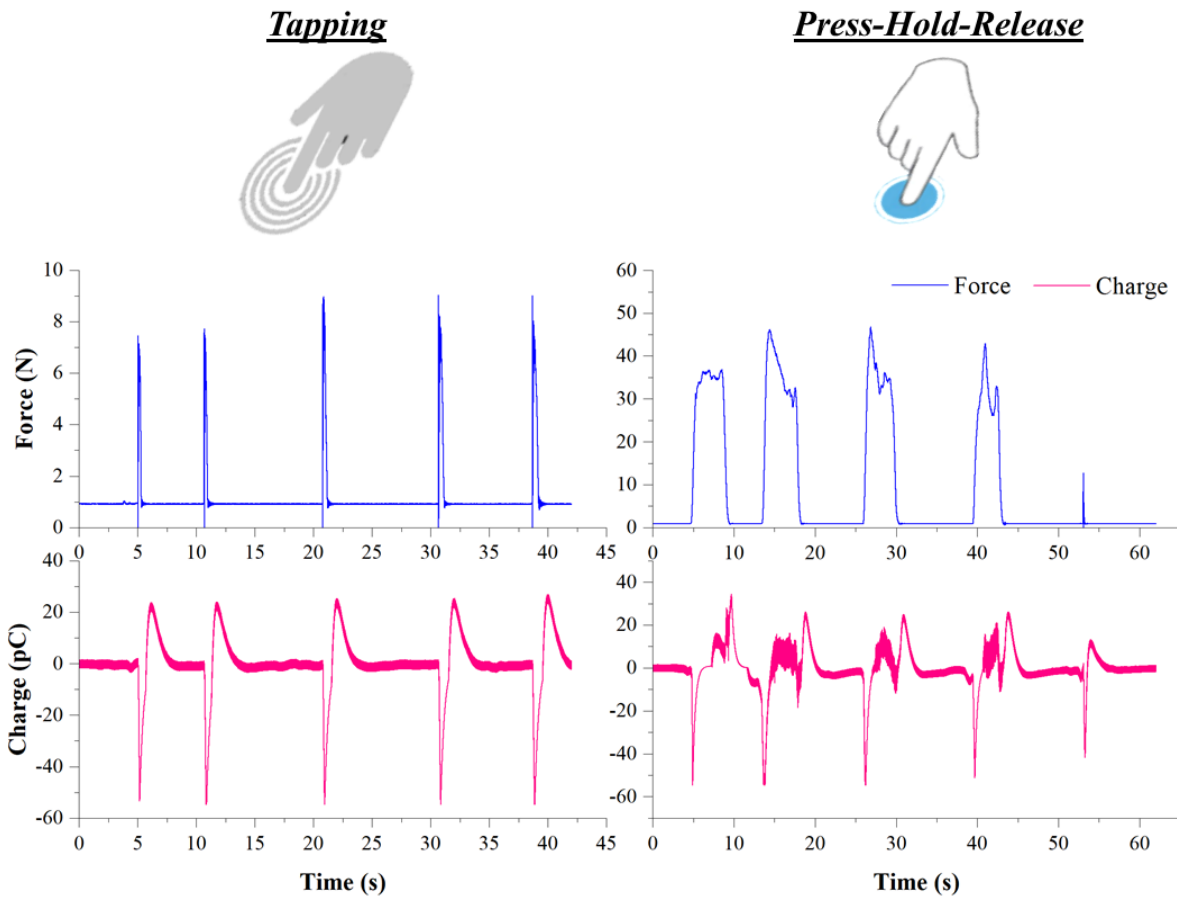


Figure 5.10 Response of the single sensor to tapping (left) and press-hold-release (right) touch patterns.

the tests, the experimenter applied one of the aforementioned patterns on a single sensor using his/her finger. Representative results from the sensing system validation experiments are shown in Figure 5.10 and Figure 5.11. The two figures show the force stimulus detected by the load cell and the corresponding charge response. In particular, Figure 5.10 shows the response of a single sensor to the tapping and Press-hold-release patterns. Similarly, Figure 5.11 shows the continuous touch patterns and the corresponding sensor response.

The results show that the sensor captures the dynamic features of the mechanical event by generating two phasic bursts. The contact onset is associated with a decrease whereas contact release generates a signal increase which is aligned with the result

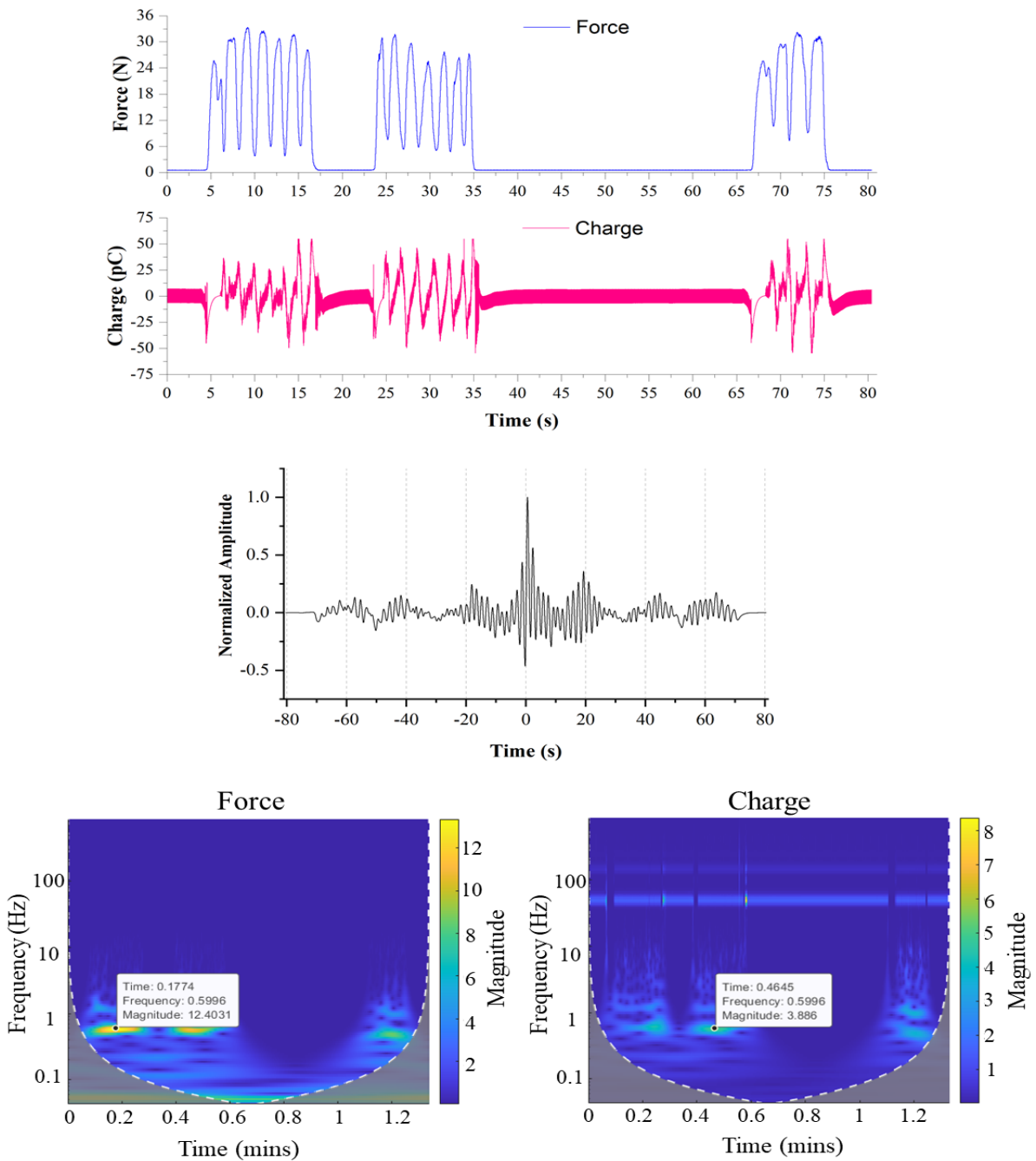


Figure 5.11 Response of single sensor to a continuous touch pattern (Top) and the correlation between the applied stimulus and the sensor response (Middle). Bottom: continuous wavelet transform (CWT) of the applied stimulus and the sensor response.

obtained in the previous section. The signal peaks are arranged in a sequence reflecting the fact that the touches were applied to the sensors sequentially. The Press-Hold-Release pattern was presented by the sensor by two bursts corresponding to the press

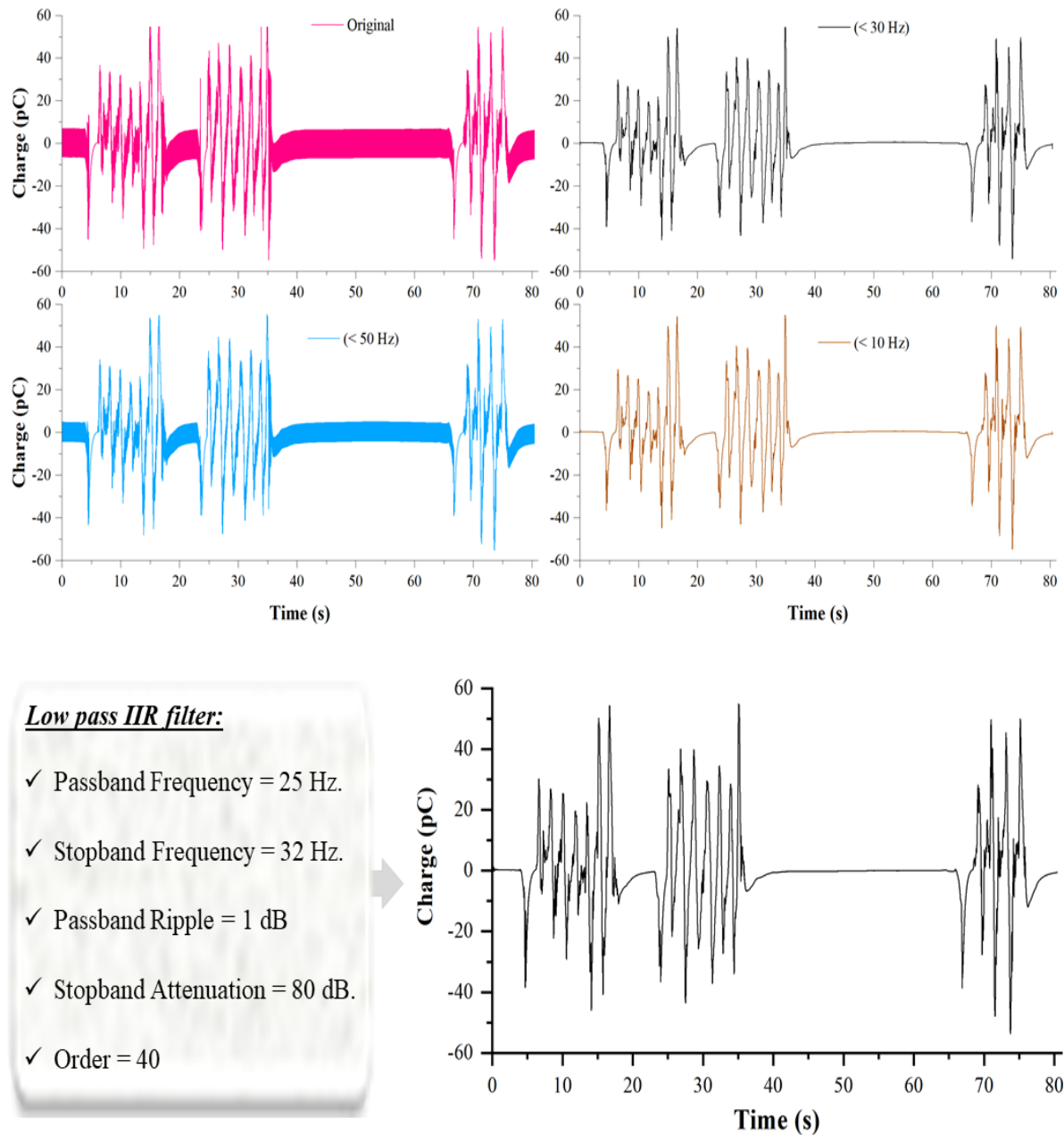


Figure 5.12 The Output of inverting the continuous wavelet transform over three frequency ranges (< 50 Hz, < 30 Hz, and < 10 Hz) Bottom: Specification of a low-pass IIR filter that could be used to reduce the noise level and the output signal.

and release events, while in-between the bursts there was some wiggling. The Press-Hold-Release event was not stable because it was applied using the finger, which makes it difficult to maintain the force level. Finally, the plot presented in Figure 5.11 (Top) indicates that the sensor responds to a change in the applied force in which the charge

response follows the force stimulus. Interestingly, the sensor response pattern, in this case, is more complex; the press and release peaks are still visible, but they are not as sharp as in Figure 5.10. The cross-correlation between the continuous touch pattern and its charge response was computed and plotted in Figure 5.11 (Middle). The plot shows a high correlation between the force stimulus and the sensor response with a small-time lag.

In all the experiments implemented so far, a high noise level was detected in the response of the sensors. This was more observed when using the sensing system in more realistic scenarios i.e., the setup shown in Figure 5.9. Such behavior or issue was observed more when plotting the time-Frequency analysis (Continuous Wavelet Transform) of the continuous touch pattern and the corresponding charge response (see Figure 5.11 (Bottom)). The plot shows a high power for 60 Hz which is the common noise frequency. Moreover, using the Time-Frequency plot we can indicate that the frequency range of the sensor response is below 30 Hz.

To better define the frequency range of the sensor output, we used the Inverse continuous 1-D wavelet transform function on Matlab (MathWorks, US) to invert the continuous wavelet transform as shown in Figure 5.11 (Bottom) over multiple frequency ranges. The results are shown in Figure 5.12 (Top). The plots show that the frequency range < 30 Hz contains the most power of the signal, moreover, it cleans the signal from noise. Such frequency range could be extracted by applying a simple low-pass digital filter. As an example, Figure 5.12 (Bottom) shows the output signal after applying a low pass IIR filter with the stopband frequency of 32 Hz. The outcome of the test is important to reduce the noise in the sensing system and implement a digital filter in the interface electronic firmware to add such preprocessing in the online feedback loop. This will be more discussed and explained in the next subsections.

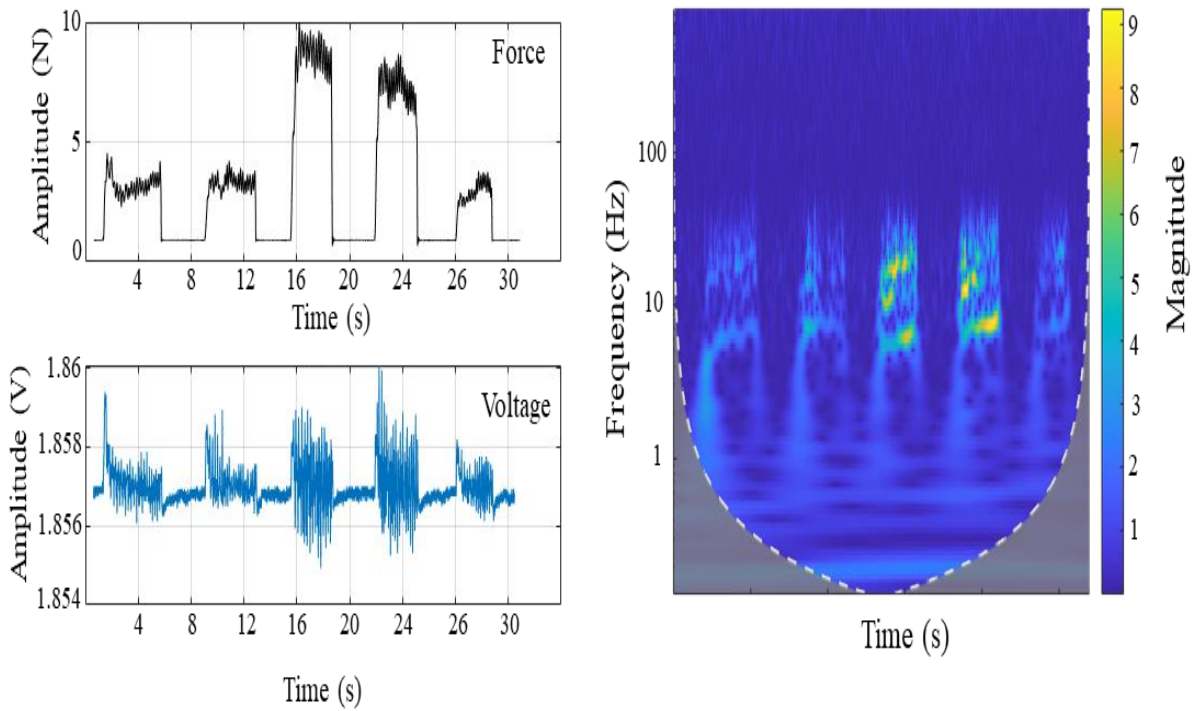


Figure 5.13 The output of the FIR filter after being implemented in the firmware of the interface electronics. Left: response of the sensor to Press-Hold-Release touch pattern. Right: continuous wavelet transform (CWT) of the sensor response.

5.5 Implementation of tactile signal processing

As indicated in the previous section, a signal processing strategy is required to improve the response of the sensors and interface electronics in capturing signals with low-frequency content and reduce the effect of noise (harmonics). For this purpose, we developed and implemented in the interface electronics two filtering methods: finite impulse response filter (FIR) and moving average filter (MAF). The implementation process is introduced and the results of the two methods are discussed next sections.

5.5.1 Filtering using Finite Impulse Response method

The design of the FIR filter is composed of two main parameters: cutoff frequency and filter order. Using the findings of previous experiments and especially the results shown in Figure 5.12, the cutoff frequency should be < 50 Hz. The filter order generally is

recommended to be high to result in a smooth signal. However, high filter order results in many multiply-accumulate (MAC) operations that are required to filter out only one sensor signal. Thus, implementing high-order filters to smoothen signals from 32 channels will introduce a huge delay in the extraction of tactile information and thus in the feedback loop. Therefore, a trade-off between the accuracy of the filter and the order should be considered while designing the filter.

After running several tests to find the trade-off among the filter parameters, an FIR filter with a cutoff frequency of 30 Hz and order 58 has been implemented in the firmware of the interface electronics. Applying such filter to all the interface electronics channels is challenging as the controller memory was limited to run 10 filters for 10 channels. To assess the behavior of the IE with the FIR implemented in its firmware, we used the setup shown in Figure 5.9 to apply one of the touch patterns (see Section 5.4) on a single sensor. Figure 5.13 shows the response of the sensing system (sensor and interface electronics) to the Press-Hold-Release touch pattern. The plots show that the output of the filter is smooth where the noise frequencies components were eliminated. The time-frequency plot on the right of Figure 5.13 confirms that the implemented filter eliminated the noise frequencies. Although the implemented FIR filter enhances the sensor signal and reduces the noise level, it is not possible to use it to filter signals from all the channels due to memory limitations. Moreover, the low filtering accuracy would make it difficult to construct light touches. To tackle such problems, in the next section we present a new filtering method.

5.5.2 Filtering by Moving Average Filter

Moving average filter (MA) is one of the popular digital filtering techniques that can smoothen all kinds of data and reduce random noise. Exponential moving average filter (EMA) is a type of MA filter that operates with a low computational burden and can be implemented easily and efficiently. EMA filter computes a weighted average of the

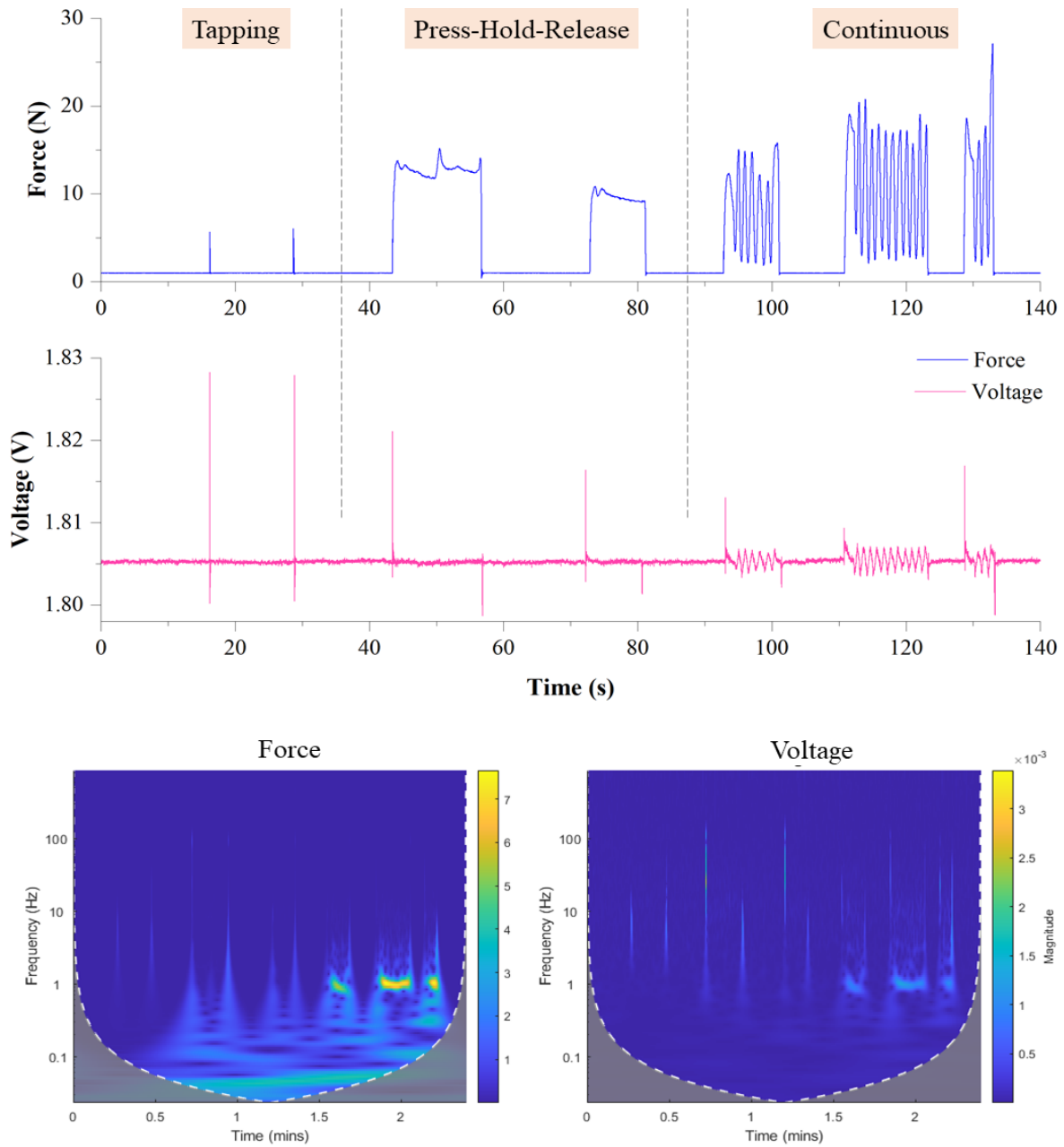


Figure 5.14 The output of the moving average filter after being implemented in the firmware of the interface electronics. Top: response of the sensor to the Tapping, Press-Hold-Release, and continuous touch patterns. Bottom: continuous wavelet transform (CWT) of the force stimulus and the sensor response.

time-ordered sequence by applying to the weights of the previous input that decrease exponentially [170]

The exponential moving average filter is expressed in a simple equation:

$$y[n] = \alpha x[n] + (1 - \alpha)y[n - 1]. \quad (5.1)$$

Where $x[n]$ is the current input, $y[n]$ is the current output, and $y[n - 1]$ is the previous output; α is a factor used to set the cut-off frequency. The EMA behaves as a low pass filter where low frequencies have a near-unit gain, and high frequencies are attenuated. The filter has been implemented on the interface electronics, performing filtering at around 30 Hz cut-off frequency. The filter α value has been computed and set to 0.09, which corresponds to the cut-off of 30 Hz. This allows the interface electronics to perform filtering with minimum delay and at a high sampling rate without losing samples during the run-time.

Figure 5.14 shows the response of the sensing system to the three touch patterns after implementing the EMA filter in the firmware of the interface electronics. The plots demonstrate the lower noise level compared to the output of the FIR filter and smoother signal. This result is confirmed in the spectral plot of the force stimulus and the sensor response as shown in Figure 5.14. The implementation of the filter on the interface electronics and applying it for the 32 sensors, results in a significant improvement in the performance of the interface electronics in terms of noise cancellation and detection of touch events.

5.6 Conclusion

This chapter presented the development of a novel skin patch that is based on PVDF sensors. The skin patch is composed of the sensing arrays, shielding layer, and protective layers. It was developed to be applied on different types of surfaces. In this chapter, two experimental setups were developed to test the developed skin patch and assess the response of the sensing system i.e., skin patch and the interface electronics. The system

was first tested in a controlled environment where we checked the linear relationship between the sensor response and the applied stimulus. Moreover, we tested the response of the sensors to different stimulus waveforms. Secondly, the system was tested in a more realistic scenario where we checked the ability of the sensor to detect three touch patterns. Based on the output of the latter experiment, we developed signal processing methods for noise cancellation and touch detection enhancement. The study described in this chapter presents the first step toward integrating the sensing system in different applications (e.g., sensorize prosthetic hand). Moreover, the results demonstrated that the sensing system could detect different touch modalities. Therefore, the system could be easily integrated into a feedback system where it detects different touch modalities and extracts tactile information that might be delivered to the user.

Chapter 6

Embedded Electrotactile Feedback System for Hand Prostheses using Matrix Electrode and Electronic Skin

6.1 Introduction

Upper limb loss leads to substantial disability and thus dramatically reduced quality of life of an amputee. Myoelectrically controlled prosthetic hands have been developed to substitute the functions of the biological hand (e.g. [171]). Such prostheses are controlled by recording electromyography (EMG) signals from the residual limb muscles to estimate user movement intention, which is then converted into commands for the prosthesis [172]. Despite remarkable progress in improving the control, amputees often reject their prosthetic hands [27, 173]. One of the drawbacks of the contemporary prostheses, which might contribute to their rejection, is the lack of somatosensory feedback from the prosthesis to the user; hence, the amputees do not “feel” their bionic limbs. Restoring the missing tactile feedback can have a positive impact on the utility and user experience by improving performance and facilitating the feeling of ownership

[136]. A system for feedback restoration comprises the following components [174]: (i) a sensing system for the detection of tactile stimuli; (ii) a readout circuit for data acquisition and the encoding of tactile data into stimulation profiles; and (iii) a stimulation system to deliver the stimulation patterns to the prosthesis user. Preferably, the technical solution should be simple, compact in size, portable, and durable.

To provide artificial tactile feedback, the prosthesis is equipped with sensors measuring the interaction with the environment (e.g., grasping force). Acquired sensor data are translated into stimulation patterns and delivered to the user invasively by stimulating peripheral nerves [175], or non-invasively through electrotactile, mechanotactile, and vibrotactile interfaces [135, 21]. These methods have been extensively described and compared in several recent reviews [135, 21, 176, 177]. Despite many different approaches that are presented in literature, a common characteristic of these systems is that they typically transmit only one or two global prosthesis variables [178]. Most often [136], the total grasping force is selected as the feedback variable since this is a critical parameter during grasping where an inappropriate force can lead to object slipping or breaking. Sometimes, the feedback also includes hand aperture, which in combination with force allows recognizing object size and stiffness [179, 180]. To provide such artificial exteroceptive and proprioceptive feedback, the prosthesis needs to be endowed with sensors that measure position and force [14]. Typically, the measured sensor information is transmitted to the subject by using only a few stimulation channels, for instance, several electrodes [181], vibration motors [182] and mechanical pushers [183] that provide stimulation to several discrete points along the residual limb. These feedback systems enable the user to feel “global” sensations, e.g. contact, slippage, hand aperture and applied force, and it has been demonstrated that such feedback can indeed improve performance and user experience. Nevertheless, an effective feedback system is still an open challenge as the impact of feedback depends on multiple interacting factors [136]. The aforementioned approaches are

limited in the number of sensors and stimulation points, and this substantially limits the bandwidth of information that can be transmitted through the feedback interface. This is in a sharp contrast to the human hand, which is covered with a dense network of tactile mechanoreceptors and hence the natural feedback provides spatially distributed pressure information.

Importantly, advanced sensing solutions that allow capturing spatially distributed mechanical interaction are becoming more common. Several of such sensor systems have been developed for robotic hands and are commercially available. The most relevant for tactile sensing are BioTac, TekscanTM, and DigiTacts. BioTac [84] is a sensorized finger equipped with a matrix of pressure sensors across the fingertip, as well as a vibration and temperature sensor. Electronic skins integrating matrices of sensing elements embedded into flexible structures have been fabricated (e.g., [61, 184–188]). Most of these sensors were originally developed in the robotic framework. However, they can be utilized in prosthetics, and some solutions have been already developed specifically for this application [39, 53, 30, 189–191].

Since such sensing systems embed a network of sensors, they are attractive solutions for providing an advanced feedback to a prosthesis user. However, a critical question in this approach is how to transmit the rich tactile information recorded by an e-skin as the feedback to the user of a prosthesis. Electrotactile stimulation is particularly attractive technology for this application since it is compact and allows printing electrodes in different shape, size and configuration of the conductive pads (stimulation points) [192]. In addition, it is characterized with fast response since there are no moving mechanical elements, which may be particularly important when delivering feedback during dynamic interactions. Finally, it also allows independent modulation of stimulation parameters, namely, intensity and frequency, which enables flexibility in encoding of the tactile information [193, 194]. In our previous work, [195, 196], we have investigated the possibility of communicating tactile information

from 64 piezoelectric sensors (PVDF-based sensor array) using matrix electrodes placed on the forearm. However, the skin sensor was not designed for a prosthetic hand and was placed on a table surface. In addition, the electronics and acquisition system was not integrated but implemented on a dedicated PC.

The development of an embedded real-time feedback interface that is capable of distributed sensing (i.e. sensors all over the hand) and stimulation is an important step towards the clinical application of this approach. Most of the embedded solutions that were presented in the literature are based on a few FSR or strain gauge sensors with either electrotactile [197–200], mechanotactile [201, 202, 174], or vibrotactile [203–206] stimulation for delivering feedback information (e.g. touch position and force level) to the subject. Similarly, [207] developed a multi-modal sensory feedback system that maps sensory information from five piezoelectric barometric sensors into stimulations through vibrotactile or mechanotactile feedback. Compared to conventional approaches to sensorization of prosthetic hands, which rely on a few sensors (e.g., overall grasping force, contact on the fingertip), the integration of an e-skin with many sensors distributed over the fingers and/or palm combined with surface stimulation through matrix electrodes endows a bionic limb and its user with high fidelity sensing and feedback. Such system can provide prosthesis users with sensations that cannot be restored using conventional methods. For instance, when a prosthetic hand grasps an object, the users can feel spatially distributed sensations that reflect contact surface and texture, as well as movement of an object within and across the hand. Such feedback can increase performance, enable social and passive touch, and promote the feeling of embodiment [208]. Furthermore, the distributed contact and pressure information detected by an e-skin can be used to detect slippage and estimate/control grasp stability (semi-autonomous control [209]). However, the drawbacks of this technology can be increased cost and system complexity. To achieve this functionality, several components need to be developed and connected into an online pipeline. The components

have to be compact so that, in the future, they can be integrated into a socket and economical in power consumption (wearable system). Finally, the sensing (e-skin) and stimulation (electrode) interfaces need to be conformable to the curved shape of the hand (prosthesis) and limb (user), respectively. Recently in [210], we demonstrated a preliminary version of an embedded feedback system that transferred tactile data from flexible piezoelectric sensing array onto the forearm of three subjects using discrete electrotactile stimulation. The sensing arrays were placed on the table and tapping on one of the sensing arrays was delivered to the subject in the form of electrotactile patterns through three concentric electrodes. The present chapter describes a novel embedded system for tactile feedback based on distributed sensing and stimulation. The system comprises a flexible piezoelectric sensing array with 16 sensors integrated on the index finger of the Michelangelo prosthetic hand mockup, an embedded electronics and multichannel stimulator connected to a flexible matrix (24 pads) electrode placed on the forearm. In this first version of the prototype, the online feedback delivered contact information (binary detections) from the e-skin to the subjects. The system is compact, portable and thereby suitable for integration into a myoelectric prosthesis. The system increases the bandwidth of tactile information that can be detected and transmitted to the user leading thereby to a rich tactile feedback, which can potentially improve utility and facilitate embodiment. There are many compact solutions for restoring tactile feedback in upper limb prostheses [135]. However, to the best of our knowledge, this is the first solution that integrates all the required components to provide online multichannel feedback from an e-skin. To achieve this, we have developed a new approach of integrating an e-skin onto the curved surfaces of a prosthetic finger. Next, a method was developed to process the tactile data and extract contact information from the e-skin. The data processing method as well as a communication protocol to transmit the processed data to the stimulation unit were implemented within an embedded electronic system. Finally, an experimental assessment was conducted to demonstrate

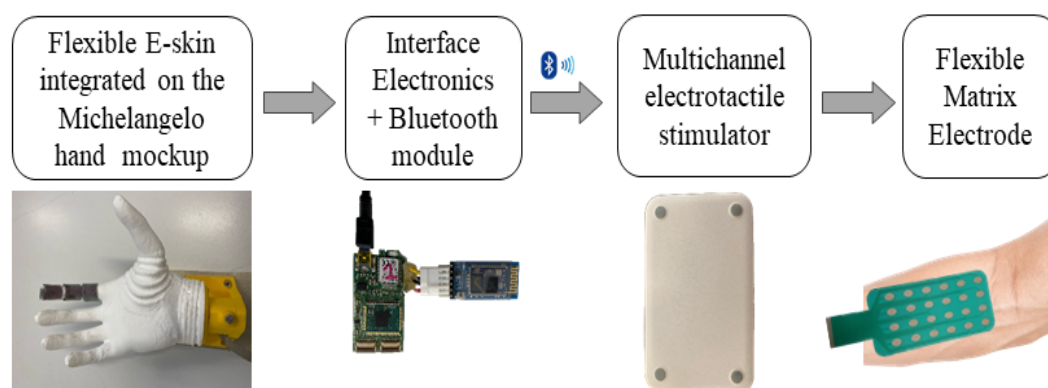


Figure 6.1 System Architecture. The system comprises an e-skin with 16 sensors, interface electronics for signal acquisition, and a multichannel stimulator with flexible matrix electrodes integrating 24 electrode pads to deliver the electrotactile stimulation to the subject. The system therefore translates the tactile data recorded by the e-skin into stimulation profiles that are delivered online to the skin of the subject.

that the developed components properly work together. The experimental assessment demonstrated that the developed system indeed delivered the desired functionality – a timely multipoint electrotactile feedback on the static and dynamic contact patterns, which was easily perceived and interpreted by the subjects. In this chapter, the system components, including hardware and signal processing are described and the results of the online assessment of the system in able-bodied subjects are reported.

The chapter is organized as follows: Section 7.2 presents the materials and methods. Section 6.3 describes the experimental assessment of the developed feedback system. The results related to the assessment of the system are reported in Section 7.5. Finally, our discussion and conclusive remarks are given in Section 6.5. The content of this chapter is presented in [211].

6.2 Materials and Methods

6.2.1 System Architecture

The designed embedded system for electrotactile feedback (Figure 6.1) includes 1) piezoelectric sensing arrays (electronic skin), 2) an interface electronics, 3) a master Bluetooth module, 4) an electrotactile stimulator, and 5) a flexible matrix electrode. The e-skin converts mechanical contacts into a set of electrical signals (one signal per sensor). The sensor signals are sampled by the interface electronics, processed and mapped into stimulation patterns using a predefined encoding scheme. More specifically, the signals are filtered and thresholded to detect contact events, and the contact information is used to set the state (on/off) of the corresponding stimulation channels. To this aim, the interface electronics generates appropriate stimulation commands and sends them through the Bluetooth module to the stimulator. The electrotactile stimulation is delivered to the subject through the matrix electrode placed on the subject's forearm. The electrode is placed on the forearm to mimic the envisioned application in prosthetics, in which the interface would be located on the residual limb of a transradial amputee. The feedback pipeline runs in real time and therefore, the tactile interaction (contact information) registered by the electronic skin is translated online into dynamic tactile sensations elicited across the subject's forearm. The block diagram of the overall system is shown in Figure 6.1.

6.2.1.1 Tactile sensors Arrays

Based on the results of the study present in Chapter 3, A new batch (new version) of sensing array was fabricated by JOANNEUM RESEARCH [154]. The sensing arrays were fabricated using the same procedure presented in Chapter 3, however taking into account the problems discovered in the validation of the sensors (see Section 3.3.1). Figure 6.2.a shows the new structure of a single sensor.

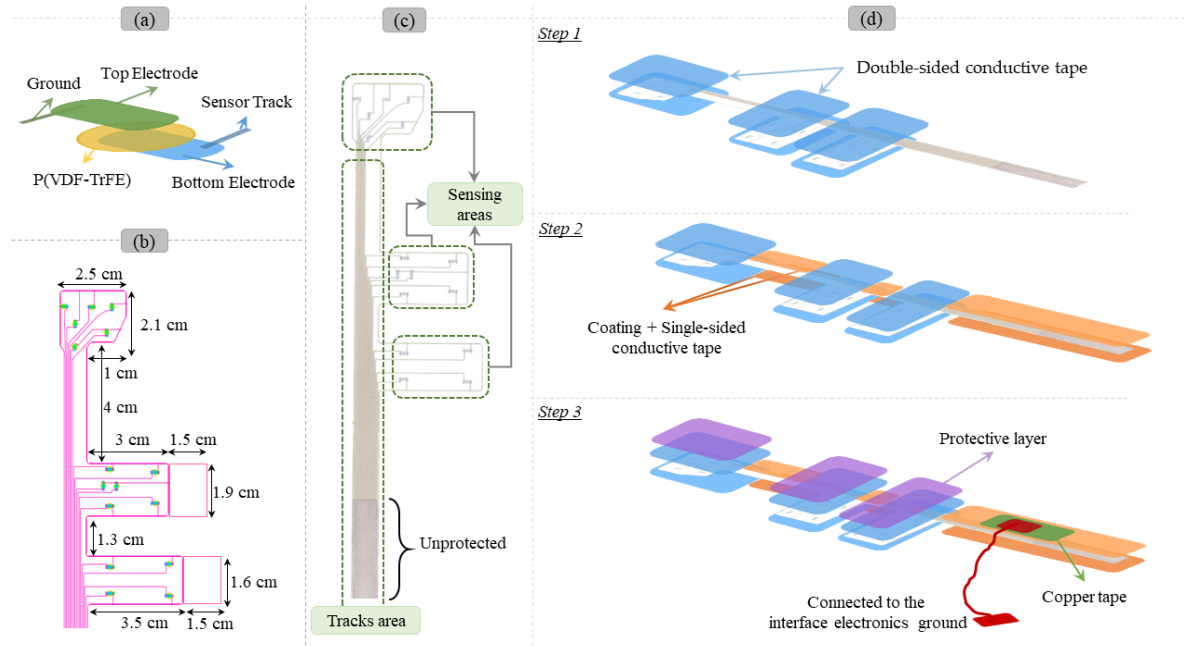


Figure 6.2 (a) Single sensors structure, a P(VDF-TrFE) layer sandwiched between two electrodes. (b) Layout and dimension of the sensing array dimensioned to cover the index finger of the Michelangelo hand prosthesis. (c) The sensing array is composed of three sensing areas and a tracks area. (d) Skin patch development process. The sensing array is shielded using conductive tapes and a thin protective layer is used to protect the sensing areas.

The fabrication process presented in Chapter 3 was used to fabricate a new version of the sensing arrays designed for the Michelangelo prosthetic hand (see Figure 3.3.c). A complete set of sensing arrays with different geometries and sensor distribution has been designed to fit the fingers and palm of a Michelangelo prosthetic hand [14]. The fingers sensing arrays are designed to fit easily on the prostheses phalanges, without the need for special disassembly or mechanical manipulation of the device. In the present study, a single array made for the index finger of the prosthesis was integrated into the feedback system. The index finger is most commonly used during grasping and manipulation, and it was therefore covered with the sensors most extensively. Specifically, the sensors were arranged to cover the volar and lateral sides of the fingertip (5 and 2 sensors), middle (2 and 2 sensors) and proximal phalange (2 and 2 sensors), as shown in Figure 6.3.a. The sensors on the lateral aspect of the index

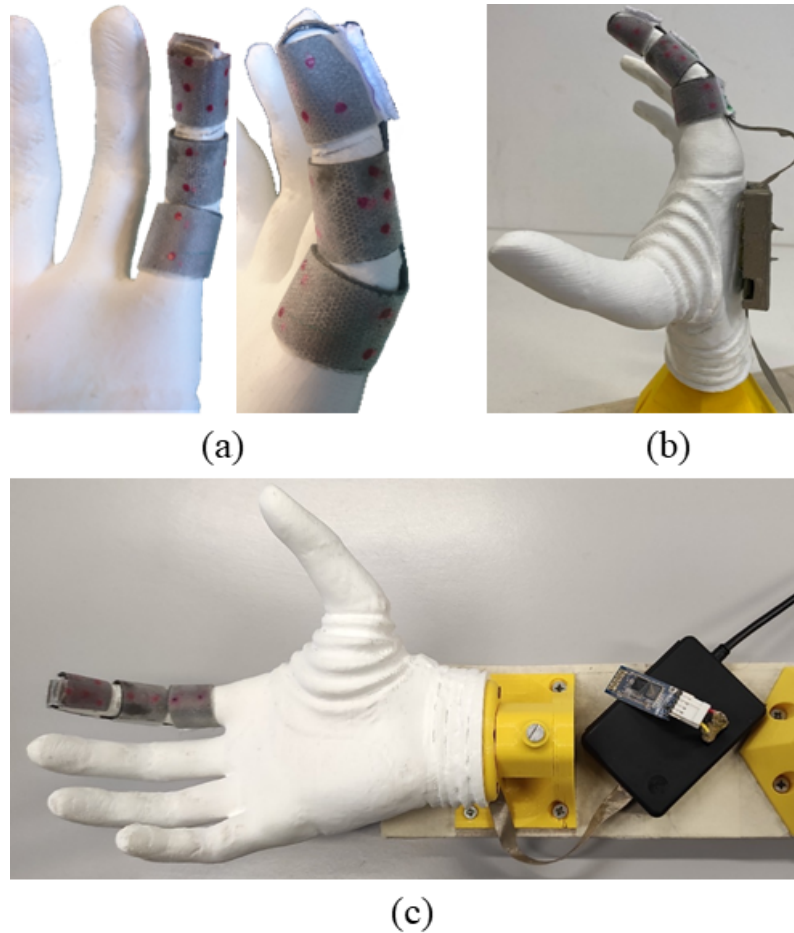


Figure 6.3 Sensing system integrated on the Michelangelo hand mockup. (a) The sensing array with 16 sensors attached to the index finger (b) Sensing array connected to a PCB placed inside a shielding box and attached to the back of the hand. (c) A shielded flat cable connects the PCB on the back to the interface electronics, and the interface electronics with Bluetooth module were placed inside a shielding box.

finger were added to allow contact detection when lateral grasp is used. In this case, an object is grasped between the thumb and the lateral side of the index finger, as when grasping a key. Figure 6.2.b shows the geometry, sensor distribution, and dimensions of the index finger sensing array while Figure 6.2.c depicts the sensing and tracks areas.

The same structure of the skin patch developed in Chapter 5 was used to integrate the sensing array on the index finger. However, the geometries of the different layer were modified because of the curved surface (finger). In order to apply the sensing arrays on the prosthetic fingers, an integration process was invented to protect the skin

electrically and mechanically, while allowing it to conform to the shape of the finger. In the present study, the sensing arrays for the index finger have been chosen as a representative example to test the newly developed procedure for the integration of the skin on the hand mockup as well as to demonstrate the online operation of the complete feedback pipeline (Fig. 1). Figure 6.2.d shows the integration process of the skin on the mockup model of the prosthesis. The integration process was done in three main steps. Since the sensing system might be exposed to external charge especially when the arrangement is based on piezoelectric sensor and charge amplifiers, the sensing areas were first sandwiched between two double-sided electrically conductive tapes (Model tesa 60262, tesa). The conductive tape was used as a shielding layer, which guarantees a minimum sensitivity to noise. The mockup was 3D printed using P.L.A (polylactic acid) plastic with the Fused Deposition Modeling (FDM) technique. The texture of the mockup is semi-rough and not completely soft. For that reason, the skin patch was coupled from the bottom side with a flexible cylindrical shape substrate (PVC of 0.25 mm thickness) using a double-sided adhesive tape (Model 3M 9485, 3M). The resulted structure was then wrapped around the index finger of the mockup. In the second step, a small PCB comprising two FPC sockets was fixed using hot glue to the back of the hand to route sensor signals to the interface electronics. The skin patch was connected to the PCB, and then hot glue was applied to ensure the stability of the tracks-socket connection. An insulating coating (Model PLASTIK 70, KONTAKT CHEMIE) was applied to the unprotected part of the tracks area to protect and insulate the sensor tracks. The tracks area was shielded using single-sided electrically conductive tape (Model tesa 60234, tesa). Both conductive tapes (single-sided and double-sided) are conductive from both sides and hence they were electrically connected once they were coupled to each other. The shielding layers were connected to the ground of the interface electronics (see Section 6.2.1.2) using a self-adhesive copper foil tape and a wire (Figure. 6.2.d). Finally, a thin flexible cylindrical shape protective layer (Art. 5500

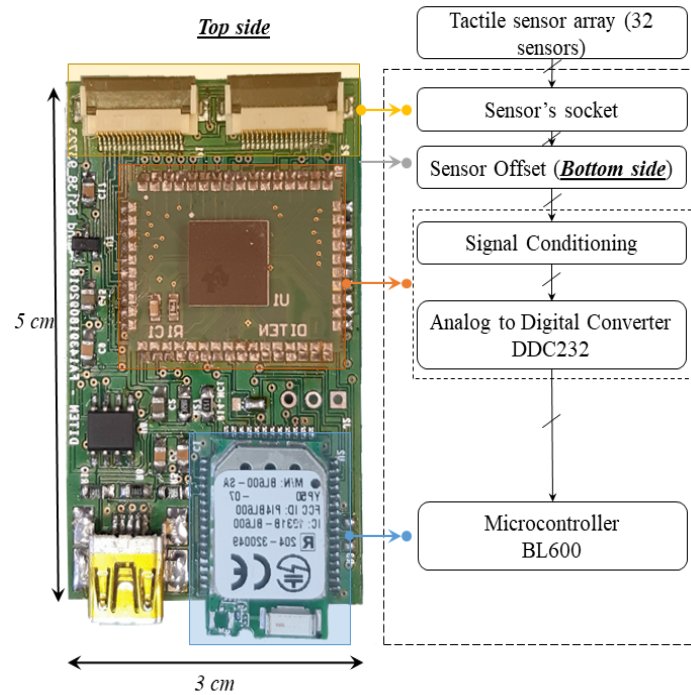


Figure 6.4 Interface electronics printed board circuit (left) and its block diagram (right). The module can sample 32 tactile signals, process and transmit them wirelessly with a remote host via a Bluetooth connection. The module also implements the encoding scheme mapping the tactile signals into stimulation profiles and a command protocol to set the stimulation parameters of an electrotactile stimulator.

Dream, Framisitalia) was added on the top of the sensing area to protect the sensors from damage and increase the lifetime of the integrated sensing system, forming the skin patch. Figure. 6.3 shows the sensing system integrated into the mockup. The PCB on the back of the hand and the interface electronics were placed in small shielded boxes, respectively (see Figure 6.3.b and Figure 6.3.c, respectively). A shielded FPC cable was used to connect the PCB to the interface electronics. All the materials used in the integration process (i.e. substrate and protective layer) were produced by Smartex, Italy [212] and they are biocompatible.

6.2.1.2 Interface Electronics

Figure 6.4 shows the Printed Circuit Board (PCB) and the block diagram of the interface electronics design presented and validated in Chapter 4. Based on the results presented

in Chapter 4, the DDC232 chip of the interface electronics was configured to use 16-bit resolution and cover the maximum input charge response.

In the present study, the firmware for the interface electronics comprised 1) a novel signal processing method to detect contact events, 2) the mapping of the contact information into stimulation parameters, and 3) the communication protocol to transmit the computed parameters to the electrotactile stimulator, as described in Section 6.2.3. The interface electronics was configured to sample and process tactile data from 16 sensors at 2K samples/second. The 2 kHz sampling rate was used to capture the full bandwidth of the sensors (see Section 6.2.1.1), which is beneficial for detecting the timing of contact events, that are characterized by a steep increase/decrease in the signal. However, the sampling frequency was not optimized in the present study and it might be that similar results could be obtained with lower sampling rates. Importantly, the transmission rate via UART and Bluetooth interface was much lower, since it was event driven – the command was sent to the stimulator only when a contact event (press or release) has been detected (see Section 6.2.3).

6.2.1.3 Electrotactile Stimulator

The stimulation block employs a 24-channel programmable battery-powered research prototype stimulation system based on Tecnia technology of spatio-temporal distribution of pulses [192]. The device generates current-controlled, charge-balanced biphasic pulses with current amplitude in the range of 0-10 mA (0.1 mA step), frequency from 1 to 400 Hz (1 Hz step), and pulse width from 50 to 500 μ s (10 μ s step). The stimulator is equipped with a BT interface to receive commands controlling the stimulation parameters and the channel states (on/off). In the present study, the stimulator was controlled directly by the interface electronics by implementing the communication protocol in the firmware. The protocol comprised the commands for configuring the role of the stimulation channels (i.e. anode or cathode), modulating the pulse width of each

channel and the frequency of all channels, and setting the state (on/off) and amplitude of each channel. Once the feedback system is launched, the interface electronics sends the first four commands to initialize the stimulation parameters and then uses only the channel state and amplitude command to implement the online feedback.

6.2.1.4 Electrodes

In the present study, the stimulator was connected to a biocompatible flexible matrix electrode produced by Tecnia Serbia. The electrode was made of a polyester layer, Ag/AgCl conductive layer, and an insulation coating covering the conductive leads. It integrated 24 oval units (pads) with a longitudinal radius of 1 cm and a transverse radius of 0.5 cm arranged into a 6×4 grid. The center-to-center distance between the adjacent pads is 2 cm in longitudinal and 1.2 cm in the transverse direction, which is higher than the spatial discrimination threshold on the forearm [213]. The pads on the matrix were used as active pads to elicit sensations, whereas a single self-adhesive electrode placed on the dorsal side of the forearm acted as the common reference. To improve electrode-skin contact, the electrode pads were covered with conductive biocompatible hydrogel (AG725, Axelgaard, DK).

6.2.2 Signal processing to detect contact events

Figure 6.5 depicts the electrical response of one sensor to a press-hold-release contact pattern captured by the interface electronics. As shown in the figure, the sensors capture the dynamic features of the mechanical event by generating two phasic bursts in charge-mode output signals (Figure 6.5). The bursts correspond to the press and release events, while in-between the bursts there was almost no response apart from some wiggling. The contact event was indicated with a decrease whereas the release generated an increase in the signal. To reduce the signal noise and therefore detect light touches, the Exponential Moving Average (EMA) digital filter presented in Chapter 5

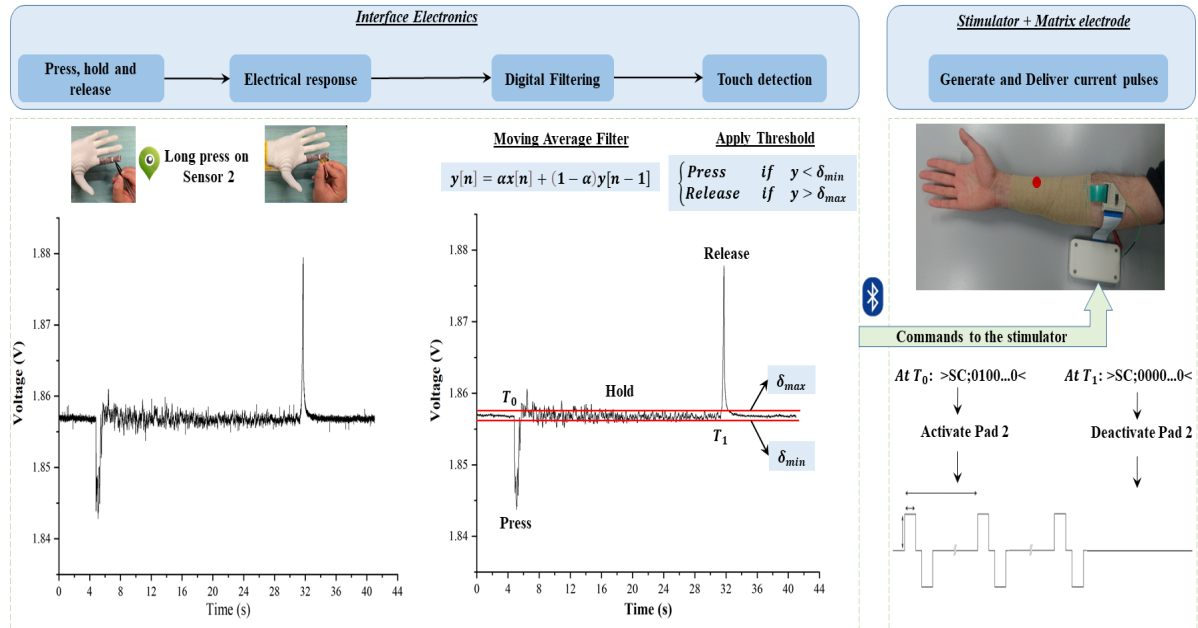


Figure 6.5 The online processing pipeline of the embedded feedback system. The left panel shows an electrical response (sensor signals) due to a contact applied to the e-skin by an experimenter using a pen tip (press-hold-release). The exponential moving average filter was applied and then the signal was thresholded to detect press and release (middle panel). Finally, the interface electronics sent stimulation commands to the stimulator to activate or deactivate stimulation at the corresponding channel, thereby eliciting tactile sensations (right panel) over the subject's forearm.

was implemented in the firmware of the interface electronics. To detect contact events, the Detection Thresholds (DT) of the 16 sensors were calibrated. To this aim, the interface electronics recorded signals from the skin for approx. 3 s with no mechanical interaction. The DTs were set to the lowest (δ_{min}) and the highest amplitude (δ_{max}) of the filtered signals measured during the 3 s calibration period to detect the press and release events, respectively.

6.2.3 Online feedback

Figure 6.5 illustrates the online processing pipeline of the feedback system. The interface electronics digitizes, acquires, and stores the electrical response of the 16 sensors. The EMA filter (described in Chapter 5) is then applied over the electrical

response of all the sensors, and the resulting signals are compared to the thresholds (δ_{min} and δ_{max}) to detect the press and release events. Once the interface electronics detected an event, it created and then wirelessly transmitted appropriate commands to the stimulator. As explained in the next section, the mapping was defined between the e-skin sensors and stimulation channels, so that a contact event activated corresponding stimulation channels while the release event turned off the stimulation on those channel. Hence, the subject felt a localized sensation each time a sensor on the e-skin changed the state (on/off). As an example, Figure 6.5 shows the electrical response of sensor 2 to a press-hold-release pattern and the corresponding feedback delivered through the electrode matrix. In response to the press, the command was sent to the stimulator to start the delivery of the electrical pulses through the pad 2 while the release deactivated the pad. The commands were transmitted as text messages, where ‘>’ and ‘<’ indicates the beginning and end of the message, and ‘SC’ is the message code for changing the channel state (0 and 1 – stop and start stimulation). The stimulation parameters (pulse intensity and frequency) were adjusted beforehand to elicit sensations that were clear and comfortable, as explained in the next section. The total delay from the applied contact to the stimulation is the summation of the delays throughout the different components of the pipeline. The overall delay was measured to be around 32 ms, which means that the response of the system is fast enough to transmit the desired signal without a perceptible delay.

6.3 Experimental Assessment

6.3.1 Experiments

Three experiments (Table 7.2) were designed to assess if the feedback system can convey static patterns (contact location) with two different spatial resolutions and dynamic patterns in which the contact changes over time (i.e., sliding along and/or

across the finger). In the tests, the experimenter touched the e-skin, the system detected the contact, and then transmitted tactile information to the subjects, who were asked to focus on the elicited sensations and interpret the feedback.

- **Group-to-Group experiment (G2G):** The aim of this assessment was to evaluate if the feedback system can successfully detect and convey to the subject the information on static contacts with low spatial resolution. The sensing areas of the e-skin patch were divided into 6 groups as shown in Figure 6.6.a. The 6 groups covered the three phalanges of the index finger from the volar and lateral sides. Similarly, 16 pads in the electrode matrix were selected and organized into 6 groups as shown in Figure 6.6.b. The pad groups were chosen to mimic the sensors groups in the number of pads and spatial arrangement. Touch information was transmitted to the subject using spatial coding. Touch applied to one of the sensing groups on the e-skin was mapped into the activation of the corresponding group of pads in the matrix electrode. The sensor group was deemed activated if any of the sensors belonging to the group registered a contact event, and in this case, all pads in the corresponding pad group started stimulating.
- **Sensor-to-Pad experiment (S2P):** The goal of this experiment was to test the effectiveness of the feedback system in detecting and delivering touch information with higher resolution compared to that used in G2G experiment. In this case, the contact applied to an individual sensor was conveyed to the subject by activating stimulation at the corresponding individual pad as shown in Figure 6.6. Hence, the subject was asked to discriminate between 16 different pads that could be activated/deactivated individually in response to contact/release events detected by the e-skin.
- **Sliding patterns experiment (SLP):** The aim of the test was to evaluate if the system can successfully detect and deliver the information about moving contacts

to the subject. The sensor to pad mapping was the same as in S2P experiment. The sliding movement applied on a sequence of sensors was conveyed to the subject by activating the corresponding sequence of pads in real-time (see Figure. 6.6.b). The movement patterns included sliding along the volar and lateral aspects of the index finger, and transversally, across each phalange.

6.3.2 Setup and Protocol

Six healthy subjects (male, age 28 ± 4 years) participated in the three experiments described in Section 6.3.1. All experiments were approved by the local Ethical committee of the Specialized Hospital for Rehabilitation and Orthopedic Prosthetics (approval number 1172). Before starting, the subjects signed an informed consent form.

Figure 6.7 shows the experimental setup used in all the experiments. The subjects were seated comfortably on a chair in front of a monitor used for visualization. The forearm of the dominant arm was placed on the table surface and the matrix electrode was then positioned on the volar side of the subject's forearm. The electrode was covered with a medical bandage to prevent movement and improve contact. Figure 6.7.b shows the view from the subject's perspective. The sensorized Michelangelo hand mockup was mounted on a support and placed so that the subject could not see the hand nor the experimenter interacting with the hand (see Figure 6.7.a). The interface electronics was connected to a host PC through a USB and paired with the stimulator

Table 6.1 Summary of Performed Experiments

Name	Description	Touch patterns
G2G	Spatial coding with six classes (static pads)	G1, G2, G3, G4, G5, G6
S2P	Spatial coding with sixteen classes (static pads)	Sensor 1 (S1), Sensor 2 (S2), ..., Sensor 16 (S16)
SLP	Spatial coding with five classes (dynamic patterns)	Distal, Middle, Proximal, Lateral, Medial sliding movement

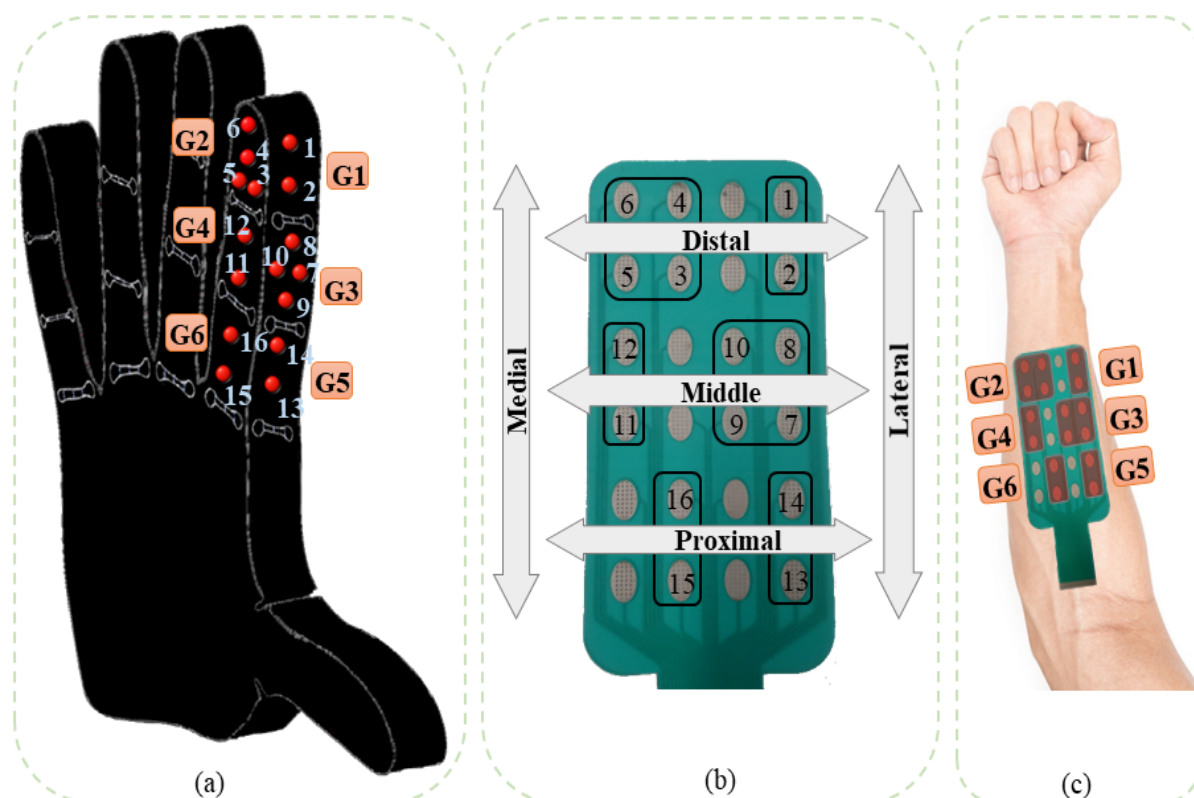


Figure 6.6 (a) Sensor distribution within the electronic skin placed on the index finger of the Michelangelo mockup. The sensors are numbered and each sensor is associated to a stimulation pad on a matrix electrode placed on the subject's forearm as shown in (c). The sensor and pads were also grouped into six corresponding groups (G1-6, boxes in (b) and (c)) where G1 corresponds to Group 1 and G6 corresponds to Group 6. (b) Three experiments were conducted to assess the subject's ability to perceive and interpret the feedback: 1- touch on a group of sensors (low spatial resolution), 2- touch on individual sensors (full spatial resolution), and 3- dynamic touch (i.e. sliding across medial, lateral, distal, middle, and proximal lines in two directions).

through the Bluetooth. Two screen monitors were used during the experiments, one positioned just behind the prosthesis and oriented towards the subject and the second oriented towards the experimenter. A LabVIEW software was developed on the host PC to visualize the activity of the sensors and the electrode pads. The software was used by the experimenter to monitor the tests and as the visual feedback to the subject during training, as explained below. Prior to the experiments, the Sensation Thresholds (ST) was determined for each of the 16 pads using the methods of limits by varying the pulse amplitude [214]. During the rest of the experiment, the pulse amplitude was

set to $1.5 \times ST$, which ensured that the sensations elicited by the feedback were clear and comfortable. The amplitudes were additionally fine-tuned by the experimenter until the subject reported that the perceived intensity was similar for all the pads. The pulse rate and pulse width were common to all the pads and set to 50 Hz and 140 μs , respectively.

As explained before, the aim of the experiments was to assess the subject's ability to identify the contact patterns applied to the e-skin, captured by the integrated sensing system and delivered to the subject through electrotactile stimulation via electrode matrix. Each test started with an introductory phase, in which the subject was presented with an explanation of the working principles of the sensory feedback system and the feedback mapping. The same experimental protocol was followed in the three tests (G2G, S2P and SLP) comprised of familiarization, reinforced learning, and validation phase. In all phases, each touch pattern (i.e. activation of a group of sensors, individual sensor activation, or sliding movement) was presented 5 times to the subject.

- Phase 1: Familiarization

In the familiarization phase, the subjects received online visual feedback on the screen monitor showing the applied touch pattern (sensor activity) and the corresponding stimulation pattern (pad activity). The subject was asked to use the visual feedback to build a mental mapping between the experienced sensation and the visual description (i.e. touched sensors, group of sensors, or sequence of sensors).

- Phase 2: Reinforced learning

In the reinforced learning phase, online visual feedback was removed, the contact patterns were randomly applied, and the subjects were asked to guess the applied patterns. The experimenter then provided visual and verbal feedback on the correct answer. Specifically, the experimenter said "correct" if the subject successfully

guessed the active pattern or “incorrect” otherwise. In the latter case, the correct answer was shown to the subject on the computer screen.

- Phase 3: Validation

During this phase, the protocol was the same as during the reinforced learning, however, no feedback on the correct answer was given to the subject. The validation phase was the main part of the experiment and the results from this phase were used to assess the performance, while the previous two phases were used as the training.

An additional experiment (Delay-Exp) has been implemented to measure the noticeable delay in the feedback system. The aim was to demonstrate that the feedback pipeline operates significantly below the delay that can be registered by the subject, ensuring thereby that visual and tactile feedback are perceived as essentially synchronous. Table 7.2 summarizes the description of the experiment and Figure 6.7.c shows the experimental setup used to measure the delay detectable by the subject. The subject wearing the electrode connected to the stimulator was seated on a chair in front of the sensorized Michelangelo hand mockup. During the experiment, the delay between the contact time and the activation of the stimulation was gradually increased in steps of 10 ms by the experimenter. This was done by introducing a delay in the command transmission in the firmware of the interface electronics. The subject was asked to report if he could perceive the delay between the moment when the experimenter touched one of the sensors and the start of the electrotactile stimulation. The subjects therefore compared the correspondence between the timing of the visual and tactile feedback. The experiment terminated once the subject reported that he perceived the added delay. Each of the three spatial discrimination experiments lasted approximately half an hour, whereas the delay test took approximately 10 min. A complete experimental session (setup and tests) lasted around 1 hour.

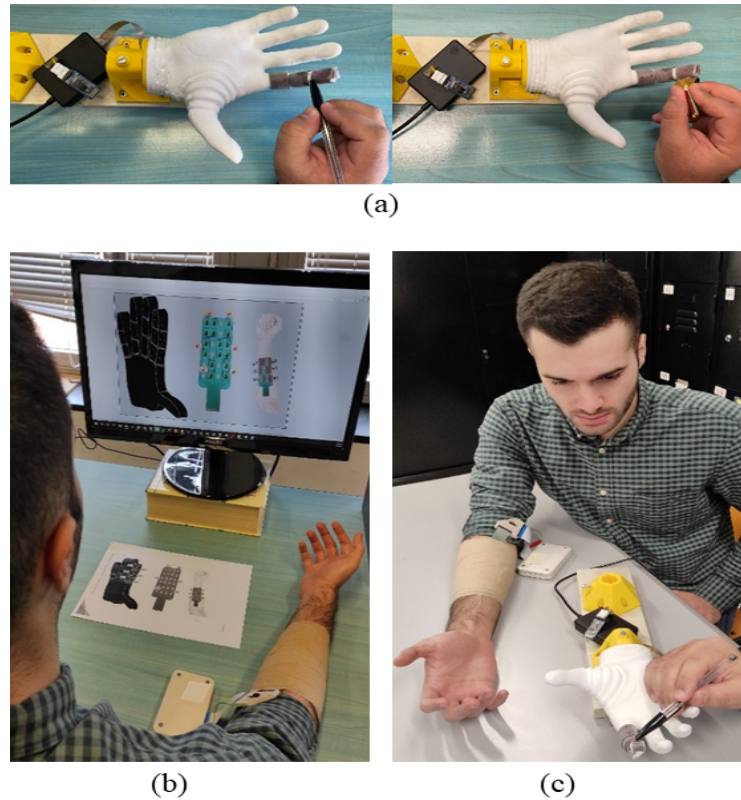


Figure 6.7 Experimental setup. (a) Experimenter interacting with the sensing system, (b) Subject received electrotactile feedback through a matrix electrode placed on the right forearm and covered with a medical bandage. The subject received visual feedback shown on the computer screen only during the familiarization phase. (c) In an additional experiment, the setup was used to measure the acceptable touch-stimulation delay. In this test, the subjects received the tactile feedback while looking at the experimenter touching the hand, and they were asked to report when the delay (intentionally added in the system) between tactile and visual feedback became noticeable.

6.3.3 Data Analysis

The main outcome measure in all experiments was the success rate (SR) defined as the percent of correctly recognized stimuli, namely, groups in G2G, individual sensors in S2P and sliding movements in SLP, where the latter included both movement type (distal, middle, proximal, lateral and medial sliding) and direction (from top to bottom, left to right and vice versa). In the S2P test, the group level SR was also computed and compared to that achieved in G2G. In this case, the recognition was deemed correct if the subject guessed the sensor that was possibly wrong but still belonged to the same

group as the actually activated sensor. This assessment was performed to test if the group level recognition was impacted by the higher spatial resolution of the feedback. The following marginal SRs were computed in the SLP experiment (in addition to the overall SR): 1) the marginal SR for sliding line recognition regardless of the direction, and 2) the marginal SR for the sliding direction regardless of the line type. The SRs were computed per subject for each touch modality (i.e. contacted sensors, group of sensors, or sequence of sensors) and they were then averaged to obtain the overall mean and standard deviation. The results were reported as mean \pm standard deviation in the text and figures. The performance was also presented in the form of confusion matrices to identify prevalent mistakes.

The Friedman test was applied to assess statistically significant differences at the level of the group followed by Tukey's honestly significant difference test for post hoc pairwise comparison. The threshold for the statistical significance was adopted at $p < 0.05$, and the statistical analysis was conducted in OriginPro 2018 (OriginLab, US).

6.4 Results

The average SRs from all the experiments are summarized in Table 6.2 and the confusion matrices are provided in Figure 6.8. The subjects were able to correctly recognize the touched group of pads (test G2G) with a high success rate (SR of $91.25 \pm 3.97\%$). The

Table 6.2 Summary Results (Mean \pm Stand Dev) of Experiments

Test		SR \pm standard deviation [%]
G2G		91.25 ± 3.97
S2P	Pads	57 ± 10.1
	group	80.11 ± 9.03
SLP	Line	94 ± 3.57
	Direction	97.95 ± 3

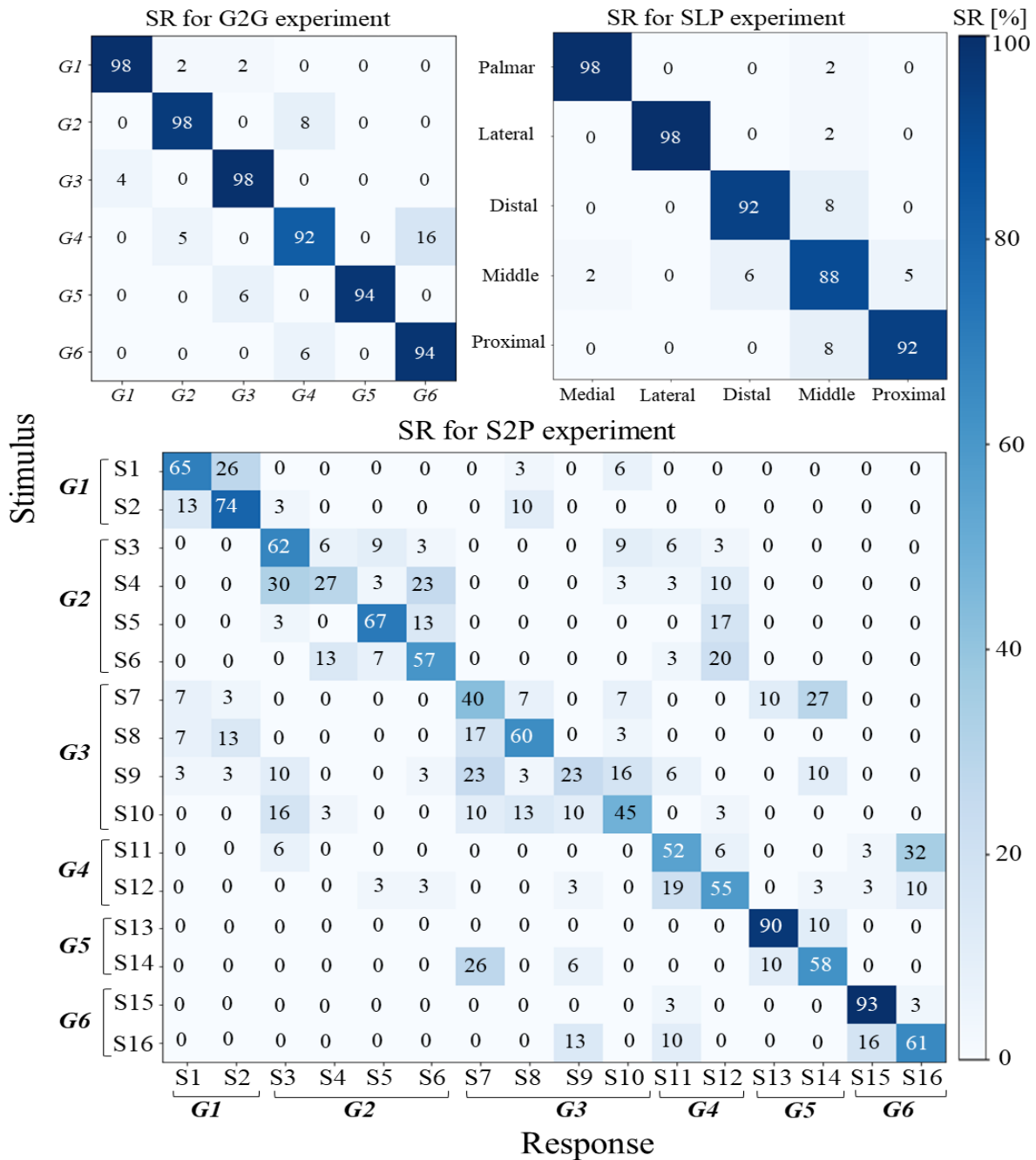


Figure 6.8 Confusion matrices for the G2G (Top left) and S2P (Bottom) and SLP experiments (Top right). The results demonstrate a good recognition of 6 classes in G2G experiment, 16 classes in S2P experiment, and 5 classes in SLP experiment (well-focused diagonal line). The confusion matrix of S2P experiment demonstrates the superior performance in recognizing pads on the borders.

confusion matrix demonstrates a dominant diagonal line standing for a correct group recognition. From the pattern of misrecognitions in the matrix, it seems that it was

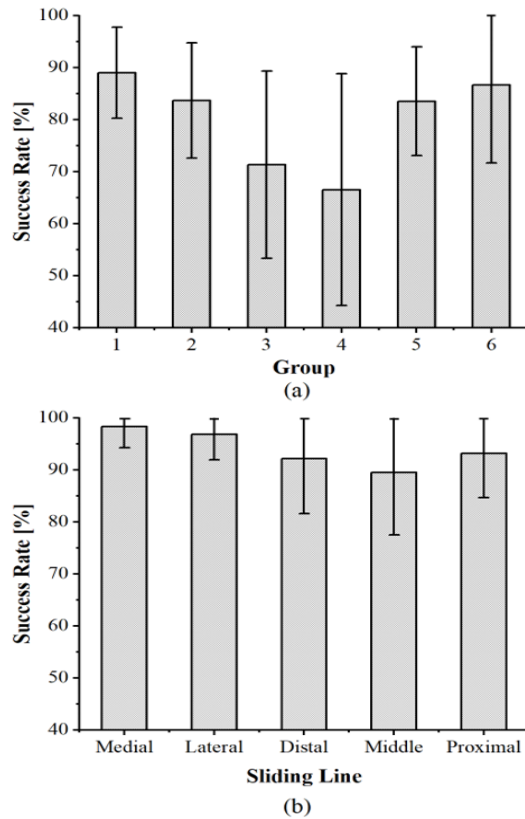


Figure 6.9 The overall success rate of recognizing tactile patterns: (a) sensor group in experiment S2P, (b) sliding movements in experiment SLP.

easier for the subjects to discriminate between the groups along the transversal axis compared to those along the longitudinal axis. When the subjects made an error, they pointed to a directly neighboring group placed distally or proximally with respect to the correct group (G2 to G4, G4 to G6 etc.), see the second parallel diagonals above and below the main diagonal. Contrary to recognizing the groups, the recognition of the individual pads was not an easy task for the subjects. The overall SR from experiment S2P was $57.9 \pm 10.1\%$. Nevertheless, this SR is still approximately 9 times higher than the chance level (i.e., 1 out of 16 or 6%). The confusion matrix characterizing the transmission of touch on a single sensor (i.e. S2P experiment) exhibited high diagonal values for sensors mapped to pads on the border of the electrode (e.g., pads 13, 15) compared to lower diagonal values for the middle pads (e.g., pads 9, 10). Importantly,

the mistakes were typically confined to adjacent pads, and within the same groups of pads. Indeed, when the group level SR was computed from the single pad results, the performance was high ($\sim 80\%$, Table 6.2) although still significantly lower than in a dedicated G2G test ($\sim 91\%$, Table 6.2) and the difference was statistically significant ($p < 0.05$). The mean SR for each group in the S2P experiment is presented in Figure 6.9.b. There is tendency for a drop in performance for groups 3 and 4, which are located on the middle phalange; however, the difference was not statistically significant.

The confusion matrix reported in Figure 6.8 (Top right) describes the overall SR obtained in experiment SLP. The features of the dynamic patterns (SLP experiment) were recognized with a high success rate. The SR for recognizing the sliding movement (distal, middle, proximal, medial, and lateral) was $94 \pm 3.57\%$. The subjects made most errors when discriminating the transversal lines (Distal, Middle, and Proximal), in particular middle, while Lateral and Medial lines were recognized almost perfectly. The sliding direction was easy to discriminate ($97.95 \pm 3\%$). Figure 6.9.b shows mean SR for each sliding movement in SLP. The bars reflect the trends from the confusion matrix (e.g., lower mean SR for the middle line) but the difference was not statistically significant.

The sensory feedback system operates with a nominal delay between contact time and activation of stimulation of around 32 ms. This delay was not perceived by any of the 6 subjects. The results of the Delay-Exp established that the average detectable delay was 258 ± 49 ms.

6.5 Discussion and Conclusion

A novel tactile feedback system was developed to transmit mechanical information from a multipoint tactile sensor (e-skin) to the human subject using multichannel electrotactile stimulation delivered through the matrix electrodes placed on the subject's

forearm. The system was evaluated by using it to detect mechanical interaction with the e-skin, capture contact events and translate them into spatial profiles of stimulation, which conveyed online tactile feedback to the subjects. We have tested the ability of the subjects to perceive such feedback and estimate the properties characterizing dynamic (sliding line) and static (touch position) patterns of interaction with the e-skin. To the best of our knowledge, this is the first development integrating an advanced tactile sensor with distributed sensing elements and an electrotactile stimulation unit with a flexible matrix of electrodes into an embedded system for online transmission of tactile data from artificial to the human skin (forearm). As shown in the experiments, such a system allows providing spatially distributed tactile feedback that thereby mimics the natural feedback provided by the limbs (distributed touch).

The power consumption of the interface electronics is 300 mW. When supplied with a single 2 Ah Lithium polymer battery with a voltage of 3.7 V, the battery life-time expectancy is 22 h of working time, and this includes continuous sampling and processing of tactile signals and sending of commands to the stimulator when contact events are detected. Similarly, the rechargeable battery of the stimulator has a lifetime of 4 h when stimulating constantly. However, considering that the stimulation will be delivered only occasionally, when there is an interaction between the hand and an object, the expected lifetime is substantially longer. The system is therefore economical in terms of power consumption and can provide a long-term usage (> 8 h, the duration of a working day). Importantly, the developed feedback system is modular and other Bluetooth-enabled stimulators could replace the device used in the present study. This would require a change in the firmware of the interface electronics to implement the appropriate communication protocol and possibly remapping/grouping of the pads in case of different number of stimulation channels. In particular, a recently presented system [215] would be an interesting option as it allows simultaneous stimulation and EMG recording, hence a single compact unit that provides both feedback and prosthesis

control, respectively. The current interface electronics includes 32 channels, of which 16 have been used in the present experiment. Therefore, 16 additional channels can be exploited to add more sensing arrays placed on other fingers.

The conducted tests have demonstrated that the system indeed provided timely feedback that could be successfully perceived and interpreted by the subjects. The implemented feedback pipeline relies on simple processing, namely, filtering and thresholding, to detect contact and release events, and control the stimulation of the associated pads of the matrix electrode. In all the tests, the feedback was generated by an experimenter interacting with the skin. Such setup activated all components of the feedback pipeline (Figure 6.1): sensing, tactile signal processing, wireless transmission, and stimulation. Therefore, the experiments demonstrated that the e-skin was successfully integrated on the mockup and that the pipeline operated properly. In addition, the results were obtained with interaction patterns that included natural variability due to slight variations in the way experimenter touched the skin (e.g., inconsistent timing, different pad activations). The subjects recognized the activation of the six groups of sensors easily and reliably. Importantly, even such low-resolution feedback is functionally relevant since it demonstrates that the subjects can perceive the contact with all relevant finger areas, i.e., volar and lateral aspect of each phalange of the index finger. Such sensorization can facilitate both palmar (pinch) and lateral grasping. In addition, the system detected mechanical interaction, computed and transmitted the online feedback fast enough to allow the subjects to perceive contact information that was dynamically moving across the finger. Consequently, they recognized both location and direction of the dynamic movements with no difficulties. Recognizing the dynamic stimuli might assist in slip detection and prevention [216], as well as in promoting the feeling of embodiment (e.g., the perception of passive touch [208]). The success rate when recognizing individual pads was significantly lower despite the distance between the pads was higher than the spatial discrimination

threshold. Nevertheless, this is not surprising considering that the subjects needed to discriminate between 16 randomly stimulated locations spread across a relatively small area of the forearm, while receiving only a brief training. Nevertheless, the mistakes were still confined to the neighboring pads and within the same pad group (finger aspect). The present experiment demonstrated the feasibility of such high-resolution feedback, and it is to be expected that the success rates in this case will increase with prolonged training [192].

The ability of human subjects to identify the position of electrotactile stimuli delivered through the matrix electrode has been investigated in earlier studies [217, 218]. It was found that subjects had more difficulties to discriminate between the groups along transversal compared to the longitudinal axis (Figure 6.8 (Top left)), which is in accordance with the results of the present experiment. For the high-resolution feedback, the success rate was variable across pads. The subjects could still recognize some specific sensors quite reliably (Figure 6.8 (Bottom)), for instance those located on the border of the electrode, and especially in the corners of the electrode matrix.

The test employed in the dynamic experiment (SLP) are similar to those used to assess the ability of the human subjects to identify the line and direction of motion over the skin to obtain insights into normal human sensory processing [219]. In the present study, while applying a sliding stimulus to the e-skin, the experimenter would occasionally activate sensors and electrodes that did not belong to the target line. This is a likely reason for the worse performance in recognizing the transversal lines with respect to the longitudinal lines since the latter contain higher number of sensors that are also more closely spaced. Hence, the perception of feedback was in this case less affected by an occasional deviation. Moving tactile stimuli can be a particularly effective method for information transmission to the user, because mechanoreceptors respond stronger to this type of stimuli compared to simple static patterns [220]. For example, such perception can be the basis for the haptic exploration of the environment

[59], as when the subject tries to assess the texture of an object by relying on artificial tactile stimulation [221]. In this case, the tactile feedback would arise as an interaction between the movements of the user and the objects with which the user interacts.

The response time in communicating sensations has not been widely reported when examining the performance of a sensory feedback system. A healthy nervous system can take approximately 14-25 ms to deliver tactile information to the brain [222]. Some sensory feedback systems were developed with a latency compared to the one of the healthy nervous system. Two sensory feedback systems that are based on FSR sensors and electrotactile [200] or vibrotactile [223] stimulation are capable of delivering tactile information within 15 ms. Authors in [224] used tension sensors integrated on the finger of a robotic hand to measure the applied force. The system can deliver tactile information with a delay of 0.03-0.4 sec. The majority of the aforementioned systems operate with a delay comparable to that of the natural feedback, but they considered simple position and force sensors combined with discrete stimulation channels. The system presented in this study delivers tactile information coming from a distributed sensing array, which is then wirelessly transmitted to a distributed stimulation array within a delay of 32 ms. The delay experiment (Delay-Exp) estimated that an extra delay of 250 ms could be added on top of the existing system latency before the subjects noticed the discrepancy between visual and tactile feedback. Therefore, the developed system has a sufficient latency margin to implement more advanced data processing and encoding. The noticeable delay obtained in the present study is larger than what is reported in the recent work [225], however, that study used invasive stimulation and the subjects self-administrated the touch (instead of the experimenter).

In this first study with the developed embedded system, the processing was simple and the information transmitted by the feedback was limited to contact events. As demonstrated in the present experiment, this information can nevertheless lead to diverse patterns of tactile sensations that can be functionally relevant. The next step in

this research is to extract further information from the tactile data, e.g., the contact pressure. The sensing array is based on piezoelectric sensors that register only the transient events, but the steady state information could still be extracted by a suitable processing, for instance, from the amplitude of the contact peak. The magnitude of the estimated pressure could be then transmitted to the subject by modulating the intensity of stimulation (in addition to the active pad, as in the present study). In addition, the present assessment considered only a single active pad at a time (static or dynamic), while it would be interesting to investigate if the subjects would be able to detect multiple points of contact. The latter tactile pattern arises during normal human grasping where multiple areas of the finger form contact with an object.

The present study has described the system and demonstrated the feasibility by testing it in able-bodied subjects, while the next step is to assess the utility of the proposed system in a functionally relevant application. To this aim, the sensing arrays will be used to cover a myoelectric prosthetic hand in order to test the closed-loop system during functional tasks. In this scenario, the feedback will be delivered to the residual limb of a prosthesis user, including amputee subjects, in whom the skin sensitivity might depend on the condition of the residual limb (e.g., scar tissue). Nevertheless, this can be addressed by a custom design of the stimulation matrix that can be printed in arbitrary shapes, sizes and pad configurations. Importantly, the developed feedback system is compact and hence suitable for integration in a prosthetic socket. In addition, in the present study, the sensors were produced to fit the layout of the Michelangelo hand but the technology is flexible enough to cover an arbitrary prosthesis. Endowing a prosthetic hand with such sensing and stimulation interface would enable high-bandwidth connection between the user and his/her bionic limb, especially if the system would include a full set of sensing arrays that covers both fingers and palm of the prosthetic hand (as proposed in [32]). The provided high-density

feedback could increase the utility of the device as well as facilitate the feeling of embodiment.

Chapter 7

Full-hand electrotactile feedback using electronic skin and matrix electrodes for high-bandwidth human-machine interfacing

7.1 Introduction

Human-machine interface that connects a human operator and an artificial system (e.g., robot, or virtual avatar) is the key element for achieving seamless interaction. Ideally, such an interface should transmit commands from the human brain to the artificial system as well as sensor information from the system back to the operator to provide feedback and close the control loop. For instance, haptic feedback can enrich interaction fidelity and facilitate the feeling of immersion when interacting with a virtual world or controlling a remote robotic system [19, 133].

In teleoperation, haptic interfaces in the form of desktop devices, hand exoskeletons, data gloves and tactile displays have been proposed [134]. Interaction forces

detected by the robot can be transmitted to the operator (kinaesthetic feedback) using exoskeletons that can be mounted on the hand [226–231], or over the full arm [232], and some solutions are already commercially available (e.g., CyberGrasp from CyberGlove Systems, CA). Although such kinaesthetic systems provide most realistic feedback, they are also cumbersome, complex and expensive. An alternative approach, which can substantially simplify the design of the interface is to transmit feedback information using tactile stimulation delivered through miniature vibration motors [233, 234] or tactors [20, 234, 235]. These techniques have been extensively described and compared in several recent reviews [20]. For example, in [121], a vibrotactile display system stimulating the fingertip through a 4×4 array of tactors was developed and integrated on an Omega7 force feedback device for the teleoperation of an LWR KUKA manipulator. Authors in [236] equipped a soft robotic hand with 6-axis force sensor and used two wearable vibrotactile armbands to convey information about collisions. Electrotactile stimulation, which relies on delivering low-intensity current pulses to activate skin afferents and elicit tactile sensations, was also used to provide feedback in teleoperation [237–245]. For instance, in [246] a feel-through interface “Tacttoo” consisting of an array of 8 equispaced circular electrodes was developed to stimulate the finger. A data glove enhanced with six stimulation electrodes placed on the dorsal side of the hand was used to deliver contact information from a mobile robot [244] and force from the end effector of a robotic arm [237]. Apart from teleoperation, tactile stimulation has been used to provide feedback to the user of a prosthetic hand [21, 27, 135, 136, 176, 177], to improve utility [178] and promote feeling of embodiment [7], as well as, in virtual reality to establish an immersed experience by enabling users to sense virtual objects. Recently, in [247] the authors examined the impact of electrotactile stimulators and several types of vibrotactile actuators on mimicking touch interactions in virtual and augmented reality. Despite important developments, the conventional tactile feedback interfaces are characterized with a limited communica-

tion bandwidth. They rely on a few stimulation points, which limits the amount of information that can be transmitted to the user. Indeed, this is very different from the natural feedback provided by, e.g., human hand, which is covered with a dense network of tactile mechanoreceptors measuring spatially distributed contact information with high resolution.

To provide high resolution tactile information mimicking the human sense of touch, this information first needs to be measured by artificial systems integrating high-density network of sensing units. To this aim, electronic skin (e-skin) has been developed [46, 248–252, 184, 186] and successfully applied in robotics [36, 32, 253, 61, 188], prosthetics [30, 39, 53, 189–191, 254], and health-monitoring technologies [131, 255]. However, a critical question still remains: how to convey the rich tactile information recorded by an e-skin as the feedback to the user. This challenge can be tackled by using electrotactile stimulation, as this technology leads to compact design and allows printing electrodes in different shapes, sizes and configurations of the conductive pads (stimulation points) for the stimulation of different parts of the user body [192]. For instance, in tactile feedback for a prosthesis, the electrode is shaped to cover the residual limb [192], while for the applications in teleoperation and virtual reality the electrode needs to be placed on the user's hand [256].

Endowing an end effector with a distributed sensing system combined with distributed feedback system would enable high-bandwidth bilateral communication between the user and the machine/computer. Our recent research efforts are directed towards developing such a high-bandwidth feedback system [210, 211]. The system described in [211] comprised a sensing array (with 16 sensors) integrated on the index finger of the mockup of the Michelangelo prosthetic hand, a 32 channel embedded electronics for signal acquisition and conditioning, a multichannel electrotactile stimulator, and matrix electrode (with 24 pad) placed on the subject's forearm. This chapter describes further development of this initial solution into a feedback interface that con-

veys comprehensive full-hand tactile information (all fingers and palm) from a robotic system to the human subject. In particular, the system captures contact information (binary detections) using 57 sensors integrated on the fingers and palm of the mockup of a robotic hand and delivers the tactile information to the user using a multichannel stimulator (32 channels) and 64 stimulation pads distributed over the fingers and palm of the subject's hand. Furthermore, the current study investigated the best placement of the anodes, which can be distributed within the electrode or placed outside of the hand as a dedicated common pad. The chapter also reports on the validation of the sensing system as well as on the psychometric assessment of the whole-hand feedback. The tests were conducted to assess the ability of the developed system to capture distributed tactile information on localized (*static*) and sliding (*dynamic*) contacts and to deliver such information as the feedback to the subject.

The chapter is organized as follows: Section 7.2 illustrates materials and methods. Section 7.3 presents the validation of the sensing system. Section 7.4 describes the experimental protocol for psychometric assessment of the developed feedback system. The results of the psychometric assessment are reported in Section 7.5. Finally, our discussion and conclusive remarks are given in Section 7.6.

7.2 Materials and Methods

7.2.1 System Description

The proposed system (Figure 7.1) includes: 1) piezoelectric sensing arrays (electronic skin), 2) embedded electronics for signal acquisition and conditioning, 3) electrotactile stimulator, 4) flexible surface electrodes, and 5) host laptop PC (1.9 GHz, 16 GB). The e-skin converts mechanical contact into a set of electrical signals (one signal per sensor). Sensor signals are sampled by the embedded electronics, processed, and sent to the host PC. The signals are then filtered and when sensor output exceeds a

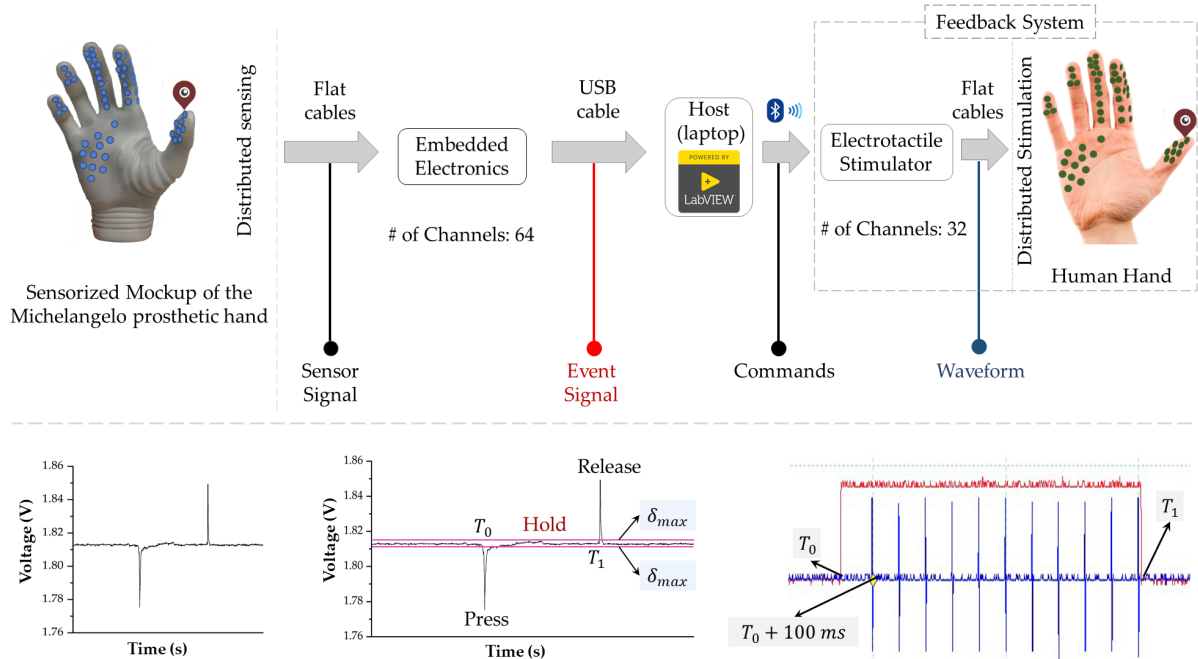


Figure 7.1 Top: System structure. The system comprises an e-skin including 57 sensors, embedded electronics for signal acquisition, processing and communication, and a multichannel electrotactile stimulator with flexible matrix electrodes (32 electrode pads). Bottom: The online operation of the feedback system. The black signal (left) corresponds to a sensor output due to a specific type of contact (“long press”). The embedded electronics uses two thresholds to detect press and release, and based on that generate the event signal (red signal) and send it to the host PC. The PC sends commands to the stimulator and the train of stimulation pulses (blue signal) is delivered through the corresponding electrode pad as tactile feedback to the subject’s hand.

given threshold contact events are detected, and the activated sensors are highlighted on the graphical user interface on the PC (visual feedback). This information is used to set the state (on/off) of the corresponding stimulation channels (mapping between sensors and stimulation pads is presented in Section 7.2.2). The PC generates appropriate stimulation commands and sends them to the stimulator via Bluetooth. The electrotactile stimulation is delivered to the subject through matrix electrodes placed on the volar side of the hand. As the feedback pipeline runs in real-time, the tactile interaction recorded by the electronic skin is translated online into dynamic tactile sensations elicited across the subject’s hand. Figure 7.1 (Bottom) illustrates the online

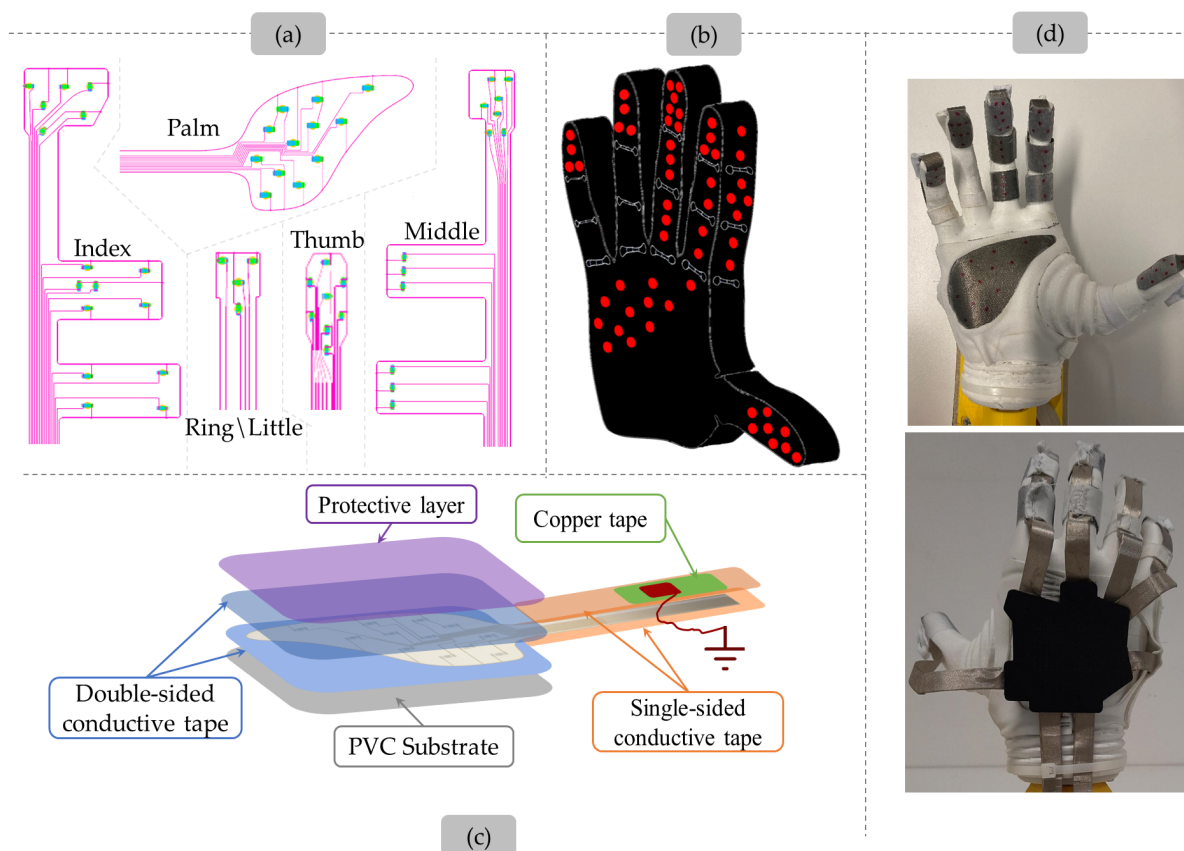


Figure 7.2 (a) Layout of the sensing arrays for the fingers and palm of the Michelangelo robotic hand. (b) Sensor distribution over the hand. (c) Skin patch. (d) Sensing system integrated on the mockup of the Michelangelo hand (front and back views).

pipeline of the system, which was implemented following the approach presented in chapter 6.

7.2.1.1 Sensorized mockup of the Michelangelo hand

- **Tactile sensor arrays:**

The complete set of sensing arrays with different geometries and sensor distributions was deployed to sensorize the fingers and palm of a Michelangelo prosthetic hand [14]. Figure 7.2.a shows the geometry, sensor distribution, and size of the sensing arrays while Figure 7.2.b highlights sensor distribution over the fingers and palm of a mockup of the Michelangelo hand. The finger sensing arrays were

designed to easily fit on the phalanges. Due to its prominent role in grasping and manipulation, the index finger was covered most extensively with the sensors. Specifically, sensors were distributed on the volar and lateral sides of the fingertip (4 and 2 sensors, respectively), and the middle (2 and 4 sensors), and proximal (2 and 2 sensors) phalanges. The sensors on the lateral aspect were added to allow for contact detection when lateral grasp is used, in which an object is grasped between the volar aspect of the thumb and the lateral side of the index. Similarly, the middle finger was provided with 13 sensors covering the fingertip (7 sensors), and the middle (3 sensors), and proximal (3 sensors) phalanges. The fingertips of the thumb, ring, and little fingers were equipped with 8, 4, and 4 sensors, respectively. Finally, 12 sensors were distributed over the palm.

- **Sensor Integration:**

Sensing arrays reported in Figure 7.2.a were integrated on the mockup following the same approach described in chapter 6 and 5. All six sensing arrays were integrated on the mockup following the procedure. Figure 7.2.c shows the structure of the skin patch for the palm whereas Figure 7.2.d shows the complete sensing system integrated on the mockup. Four shielded FPC cables were used to connect the PCB to the embedded electronics.

7.2.1.2 Embedded Electronics

Figure 7.3.a shows the Printed Circuit Board (PCB) whereas Figure 7.3.b shows the block diagram of the embedded electronics. The embedded electronics shown in Figure 7.3.a is an extended version of the systems presented in chapter 4. Compared to the previous design that can accommodate up to 32 sensors, the current design can handle up to 64 sensors through two daisy-chained DDC232 [257] mounted on the top and bottom side of the PCB. The two DDC232 were daisy chained in order to avoid data

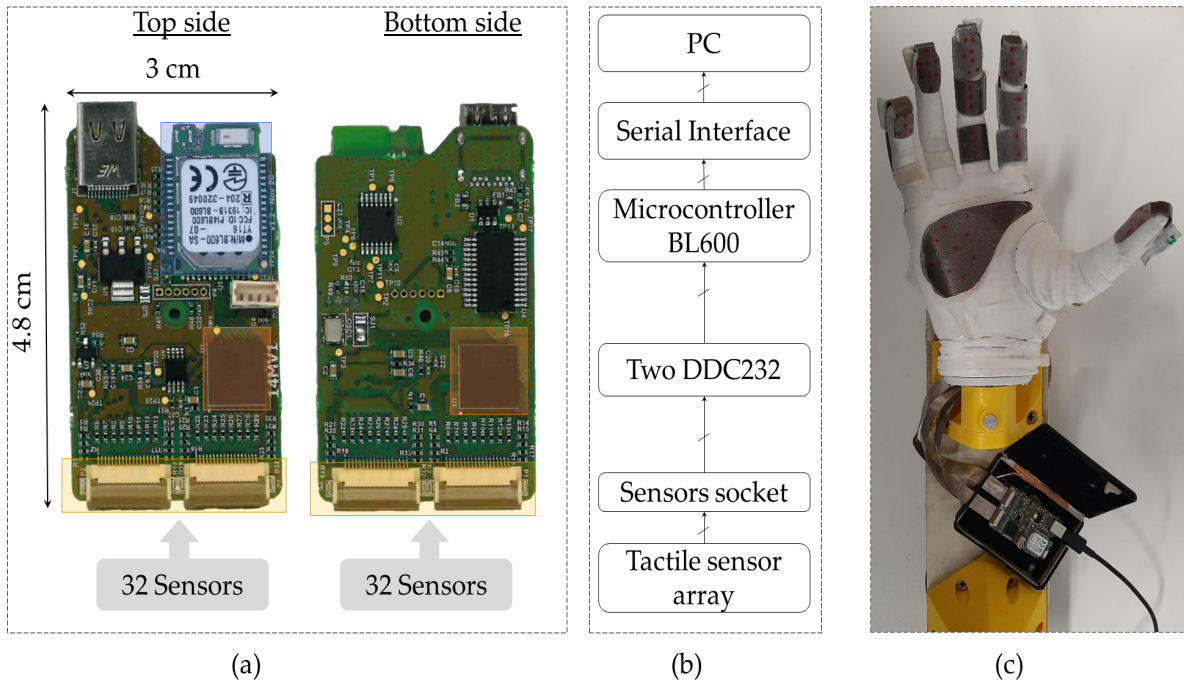


Figure 7.3 (a) Top and Bottom view of the printed circuit board of the embedded electronics. (b) Block diagram. (c) Sensing system integrated on the mockup of the Michelangelo hand. Individual sensors are marked as red dots.

loss during the acquisition process. Four sockets (2 on the top side and 2 on the bottom side) acquire signals from 64 sensors where each block accommodates 16 sensors. BL600 module is used to read, process, and transmit sensor data.

In the present study, the embedded electronics was configured to collect and process tactile data from 57 sensors at 2 ksamples/s. The 2 kHz sampling rate was used to capture the full bandwidth of the sensor (see Section 7.2.1.1), which is beneficial for detecting the onset of contact events characterized by a steep increase/decrease in the signal. An Exponential Moving Average (EMA) digital filter was implemented in the firmware of the embedded electronics to filter signals from the sensors. To enable the system to detect contact events, the Detection Thresholds (DT) of the 57 sensors were first determined. To this aim, the interface electronics recorded signals from the skin for approx. 3-s with no contact. The DTs were set to the lowest (δ_{min}) and the highest amplitude (δ_{max}) of the filtered signals measured during the 3-s calibration

period. Exceeding those thresholds was used as an indication that contact and release occurred, respectively. As an example, Figure 7.1 (bottom) shows the filtered voltage signal of a single sensor generated in response to a press-hold-release contact as well as the corresponding event signal that controls the start and stop of the stimulation delivered to the subject's hand. The embedded electronics was placed inside a shielded box as shown in Figure 7.3.c.

7.2.1.3 Feedback System

- **Electrotactile Stimulator**

The feedback interface employs a 32-channel programmable battery-powered stimulator ('Tactility', Tecnia Research and Innovation, Spain [258]). The stimulator generates biphasic symmetric current- pulses that are distributed in time and space over 32 channels. The stimulator is fully programmable, and the stimulation parameters can be adjusted online by sending text commands from the host PC via a Bluetooth connection. The amplitude of the current pulses can be modulated in the range of 0-10 mA with increments of 0.1 mA, the pulse width, from 50 to 5000 μ s in steps of 10 μ s; the frequency resolution is 1 Hz with the maximum rate of 400 Hz. Each stimulation channel could be set to act as anode or cathode.

In the present study, the PC sends stimulation commands to the stimulator to activate/deactivate the stimulation through the respective electrode pads. Specifically, the stimulation is activated by a press and deactivated by a release event (see Figure 7.1). The output channels of the stimulator were connected to a small PCB that routes 32 stimulation channels to 64 pads of the electrode, as described in the next section.

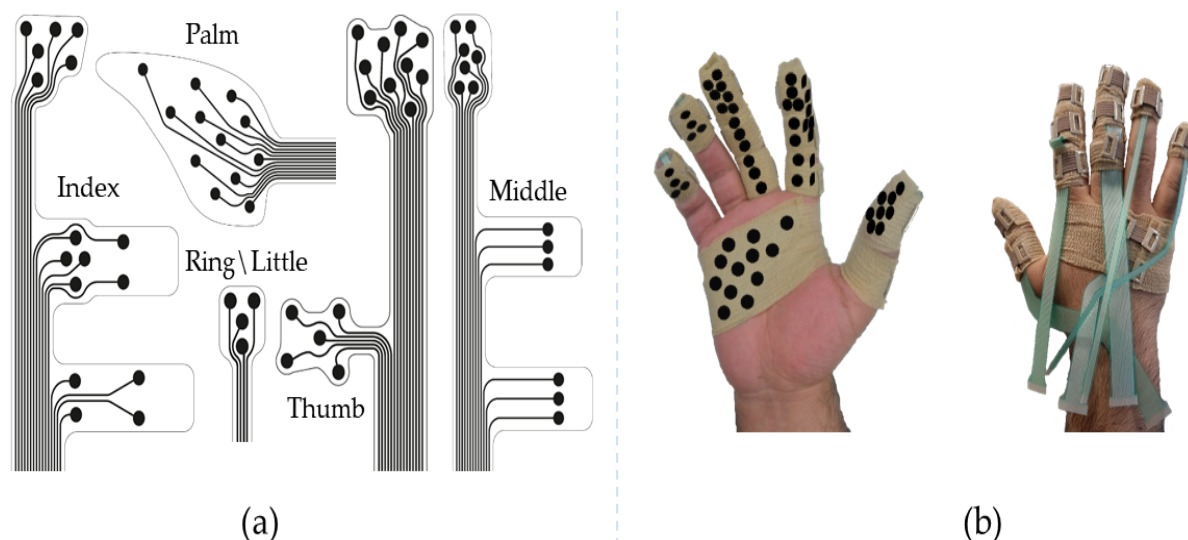


Figure 7.4 Flexible electrodes for the electrotactile stimulation of the hand. (a) Layout of the pad arrays to cover the fingers and palm. (b) Volar and dorsal view of a human hand covered with the electrode arrays. Stimulation pads are indicated as black dots (volar) and rectangles (later index).

• Electrodes

In the present study, the stimulator was connected to six flexible matrix electrodes developed by Tecnia Research and Innovation. The electrodes are made of a polyester layer, an Ag/AgCl conductive layer, and an insulation coating covering the conductive leads. Pad distributions on the six electrodes are shown in Figure 7.4.a. The electrodes were designed to be placed on the human hand and the pad distribution mirrors the design of the sensing arrays (see Section 7.2.1.1). Sixty four circular pads were distributed over 6 electrodes in total (5 electrodes for the fingers and one electrode for the palm, Figure 7.4.b).

7.2.2 Mapping Sensors to Pads

The electrotactile stimulator used in the current study has 32 stimulation channels while the electrode arrays integrate 64 pads. Therefore, some electrode pads were grouped together and driven by a same stimulation channel. In addition, a reference electrode (anode) needed to be defined to close the stimulation circuit. To this aim,

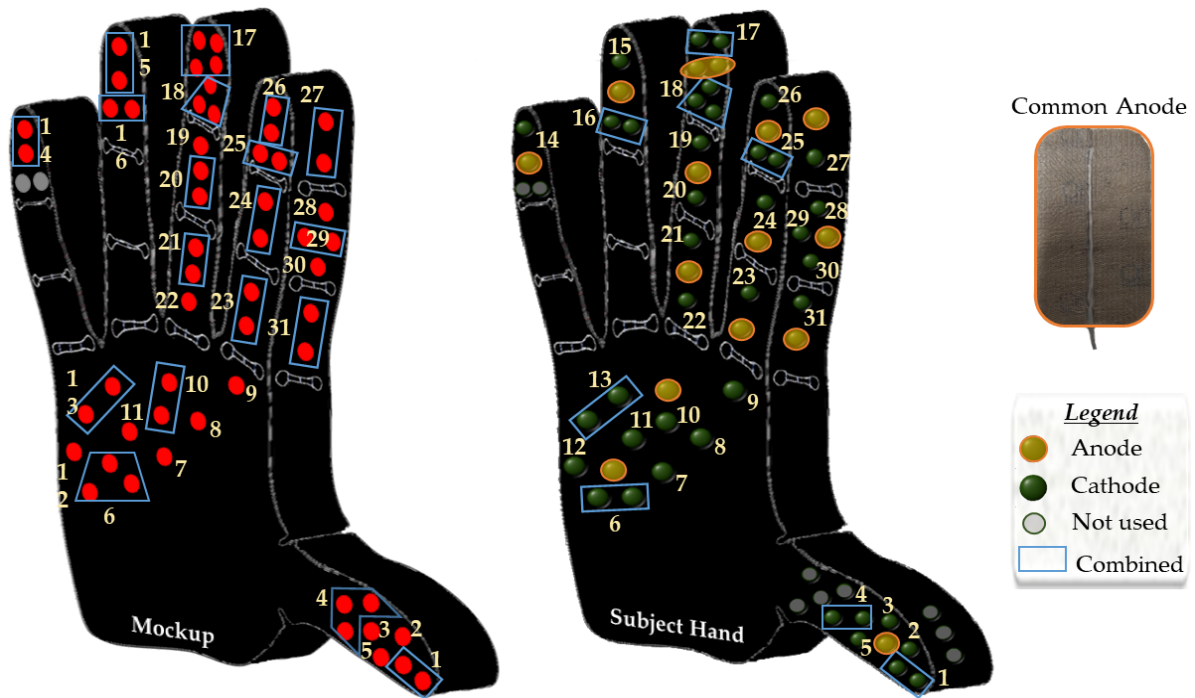


Figure 7.5 E-skin (left) and Electrode Arrays (right): Cathode and anode distributions within the electrode arrays (subject hand). The numbers on the e-skin and electrode array indicate the mapping of sensor sets to corresponding groups of pads connected to a single stimulation channel. Two anode configurations were considered: a) a distributed anode comprised of a subset of pads (DAC), and b) a single dedicated electrode placed on the dorsal side of the hand (SAC).

a small PCB was developed to route the pads to the channels and to implement two anode configurations (Figure 7.5). The first configuration features an anode that was embedded within the electrode: in this case, 15 pads distributed over the volar side of the phalanges and the palm (distributed anode configuration, DAC) were connected to one of the stimulation channels configured as the anode, while the rest of the pads were connected to the remaining 31 channels configured as cathodes. This configuration was selected in order to localize the current flow, from a cathode to its closest anode segment, eliciting thereby a localized tactile sensation. A second configuration consists of a single large anode electrode placed on the dorsal side of the hand (single anode configuration, SAC). It is important to note that the number of cathodes was identical in both configurations, as the distributed anodes were deactivated (unused) in the

Table 7.1 System features

Component	Feature	Specifications
Sensorized mockup	Number of Sensors	57 (distributed on the fingers and palm of the mockup)
	Sensor frequency band-width	1-1kHz
	Size	4.8 cm × 3 cm
	Number of channels	64
	Sampling Rate	Up to 6 ksamples/second
Embedded Electronics	Connectivity	USB-C port communication interface and Bluetooth
	Power consumption	200 mW
	Overall Latency	100 ms
Feedback System	Connectivity	USB and Bluetooth
	Number of stimulation pads	64 (distributed on the fingers and palm of the hand of the participant)

SAC configuration. In the present study, we compared the effectiveness of the two configurations (see Section 7.4.1.1).

To map 57 tactile sensor outputs to the 31 channels of the stimulator, some neighboring sensors were grouped together and connected to a same stimulation channel. The mapping between sensor sets and groups of electrode pads is shown in Figure 7.5 (left). The stimulation channel connected to a group of pads was activated if any of the sensors belonging to the corresponding sensor set detected a contact event.

7.3 Sensing System Validation

To assess that the sensors properly responded, validation experiments were conducted. In the first test, the experimenter holding a pen performed indentation tests by applying press-hold-release patterns on all 57 sensors, one at a time. In the second test, the experimenter used two pens to apply the press-hold-release pattern on two sensors simultaneously. Finally, the experimenter performed shear tests by applying a sliding pattern along the e-skin following specific sliding directions. In order to visualize the response of the sensing system, the embedded electronics was configured to acquire, filter, and send signals generated by the sensors to a host PC through USB. A LabVIEW software was developed to receive, visualize and save the tactile signals.

Table 7.1 summarizes the specifications of the different components of the system. In particular, the embedded electronics consumes 200 mW while continuously sampling and processing tactile signals and sending commands to the host. When supplied with a single 2 Ah Lithium polymer battery with a voltage of 3.7 V, the battery lifetime expectancy is 24 h.

Representative results from the sensing system validation experiments are shown in Figure 7.6. The figure depicts the electrical response of six sensors to indentation tests (Figures 7.6.a-c) and to shear tests (Figure 7.6.d), as defined above. Figure 7.6a and Figure 7.6b show the six sensors capturing the dynamic features of the mechanical event by generating two phasic bursts in charge-mode output signals. The bursts correspond to the press and release events, while there was almost no response in-between. The contact onset is associated to a decrease whereas contact release generates a signal increase. The signal peaks are arranged in sequence reflecting the fact that the touches were applied to the sensors sequentially. Figure 7.6.c shows that the sensing system can capture multiple touches when they were applied simultaneously. Finally, Figure 7.6.d shows a sliding pattern that started on the palm, crossed the volar side of the index finger and ended on the fingertip of the index finger. The plot indicates that the

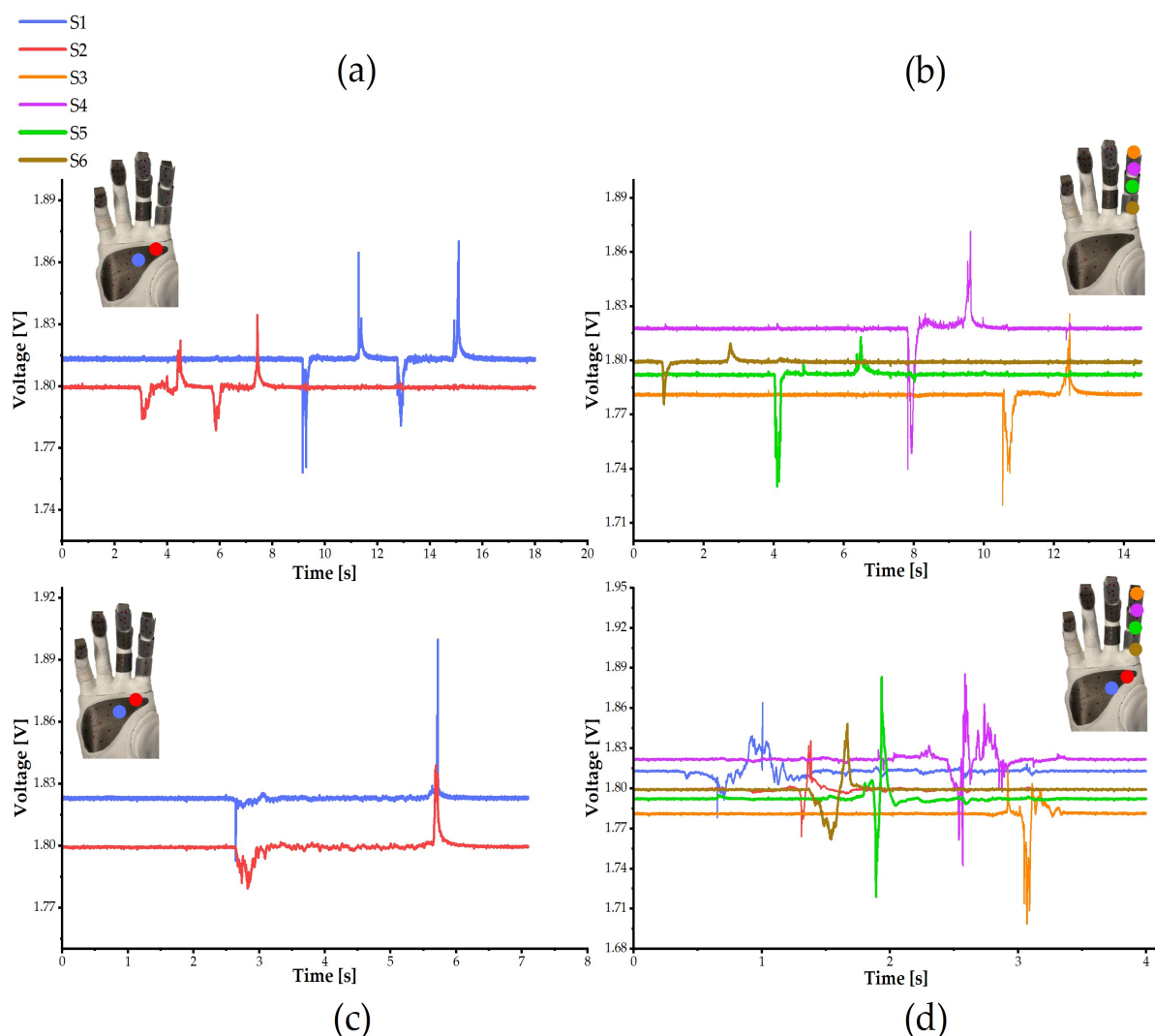


Figure 7.6 Illustrative data showing sensor outputs. Signals from six sensors are shown during touch interactions. The legend attributes colours to each specific sensor output. Indentation tests: (a) long press on two sensors located on the palm; (b) long press on the three phalanges of the index finger starting from the proximal phalanx; (c) long press on two sensors (on the palm) at the same time. Shear tests: (d) sliding movement starting from the palm and moving toward the tip of the index finger.

six sensors respond to shear tests and that the sliding direction could be easily inferred from the sequence of sensor activations. Interestingly, the sensor response pattern is in this case more complex; the press and release peaks are still visible, but they are not as sharp as in Figure 7.6.a and Figure 7.6.b. This reflects a different sensor response to the different type of mechanical interaction (shear forces). The sliding movement

provoked more gradual activation and deactivation of the sensors compared to previous indentation tests.

7.4 Psychometric assessment

7.4.1 Experiments

Two experiments (Table 7.2) were conducted to assess if the system could convey information on contact location (indentation tests) and on the sliding movement along and/or across fingers (shear tests). In both experiments, the stimulation was delivered to the subject according to the mapping described in Section 7.2.2 and shown in Figure 7.5.

7.4.1.1 (Static pattern experiment (SPE))

This experiment evaluated if the feedback system could successfully convey the information about static contacts to the subject. The sensor sets shown in Figure 7.5 were divided into 14 groups and labelled as shown in Figure 7.7 (left). The groups were

Table 7.2 Summary of experiments

Name	Anode configuration	Description	Touch patterns
<i>Static patterns</i>	SAC	Spatial coding with 21 classes (static patterns)	Single touch: G1, G2, ..., G14
	DAC		<u>Two simultaneous touches:</u> G4-G1, G4-G3, G5-G4, G5-G6, G5-G1, G3-G1, G5-G10
<i>Dynamic patterns</i>	DAC	Spatial coding with twelve classes (dynamic patterns)	Single sliding line: IV, IL, M, PF, PTh, FT, PM, PIV <u>Two simultaneous sliding lines:</u> IV-M, PIV-PM, PIV-PTh, PM-PTh



Figure 7.7 Left: Sensor distribution within the electronic skin placed on the fingers and palm of the mockup of the Michelangelo hand. The sensors were grouped into fourteen groups (G1-14, boxes). Right: Two psychometric experiments were conducted: 1- SPE – skin indentation aligned on specific sensors (*Static* pattern) and 2- DPE - shear tests (*Dynamic* pattern), i.e. sliding across M, IV, PTh, IL, PF and FT lines in two directions).

defined to assess if the subject could recognize touch delivered to each of the important functional areas (fingertips and phalanges). Moreover, the test comprised single and double touch (see Table 7.2), where the experimenter pressed the skin to activate a single group or two groups, respectively. In the latter case, the tested combinations of two groups were defined so that they are functionally relevant, i.e., they were expected to be activated when closing the hand using different grasp types (e.g., pinch, lateral grasp). The experiment was conducted twice, one with distributed anode (DAC) and once with single dedicated anode (SAC).

7.4.1.2 (Dynamic pattern experiment (DPE))

The experiment evaluated if the system could successfully deliver information about moving contacts to the subject. The experimenter interacted with the e-skin to activate

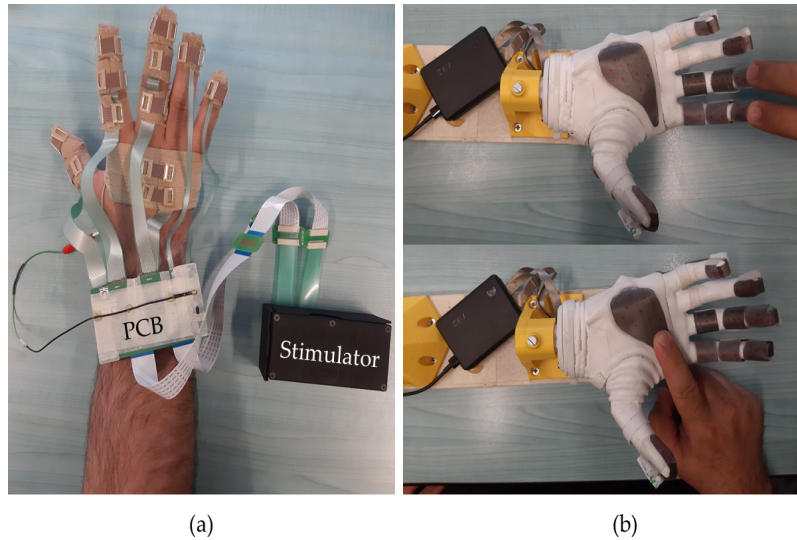


Figure 7.8 Experimental setup. (a) The subject received electrotactile feedback through electrode arrays placed on the right hand and covered with a medical bandage. The electrodes were connected to a small PCB routing 64 pads to 32 stimulation channels. The PCB includes a small jumper that was used to switch between the anode configurations, i.e., SAC and DAC. (b) Example of the experimenter interacting with the sensors: (bottom) the experimenter applies single touch on a set of sensors on the palm and (top) the experimenter touches the index and middle fingers simultaneously.

a sequence of pads. The movement patterns included sliding along the volar and lateral aspects of the index finger, and the volar aspect of all fingers and palm. Moreover, the test comprised applying single and double sliding lines (see Table 7.2 and Figure 7.7 (right)) shows the sliding patterns. In this experiment, the sliding lines were delivered to the subject using the SAC anode configuration only.

7.4.2 Setup and Protocol

Seven healthy subjects (male, age 28 ± 4 years) participated in the two experiments described in Section 7.4.1. Before starting, the subjects signed an informed consent form. Figure 7.8 shows the experimental setup. The subjects were seated comfortably on a chair in front of a monitor used for visualization. The forearm of the right arm was placed on a table surface and, the electrodes were placed on the fingers and palm of the subject's hand and secured with a self-adhesive bandage as shown in Figure

7.4.b. Each phalange was secured separately in order not to block the movements of the subject's fingers. Figure 7.8.a shows the view from the subject perspective. The sensorized mockup of the Michelangelo hand was mounted on a support and placed so that the subject could not see the hand nor the experimenter interacting with the hand (see Figure 7.8.b). Before the experiments, the Sensation Thresholds (ST) were determined for each of the 31 pad groups (Figure 7.5), using the methods of limits by varying the pulse amplitude value [214]. During the rest of the experiment, the pulse amplitude was set to $1.1 \times \text{ST}$, which ensured that the sensations elicited by the feedback were clear and comfortable. The amplitude was additionally fine-tuned by the experimenter until the subject reported that the perceived intensity was similar across the pad groups. The pulse rate and pulse width were common to all the pads and set to 50 Hz and 100 μs , respectively. Each experiment started by introducing the subject to the sensory feedback system and feedback mapping. Both experiments (SPE and DPE) comprised three phases: learning, reinforced learning, and validation. In the learning phase, the patterns described in Table 7.2 were delivered and the subjects were informed beforehand which pattern will be presented.

During reinforced learning, the contact patterns were randomly applied, while the subjects were asked to guess the applied patterns. The experimenter then provided verbal feedback on the correct answer by saying "correct" or "incorrect" and, in the latter case, disclosing the correct pattern. During the final validation phase, the patterns were again presented randomly, the subject verbally indicated the pattern, but no verbal feedback was given. Each stimulus was presented to the subject 3 times during the first two sessions and 5 times during the validation phase.

7.4.3 Data Analysis

The outcome measure was the success rate (SR) defined as the percent of correctly recognized contact patterns, namely, activated groups in SPE and sliding movements

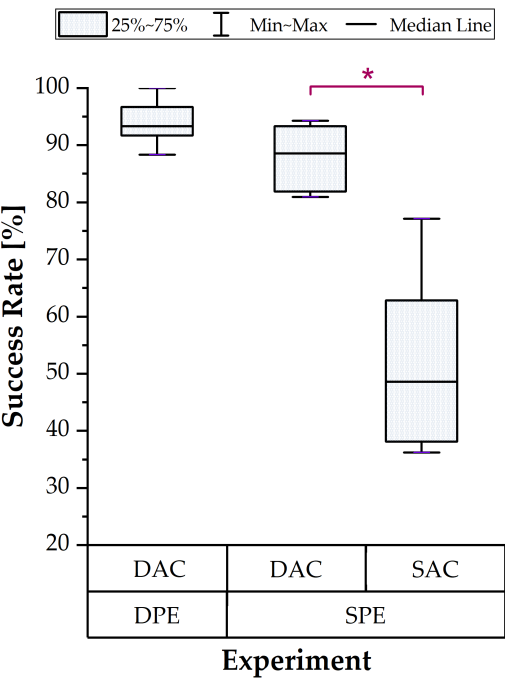


Figure 7.9 The overall success rate (SR) of recognizing sliding lines in experiment DPE for DAC (left) and groups of sensors in SPE experiment for SAC and DAC (right). Asterisks indicates the statistically significant difference in mean SR for the different anode configurations. (*, $p < 0.05$).

in DPE. The SRs were computed per subject for each contact pattern. In SPE, the SR obtained with DAC was compared to that achieved with SAC to test if the recognition was impacted by the anode configuration. The results of the tests are reported as median{interquartile range (IQR)}. The overall performance is also presented in the form of confusion matrices to identify prevalent mistakes.

The paired sample Wilcoxon signed rank test was applied to assess statistically significant differences between SAC and DAC. Non-parametric tests were used due to the small number of subjects. The threshold for the statistical significance was set at $p < 0.05$, and the statistical analysis was conducted in OriginPro 2018 (OriginLab, US).

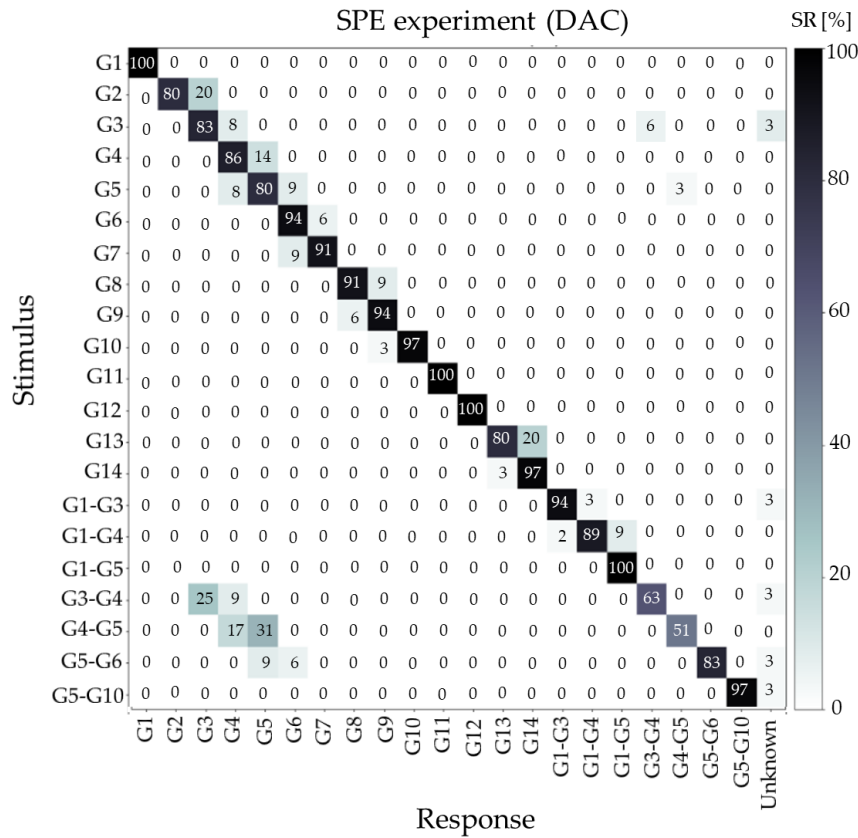


Figure 7.10 Confusion matrix for SPE experiment.

7.5 Results

The box plot of the success rates (median{IQR}) from all the experiments are presented in Figure 7.9. The subjects achieved a high overall success rate (both single and double touches) when recognizing the touched group of sensors (SPE test) using DAC with median{interquartile range} of 88.57{11} %. The SAC resulted in a significant drop ($p < 0.05$) in performance (48.57{25} %).

With DAC, the subjects were more successful ($p < 0.05$) when recognizing single touches (90{7.14} %) compared to recognizing double touches (85{20} %). Importantly, the subjects could easily differentiate if the touch was single versus double (SR of 95.23{3.81} %). The dynamic patterns (DPE experiment) were recognized with a high success rate (93.3{5} %).

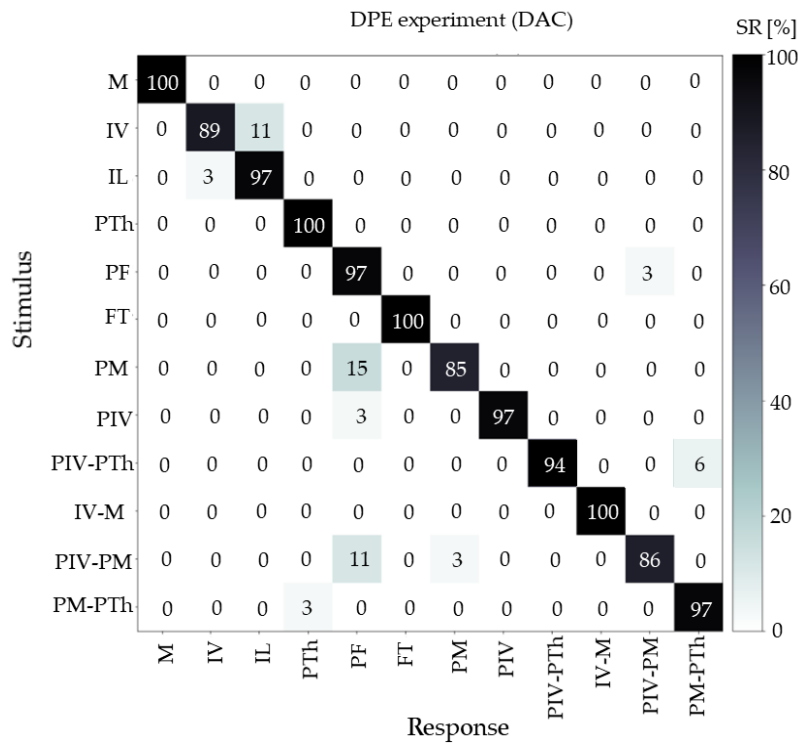


Figure 7.11 Confusion matrix for DPE experiment.

The confusion matrix for SPE test with DAC is shown in Figure 7.10. The ‘unknown’ class was introduced to indicate that in few trials the subjects reported a group combination (multiple touches) that did not exist in the experiment (e.g., G2-G3). The confusion matrix exhibits a dominant diagonal line demonstrating that subjects could reliably recognize the applied single and double touches in most cases, where the latter were slightly more difficult to estimate correctly. When the subjects were wrong for the single touch (G1, .., G14), they mostly pointed to a directly neighbouring group placed distally or proximally with respect to the correct group (G3 to G4, G5 to G6 etc.), see the second parallel diagonals above and below the main diagonal. Excluding the misrecognition registered for G3 (predicted as G2-G3, 1 out of 35 trials, i.e. 3%), most of the “unknown” predictions were registered for double touches where the subjects predicted one group correctly while misrecognizing the second group. The confusion matrix exhibited higher diagonal values for double touches that involve groups from

different fingers (e.g., G1-G5, G5-G10) compared to groups residing on the same finger (e.g., G3-G4, G4-G5). Importantly, the mistakes were typically confined to groups within the same finger (see bottom left of Figure 7.10). Interestingly, in a few cases, double touches were mistakenly interpreted by the subjects as a single touch. For example, applying touch at G3 and G4 simultaneously (G1-G4) was mostly mistaken for G3 only.

The confusion matrix for DPE test with DAC is shown in Figure 7.11. In some trials, the subjects confused “IL” line with “IV” line and “PM-PIV” line with “PF”, and this was likely because the experimenter would occasionally activate sensors that did not belong to the target line due to the natural variability when executing the sliding patterns. The subjects made most errors when discriminating two simultaneous sliding patterns (IV-M, PIV-PM, PIV-PTh, PM-PTh).

7.6 Discussion and Conclusion

In this study, we presented and evaluated a high-density tactile feedback system for human-machine interfacing. The system comprises 57 distributed tactile sensors (e-skin) integrated on the fingers and palm of the robotic hand mockup, multichannel embedded electronics and a distributed electrotactile stimulation interface placed on the volar side of the subject hand. It is worth noting that sensors have been distributed on such areas that are expected to be more relevant functionally, e.g. the fingertips or areas activated when closing the hand using different grasp types (e.g., pinch, lateral grasp, palmar grasp). The contact information captured by the electronic skin was delivered to the subject through a matrix electrode comprising 64 stimulation pads distributed over the fingers and the palm of the subject’s hand. The experiments have been conducted to validate the operation of the sensing component (electronic skin and embedded electronics) as well as to test the ability of the full feedback interface to

acquire and transmit the mechanical interaction (applied on the electronic skin) to the subjects' hand.

The validation of the sensing component demonstrated that the e-skin and the embedded electronics can indeed detect mechanical indentation on the e-skin surface, centred on different sensors and applied sequentially and simultaneously (*static patterns*), as well as contacts sliding across the e-skin (*dynamic patterns*). Such mechanical stimuli are the basic building blocks for more complex tactile interactions that arise during functional activities.

The design and placement of the anode is an important issue for the practical application, especially when the feedback is delivered to a confined area (subject hand), and both approaches (*distributed vs single anode*) tested in the present study were used before in the literature [245, 259]. In general, the anode should be substantially larger in size compared to a cathode, as it should serve only as a return path for the current without eliciting sensations. The “distributed” anode is a compact solution, as the anode is “within” the stimulating electrode, but the drawback is that each anode requires a single pad, strongly reducing the number of available pads to elicit sensations. Nevertheless, the conducted experiments demonstrated that this approach (DAC) resulted in significantly higher performance compared to a single anode placed on the hand dorsum (SAC). More specifically, the SAC negatively impacted on the ability of the subjects to predict static and especially double contacts. They had difficulties to distinguish between neighboring groups, particularly when stimulating the index finger. A strong spreading of sensations was reported by most subjects. Contrarily, when using DAC, the subjects predicted single and double contacts with high success rates, and they reported a well localized sensation. DAC has been therefore selected to complete the experimental campaign.

The psychometric experiments with DAC demonstrated that the subjects could identify contact patterns delivered to the most important functional areas of the hand,

including the lateral and volar side of the index finger, fingertips of all fingers and thumb, and the palm. This included simple patterns, such as contact on a single area, as well as more complex sensations arising from simultaneous touches on two areas, single and double sliding contacts, and comprehensive patterns activating many pads simultaneously. While we have previously demonstrated that such patterns can be perceived from a single finger [211], in the present work we show that the electrotactile stimulus can be delivered to a larger area, following mechanical interactions across the whole hand. An important point is that the current system provided somatotopic feedback, which is expected to facilitate perception and interpretation of the stimulus [260]. In combination with the validation of the sensing system, the psychometric assessment demonstrates that the developed system not only detects a variety of tactile interactions but can also create tactile sensations that allow the subjects to correctly perceive and interpret such interactions, after only a brief familiarization with the system. This is an encouraging outcome implying that the novel system might be able to provide a functionally relevant feedback that can assist the subject while using a robotic hand, e.g., in slip detection and prevention [216] or for estimation of objects properties such as compliance, hardness, texture by using exploratory motions [261–263]. Importantly, the proposed technology is versatile as it is not constrained to a specific robotic hand. While the sensing system was developed to sensorize the Michelangelo hand, the modular approach that we propose can be adapted to fit other prosthetic or robotic hands. Likewise, the electrodes can be easily printed in different geometries so that they can be applied to different parts of the body (e.g., a rectangular and/or circular matrix electrode to be placed on the residual limb of an amputee subject).

The proposed system transmits tactile information to the user with a delay of 100 ms. This delay strongly depends on the communication channel between the sensing and feedback systems. In the present solution, a host PC acts as a “bridge” between

the embedded electronics and the stimulator. Nevertheless, since both the embedded electronics and the stimulator integrate a Bluetooth interface, the system latency can be reduced by establishing a direct connection through Bluetooth.

To summarize and conclude, in the present study we proposed a system that provides spatially distributed feedback to the whole hand using a dense matrix of sensing and stimulation pads and we demonstrated its applicability by conducting experiments in able-bodied subjects. To the best of our knowledge, this is the first feedback system that can convey high-density tactile information to the whole hand using electrotactile stimulation. The provided feedback could improve utility and performance, as well as facilitate the feeling of embodiment and immersion in human-machine interfacing across fields, from teleoperation and prosthetics to virtual reality and gaming. All in all, this is an important step towards implementing a full high-bandwidth human machine interface that will allow a bidirectional connection between the subject and a machine (robotic system) for dexterous control and comprehensive feedback [177]. To this aim, the system described here could be supplemented with an interface that provides high density recording of electrical muscle activity. The latter can be used to decode the subject motion intention and translate those into commands for the robot [264]. Importantly, the recording of EMG could be realized through the same electrode technology as the one used in the present study to implement stimulation [215].

Chapter 8

Touch Modality Classification Using Recursive Neural Networks

8.1 Introduction

Tactile sensing systems attract the research interest in many application domains such as robotics, prosthetic devices, and industrial automation[132, 265]. The main focus is in the areas of sensors and transducers, front end electronics, and smart data processing algorithms. A tactile sensing system is composed of: 1) an array of tactile sensors to sense the applied mechanical stimuli, 2) an interface electronics for signal conditioning and data acquisition, and 3) an embedded digital processing unit for tactile data decoding. The goal is either to mimic the human capabilities in capturing and interpreting tactile data or to respond to the application demands. To be effective, tactile sensors have to sense and extract meaningful information from the contact surface such as force direction and intensity, position, vibrations, objects and texture, or touch modality classification. Such information can be extracted by employing algorithms rooted in machine learning, which have proven their effectiveness in processing tactile data [35].

The adoption of tactile sensing systems in real world application is still limited and challenging [195], [123]. One key aspect is the complexity of the processing algorithms (basically the number of Floating Point Operations - FLOPs) when the hardware implementation is targeted. This affects mainly the energy consumption and time latency.

In this chapter, a novel touch modality classification framework using Recurrent Neural Networks (RNNs) is presented. RNNs are mainly designed to deal with sequence prediction problems. They have been very successful in processing natural language, i.e., working on sequences of texts and spoken language that are represented as time series [266, 267]. Data acquired from tactile sensors have 3-dimension tensor structure (similar to a video) where the first two dimensions are defined by the geometry of the sensor array while time defines the third dimension. Hence, given this representation of tactile data, in this study we adopt RNNs as they are effective in processing data time series. The main contributions of this study are summarized as follows:

- It explores the potential of RNN models for touch modality classification. For this purpose, we specifically propose two methods that are based on two separate RNN architectures, namely Long Short Term Memory (LSTM) [268] and Gated Recurrent Unit (GRU) [269] networks to capture long-term dependence from tactile data.
- It proposes a case-specific approach to dataset organization to address the peculiarities of tactile data within the aforementioned architectures. For both LSTM and GRU models, averaging with overlap is applied to the input tensor aiming to maintain data about previous time-step in the current time-step.
- The proposed RNN framework for tactile data classification has been experimentally validated with a real dataset and compared to the state of the art achievements. The experimental results demonstrate that the proposed approach achieves a reduction in the number of FLOPs by 99.98% and by 98.34% in memory storage compared to the same problem in the state of the art [270]. Moreover, The computing architecture is

scalable, i.e. the complexity is still acceptable when the system is scaled up in terms of input matrix size and number of classes to be recognized. Nonetheless, the classification has reached an accuracy of 84.23% on a 3-class touch modality data set (explained in Section 8.4), which is higher than state of art solutions on the same dataset [271, 272]. The proposed solutions reduce the number of FLOPs by 99.989% compared to the same problem in the state of the art [270]. The computing architecture is scalable, i.e. the complexity is still acceptable when the system is scaled up in terms of input matrix size and number of classes to be recognized.

The rest of the chapter is organized as follows. Section 8.2 reviews the related works in tactile data processing. Section 8.3 gives a brief discussion on the methodology followed in the proposed approach. Section 8.4 introduces the experimental setup with the details of the different proposed models. In Section 8.5, we report and analyze the experimental results with a discussion. Finally, we conclude the study in Section 8.6. The content of this chapter is presented in [273].

8.2 Background

Different works in the literature have addressed tactile data processing using machine learning and deep learning, including the use of LSTM networks. In general, these works address both static and dynamic tactile data perception. In static perception, a single reading is captured for a sensor array, while the dynamic aspect deals with tensorial data collected as frames; each frame corresponds to readings at a single time, and the whole tensor is considered as a sample to be processed. In [274] and [275], nine static touch modalities (tap, pat, push, stroke, scratch, slap, pull, squeeze, and no-touch) are classified using LogitBoost[276] and SVM respectively. LogitBoost in [274] degrades in performance when trained on data collected by 40 participants (71%), while SVM achieves an accuracy range of 80.10% - 81.85% in [275].

In [277] two approaches are used to classify eight objects, i.e., finger, hand, arm, pen, scissors, pliers, sticky tape, and Allen-key, using a 28×50 tactile sensory array attached to a robotic arm to collect static pressure maps. For feature extraction, the first approach uses Speeded-Up Robust Features (SURF) descriptor[278], while the second uses a pre-trained AlexNet CNN[279]. Finally, a Support Vector Machine (SVM)[280] classifier is employed for both approaches. In [281], authors use a shallow CNN (only three convolutional layers inside) based on AlexNet to identify 22 objects using static pressure maps, collected from a 28×50 tactile sensory array. While in [272], an optimised embedded implementation of the latter solution is achieved on various hardware platforms.

Rouhafzay et al. [282] employ a combination of virtual tactile sensors (32×32) and visual guidance to distinguish eight classes of simulated objects. Two neural networks are used: a 3D ConvNet for the series of object images coming from tactile sensors and a 1D ConvNet for the series of the normal vectors to the object surface. Abderrahmane et al. [283] introduce a zero-shot object recognition framework, to identify previously unknown objects based on haptic feedback using BioTac sensors [284]. Two CNNs are employed: one for visual data and another for tactile data where the time dimension in the data is transformed into spatial dimension. In [281], authors use a shallow CNN (only three convolutional layers inside) based on AlexNet to identify 22 objects using pressure maps, collected from a 28×50 tactile sensory array. While in [272], an optimised embedded implementation of the latter solution is achieved on various hardware platforms. Gastaldo et al. [271] propose tensor-SVM and tensor-RLS to classify three touch modalities collected as tensorial data from a sensory array. In [285] the same problem is solved using Deep Convolutional Neural Network (DCNN) and transfer learning. In the latter, tensorial sensory data is transformed into synthetic RGB images, and then pre-trained CNN models on ImageNet [286] is used for feature extraction.

In [287], authors collect frames of pressure maps from squeezing an object in contact with a TekScan sensor. 3D CNN are compared to 2D CNN in order to classify three different datasets achieving a higher accuracy when 3D CNN have been employed. Various other works on tactile data processing can be found in [288], [289], and [290] as well.

LSTM networks have recently attracted attention in tactile data processing, especially for the case of data presented in time-series, i.e., each sensor acquires time series of readings, defined by the data readout frequency.

In [291], an LSTM is used to predict shape independent hardness of objects from data generated as video from a GelSight sensor with a grid of 960×720 pixels. Features from five video frames are extracted using a CNN and then used as an input for an LSTM network.

In [292], a CNN is used for active tactile clothing perception. Color RGB pressure maps generated from a large tactile sensor attached to a robotic arm grasping clothes, are used to classify different textile properties: thickness, smoothness, textile type, washing method, softness, stretchiness, durability, woolen, and wind-proof. Static and dynamic perception are explored, different CNN models are experimented for single image classification, the best performing being the VGG-19 pretrained on ImageNet [286], while a CNN+LSTM model is used for dynamic data, the LSTM is composed has hidden state of dimension 2048.

In [293], authors use an LSTM for slipping prediction over six different material surfaces, using three different tactile sensors, attached to three fingers of a robotic arm. A 20-neuron single-layer LSTM is used in this study. In [294], authors use a CNN and a Graph Convolutional Network [295] for binary grasp stability detection, and an LSTM and a ConvLSTM for detecting slipping direction (translational and rotational). The number of LSTM units is not mentioned for LSTM, instead for ConvLSTM, 5 ConvLSTM layers were used, then pooling, and two fully connected layers, the input for ConvLSTM

is 11×12 RGB image. In [296], Dong et al. use high resolution tactile sensor (GelSlim) to control the insertion of objects in a box-packing scenario, they employ two distinct models based on CNN+LSTM, the first network for detecting the direction of the error, and the other for detecting the magnitude of the error, the CNN model used to extract features is a pretrained AlexNet model. The LSTM contains 170 units.

The aforementioned works generally have a high complexity in the learning and inference phases, especially when deep learning is used, which raises challenges for hardware implementation requirements[297]. Here arises the need of low-complexity but high-accuracy touch modality classification solutions suitable for the embedded hardware implementation, where resources are usually limited (e.g., power, memory). In this respect, LSTM is a promising candidate, especially when shared weights are used.

To the best of our knowledge, no works were done, yet, to explore the potential of LSTM for solving the touch modality classification problem. According to the state-of-art, different methods were used to address tactile data processing and touch modality classification. In this framework, the capability of deep learning architectures to extract meaningful data representations from high-dimensional spatio-temporal data, without the need for handcrafting features, conveys an especially promising potential. Here, we leverage on this potential to propose two novel methods for tactile data classification, based on recurrent architectures. On one hand, the planar topology of a tactile array may generally prompt the use of CNN architectures. This strategy is expected to be promising especially if large-area arrays, made of many individual sensors and acquiring tactile imagery with relatively high resolution, are used. On the other hand, highly effective CNN architectures may include a large set of parameters, which creates a challenge for real-time processing, power consumption, and training set size. Touch modality data have relevant spatio-temporal characteristics: touch occurs in time (temporal aspect) and takes place on the surface of the tactile sensory array (spatial

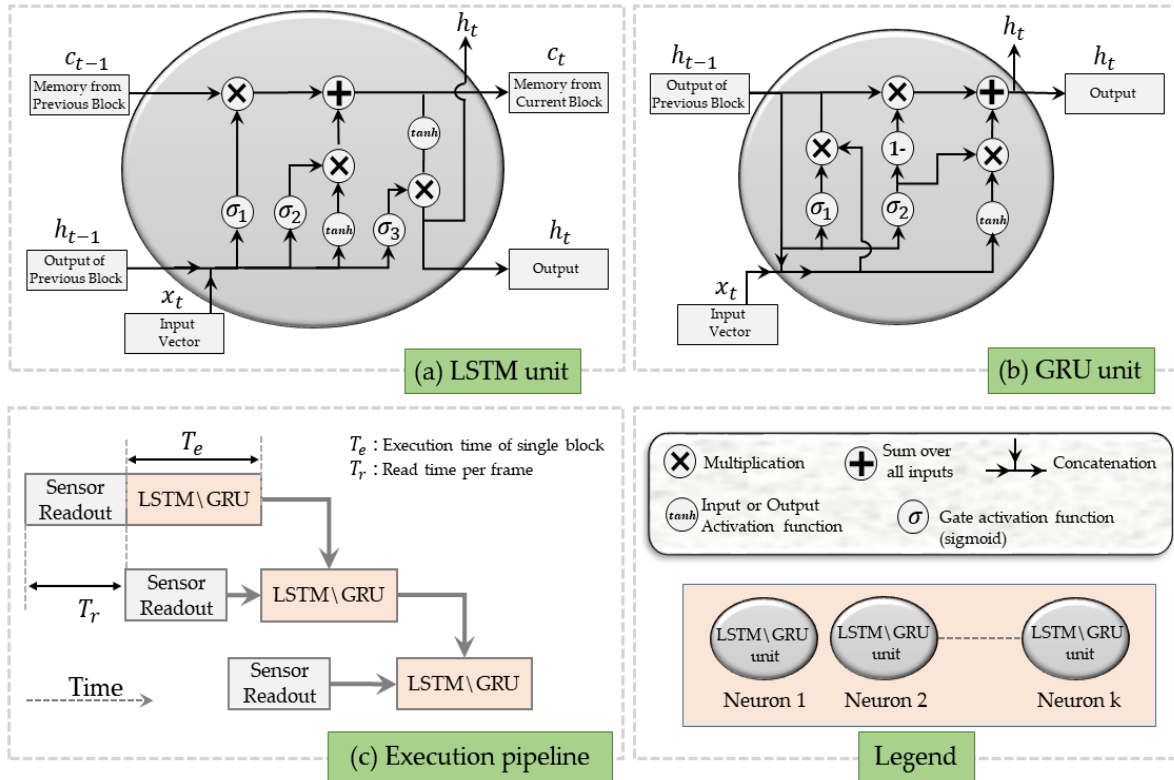


Figure 8.1 (a) LSTM unit (b) GRU unit (c) LSTM\GRU Execution pipeline

aspect). Using CNN in [285], necessitates to transform temporal characteristics into spatial characteristics, by generating a single synthetic image for each tensorial sample. Instead, RNN intrinsic capabilities to capture time-dependent behaviors makes them a promising approach for the analysis of such data. This is achieved by making a recursive input into the network, which comes from the output at previous time-step. Another important consequence of using RNNs is that the weights are shared across time, i.e., weights are defined for a single RNN block, and these weights will be shared upon execution over all time-steps. This means a reduction in number of stored trained parameters and of complexity as well.

Here, the RNN approach to the classification of touch modalities is explored and two RNN models (LSTM and GRU) are proposed.

8.3 Methodology

8.3.1 LSTM network

LSTM networks are RNNs capable of modeling long-range temporal dependencies [298]. RNNs are composed of a chain of units whose output is connected not only to the next layer but also fed back to the unit itself as an input, thus allowing the information to persist. LSTM behaves in a temporal manner that is appropriate for learning sequential models [299]. A clear example of LSTM usage is the prediction of the next word in a sentence, having observed the previous words [300]. Moreover, LSTM can act as a classifier for time series of data [301, 302]. A key characteristic of LSTM is its memory cell, which acts as an accumulator of the state information. Several self-parameterized controlling gates are used to access, write, and clear the cell (output, input, and forget gates).

Figure 8.1.a illustrates the architecture of the LSTM unit. It is composed of a cell, which is characterized by a state vector c_t and a hidden state vector h_t ($t \in \{1, 2, \dots, T\}$) indicates the time index and T is the number of time-steps. Each LSTM unit uses a forget gate, associated with a sigmoid activation function (σ_1), to decide which information it should forget from the previous state c_{t-1} . A new input x_t ($t \in \{1, 2, \dots, T\}$) is accumulated to the state of the memory cell c_t using a hyperbolic tangent activation function (\tanh) and an input gate with sigmoidal activation function σ_2 . At the end of the LSTM unit, an output gate using sigmoidal (σ_3) and tangential (\tanh) activation functions are used to decide the outputs of the LSTM unit (c_t and h_t). Note that x_t is a vector with dimensionality equal to the number N of features, which represents the number of individual sensors in the array.

In order to get the number of parameters in an LSTM unit, the formula is the following:

$$p = 4 \times (H \times (D + H) + H) \quad (8.1)$$

where H is the number of hidden layers(neurons), D the dimension of the input vector (in our case 16). For each sigmoid function, the input is the concatenation of x_t and h_t , hence the total dimension of the input is $D + H$, this number is multiplied by number of neurons H , in addition we have H biases for each sigmoid function. so that the total number of weights of each sigmoid function is $(H \times (D + H) + H)$. Since an LSTM unit is composed of 4 sigmoid functions according to Figure 8.1, this number is multiplied by 4 as shown in equation 8.1. More details about LSTM networks can be found in [300].

8.3.2 GRU network

Similar to the LSTM unit, the GRU unit has gates that modulate the flow of information inside the unit. However, it does not use the memory cell state and uses the hidden state h_t to transfer information [269]. A typical GRU cell is composed of only two gates, the reset gate (whose role is similar to the forget gate of the LSTM) and the update gate (whose role loosely matches the input gate of the LSTM). Thus, a single GRU unit involves fewer operations and trainable parameters compared to a single LSTM unit. Figure 8.1.b shows the architecture of the GRU unit. In order to get the number of parameters in a GRU unit, the formula is the following :

$$p = 3 \times (H \times (D + H) + H) \quad (8.2)$$

The only different compared to equation 8.1, is the number 3 instead of 4, because the GRU block is composed of Three sigmoid functions instead of Four in the case of LSTM, as illustrated in Figure 8.1.

8.3.3 CNN-LSTM network

CNN-LSTM is a the series of a CNN and LSTM. The CNN-LSTM model is based on using pre-trained CNN layers, to produce a fixed-length vector representation of an input image to be used as a feature vector. This consists of cutting out the classification layer of the CNN, and just keeping all the layers before, whose final output is the feature vector. The feature vectors are then passed into an LSTM network, to implement the classification of a sequence of images. Figure 8.4 depicts the structure of the CNN-LSTM model.

8.3.4 ConvLSTM network

ConvLSTM networks [298] are used for capturing Spatio-temporal information in an image data sequence. These networks use convolutional layers inside their cells instead of fully connected layers used in standard LSTM networks. The main difference between LSTM and ConvLSTM is the type of operations performed in their units, but the logic keeps the same. That is, ConvLSTM networks still have a memory cell c_t that keeps a state at time t , and uses the same gates used in the LSTM unit to access, clear, and write the memory cell. However, a ConvLSTM operates with 3D tensors (e.g., RGB images) instead of 1D vectors (feature vectors) so it performs spatial convolutions with the data that go through it. Therefore, tensorial tactile images that presents a touch modality, can be used to train the ConvLSTM model and predict the type of such touch.

Based on the general architecture of the LSTM unit, three parameters are required to build an LSTM network: feature vector length, time-steps, and the number of neurons; the same applies to GRU as well. For these two RNN models, each input pattern is a feature vector representing a sampled time signal. In this perspective, raw data should be pre-processed in order to be suitable for RNN models. The pre-processing has three main objectives: 1) reduce the input data size to simplify the training, 2) normalise the data as a general consideration in training neural networks,

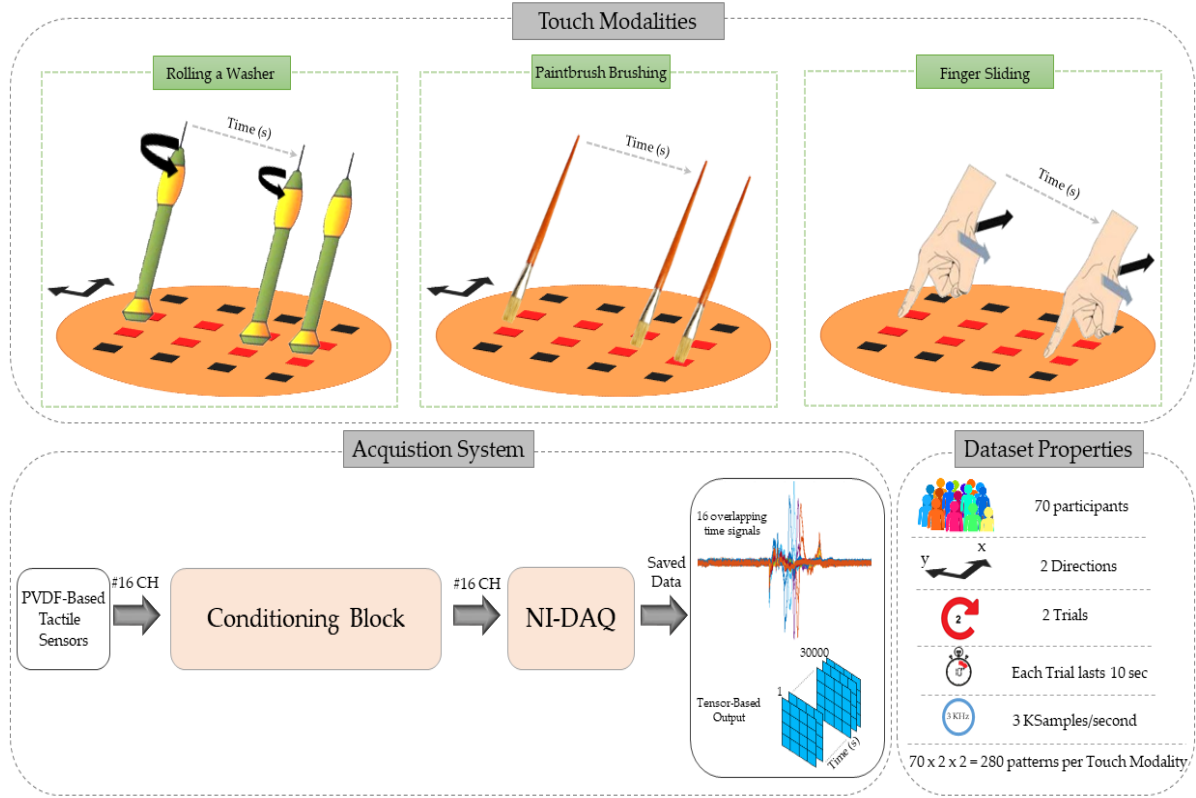


Figure 8.2 Scheme of touch modalities, tactile acquisition system and dataset properties.

and 3) make the dataset format compatible with the network's input format. The feature vector length for both LSTM and GRU was chosen equal to the size of the tactile array, therefore each sensor in the tactile array is considered as a feature. The number of neurons was selected on trial basis, in order to have the fewest trainable parameters possible, while achieving an acceptable accuracy with respect to the state of the art. Detailed description of each model is presented in Section 8.4.B.

8.4 Experimental Setup

The dataset collected in [271] has been considered in this study. Figure 8.2 illustrates the dataset used in this work. A tactile acquisition system (Figure 8.2) that is based on a charge amplifier and a Data Acquisition board (DAQ) was used to collect the data from the sensory array. Seventy subjects were asked to perform predetermined touch

modalities i.e. sliding the finger, brushing a paintbrush, and rolling a washer. Each participant touches the top surface of a 4×4 piezoelectric tactile sensory array in two moving directions twice. For every single touch, 10 seconds acquisition was done at 3 kSamples/second, the collected data were arranged into a 3-dimensional tensor: tactile sensory array size \times number of acquired samples = $4 \times 4 \times 30000$. 280 patterns per touch modality in a total of 840 patterns are available. This dataset can be downloaded from: <https://data.mendeley.com/datasets/dmcdp33ctt/2>

8.4.1 Dataset Organisation

In order to use RNNs for this dataset, pre-processing was applied to the dataset. The first step is to generate a 3D tensor that contains only the useful touch information from the original raw data. In other words, in the first step, we selected the time period where touch is applied as shown in Figure 8.3.A. This was done by checking at which time instant T any of the sensor output value exceeds a predefined threshold. The resulting time T indicates the starting point of the useful touch data. To have a constant number of frames over all the patterns, we fixed the size of the data to 6144 samples per sensor, i.e., in the $[T, T + 6143]$ range. The average activity time duration for all users is around 2 seconds i.e., 6000 samples. We selected 6144 samples per sensor i.e., 6144×16 to make the tensor size a multiple of 64×64 , which make it suitable for comparison with CNN based networks, mentioned in section 8.4.B.

The result from the first step is a 3D tensor of size $4 \times 4 \times 6144$ each, having the same original frequency of 3 kSamples/second, and starting at time instant T until reaching 6144 frames. Sixty patterns out of 840 were excluded since no sensor readings exceeded the activity threshold in these patterns. The refined dataset referred later on as Dataset (A), is composed of $D \times (4 \times 4 \times 6144)$ tensors per touch modality (three touch modalities), where D is the number of patterns ($D = 260$). From Dataset (A) are then derived two different datasets that fit the used models.

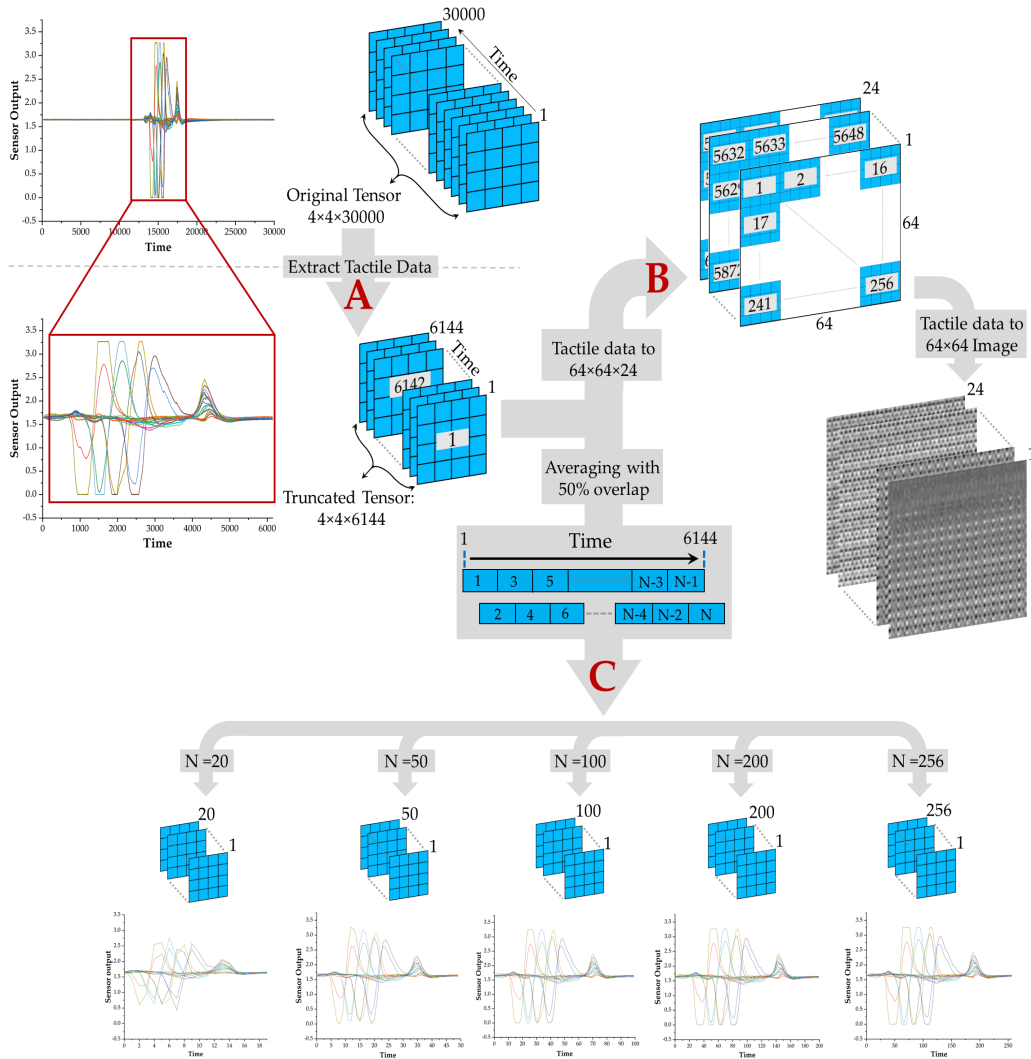


Figure 8.3 Dataset Organisation

CNNs use convolutional layers to transform images into feature vectors, following that requirement, each pattern in Dataset (A) of size $4 \times 4 \times 6144$ has been transformed into a time series of larger images. Each pattern is presented by $64 \times 64 \times 24$ samples (image size \times time-steps). The resulted dataset is called Dataset (B). It is important to note that the time sequence order was also maintained within each 64×64 image (im_{64}), i.e., each im_{64} consists of 256 images of 4×4 pixels as shown in Figure 8.3.B.

The third dataset called Dataset (C) is composed of five different sub-sampling of Dataset (A), as shown in Figure 8.3.C. An averaging with 50% overlap was used

Algorithm 1: Generate Dataset (C)

```

Input: Dataset (A), Output: Dataset (C)
a = single pattern from Dataset (A);
K = number of frames in a;
C = output pattern;
F = number of sensors;
N = number of output frames;
slot  $\leftarrow K/N$ ;
for i  $\leftarrow 1$  to F do
    sen  $\leftarrow a(1 : \text{end}, i)$ ; // sen: single sensor output
    u  $\leftarrow 1$ ;
    for j  $\leftarrow 1$  to N do
        if u < N then
             $C(j, i) \leftarrow \text{Average}(\text{sen}(u : \text{slot} + u))$ ;
        if u = N then
             $C(j, i) \leftarrow \text{Average}(\text{sen}(u : \text{end}))$ ;
         $u \leftarrow u + \text{slot}/2$ ;

```

to down-sample the tensor from $4 \times 4 \times 6144$ to $4 \times 4 \times N$, where N represents the number of the input time-steps for the LSTM and GRU networks. N varies in the following set of values 20, 50, 100, 200, and 256. The overlapping helps maintaining data about previous time-step in the current time-step, the increment of ($\text{slot}/2$) in the sub-sampling algorithm clarify this overlapping. The whole process is described in Algorithm 1.

The three datasets are shown in Figure 8.3, where one pattern was used as an example to illustrate the difference in the presentation of the original dataset.

8.4.2 Implementation

As mentioned in Section 8.3, two models have been implemented. For each model a dense layer is added at the end for the classification. For a further comparison, two CNN-based models are tested.

8.4.2.1 LSTM network

the LSTM network composed of one LSTM layer (10 neurons) and a flat input layer of length 16, was trained on Dataset (C). As for the time-steps, the LSTM network was trained for each of the time-step configurations i.e., $N \in \{20, 50, 100, 200, 256\}$.

8.4.2.2 GRU network

The GRU network is composed of a single GRU layer, applied within two alternatives: 10 neurons and 12 neurons per GRU layer. This GRU network has as well a flat input layer of length 16. As for the time-steps, the training process was done only on ($N = 20$) configuration of Dataset (C), based on the best achieved results with LSTM.

8.4.2.3 CNN-LSTM network

Four different pre-trained CNN models (ResNet50 [303], ResNet150V2 [303], MobileNetV2 [304] and VGG16 [302]) were considered for comparison purposes to play the role of the CNN model shown in Figure 8.4. The four CNN models were trained using the ImageNet dataset [286]. These models were selected based on the results of our previous work [285], which showed that the four models were effective in extracting features from the considered dataset. The models were used to transform each image in Dataset (B) into a fixed-length feature vector. Therefore, each CNN model transform Dataset (B) into a 4-Dimension tensor of shape $D \times 24 \times 1 \times K$, where D is the number of patterns, K is the size of the output feature vector in each model,

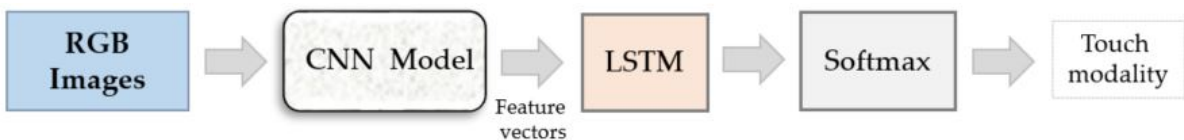


Figure 8.4 CNN-LSTM Structure.

and 24 is the time-steps in each pattern. Thus, the input of the LSTM block has K features, and 24 time-steps.

8.4.2.4 ConvLSTM network

The second CNN-based model used for comparison is composed of single ConvLSTM layer (32 filters of 3×3) followed by one fully-connected layer with 100 units and ReLU activation. Dataset (B) is used, the input of the network is a im_{64} , and the time-steps are 24.

8.4.3 Training

The training and application of the proposed networks were done using Keras with Tensorflow back-end on an NVIDIA GPU. Dataset (C) was normalized before being used to train and test the LSTM and GRU models.

For training / testing split, an 80 / 20 percentage was chosen. Five folds were generated, in a way that the intersection of testing samples is empty across all folds. The Adam optimiser [305] was used to train the networks, with categorical cross entropy as a loss function and Softmax activation for the output layer. Different runs were made also for each fold, including different batch sizes and epochs, in order to find the hyper-parameters that lead to better accuracy. Finally the choice was limited to $batch_size = [48, 69]$ and $epochs = [48, 96]$, such that we have 4 combinations in total. For each combination, ten training runs with random initialization and random batch selection have been made i.e., the batch size is fixed, but choosing the samples for a batch is random. Therefore, for each model mentioned in 8.4.B, $4 \times 10 \times 5$ (combinations \times runs \times folds) training runs have been made. Finally the accuracy is obtained by averaging all runs across a fold for all the combinations of $(batch_size, epochs)$. Results in the next section corresponds to the best $(batch_size, epochs)$ combination, i.e., the combination that gave the highest accuracy, in our case it is $batch_size = 48$

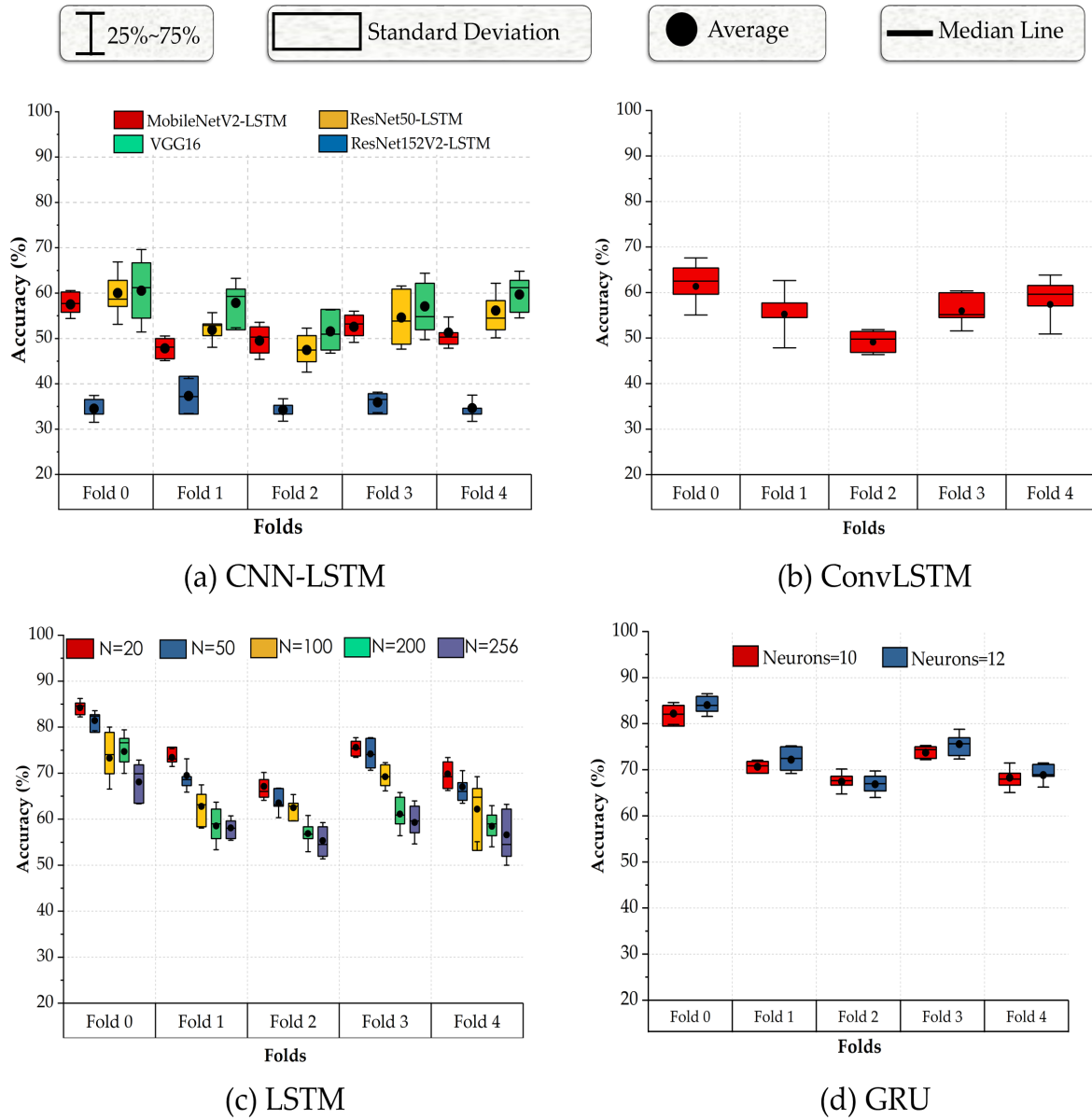


Figure 8.5 (a) Average Accuracy achieved varying the input to the CNN-LSTM network for five different folds of Dataset B; (b) Average Accuracy of ConvLSTM network for five different folds of Dataset B; (c) Average Accuracy achieved varying the input to the LSTM network for five different folds of Dataset C; (d) Average Accuracy achieved varying the number of neurons in the GRU network for five different folds of $N = 20$ Dataset C.

Table 8.1 Comparison of accuracy, number of parameters, and FLOPs

Model	Accuracy	Average Accuracy \pm Stdev (%)	Model parameters	FLOPs
ResNet50-LSTM	67.56	60.82 ± 6.74	26M	107M
ResNet150V2-LSTM	37.58	34.48 ± 3.10	61M	246M
VGG16-LSTM	69.67	62.39 ± 7.28	15M	62M
MobileNetV2-LSTM	60.76	57.5 ± 3.26	4M	17M
ConvLSTM	65.56	59.3 ± 6.26	314M	1G
LSTM20 (10 neurons)	84.23	74.02 ± 6.56	1113	2950×20
LSTM50 (10 neurons)	79.84	70.72 ± 6.24	1113	2950×50
LSTM100 (10 neurons)	73.26	65.98 ± 5.01	1113	2950×100
LSTM200 (10 neurons)	74.67	61.92 ± 7.29	1113	2950×200
LSTM256 (10 neurons)	68.07	59.47 ± 5.03	1113	2950×256
GRU20 (10 neurons)	81.92	72.06 ± 6.60	843	2228×20
GRU20 (12 neurons)	83.78	73.07 ± 6.53	1083	2960×20
Tensor-SVM [271] [270]	76.6	71 ± 5.6	67200	545M
Tensor-RLS [271]	77.3	73.7 ± 3.6	-	-
DCNN (InceptionResNetV2) [285]	76.9		54M	109M

and $epochs = 96$. Figure. 8.5 shows the accuracy obtained on each fold, for the selected $(batch_size, epochs)$ combination, using the four different models.

8.5 Results and Discussion

According to Figure 8.5.c, the use of LSTM with $N = 20$ time-steps referred later as LSTM20, i.e. using the Dataset (C) with sub-sampling into 20 samples for each pattern, shows a higher accuracy according to other sub-sampling alternatives, and with respect to other tested models. LSTM20 has achieved the highest accuracy: 84.23%, the smallest number of trainable parameters: 1113, and the smallest number of FLOPs: 2950 per LSTM block as shown in Table 8.1.

Regarding the GRU, GRU20 also proved a high accuracy with a smaller number of parameters and a comparable number of FLOPs with respect to LSTM20 as shown in Figure 8.5.d. The 10-neuron GRU achieved an accuracy of 81.92% with 843 trainable

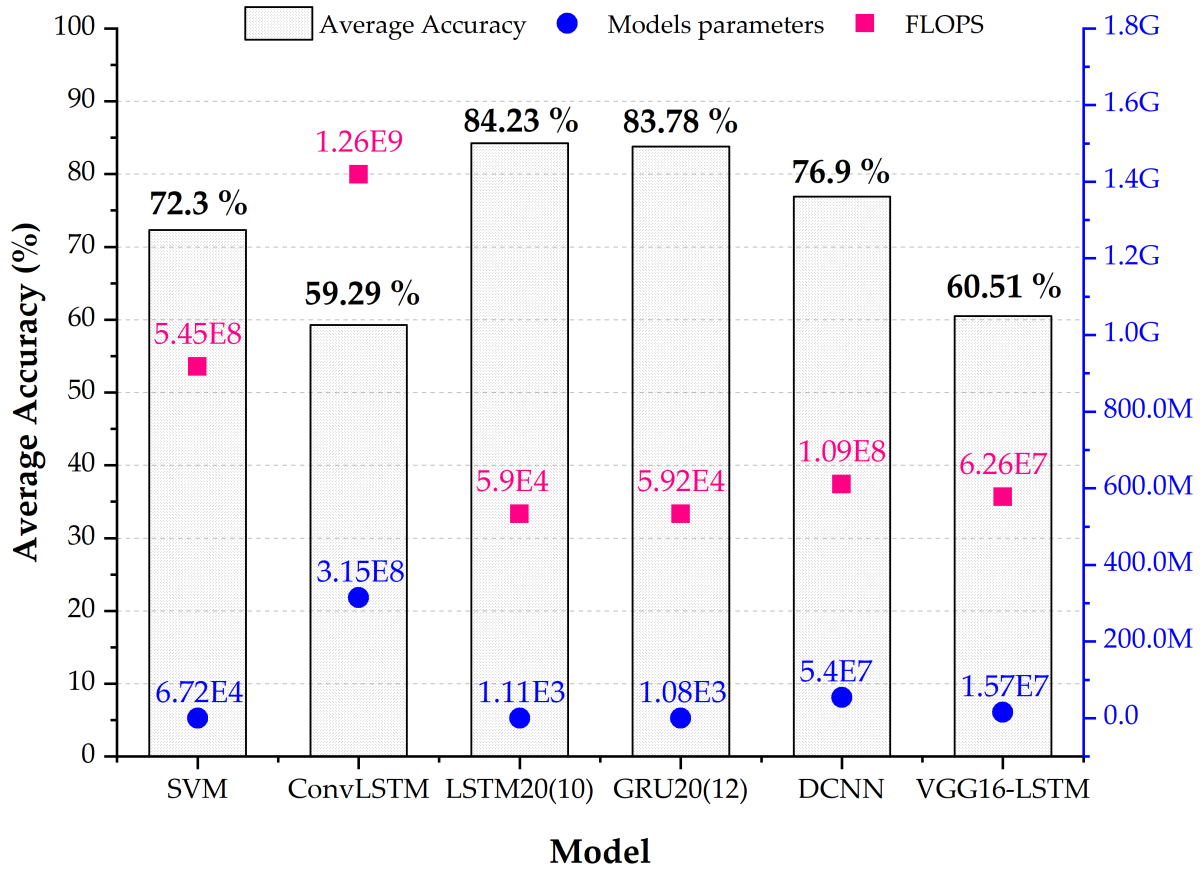


Figure 8.6 Accuracy of the best performing networks. LSTM20(10) stands for LSTM network with 10 neurons and $N = 20$. GRU20(12) stands for GRU network with 12 neurons and $N = 20$.

parameters and 2228 FLOPs. While a 12-neuron GRU, with 1083 trainable parameters, and 2960 FLOPs per single GRU block achieved 83.78% as shown in Figure 8.6 and Table 8.1. Both the GRU and LSTM models have achieved an accuracy higher than the best accuracy achieved by state-of-the-art approaches applied to the same dataset, whether in tensor-SVM (76.6%) and tensor-RLS (77.3%) [271], or using DCNN (76.9%) [285]. If we take the average accuracy, we can see that LSTM20 has achieved the higher average accuracy across all of them.

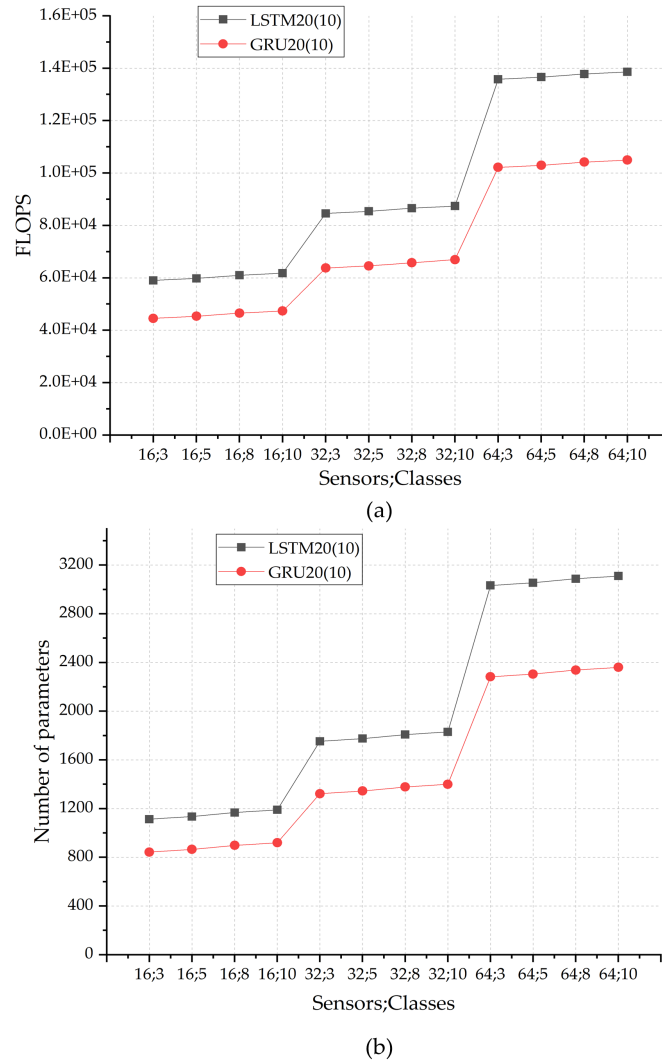


Figure 8.7 (a) Number of sensors and classes versus number of FLOPS. (b) Number of sensors and classes versus Model parameters.

As per ConvLSTM and CNN-LSTM, these models did not converge well, and the obtained accuracies did not exceed the 70% as shown in Figure 8.5.a and Figure 8.5.c. One reason behind it, is the large number of features and therefore trainable parameters, compared to the small dataset size. Notwithstanding that, the previous results in DCNN [285] were higher, but that was done using transfer learning, i.e. all the used networks (except the classifier), were pre-trained on millions of images from ImageNet [286] and thousands of classes, then a classifier was trained on the subject dataset. Instead in CNN-LSTM we are using pre-trained CNNs to extract features from Dataset (B), the

resulting feature vector may range from 2K (VGG16) to 8K (Resnet150v2) features. These features are fed into an LSTM network to train it from scratch, compared to 16 features in LSTM or GRU with Dataset (C), which induces higher number of trainable parameters for both CNN-LSTM and ConvLSTM compared to GRU and LSTM, as shown in Table 8.1. Raising the number of LSTM layers and number of neurons for ConvLSTM and CNN-LSTM lead to better results, but still not reaching a comparable accuracy.

LSTM achieved the following benefits:

- FLOPs and memory occupation i.e., number of trainable parameters are less, compared to the SOA.
- As for the computation, data can be fed into an LSTM network, as soon as all features are ready for a single time-step, i.e., when data are ready at time t , they can be forwarded into an LSTM block, without waiting for the data from all time frames. Also, data occurring at time $t + 1$ can be collected in parallel with respect to the execution of LSTM block of data at time t , as illustrated in Figure 8.1.c. Unlike other solutions like CNN or tensor-SVM, all data should be assembled before being processed.
- Higher accuracy is obtained.
- The model is highly scalable and independent on the size of the dataset, in terms of both FLOPs and number of trainable parameters, as illustrated in Figure 8.7. Unlike SVM, where the model size depends on the number of training samples and does not support multi-class labeling directly [306]. In addition, since LSTM used shared weights, e.g., when training an LSTM of $N = 20$ time-steps, weights are shared across all time-steps, which makes a model trained on N time-steps data still usable for M time-steps data.

8.6 Conclusion

In this chapter, we have investigated the potential of RNNs for touch modality classification. Two different approaches based on LSTM and GRU architectures have been proposed to extract long-term dependence from tactile data. Proposed approaches have been validated on real tactile data acquired from 4×4 piezoelectric tactile arrays. Experimental results have shown that the achieved accuracy is of 84.23% and 83.78% for LSTM and GRU respectively compared with a value of 76.9% for the best achieved accuracy in literature [271, 285]. On the other hand, the proposed architectures reduce drastically the number of FLOPs considered as the main factor affecting the hardware complexity of the system. The number of FLOPs has been reduced of 99.989% compared to the same problem in the state of the art [270] which will have the impact on time latency, hardware resources, memory storage and energy consumption when the hardware implementation will be targeted. Another important aspect offered by the proposed approach is the scalability in the computing architecture. This means that the complexity of the system remains acceptable when the system is scaled up in terms of input matrix size and number of classes to be recognized which was a main drawback limiting similar state of art solutions [306]. To mention that the proposed solution achieved less than 5ms latency time on NVIDIA GPU, compared to 75ms for the same problem using DCNN in [285]. As a conclusion, the proposed work represents a good candidate to be embedded together with tactile sensing system for robotic or prosthetic applications [132, 265]. Such applications require near-sensor processing with critical constraints such as small hardware area, low energy budget due to the limited battery size, and the low latency needed to perform real time functions. In future work, we are going to implement the proposed systems on embedded platforms integrated with the tactile sensors and their front-end electronics. Furthermore, after validating its functionality, the system is intended to be implemented on an Application

Specific Integrated Circuit (ASIC) to form a smart electronic skin system module for the target applications.

Chapter 9

Conclusion and Future work

With the significant breakthroughs in advanced robotics in recent decades, more sophisticated models of robotic hands (e.g., body-powered myoelectric prostheses) have made it through. However, most of the available robotic hands still show limited sensory. Closing the loop control through providing sensory feedback has been reported by users as a future goal, as it lessens the cognitive load needed to perform a task which improves the utility and easiness of use of the machine. The implementation of sensory feedback for both proprioception, grasping, and manipulating with the robotic hand is a critical challenge.

Peerdeman et al. [307] examined the requirements for feedback and arranged the feedback restoration priorities for the users in a hierarchical order of importance as follows:

- Continuous and proportional feedback on grasping force should be provided
- Position feedback should be provided to the user
- Interpretation of stimulation used for feedback should be easy and intuitive
- Feedback should be unobtrusive to user and others
- Feedback should be adjustable

Most of the conventional systems developed for tactile feedback provide feedback through a few sensing and stimulation units. This limits the amount of information that could be extracted during interaction with the environment. Moreover, using a few stimulations units to communicate more than one sensation may be difficult for the user to understand or result in a high cognitive load for the user. Distributed sensing systems and multichannel stimulation interfaces are promising as they could accommodate the robotic hand flexibility and translate multiple information to the user (e.g., wrist rotation, grasping force, aperture) at the same time, thus emulating the naturalness of touch. In this scope, the presented thesis proposed a distributed sensing and stimulation system for tactile feedback in robotic hands. To this aim, the robotic hand will integrate distributed sensing system (e-skin) to acquire tactile sensation, an embedded electronic system for sensor acquisition and processing, and a multichannel stimulation interface to provide high-bandwidth tactile feedback to the user.

As previously discussed, providing high-resolution tactile information that imitates the human sense of touch requires an articulated artificial sensing system that integrates high-density sensing arrays (e-skin) to measure the variable touch attribute. E-skin in the form of tactile sensing arrays (skin patches) can be integrated onto the robotic hand to record information about touch, given back to the user as sensory feedback. This thesis realized a novel, flexible, screen-printed e-skin based on P(VDF-TrFE) piezoelectric polymers, that would cover the fingertips and the palm of the prosthetic hand (particularly the Michelangelo hand by Ottobock) and assistive sensorized glove for stroke patients. Moreover, it developed a new validation methodology to examine the behavior of the sensor while being solicited. In addition, the thesis presented the validation of the interface electronics (data acquisition) for the characterized sensing arrays. The validation results motivate the integration of the proposed interface electronics design in a robotic system where the sensor array will be connected to the interface electronics mounted on the hand. Moreover, this thesis presented the

realization of a skin patch. The two components (skin patches and interface electronics) were integrated on the mockup of the Michelangelo prosthetic hand and used to develop two high-bandwidth tactile feedback systems for prosthetic hand and teleoperation. Both systems use electrotactile stimulation to deliver tactile information extracted by the sensing system. They showed the high capability to detect and deliver tactile information to the user, where users were able to receive and interpret different touch modalities applied on the e-skin.

Wider scenarios could be explored and investigated on how to give back sensor data captured by the e-skin to the user and how to help the human brain to successfully interpret the elicited artificial tactile information. One of the dilemmas is which kind of information whether raw or processed data about a touched object should be sent back to the user. On one hand, the sensor signals could be directly communicated to the user, who needs to meaningfully interpret this information. On the other hand, sensor data can be locally processed at the body periphery (embedded electronics) and high-level tactile information (e.g., texture properties, grasp stability) can be extracted and delivered to the user. In this thesis, deep learning algorithms (RNN) have been exploited to classify and interpret input touch modalities as they represent a powerful technology for tackling clustering, classification, and regression problems in complex domains. In addition, we believe that these algorithms would be an assist in optimizing the information transfer to the user, and it may decrease the cognitive load to adapt to different sensations.

A demanding focus, for the immediate future, should therefore be placed on integrating the high-bandwidth tactile feedback system into the robotic hand (e.g., prosthetic hand). The system would provide high-fidelity feedback. To do this, signal processing and machine learning methods must be used to extract meaningful information from the e-skin. Further testing on tactile feedback interfaces that combine several stimulation methods are required to deliver such high-fidelity information to the user.

Such tactile feedback systems could be practically used at home every day so that users can begin to take advantage of the benefits that such high-bandwidth human-machine interfacing could provide them.

Bibliography

- [1] Luigi Pinna, Ali Ibrahim, and Maurizio Valle. Interface Electronics for Tactile Sensors Based on Piezoelectric Polymers. *IEEE Sensors Journal*, 17(18):5937–5947, sep 2017. pages xxiii, 67, 68, 69, 75
- [2] Honghai Liu, Zhaojie Ju, Xiaofei Ji, Chee Seng Chan, and Mehdi Khoury. *Human Motion Sensing and Recognition*, volume 675 of *Studies in Computational Intelligence*. Springer Berlin Heidelberg, Berlin, Heidelberg, 2017. pages 1
- [3] Haoyong Yu, Sunan Huang, Gong Chen, Yongping Pan, and Zhao Guo. Human–Robot Interaction Control of Rehabilitation Robots With Series Elastic Actuators. *IEEE Transactions on Robotics*, 31(5):1089–1100, oct 2015. pages 1
- [4] Jingang Yi, Jun Ueda, and Xiangyang Zhu. Introduction to the focused section on intelligent robotics for rehabilitation and human assistance. *International Journal of Intelligent Robotics and Applications*, 1(1):3–5, feb 2017. pages 1
- [5] Akihiro Mori, Seiichi Uchida, Ryo Kurazume, R. Taniguchi, Tsutomu Hasegawa, and Hiroaki Sakoe. Early Recognition and Prediction of Gestures. In *18th International Conference on Pattern Recognition (ICPR'06)*, volume 3, pages 560–563. IEEE, 2006. pages 1
- [6] Christina Brown, Martin Cowell, C. Ariana Plont, Heidi Hahn, and David Mascareñas. A Vibro-Haptic Human-Machine Interface for Structural Health Monitoring Applications. pages 187–197. 2013. pages 1
- [7] Paul D. Marasco, Keehoon Kim, James Edward Colgate, Michael A. Peshkin, and Todd A. Kuiken. Robotic touch shifts perception of embodiment to a prosthesis in targeted reinnervation amputees. *Brain*, 134(3):747–758, mar 2011. pages 2, 142
- [8] Biddiss E and Chau T. Upper-limb prosthetics: critical factors in device abandonment. *American journal of physical medicine & rehabilitation*, 86(12):977–987, dec 2007. pages 2
- [9] Sören Lewis, Michael Friedrich Russold, Hans Dietl, and Eugenijus Kaniusas. User demands for sensory feedback in upper extremity prostheses. *MeMeA 2012 - 2012 IEEE Symposium on Medical Measurements and Applications, Proceedings*, pages 188–191, 2012. pages 2

- [10] Claudio Castellini, Panagiotis Artemiadis, Michael Wininger, Arash Ajoudani, Merkur Alimusaj, Antonio Bicchi, Barbara Caputo, William Craelius, Strahinja Dosen, Kevin Englehart, Dario Farina, Arjan Gijsberts, Sasha B. Godfrey, Levi Hargrove, Mark Ison, Todd Kuiken, Marko Marković, Patrick M. Pilarski, Rüdiger Rupp, and Erik Scheme. Proceedings of the first workshop on peripheral machine interfaces: Going beyond traditional surface electromyography. *Frontiers in Neurorobotics*, 8(AUG):1–17, 2014. pages 2
- [11] Matthew Schiefer, Daniel Tan, Steven M Sidek, and Dustin J Tyler. Sensory feedback by peripheral nerve stimulation improves task performance in individuals with upper limb loss using a myoelectric prosthesis. *Journal of Neural Engineering*, 13(1):1–25, 2015. pages 2
- [12] D.A. Kontarinis, J.S. Son, William Peine, and R.D. Howe. A tactile shape sensing and display system for teleoperated manipulation. In *Proceedings of 1995 IEEE International Conference on Robotics and Automation*, volume 1, pages 641–646. IEEE, 1995. pages 2
- [13] "Bebionic | Ottobock US" [online]. available: <https://www.ottobockus.com/prosthetics/upper-limb-prosthetics/solution-overview/bebionic-hand/> [accessed: 2021-10-02]. pages 2
- [14] "Michelangelo prosthetic hand | Ottobock US" [online]. available: <https://www.ottobockus.com/prosthetics/upper-limb-prosthetics/solution-overview/michelangelo-prosthetic-hand/> [accessed: 2021-03-27]. pages 2, 6, 24, 31, 34, 110, 116, 146
- [15] "Ossur Touch Solutions" [online]. available: <https://www.ossur.com/en-us/prosthetics/touch-solutions> [accessed: 2021-10-02]. pages 2
- [16] "Vincent Systems GmbH | Handprothese | Karlsruhe" [online]. available: <https://www.vincentssystem.de/> [accessed: 2021-09-26]. pages 2
- [17] Kenneth O. Johnson, Takashi Yoshioka, and Francisco Vega-Bermudez. Tactile Functions of Mechanoreceptive Afferents Innervating the Hand. *Journal of Clinical Neurophysiology*, 17(6):539–558, nov 2000. pages 3
- [18] V.G. Chouvardas, A.N. Miliou, and M.K. Hatalis. Tactile displays: Overview and recent advances. *Displays*, 29(3):185–194, jul 2008. pages 3
- [19] O. A. J. van der Meijden and M. P. Schijven. The value of haptic feedback in conventional and robot-assisted minimal invasive surgery and virtual reality training: a current review. *Surgical Endoscopy*, 23(6):1180–1190, jun 2009. pages 3, 141
- [20] Claudio Pacchierotti, Stephen Sinclair, Massimiliano Solazzi, Antonio Frisoli, Vincent Hayward, and Domenico Prattichizzo. Wearable Haptic Systems for the Fingertip and the Hand: Taxonomy, Review, and Perspectives. *IEEE Transactions on Haptics*, 10(4):580–600, oct 2017. pages 3, 142

- [21] Jonathon S. Schofield, Katherine R. Evans, Jason P. Carey, and Jacqueline S. Hebert. Applications of sensory feedback in motorized upper extremity prosthesis: a review. *Expert Review of Medical Devices*, 11(5):499–511, sep 2014. pages 3, 110, 142
- [22] Shuo Li, Yong Zhang, Yiliang Wang, Kailun Xia, Zhe Yin, Huimin Wang, Mingchao Zhang, Xiaoping Liang, Haojie Lu, Mengjia Zhu, Haomin Wang, Xinyi Shen, and Yingying Zhang. Physical sensors for skin-inspired electronics. *InfoMat*, 2(1):184–211, jan 2020. pages 3
- [23] Anindya Nag, Subhas Chandra Mukhopadhyay, and Jurgen Kosel. Wearable Flexible Sensors: A Review. *IEEE Sensors Journal*, 17(13):3949–3960, jul 2017. pages 3
- [24] N. Yogeswaran, W. Dang, W.T. Navaraj, D. Shakthivel, S. Khan, E.O. Polat, S. Gupta, H. Heidari, M. Kaboli, L. Lorenzelli, G. Cheng, and R. Dahiya. New materials and advances in making electronic skin for interactive robots. *Advanced Robotics*, 29(21):1359–1373, nov 2015. pages 3
- [25] Júlio C. Costa, Filippo Spina, Pasindu Lugoda, Leonardo Garcia-Garcia, Daniel Roggen, and Niko Münzenrieder. Flexible Sensors—From Materials to Applications. *Technologies*, 7(2):35, apr 2019. pages
- [26] Wei Chen, Heba Khamis, Ingvars Birznieks, Nathan F. Lepora, and Stephen J. Redmond. Tactile Sensors for Friction Estimation and Incipient Slip Detection—Toward Dexterous Robotic Manipulation: A Review. *IEEE Sensors Journal*, 18(22):9049–9064, nov 2018. pages 3
- [27] Benjamin Stephens-Fripp, Gursel Alici, and Rahim Mutlu. A Review of Non-Invasive Sensory Feedback Methods for Transradial Prosthetic Hands. *IEEE Access*, 6:6878–6899, 2018. pages 4, 25, 27, 109, 142
- [28] Kairu Li, Yinfeng Fang, Yu Zhou, and Honghai Liu. Non-Invasive Stimulation-Based Tactile Sensation for Upper-Extremity Prosthesis: A Review. *IEEE Sensors Journal*, 17(9):2625–2635, may 2017. pages 4, 25
- [29] Qiang Li, Oliver Kroemer, Zhe Su, Filipe Fernandes Veiga, Mohsen Kaboli, and Helge Joachim Ritter. A Review of Tactile Information: Perception and Action Through Touch. *IEEE Transactions on Robotics*, pages 1–16, 2020. pages 4, 19, 22
- [30] C. Antfolk, V. Kopta, J. Farserotu, J. D. Decotignie, and C. Enz. The WiseSkin artificial skin for tactile prosthetics: A power budget investigation. *International Symposium on Medical Information and Communication Technology, ISMICT*, pages 1–4, 2014. pages 4, 111, 143
- [31] J. Farserotu, J-D. Decotignie, J. Baborowski, P-N Volpe, C.R. Quirós, V. Kopta, C. Enz, S. Lacour, H. Michaud, R. Martuzzi, V. Koch, T. Li, and C. Antfolk. Tactile Prosthetics in WiseSkin. In *Design, Automation & Test in Europe Conference & Exhibition (DATE), 2015*, volume 6, pages 1695–1697, New Jersey, 2015. IEEE Conference Publications. pages

- [32] Jaemin Kim, Mincheol Lee, Hyung Joon Shim, Roozbeh Ghaffari, Hye Rim Cho, Donghee Son, Yei Hwan Jung, Min Soh, Changsoon Choi, Sungmook Jung, Kon Chu, Daejong Jeon, Soon-Tae Lee, Ji Hoon Kim, Seung Hong Choi, Taeghwan Hyeon, and Dae-Hyeong Kim. Stretchable silicon nanoribbon electronics for skin prosthesis. *Nature Communications*, 5(1):5747, dec 2014. pages 4, 138, 143
- [33] Dustin J. Tyler. Neural interfaces for somatosensory feedback. *Current Opinion in Neurology*, 28(6):574–581, dec 2015. pages 11
- [34] H. Henrik Ehrsson, B. Rosen, Anita Stockselius, C. Ragnö, P. Kohler, and Göran Lundborg. Upper limb amputees can be induced to experience a rubber hand as their own. *Brain*, 131(12):3443–3452, dec 2008. pages 12
- [35] Ali Ibrahim, Luigi Pinna, Lucia Seminara, and Maurizio Valle. Achievements and Open Issues Toward Embedding Tactile Sensing and Interpretation into Electronic Skin Systems. In *Material-Integrated Intelligent Systems - Technology and Applications*, pages 571–594. Wiley-VCH Verlag GmbH & Co. KGaA, Weinheim, Germany, dec 2017. pages 12, 85, 167
- [36] R.S. Dahiya, Giorgio Metta, Maurizio Valle, and Giulio Sandini. Tactile Sensing—From Humans to Humanoids. *IEEE Transactions on Robotics*, 26(1):1–20, feb 2010. pages 14, 66, 143
- [37] Lucia Seminara, Marco Capurro, Paolo Cirillo, Giorgio Cannata, and Maurizio Valle. Electromechanical characterization of piezoelectric PVDF polymer films for tactile sensors in robotics applications. *Sensors and Actuators A: Physical*, 169(1):49–58, sep 2011. pages 15, 29, 30, 42, 43, 66, 70
- [38] H.B. Muhammad, C.M. Oddo, L. Beccai, C. Recchiuto, C.J. Anthony, M.J. Adams, M.C. Carrozza, D.W.L. Hukins, and M.C.L. Ward. Development of a bioinspired MEMS based capacitive tactile sensor for a robotic finger. *Sensors and Actuators A: Physical*, 165(2):221–229, feb 2011. pages 15
- [39] Darryl P.J. Cotton, Paul H. Chappell, Andy Cranny, Neil M. White, and Steve P. Beeby. A novel thick-film piezoelectric slip sensor for a prosthetic hand. *IEEE Sensors Journal*, 7(5):752–761, 2007. pages 15, 111, 143
- [40] Indrani Dakua and Nitin Afzulpurkar. Piezoelectric Energy Generation and Harvesting at the Nano-Scale: Materials and Devices. *Nanomaterials and Nanotechnology*, 3(1):21, jun 2013. pages 15
- [41] Shinya Takamuku, Gabriel Gomez, Koh Hosoda, and Rolf Pfeifer. Haptic discrimination of material properties by a robotic hand. In *2007 IEEE 6th International Conference on Development and Learning*, pages 1–6. IEEE, jul 2007. pages 15
- [42] Calogero M. Oddo, Marco Controzzi, Lucia Beccai, Christian Cipriani, and Maria Chiara Carrozza. Roughness Encoding for Discrimination of Surfaces in Artificial Active-Touch. *IEEE Transactions on Robotics*, 27(3):522–533, jun 2011. pages 15

- [43] Weiting Liu, Ping Yu, Chunxin Gu, Xiaoying Cheng, and Xin Fu. Fingertip Piezoelectric Tactile Sensor Array for Roughness Encoding Under Varying Scanning Velocity. *IEEE Sensors Journal*, 17(21):6867–6879, nov 2017. pages 15
- [44] Sadao Omata and Yoshikazu Terunuma. New tactile sensor like the human hand and its applications. *Sensors and Actuators A: Physical*, 35(1):9–15, oct 1992. pages 15
- [45] B. C.-K. Tee, A. Chortos, A. Berndt, A. K. Nguyen, A. Tom, A. McGuire, Z. C. Lin, K. Tien, W.-G. Bae, H. Wang, P. Mei, H.-H. Chou, B. Cui, K. Deisseroth, T. N. Ng, and Z. Bao. A skin-inspired organic digital mechanoreceptor. *Science*, 350(6258):313–316, oct 2015. pages 16
- [46] Alex Chortos, Jia Liu, and Zhenan Bao. Pursuing prosthetic electronic skin. *Nature Materials*, 15(9):937–950, sep 2016. pages 16, 143
- [47] Nikola Jorgovanovic, Strahinja Dosen, Damir J. Djovic, Goran Krajoski, and Dario Farina. Virtual Grasping: Closed-Loop Force Control Using Electrotactile Feedback. *Computational and Mathematical Methods in Medicine*, 2014:1–13, 2014. pages 16
- [48] Bart J. Kane, Mark R. Cutkosky, and Gregory T.A. Kovacs. CMOS-compatible traction stress sensor for use in high-resolution tactile imaging. *Sensors and Actuators A: Physical*, 54(1-3):511–516, jun 1996. pages 16
- [49] Masoud Kalantari, Mohammadreza Ramezanifard, Roozbeh Ahmadi, Javad Dargahi, and József Kövecses. A piezoresistive tactile sensor for tissue characterization during catheter-based cardiac surgery. *The International Journal of Medical Robotics and Computer Assisted Surgery*, 7(4):431–440, dec 2011. pages 16
- [50] Risto Koiva, Matthias Zenker, Carsten Schurmann, Robert Haschke, and Helge J. Ritter. A highly sensitive 3D-shaped tactile sensor. In *2013 IEEE/ASME International Conference on Advanced Intelligent Mechatronics*, pages 1084–1089. IEEE, jul 2013. pages 16, 18, 19
- [51] H.B. Muhammad, C. Recchiuto, C.M. Oddo, L. Beccai, C.J. Anthony, M.J. Adams, M.C. Carrozza, and M.C.L. Ward. A capacitive tactile sensor array for surface texture discrimination. *Microelectronic Engineering*, 88(8):1811–1813, aug 2011. pages 16, 17
- [52] Liang Zou, Chang Ge, Z. Wang, Edmond Cretu, and Xiaoou Li. Novel Tactile Sensor Technology and Smart Tactile Sensing Systems: A Review. *Sensors*, 17(11):2653, nov 2017. pages 16
- [53] Yancheng Wang, Kailun Xi, Guanghao Liang, Meqing Mei, and Zichen Chen. A flexible capacitive tactile sensor array for prosthetic hand real-time contact force measurement. *2014 IEEE International Conference on Information and Automation, ICIA 2014*, 8(July):937–942, 2014. pages 16, 17, 111, 143

- [54] Mohsin I. Tiwana, Stephen J. Redmond, and Nigel H. Lovell. A review of tactile sensing technologies with applications in biomedical engineering. *Sensors and Actuators A: Physical*, 179:17–31, jun 2012. pages 17
- [55] Hong-Ki Kim, Seunggun Lee, and Kwang-Seok Yun. Capacitive tactile sensor array for touch screen application. *Sensors and Actuators A: Physical*, 165(1):2–7, jan 2011. pages 17
- [56] Hanna Yousef, Mehdi Boukallel, and Kaspar Althoefer. Tactile sensing for dexterous in-hand manipulation in robotics—A review. *Sensors and Actuators A: Physical*, 167(2):171–187, jun 2011. pages 17, 19
- [57] Huichan Zhao, Kevin O'Brien, Shuo Li, and Robert F. Shepherd. Optoelectronically innervated soft prosthetic hand via stretchable optical waveguides. *Science Robotics*, 1(1):eaai7529, dec 2016. pages 17
- [58] Shan Luo, Joao Bimbo, Ravinder Dahiya, and Hongbin Liu. Robotic tactile perception of object properties: A review. *Mechatronics*, 48(May):54–67, dec 2017. pages 17
- [59] S. J. Lederman and R. L. Klatzky. Haptic perception: A tutorial. *Attention, Perception & Psychophysics*, 71(7):1439–1459, oct 2009. pages 17, 26, 34, 137
- [60] Alin Drimus, Gert Kootstra, Arne Bilberg, and Danica Kragic. Design of a flexible tactile sensor for classification of rigid and deformable objects. *Robotics and Autonomous Systems*, 2014. pages 17, 19
- [61] Zhanat Kappasov, Juan-Antonio Corrales, and Véronique Perdereau. Tactile sensing in dexterous robot hands — Review. *Robotics and Autonomous Systems*, 74:195–220, dec 2015. pages 17, 19, 22, 29, 30, 111, 143
- [62] Gereon Buscher, Martin Meier, Guillaume Walck, Robert Haschke, and Helge J. Ritter. Augmenting curved robot surfaces with soft tactile skin. In *2015 IEEE/RSJ International Conference on Intelligent Robots and Systems (IROS)*, volume 2015-Decem, pages 1514–1519. IEEE, sep 2015. pages 18, 19
- [63] Danfei Xu, Gerald E. Loeb, and Jeremy A. Fishel. Tactile identification of objects using Bayesian exploration. In *2013 IEEE International Conference on Robotics and Automation*, pages 3056–3061. IEEE, may 2013. pages 18
- [64] Dirk Gögger, Nicolas Gorges, and Heinz Wörn. Tactile sensing for an anthropomorphic robotic hand: Hardware and signal processing. *Proceedings - IEEE International Conference on Robotics and Automation*, pages 895–901, 2009. pages 18
- [65] Byungjune Choi, Sanghun Lee, Hyouk Choi, and Sungchul Kang. Development of Anthropomorphic Robot Hand with Tactile Sensor : SKKU Hand II. In *2006 IEEE/RSJ International Conference on Intelligent Robots and Systems*, pages 3779–3784. IEEE, oct 2006. pages 18

- [66] Alexander Schmitz, Perla Maiolino, Marco Maggiali, Lorenzo Natale, Giorgio Cannata, and Giorgio Metta. Methods and Technologies for the Implementation of Large-Scale Robot Tactile Sensors. *IEEE Transactions on Robotics*, 27(3):389–400, jun 2011. pages 18, 22
- [67] Akio Namiki, Yoshiro Imai, Masatoshi Ishikawa, and Makoto Kaneko. Development of a high-speed multifingered hand system and its application to catching. In *Proceedings 2003 IEEE/RSJ International Conference on Intelligent Robots and Systems (IROS 2003) (Cat. No.03CH37453)*, volume 3, pages 2666–2671. IEEE, 2003. pages 18, 19
- [68] Hongbin Liu, Juan Greco, Xiaojing Song, Joao Bimbo, Lakmal Seneviratne, and Kaspar Althoefer. Tactile image based contact shape recognition using neural network. In *2012 IEEE International Conference on Multisensor Fusion and Integration for Intelligent Systems (MFI)*, pages 138–143. IEEE, sep 2012. pages 18, 19
- [69] Carlos Jara, Jorge Pomares, Francisco Candelas, and Fernando Torres. Control Framework for Dexterous Manipulation Using Dynamic Visual Servoing and Tactile Sensors' Feedback. *Sensors*, 14(1):1787–1804, jan 2014. pages 18, 19
- [70] G. Palli, C. Melchiorri, G. Vassura, U. Scarcia, L. Moriello, G. Berselli, A. Cavallo, G. De Maria, C. Natale, S. Pirozzi, C. May, F. Ficuciello, and B. Siciliano. The DEXMART hand: Mechatronic design and experimental evaluation of synergy-based control for human-like grasping. *The International Journal of Robotics Research*, 33(5):799–824, apr 2014. pages 19
- [71] Akihiko Yamaguchi and Christopher G. Atkeson. Recent progress in tactile sensing and sensors for robotic manipulation: can we turn tactile sensing into vision?1. *Advanced Robotics*, 1864, 2019. pages 19, 22
- [72] Andrew Masteller, Sriramana Sankar, Han Biehn Kim, Keqin Ding, Xiaogang Liu, and Angelo H. All. Recent Developments in Prosthesis Sensors, Texture Recognition, and Sensory Stimulation for Upper Limb Prostheses. *Annals of Biomedical Engineering*, 49(1):57–74, jan 2021. pages 19, 22, 23
- [73] Alexander Schmitz, Marco Maggiali, Lorenzo Natale, Bruno Bonino, and Giorgio Metta. A tactile sensor for the fingertips of the humanoid robot iCub. In *2010 IEEE/RSJ International Conference on Intelligent Robots and Systems*, pages 2212–2217. IEEE, oct 2010. pages 19
- [74] Hongbin Liu, Kien Cuong Nguyen, Véronique Perdereau, Joao Bimbo, Junghwan Back, Matthew Godden, Lakmal D. Seneviratne, and Kaspar Althoefer. Finger contact sensing and the application in dexterous hand manipulation. *Autonomous Robots*, 39(1):25–41, jun 2015. pages 19
- [75] "Dexterous Hand Series – Shadow Robot Company" [online]. available: <https://www.shadowrobot.com/dexterous-hand-series/> [accessed: 2021-10-02]. pages 19

- [76] Wataru Fukui, Futoshi Kobayashi, Fumio Kojima, Hiroyuki Nakamoto, Nobuaki Imamura, Tadashi Maeda, and Hidenori Shirasawa. High-Speed Tactile Sensing for Array-Type Tactile Sensor and Object Manipulation Based on Tactile Information. *Journal of Robotics*, 2011:1–9, 2011. pages 19
- [77] S. Schulz, C. Pylatiuk, A. Kargov, R. Oberle, and G. Bretthauer. Progress in the development of anthropomorphic fluidic hands for a humanoid robot. In *4th IEEE/RAS International Conference on Humanoid Robots, 2004.*, volume 2, pages 566–575. IEEE, 1969. pages 19
- [78] Caizhi Liao, Meng Zhang, Mei Yu Yao, Tao Hua, Li Li, and Feng Yan. Flexible Organic Electronics in Biology: Materials and Devices. *Advanced Materials*, 27(46):7493–7527, dec 2015. pages 19
- [79] Tetsuya Mouri, Haruhisa Kawasaki, Keisuke Yoshikawa, Jun Takai, and Satoshi Ito. Anthropomorphic Robot Hand : Gifu Hand III. *Proc. Int. Conf. ICCAS*, pages 1288–1293, 2002. pages 19
- [80] Giorgio Metta, Giulio Sandini, David Vernon, Lorenzo Natale, and Francesco Nori. The iCub humanoid robot. In *Proceedings of the 8th Workshop on Performance Metrics for Intelligent Systems - PerMIS '08*, page 50, New York, New York, USA, 2008. ACM Press. pages 19
- [81] Seiichi Teshigawara, Takahiro Tsutsumi, Satoru Shimizu, Yosuke Suzuki, Aiguo Ming, Masatoshi Ishikawa, and Makoto Shimojo. Highly sensitive sensor for detection of initial slip and its application in a multi-fingered robot hand. In *2011 IEEE International Conference on Robotics and Automation*, pages 1097–1102. IEEE, may 2011. pages 19
- [82] Barrett Heyneman and Mark R. Cutkosky. Biologically inspired tactile classification of object-hand and object-world interactions. In *2012 IEEE International Conference on Robotics and Biomimetics (ROBIO)*, pages 167–173. IEEE, dec 2012. pages 19
- [83] Liang-Ting Jiang and Joshua R. Smith. Seashell effect pretouch sensing for robotic grasping. In *2012 IEEE International Conference on Robotics and Automation*, pages 2851–2858. IEEE, may 2012. pages 20
- [84] "biotac syntouch company" [online]. available. <https://syntouchinc.com/resources/BioTAC>. [Accessed: 2021-04-17]. pages 20, 111
- [85] "Sensor fingers | WEISS ROBOTICS" [online]. available: <https://weiss-robotics.com/sensor-fingers/> [accessed: 2021-10-02]. pages 20
- [86] "Sensors for Pressure Mapping and Force Measurement | Tekscan" [online]. available: <https://www.tekscan.com/products-solutions/sensors> [accessed: 2021-10-02]. pages 20
- [87] "Peratech - Custom Force Sensing Solutions" [online]. available: <https://www.peratech.com/custom-force-sensing-solutions/> [accessed: 2021-10-02]. pages 20

- [88] "PPS Digitacts — PPS" [online]. available: <https://pressureprofile.com/sensors/digitacts> [accessed: 2021-10-02]. pages 20
- [89] Joseph L. Betthauser, Christopher L. Hunt, Luke E. Osborn, Matthew R. Masters, Gyorgy Levay, Rahul R. Kaliki, and Nitish V. Thakor. Limb Position Tolerant Pattern Recognition for Myoelectric Prosthesis Control with Adaptive Sparse Representations From Extreme Learning. *IEEE Transactions on Biomedical Engineering*, 65(4):770–778, apr 2018. pages 21
- [90] Anna Lisa Ciancio, Francesca Cordella, Roberto Barone, Rocco Antonio Romeo, Alberto Dellacasa Bellingegni, Rinaldo Sacchetti, Angelo Davalli, Giovanni Di Pino, Federico Ranieri, Vincenzo Di Lazzaro, Eugenio Guglielmelli, and Loredana Zollo. Control of prosthetic hands via the peripheral nervous system. *Frontiers in Neuroscience*, 10(APR):1–17, 2016. pages 21
- [91] Cheng Chi, Xuguang Sun, Ning Xue, Tong Li, and Chang Liu. Recent progress in technologies for tactile sensors. *Sensors (Switzerland)*, 18(4), 2018. pages 21
- [92] Mariam Turki Almansoori, Xuan Li, and Lianxi Zheng. A Brief Review on E-skin and its Multifunctional Sensing Applications. *Current Smart Materials*, 4(1):3–14, jul 2019. pages 21
- [93] Takao Someya, Tsuyoshi Sekitani, Shingo Iba, Yusaku Kato, Hiroshi Kawaguchi, and Takayasu Sakurai. A large-area, flexible pressure sensor matrix with organic field-effect transistors for artificial skin applications. *Proceedings of the National Academy of Sciences*, 101(27):9966–9970, jul 2004. pages 21
- [94] Leonardo Barboni, Ravinder S. Dahiya, Giorigio Metta, and Maurizio Valle. Interface electronics design for POSFET devices based tactile sensing systems. In *19th International Symposium in Robot and Human Interactive Communication*, pages 686–690. IEEE, sep 2010. pages 21
- [95] Maurizio Rossi, Matteo Nardello, Leandro Lorenzelli, and Davide Brunelli. Dual Mode Pressure Sensing for Lower-Limb Prosthetic Interface. *Proceedings*, 1(4):593, aug 2017. pages 21
- [96] Oscar Oballe-Peinado, Jose Antonio Hidalgo-Lopez, Julian Castellanos-Ramos, Jose Antonio Sanchez-Duran, Rafael Navas-Gonzalez, Jaime Herran, and Fernando Vidal-Verdu. FPGA-Based Tactile Sensor Suite Electronics for Real-Time Embedded Processing. *IEEE Transactions on Industrial Electronics*, 64(12):9657–9665, dec 2017. pages 21
- [97] Hendrik Kruger, Marian Rabe, Eric Ebert, Patrick Busch, Nils Andreas Damaschke, and Hartmut Ewald. A flexible measurement system for absorption spectrometry using LED light sources and a high accuracy two-channel ADC for simultaneous sampling. In *2015 9th International Conference on Sensing Technology (ICST)*, volume 2016-March, pages 652–655. IEEE, dec 2015. pages 22
- [98] V. Tyzhnevyyi, G F Dalla Betta, L. Rovati, G. Verzellesi, and N. Zorzi. BJT detector with FPGA-based read-out for alpha particle monitoring. *Journal of Instrumentation*, 6(01):C01051–C01051, jan 2011. pages 22

- [99] Elisabetta Farella, Augusto Pieracci, Davide Brunelli, Luca Benini, B. Ricco, and Andrea Acquaviva. Design and Implementation of WiMoCA Node for a Body Area Wireless Sensor Network. In *2005 Systems Communications (ICW'05, ICHSN'05, ICMCS'05, SENET'05)*, volume 2005, pages 342–347. IEEE, 2005. pages 22
- [100] Aiguo Song, Yezhen Han, Haihua Hu, and Jianqing Li. A Novel Texture Sensor for Fabric Texture Measurement and Classification. *IEEE Transactions on Instrumentation and Measurement*, 63(7):1739–1747, jul 2014. pages 23
- [101] Sungwoo Chun, Ahyoung Hong, Yeonhoi Choi, Chunho Ha, and Wanjun Park. A tactile sensor using a conductive graphene-sponge composite. *Nanoscale*, 8(17):9185–9192, 2016. pages 23
- [102] Yudong Cao, Tie Li, Yang Gu, Hui Luo, Shuqi Wang, and Ting Zhang. Fingerprint-Inspired Flexible Tactile Sensor for Accurately Discerning Surface Texture. *Small*, 14(16):1703902, apr 2018. pages 23
- [103] Longhui Qin, Zhengkun Yi, and Yilei Zhang. Enhanced surface roughness discrimination with optimized features from bio-inspired tactile sensor. *Sensors and Actuators A: Physical*, 264:133–140, sep 2017. pages 23
- [104] Samsul Ariffin Abdul Karim, Mohd Hafizi Kamarudin, Bakri Abdul Karim, Mohammad Khatim Hasan, and Jumat Sulaiman. Wavelet Transform and Fast Fourier Transform for signal compression: A comparative study. In *2011 International Conference on Electronic Devices, Systems and Applications (ICEDSA)*, pages 280–285. IEEE, apr 2011. pages 23
- [105] Florian De Boissieu, Christelle Godin, Christine Serviere, and Daniel Baudois. Tactile Texture Recognition with a 3-axial Force MEMS Integrated Artificial Finger. In *Robotics*, volume 5, pages 49–56. The MIT Press, 2010. pages 23
- [106] Ting Zhang, Li Jiang, and Hong Liu. Design and Functional Evaluation of a Dexterous Myoelectric Hand Prosthesis With Biomimetic Tactile Sensor. *IEEE Transactions on Neural Systems and Rehabilitation Engineering*, 26(7):1391–1399, jul 2018. pages 23
- [107] Roberta L. Klatzky and Susan J. Lederman. Touch. In *Handbook of Psychology*, volume 14, pages 147–176. John Wiley & Sons, Inc., Hoboken, NJ, USA, apr 2003. pages 24
- [108] J.G. Webster Kaczmarek, K.A.(Dept. of Electr. Eng., Wisconsin Univ., Madison, WI, USA) and USA) (Dept. of Electr. Eng., Wisconsin Univ., Madison, WI. Electrotactile and vibrotactile displays for sensory substitution systems. *IEEE Transactions on Biomedical Engineering (Volume: 38 , Issue:)*, 38(1):1–16, 1991. pages 24
- [109] Roger W. Cholewiak and Amy A. Collins. Vibrotactile localization on the arm: Effects of place, space, and age. *Perception & Psychophysics*, 65(7):1058–1077, oct 2003. pages 24

- [110] Mathis Fleury, Giulia Lioi, Christian Barillot, and Anatole Lécuyer. A Survey on the Use of Haptic Feedback for Brain-Computer Interfaces and Neurofeedback. *Frontiers in Neuroscience*, 14(June):1–16, jun 2020. pages 24, 25
- [111] J.L. Pons, E. Rocon, R. Ceres, D. Reynaerts, B. Saro, S. Levin, and W. Van Moorleghem. The MANUS-HAND Dextrous Robotics Upper Limb Prosthesis: Mechanical and Manipulation Aspects. *Autonomous Robots*, 16(2):143–163, mar 2004. pages 24
- [112] Artem Kargov, Oleg Ivlev, Christian Pylatiuk, Tamim Asfour, Stefan Schulz, Axel Graeser, Ruediger Dillmann, and Georg Bretthauer. Applications of a Fluidic Artificial Hand in the Field of Rehabilitation. In *Rehabilitation Robotics*, number August. I-Tech Education and Publishing, aug 2007. pages 24
- [113] Christian Antfolk, Christian Balkenius, Birgitta Rosén, Gran Lundborg, and Fredrik Sebelius. SmartHand tactile display: A new concept for providing sensory feedback in hand prostheses. *Journal of Plastic Surgery and Hand Surgery*, 44(1):50–53, 2010. pages 24
- [114] Lynette A. Jones and Nadine B. Sarter. Tactile Displays: Guidance for Their Design and Application. *Human Factors: The Journal of the Human Factors and Ergonomics Society*, 50(1):90–111, feb 2008. pages 25
- [115] Kurt A. Kaczmarek. Electrotactile adaptation on the abdomen: Preliminary results. *IEEE Transactions on Rehabilitation Engineering*, 8(4):499–505, 2000. pages 25
- [116] Ian R. Summers, Philip R. Dixon, Philip G. Cooper, Denise A. Gratton, Brian H. Brown, and John C. Stevens. Vibrotactile and electrotactile perception of time-varying pulse trains. *The Journal of the Acoustical Society of America*, 95(3):1548–1558, mar 1994. pages 25
- [117] K.A. Kaczmarek and S.J. Haase. Pattern identification as a function of stimulation on a fingertip-scanned electrotactile display. *IEEE Transactions on Neural Systems and Rehabilitation Engineering*, 11(3):269–275, sep 2003. pages 25
- [118] Katrin Wolf and Timm Bäder. Illusion of Surface Changes Induced by Tactile and Visual Touch Feedback. In *Proceedings of the 33rd Annual ACM Conference Extended Abstracts on Human Factors in Computing Systems*, volume 18, pages 1355–1360, New York, NY, USA, apr 2015. ACM. pages 25
- [119] Aadeel Akhtar, Mary Nguyen, Logan Wan, Brandon Boyce, Patrick Slade, and Timothy Bretl. Passive Mechanical Skin Stretch for Multiple Degree-of-Freedom Proprioception in a Hand Prosthesis. In *Lecture Notes in Computer Science (including subseries Lecture Notes in Artificial Intelligence and Lecture Notes in Bioinformatics)*, volume 8619, pages 120–128. Springer Verlag, 2014. pages 25
- [120] Thomas Massie. The PHANToM Haptic Interface: A Device for Probing Virtual Objects. *Engineering*, 1994. pages 25

- [121] Ioannis Sarakoglou, Nadia Garcia-Hernandez, Nikos G. Tsagarakis, and Darwin G. Caldwell. A High Performance Tactile Feedback Display and Its Integration in Teleoperation. *IEEE Transactions on Haptics*, 5(3):252–263, 2012. pages 25, 142
- [122] E. López-Larraz, A. Sarasola-Sanz, N. Irastorza-Landa, N. Birbaumer, and A. Ramos-Murguialday. Brain-machine interfaces for rehabilitation in stroke: A review. *NeuroRehabilitation*, 43(1):77–97, 2018. pages 25
- [123] Ravinder Dahiya, Nivasan Yogeswaran, Fengyuan Liu, Libu Manjakkal, Etienne Burdet, Vincent Hayward, and Henrik Jorntell. Large-Area Soft e-Skin: The Challenges Beyond Sensor Designs. *Proceedings of the IEEE*, 107(10):2016–2033, oct 2019. pages 26, 168
- [124] Z. Stojiljkovic and J. Clot. Integrated Behavior of Artificial Skin. *IEEE Transactions on Biomedical Engineering*, BME-24(4):396–399, jul 1977. pages 26
- [125] Laurent Misery. Sensitive Skin. In *Pruritus*, volume 1, pages 127–129. Springer International Publishing, Cham, 2016. pages 26
- [126] Heather Culbertson, Samuel B. Schorr, and Allison M. Okamura. Haptics: The Present and Future of Artificial Touch Sensation. *Annual Review of Control, Robotics, and Autonomous Systems*, 1(1):385–409, may 2018. pages 26
- [127] Carlos García Núñez, William Taube Navaraj, Emre O. Polat, and Ravinder Dahiya. Energy-Autonomous, Flexible, and Transparent Tactile Skin. *Advanced Functional Materials*, 27(18):1606287, may 2017. pages 26
- [128] P. Mittendorfer, E. Yoshida, and G. Cheng. Realizing whole-body tactile interactions with a self-organizing, multi-modal artificial skin on a humanoid robot. *Advanced Robotics*, 29(1):51–67, jan 2015. pages 26
- [129] Ravinder Dahiya. E-Skin: From Humanoids to Humans [Point of View]. *Proceedings of the IEEE*, 107(2):247–252, feb 2019. pages 26
- [130] Wenting Dang, Libu Manjakkal, William Taube Navaraj, Leandro Lorenzelli, Vincenzo Vinciguerra, and Ravinder Dahiya. Stretchable wireless system for sweat pH monitoring. *Biosensors and Bioelectronics*, 107(February):192–202, jun 2018. pages 26
- [131] D.-H. Kim, N. Lu, R. Ma, Y.-S. Kim, R.-H. Kim, S. Wang, J. Wu, S. M. Won, H. Tao, A. Islam, K. J. Yu, T.-i. Kim, R. Chowdhury, M. Ying, L. Xu, M. Li, H.-J. Chung, Hohyun Keum, M. McCormick, Ping Liu, Y.-W. Zhang, Fiorenzo G Omenetto, Y. Huang, T. Coleman, and J. A. Rogers. Epidermal Electronics. *Science*, 333(6044):838–843, aug 2011. pages 26, 143
- [132] Ravinder S. Dahiya, Philipp Mittendorfer, Maurizio Valle, Gordon Cheng, and Vladimir J. Lumelsky. Directions Toward Effective Utilization of Tactile Skin: A Review. *IEEE Sensors Journal*, 13(11):4121–4138, nov 2013. pages 26, 167, 188
- [133] Paul Bach-y Rita and Stephen W. Kercel. Sensory substitution and the human-machine interface. *Trends in Cognitive Sciences*, 7(12):541–546, dec 2003. pages 27, 141

- [134] Panagiotis Kourtesis, Ferran Argelaguet, Sebastian Vizcay, Maud Marchal, and Claudio Pacchierotti. Electrotactile feedback for hand interactions: A systematic review, meta-analysis, and future directions. pages 1–15, may 2021. pages 141
- [135] Pamela Svensson, Ulrika Wijk, Anders Björkman, and Christian Antfolk. A review of invasive and non-invasive sensory feedback in upper limb prostheses. *Expert Review of Medical Devices*, 14(6):439–447, jun 2017. pages 110, 113, 142
- [136] Jonathon W Sensinger and Strahinja Dosen. A Review of Sensory Feedback in Upper-Limb Prostheses From the Perspective of Human Motor Control. *Frontiers in Neuroscience*, 14(June):1–24, jun 2020. pages 27, 110, 142
- [137] Lucia Seminara, Marco Capurro, and Maurizio Valle. Tactile data processing method for the reconstruction of contact force distributions. *Mechatronics*, 27:28–37, 2015. pages 29
- [138] Wojciech Wasko, Alessandro Albini, Perla Maiolino, Fulvio Mastrogiovanni, and Giorgio Cannata. Contact modelling and tactile data processing for robot skins. *Sensors (Switzerland)*, 19(4):1–25, 2019. pages 29
- [139] Jeremy A. Fishel and Gerald E. Loeb. Bayesian Exploration for Intelligent Identification of Textures. *Frontiers in Neurorobotics*, 6(JUNE):1–20, 2012. pages 29
- [140] Nawid Jamali, Carlo Ciliberto, Lorenzo Rosasco, and Lorenzo Natale. Active perception: Building objects’ models using tactile exploration. In *2016 IEEE-RAS 16th International Conference on Humanoid Robots (Humanoids)*, pages 179–185. IEEE, nov 2016. pages 29
- [141] P. Gastaldo, L. Pinna, L. Seminara, M. Valle, and R. Zunino. A tensor-based approach to touch modality classification by using machine learning. *Robotics and Autonomous Systems*, 63(P3):268–278, jan 2015. pages 29
- [142] Barbara Stadlober, Martin Zirkel, and Mihai Irimia-Vladu. Route towards sustainable smart sensors: ferroelectric polyvinylidene fluoride-based materials and their integration in flexible electronics. *Chemical Society Reviews*, 48(6):1787–1825, 2019. pages 29, 30, 34, 41, 54
- [143] P.P.L. Regtien. Sensors for applications in robotics. *Sensors and Actuators*, 10(3-4):195–218, nov 1986. pages 30
- [144] Saleem Khan, Sajina Tinku, Leandro Lorenzelli, and Ravinder S. Dahiya. Flexible Tactile Sensors Using Screen-Printed P(VDF-TrFE) and MWCNT/PDMS Composites. *IEEE Sensors Journal*, 15(6):3146–3155, jun 2015. pages 30
- [145] Yu-Jen Hsu, Zhang Jia, and Ioannis Kyriassis. A Locally Amplified Strain Sensor Based on a Piezoelectric Polymer and Organic Field-Effect Transistors. *IEEE Transactions on Electron Devices*, 58(3):910–917, mar 2011. pages 30, 55

- [146] Nguyen Thanh Tien, Sanghun Jeon, Do-Il Kim, Tran Quang Trung, Mi Jang, Byeong-Ung Hwang, Kyung-Eun Byun, Jihyun Bae, Eunha Lee, Jeffrey B.H. Tok, Zhenan Bao, Nae-Eung Lee, and Jong-Jin Park. A Flexible Bimodal Sensor Array for Simultaneous Sensing of Pressure and Temperature. *Advanced Materials*, 26(5):796–804, feb 2014. pages 30
- [147] Beatrix Ploss, Bernd Ploss, F. G. Shin, H. L. W. Chan, and C. L. Choy. Pyroelectric or piezoelectric compensated ferroelectric composites. *Applied Physics Letters*, 76(19):2776–2778, may 2000. pages 30
- [148] Xiaomei Wang, Fazhe Sun, Guangchao Yin, Yuting Wang, Bo Liu, and Mingdong Dong. Tactile-Sensing Based on Flexible PVDF Nanofibers via Electrospinning: A Review. *Sensors*, 18(2):330, jan 2018. pages 30
- [149] Yi Xin, Hongying Tian, Chao Guo, Xiang Li, Hongshuai Sun, Peiyuan Wang, Jun Lin, Shuhong Wang, and Cheng Wang. PVDF tactile sensors for detecting contact force and slip: A review. *Ferroelectrics*, 504(1):31–45, nov 2016. pages 31
- [150] H. Fares, L. Seminara, L. Pinna, M. Valle, J. Groten, M. Hammer, M. Zirkl, and B. Stadlober. Screen Printed Tactile Sensing Arrays for Prosthetic Applications. In *2018 IEEE International Symposium on Circuits and Systems (ISCAS)*, volume 2018-May, pages 1–4. IEEE, 2018. pages 31, 65
- [151] Lucia Seminara. Modeling Electronic Skin Response to Normal Distributed Force. *Sensors*, 18(2):459, feb 2018. pages 32, 36, 41, 42, 47, 63
- [152] Hoda Fares, Yahya Abbass, Maurizio Valle, and Lucia Seminara. Validation of Screen - printed Electronic Skin Based on Piezoelectric Polymer Sensors. *Sensors (Basel, Switzerland)*, 20(4):26, 2020. pages 32
- [153] "Startseite | JOANNEUM RESEARCH" [online]. available: <https://www.joanneum.at/> [accessed: 2021-03-24]. pages 32
- [154] Martin Zirkl, Anurak Sawatdee, Uta Helbig, Markus Krause, Gregor Scheipl, Elke Kraker, Peter Andersson Ersman, David Nilsson, Duncan Platt, Peter Bodö, Siegfried Bauer, Gerhard Domann, and Barbara Stadlober. An all-printed ferroelectric active matrix sensor network based on only five functional materials forming a touchless control interface. *Advanced Materials*, 23(18):2069–2074, 2011. pages 33, 57, 115
- [155] EP2431404A1 - Solution or suspension containing fluoropolymer, method for producing same and use of same in the production of piezoelectric and pyroelectric coatings - Google Patents. pages 33, 34, 39, 41
- [156] LUIGI PINNA and MAURIZIO VALLE. CHARGE AMPLIFIER DESIGN METHODOLOGY FOR PVDF-BASED TACTILE SENSORS. *Journal of Circuits, Systems and Computers*, 22(08):1350066, sep 2013. pages 40, 67
- [157] Alexi Charalambides and Sarah Bergbreiter. A novel all-elastomer MEMS tactile sensor for high dynamic range shear and normal force sensing. *Journal of Micromechanics and Microengineering*, 25(9), 2015. pages 65

- [158] Byungjune Choi, Hyouk Ryeol Choi, and Sungchul Kang. Development of tactile sensor for detecting contact force and slip. In *2005 IEEE/RSJ International Conference on Intelligent Robots and Systems*, pages 2638–2643. IEEE, 2005. pages 65
- [159] Ravinder S. Dahiya, Andrea Adami, Cristian Collini, Maurizio Valle, and Leandro Lorenzelli. POSFET tactile sensing chips using CMOS technology. In *2013 IEEE SENSORS*, pages 1–4. IEEE, nov 2013. pages 65
- [160] Moustafa Saleh, Ali Ibrahim, Flavio Ansovini, Yasser Mohanna, and Maurizio Valle. Low Power Electronic System for Tactile Sensory Feedback for Prosthetics. *Journal of Low Power Electronics*, 15(1):95–103, mar 2019. pages 66, 67, 68, 70
- [161] Moustafa Saleh, Yahya Abbass, Ali Ibrahim, and Maurizio Valle. Experimental Assessment of the Interface Electronic System for PVDF-Based Piezoelectric Tactile Sensors. *Sensors (Switzerland)*, 19(20):1–12, 2019. pages 66
- [162] Merve Acer, Marco Salerno, Kossi Agbeviade, and Jamie Paik. Development and characterization of silicone embedded distributed piezoelectric sensors for contact detection. *Smart Materials and Structures*, 24(7):075030, jul 2015. pages 67
- [163] Ping Yu, Weiting Liu, Chunxin Gu, Xiaoying Cheng, and Xin Fu. Flexible Piezo-electric Tactile Sensor Array for Dynamic Three-Axis Force Measurement. *Sensors*, 16(6):819, jun 2016. pages 67
- [164] Ali Ibrahim, Luigi Pinna, and Maurizio Valle. Experimental characterization of dedicated front-end electronics for piezoelectric tactile sensing arrays. *Integration*, 63(December 2017):266–272, sep 2018. pages 68, 79
- [165] Lucia Seminara, Luigi Pinna, Marco Capurro, and Maurizio Valle. A Tactile Sensing System Based on Arrays of Piezoelectric Polymer Transducers. In *Smart Actuation and Sensing Systems - Recent Advances and Future Challenges*. InTech, oct 2012. pages 70
- [166] Stefan C. B. Mannsfeld, Benjamin C.K. Tee, Randall M. Stoltenberg, Christopher V. H-H. Chen, Soumendra Barman, Beinn V. O. Muir, Anatoliy N. Sokolov, Colin Reese, and Zhenan Bao. Highly sensitive flexible pressure sensors with microstructured rubber dielectric layers. *Nature Materials*, 9(10):859–864, oct 2010. pages 70
- [167] "Current-Input Analog-to-Digital Converter" [online]. available: <https://www.ti.com/lit/ds/symlink/ddc232.pdf> [accessed: 2021-03-24]. pages 71, 76
- [168] Waveform Generation Measurement and Analysis Technical. *IEEE Standard for Terminology and Test Methods for Analog-to-Digital IEEE Instrumentation & Measurement Society*, volume 2010. 2011. pages 79
- [169] "Analog devices" [online]. available: <https://www.analog.com/media/en/training-seminars/tutorials/MT-003.pdf> [accessed: 2021-03-24]. pages 80

- [170] Steven W. Smith. Moving Average Filters. In *Digital Signal Processing*, pages 277–284. Elsevier, 2003. pages 105
- [171] "Kontakt | Vincent Systems" [online]. available: <https://www.vincentssystems.de/kontakt> [accessed: 2021-03-27]. pages 109
- [172] Mohammadreza Asghari Oskoei and Huosheng Hu. Myoelectric control systems—A survey. *Biomedical Signal Processing and Control*, 2(4):275–294, oct 2007. pages 109
- [173] Stefan Salminger, Heiko Stino, Lukas H. Pichler, Clemens Gstoettner, Agnes Sturma, Johannes A. Mayer, Michael Szivak, and Oskar C. Aszmann. Current rates of prosthetic usage in upper-limb amputees – have innovations had an impact on device acceptance? *Disability and Rehabilitation*, 0(0):1–12, dec 2020. pages 109
- [174] Katherine R. Schoepp, Michael R. Dawson, Jonathon S. Schofield, Jason P. Carey, and Jacqueline S. Hebert. Design and Integration of an Inexpensive Wearable Mechanotactile Feedback System for Myoelectric Prostheses. *IEEE Journal of Translational Engineering in Health and Medicine*, 6(April):1–11, 2018. pages 110, 112
- [175] Cristian Pasluosta, Patrick Kiele, and Thomas Stieglitz. Paradigms for restoration of somatosensory feedback via stimulation of the peripheral nervous system. *Clinical Neurophysiology*, 129(4):851–862, apr 2018. pages 110
- [176] Sliman J. Bensmaia, Dustin J. Tyler, and Silvestro Micera. Restoration of sensory information via bionic hands. *Nature Biomedical Engineering*, nov 2020. pages 110, 142
- [177] Dario Farina, Ivan Vujaklija, Rickard Brånemark, Anthony M. J. Bull, Hans Dietl, Bernhard Graimann, Levi J. Hargrove, Klaus-Peter Hoffmann, He (Helen) Huang, Thorvaldur Ingvarsson, Hilmar Bragi Janusson, Kristleifur Kristjánsson, Todd Kuiken, Silvestro Micera, Thomas Stieglitz, Agnes Sturma, Dustin Tyler, Richard F. ff. Weir, and Oskar C. Aszmann. Toward higher-performance bionic limbs for wider clinical use. *Nature Biomedical Engineering*, pages 1–13, may 2021. pages 110, 142, 165
- [178] Christian Antfolk, Marco D’Alonzo, Birgitta Rosén, Göran Lundborg, Fredrik Sebelius, and Christian Cipriani. Sensory feedback in upper limb prosthetics. *Expert Review of Medical Devices*, 10(1):45–54, jan 2013. pages 110, 142
- [179] Matteo Rossi, Matteo Bianchi, Edoardo Battaglia, Manuel G. Catalano, and Antonio Bicchi. HapPro: A Wearable Haptic Device for Proprioceptive Feedback. *IEEE Transactions on Biomedical Engineering*, 66(1):138–149, jan 2019. pages 110
- [180] Edoardo D’Anna, Giacomo Valle, Alberto Mazzoni, Ivo Strauss, Francesco Iberite, Jérémy Patton, Francesco M. Petrini, Stanisa Raspopovic, Giuseppe Granata, Riccardo Di Iorio, Marco Controzzi, Christian Cipriani, Thomas Stieglitz, Paolo M. Rossini, and Silvestro Micera. A closed-loop hand prosthesis with simultaneous

- intraneural tactile and position feedback. *Science Robotics*, 4(27):eaau8892, feb 2019. pages 110
- [181] Gauravkumar K Patel, Strahinja Dosen, Claudio Castellini, and Dario Farina. Multichannel electrotactile feedback for simultaneous and proportional myoelectric control. *Journal of Neural Engineering*, 13(5):056015, oct 2016. pages 110
- [182] Patrick G. Sagastegui Alva, Silvia Muceli, S Farokh Atashzar, Lucie William, and Dario Farina. Wearable multichannel haptic device for encoding proprioception in the upper limb. *Journal of Neural Engineering*, 17(5):056035, oct 2020. pages 110
- [183] Jonathon S. Schofield, Courtney E. Shell, Dylan T. Beckler, Zachary C. Thumser, and Paul D. Marasco. Long-Term Home-Use of Sensory-Motor-Integrated Bidirectional Bionic Prosthetic Arms Promotes Functional, Perceptual, and Cognitive Changes. *Frontiers in Neuroscience*, 14(February):1–20, feb 2020. pages 110
- [184] Tsuyoshi Sekitani and Takao Someya. Stretchable, Large-area Organic Electronics. *Advanced Materials*, 22(20):2228–2246, may 2010. pages 111, 143
- [185] Takao Someya, Yusaku Kato, Tsuyoshi Sekitani, Shingo Iba, Yoshiaki Noguchi, Yousuke Murase, Hiroshi Kawaguchi, and Takayasu Sakurai. Conformable, flexible, large-area networks of pressure and thermal sensors with organic transistor active matrixes. *Proceedings of the National Academy of Sciences*, 102(35):12321–12325, aug 2005. pages
- [186] Nicholas Wettels, Veronica J. Santos, Roland S. Johansson, and Gerald E. Loeb. Biomimetic Tactile Sensor Array. *Advanced Robotics*, 22(8):829–849, jan 2008. pages 143
- [187] Y.-J. Yang, M.-Y. Cheng, W.-Y. Chang, L.-C. Tsao, S.-A. Yang, W.-P. Shih, F.-Y. Chang, S.-H. Chang, and K.-C. Fan. An integrated flexible temperature and tactile sensing array using PI-copper films. *Sensors and Actuators A: Physical*, 143(1):143–153, may 2008. pages
- [188] Sohyun Kim, Hyunho Shin, Kahye Song, and Youngsu Cha. Flexible piezoelectric sensor array for touch sensing of robot hand. *2019 16th International Conference on Ubiquitous Robots, UR 2019*, pages 21–25, 2019. pages 111, 143
- [189] Luke Osborn, Rahul R. Kaliki, Alcimar B. Soares, and Nitish V. Thakor. Neuromimetic Event-Based Detection for Closed-Loop Tactile Feedback Control of Upper Limb Prostheses. *IEEE Transactions on Haptics*, 9(2):196–206, 2016. pages 111, 143
- [190] A. Cranny, D. P.J. Cotton, P. H. Chappell, S. P. Beeby, and N. M. White. Thick-film force and slip sensors for a prosthetic hand. *Sensors and Actuators, A: Physical*, 123-124:162–171, 2005. pages

- [191] Talha Agcayazi, Michael McKnight, Peter Sotory, Helen Huang, Tushar Ghosh, and Alper Bozkurt. A scalable shear and normal force sensor for prosthetic sensing. In *2017 IEEE SENSORS*, volume 2017-Decem, pages 1–3. IEEE, oct 2017. pages 111, 143
- [192] Matija Štrbac, Minja Belić, Milica Isaković, Vladimir Kojić, Goran Bijelić, Igor Popović, Milutin Radotić, Strahinja Došen, Marko Marković, Dario Farina, and Thierry Keller. Integrated and flexible multichannel interface for electrotactile stimulation. *Journal of Neural Engineering*, 13(4):046014, aug 2016. pages 111, 120, 136, 143
- [193] Strahinja Dosen, Marko Markovic, Matija Strbac, Minja Belic, Vladimir Kojic, Goran Bijelic, Thierry Keller, and Dario Farina. Multichannel electrotactile feedback with spatial and mixed coding for closed-loop control of grasping force in hand prostheses. *IEEE Transactions on Neural Systems and Rehabilitation Engineering*, 25(3):183–195, 2017. pages 111
- [194] Martin A. Garenfeld, Christian K. Mortensen, Matija Strbac, Jakob L. Dideriksen, and Strahinja Dosen. Amplitude versus spatially modulated electrotactile feedback for myoelectric control of two degrees of freedom. *Journal of Neural Engineering*, 17(4):046034, aug 2020. pages 111
- [195] Marta Franceschi, Lucia Seminara, Strahinja Dosen, Matija Strbac, Maurizio Valle, and Dario Farina. A System for Electrotactile Feedback Using Electronic Skin and Flexible Matrix Electrodes: Experimental Evaluation. *IEEE Transactions on Haptics*, 10(2):162–172, 2017. pages 111, 168
- [196] C. Hartmann, J. Linde, S. Dosen, D. Farina, L. Seminara, L. Pinna, M. Valle, and M. Capurro. Towards prosthetic systems providing comprehensive tactile feedback for utility and embodiment. *IEEE 2014 Biomedical Circuits and Systems Conference, BioCAS 2014 - Proceedings*, pages 620–623, 2014. pages 111
- [197] G. F. Shannon. A myoelectrically-controlled prosthesis with sensory feedback. *Medical & Biological Engineering & Computing*, 17(1):73–80, 1979. pages 112
- [198] S. LINDBERG G. LUNDBORG, B. ROSÉN, K. LINDSTRÖM. Artificial sensibility based on the use of piezoresistive sensors - Preliminary observations. *Journal of Hand Surgery*, 23(5):620–626, 1988. pages
- [199] D Pamungkas and K Ward. Electro-tactile feedback system for a prosthetic hand. *22nd Annual International Conference on Mechatronics and Machine Vision in Practice, M2VIP 2015*, pages 27–38, 2015. pages
- [200] Shaona Cheng, Andong Yi, U. Xuan Tan, and Dingguo Zhang. Closed-Loop System for Myoelectric Hand Control Based on Electrotactile Stimulation. *ICARM 2018 - 2018 3rd International Conference on Advanced Robotics and Mechatronics*, pages 486–490, 2019. pages 112, 137
- [201] Nader Fallahian, Hassan Saeedi, Hamidreza Mokhtarinia, and Farhad Tabatabai Ghomshe. Sensory feedback add-on for upper-limb prostheses. *Prosthetics and Orthotics International*, 41(3):314–317, jun 2017. pages 112

- [202] Christian Antfolk. A tactile display system for hand prostheses to discriminate pressure and individual finger localization. *Journal of Medical and Biological Engineering*, 30(6):355, 2010. pages 112
- [203] Aniruddha Chatterjee, Pravin Chaubey, Jay Martin, and Nitish Thakor. Testing a prosthetic haptic feedback simulator with an interactive force matching task. *Journal of Prosthetics and Orthotics*, 20(2):27–34, 2008. pages 112
- [204] Teri Rosenbaum-Chou, Wayne Daly, Ray Austin, Pravin Chaubey, and David A. Boone. Development and Real World Use of a Vibratory Haptic Feedback System for Upper-Limb Prosthetic Users. *Journal of Prosthetics and Orthotics*, 28(4):136–144, oct 2016. pages
- [205] Christian Pylatiuk, Artem Kargov, and Stefan Schulz. Design and evaluation of a low-cost force feedback system for myoelectric prosthetic hands. *Journal of Prosthetics and Orthotics*, 18(2):57–61, 2006. pages
- [206] Hiroshi Yamada, Yusuke Yamanoi, Ko Wakita, and Ryu Kato. Investigation of a cognitive strain on hand grasping induced by sensory feedback for myoelectric hand. *Proceedings - IEEE International Conference on Robotics and Automation*, 2016-June:3549–3554, 2016. pages 112
- [207] Huaiqi Huang, Tao Li, Claudio Bruschini, Christian Enz, Jorn Justiz, Christian Antfolk, and Volker M. Koch. Multi-modal Sensory Feedback System for Upper Limb Amputees. In *2017 New Generation of CAS (NGCAS)*, pages 193–196. IEEE, sep 2017. pages 112
- [208] Philipp Beckerle, Risto Kõiva, Elsa Andrea Kirchner, Robin Bekrater-Bodmann, Strahinja Dosen, Oliver Christ, David A. Abbink, Claudio Castellini, and Bigna Lenggenhager. Feel-Good Robotics: Requirements on Touch for Embodiment in Assistive Robotics. *Frontiers in Neurorobotics*, 12(December):1–7, dec 2018. pages 112, 135
- [209] Katie Z. Zhuang, Nicolas Sommer, Vincent Mendez, Saurav Aryan, Emanuele Formento, Edoardo D’Anna, Fiorenzo Artoni, Francesco Petrini, Giuseppe Granata, Giovanni Cannaviello, Wassim Raffoul, Aude Billard, and Silvestro Micera. Shared human–robot proportional control of a dexterous myoelectric prosthesis. *Nature Machine Intelligence*, 1(9):400–411, sep 2019. pages 112
- [210] Y Abbass, M Saleh, A Ibrahim, and M Valle. Embedded Feedback System for Upper Limb Prosthetics. In *2020 27th IEEE International Conference on Electronics, Circuits and Systems (ICECS)*, pages 1–4. IEEE, nov 2020. pages 113, 143
- [211] Yahya Abbass, Moustafa Saleh, Strahinja Dosen, and Maurizio Valle. Embedded Electrotactile Feedback System for Hand Prostheses using Matrix Electrode and Electronic Skin. *IEEE Transactions on Biomedical Circuits and Systems*, XX(X):1–1, 2021. pages 114, 143, 164
- [212] "Smartex srl" [online]. available: <http://www.smartex.it/en/our-products> [accessed: 2021-03-27]. pages 119

- [213] Moshe Solomonow, John Lyman, and Amos Freedy. Electrotactile two-point discrimination as a function of frequency, body site, laterality, and stimulation codes. *Annals of Biomedical Engineering*, 5(1):47–60, mar 1977. pages 121
- [214] George A. Gescheider. *Psychophysics*. Psychology Press, New York, jun 2013. pages 126, 158
- [215] Martin A. Garenfeld, Nikola Jorgovanovic, Vojin Ilic, Matija Strbac, Milica Isakovic, Jakob L. Dideriksen, and Strahinja Dosen. A compact system for simultaneous stimulation and recording for closed-loop myoelectric control. *Journal of NeuroEngineering and Rehabilitation*, 18(1):87, dec 2021. pages 134, 165
- [216] Loredana Zollo, Giovanni Di Pino, Anna L. Ciancio, Federico Ranieri, Francesca Cordella, Cosimo Gentile, Emiliano Noce, Rocco A. Romeo, Alberto Dellacasa Bellingegni, Gianluca Vadalà, Sandra Miccinilli, Alessandro Mioli, Lorenzo Diaz-Balzani, Marco Bravi, Klaus-P. Hoffmann, Andreas Schneider, Luca Denaro, Angelo Davalli, Emanuele Gruppioni, Rinaldo Sacchetti, Simona Castellano, Vincenzo Di Lazzaro, Silvia Sterzi, Vincenzo Denaro, and Eugenio Guglielmelli. Restoring tactile sensations via neural interfaces for real-time force-and-slippage closed-loop control of bionic hands. *Science Robotics*, 4(27):eaau9924, feb 2019. pages 135, 164
- [217] Lucia Seminara, Hoda Fares, Marta Franceschi, Maurizio Valle, Matija Strbac, Dario Farina, and Strahinja Dosen. Dual-parameter modulation improves stimulus localization in multichannel electrotactile stimulation. *IEEE Transactions on Haptics*, 1412(c):1–12, 2019. pages 136
- [218] Minja Perovic, Marija Stevanovic, Tijana Jevtic, Matija Strbac, Goran Bijelic, Cedomir Vucetic, Lana Popovic-Maneski, and Dejan Popovic. Electrical stimulation of the forearm: A method for transmitting sensory signals from the artificial hand to the brain. *Journal of Automatic Control*, 21(1):13–18, 2013. pages 136
- [219] E. P. Gardner and C. I. Palmer. Simulation of motion on the skin. II. Cutaneous mechanoreceptor coding of the width and texture of bar patterns displaced across the OPTACON. *Journal of Neurophysiology*, 62(6):1437–1460, dec 1989. pages 136
- [220] E. P. Gardner and B. F. Sklar. Discrimination of the direction of motion on the human hand: a psychophysical study of stimulation parameters. *Journal of Neurophysiology*, 71(6):2414–2429, jun 1994. pages 136
- [221] Sriramana Sankar, Darshini Balamurugan, Alisa Brown, Keqin Ding, Xingyuan Xu, Jin Huat Low, Chen Hua Yeow, and Nitish Thakor. Texture Discrimination with a Soft Biomimetic Finger Using a Flexible Neuromorphic Tactile Sensor Array That Provides Sensory Feedback. *Soft Robotics*, 00(00):soro.2020.0016, sep 2020. pages 137
- [222] S. C. Gandevia and G. Macefield. Projection of low-threshold afferents from human intercostal muscles to the cerebral cortex. *Respiration Physiology*, 77(2):203–214, 1989. pages 137

- [223] Mohammad Aziziaghdam and Evren Samur. Real-Time Contact Sensory Feedback for Upper Limb Robotic Prostheses. *IEEE/ASME Transactions on Mechatronics*, 22(4):1786–1795, aug 2017. pages 137
- [224] Edoardo D’Anna, Francesco M. Petrini, Fiorenzo Artoni, Igor Popovic, Igor Simanić, Stanisa Raspopovic, and Silvestro Micera. A somatotopic bidirectional hand prosthesis with transcutaneous electrical nerve stimulation based sensory feedback. *Scientific Reports*, 7(1):10930, dec 2017. pages 137
- [225] Breanne P. Christie, Emily L. Graczyk, Hamid Charkhkar, Dustin J. Tyler, and Ronald J. Triolo. Visuotactile synchrony of stimulation-induced sensation and natural somatosensation. *Journal of Neural Engineering*, 16(3):036025, jun 2019. pages 137
- [226] Zhou MA and Pinhas Ben-Tzvi. RML Glove—An Exoskeleton Glove Mechanism With Haptics Feedback. *IEEE/ASME Transactions on Mechatronics*, 20(2):641–652, apr 2015. pages 142
- [227] C. Mavroidis, C. Pfeiffer, J. Celestino, and Y. Bar-Cohen. Design and Modeling of an Electro-Rheological Fluid Based Haptic Interface. In *Volume 7A: 26th Biennial Mechanisms and Robotics Conference*, pages 653–660. American Society of Mechanical Engineers, sep 2000. pages
- [228] Jonathan Blake and H.B. Gurocak. Haptic Glove With MR Brakes for Virtual Reality. *IEEE/ASME Transactions on Mechatronics*, 14(5):606–615, oct 2009. pages
- [229] Andrew Erwin, Marcia K. O’Malley, David Ress, and Fabrizio Sergi. Kinesthetic Feedback During 2DOF Wrist Movements via a Novel MR-Compatible Robot. *IEEE Transactions on Neural Systems and Rehabilitation Engineering*, 25(9):1489–1499, sep 2017. pages
- [230] Bukun Son and Jaeyoung Park. Haptic Feedback to the Palm and Fingers for Improved Tactile Perception of Large Objects. In *Proceedings of the 31st Annual ACM Symposium on User Interface Software and Technology*, pages 757–763, New York, NY, USA, oct 2018. ACM. pages
- [231] Inseong Jo, Yeongyu Park, Hyeonjun Kim, and Joonbum Bae. Evaluation of a Wearable Hand Kinesthetic Feedback System for Virtual Reality: Psychophysical and User Experience Evaluation. *IEEE Transactions on Human-Machine Systems*, 49(5):430–439, oct 2019. pages 142
- [232] Dan Margineanu, Erwin-Christian Lovasz, Corina Mihaela Gruescu, Valentin Ciupe, and Santra Tatar. 5 DoF Haptic Exoskeleton for Space Telerobotics – Shoulder Module. In *Mechanisms and Machine Science*, volume 52, pages 111–120. Springer Netherlands, 2018. pages 142
- [233] Ryan E. Schoonmaker and Caroline G.L. Cao. Vibrotactile force feedback system for minimally invasive surgical procedures. In *2006 IEEE International Conference on Systems, Man and Cybernetics*, volume 3, pages 2464–2469. IEEE, oct 2006. pages 142

- [234] Aaron Bloomfield and Norman I. Badler. Virtual Training via Vibrotactile Arrays. *Presence: Teleoperators and Virtual Environments*, 17(2):103–120, apr 2008. pages 142
- [235] C.-H. King, M.O. Culjat, M.L. Franco, C.E. Lewis, E.P. Dutson, W.S. Grundfest, and J.W. Bisley. Tactile Feedback Induces Reduced Grasping Force in Robot-Assisted Surgery. *IEEE Transactions on Haptics*, 2(2):103–110, apr 2009. pages 142
- [236] Joao Bimbo, Claudio Pacchierotti, Marco Aggravi, Nikos Tsagarakis, and Domenico Prattichizzo. Teleoperation in cluttered environments using wearable haptic feedback. In *2017 IEEE/RSJ International Conference on Intelligent Robots and Systems (IROS)*, volume 2017-Septe, pages 3401–3408. IEEE, sep 2017. pages 142
- [237] Daniel Pamungkas and Koren Ward. Immersive teleoperation of a robot arm using electro-tactile feedback. In *2015 6th International Conference on Automation, Robotics and Applications (ICARA)*, pages 300–305. IEEE, feb 2015. pages 142
- [238] Daniel Sutopo Pamungkas and Arjon Turnip. Electro-tactile Cues for a Haptic Multimedia Finger Motoric Learning System. In *2019 International Conference on Sustainable Engineering and Creative Computing (ICSECC)*, pages 127–132. IEEE, aug 2019. pages
- [239] Mikel Sagardia, Katharina Hertkorn, Thomas Hulin, Simon Schatzle, Robin Wolff, Johannes Hummel, Janki Dodiya, and Andreas Gerndt. VR-OOS: The DLR’s virtual reality simulator for telerobotic on-orbit servicing with haptic feedback. In *2015 IEEE Aerospace Conference*, volume 2015-June, pages 1–17. IEEE, mar 2015. pages
- [240] Johannes Hummel, Janki Dodiya, German Aerospace Center, Laura Eckardt, Robin Wolff, Andreas Gerndt, and Torsten W. Kuhlen. A lightweight electrotactile feedback device for grasp improvement in immersive virtual environments. In *2016 IEEE Virtual Reality (VR)*, volume 2016-July, pages 39–48. IEEE, mar 2016. pages
- [241] Daniel S. Pamungkas and Koren Ward. Tele-operation of a robot arm with electro tactile feedback. In *2013 IEEE/ASME International Conference on Advanced Intelligent Mechatronics*, pages 704–709. IEEE, jul 2013. pages
- [242] Ming Ying, Andrew P. Bonifas, Nanshu Lu, Yewang Su, Rui Li, Huanyu Cheng, Abid Ameen, Yonggang Huang, and John A. Rogers. Silicon nanomembranes for fingertip electronics. *Nanotechnology*, 23(34):344004, aug 2012. pages
- [243] H. Kajimoto, M. Inami, N. Kawakami, and S. Tachi. SmartTouch - augmentation of skin sensation with electrocutaneous display. In *11th Symposium on Haptic Interfaces for Virtual Environment and Teleoperator Systems, 2003. HAPTICS 2003. Proceedings.*, pages 40–46. IEEE Comput. Soc, 2003. pages

- [244] Daniel S. Pamungkas and Koren Ward. Electro-tactile feedback system for achieving embodiment in a tele-operated robot. In *2014 13th International Conference on Control Automation Robotics & Vision (ICARCV)*, volume 2014, pages 1706–1711. IEEE, dec 2014. pages 142
- [245] Hiroyuki Kajimoto, Naoki Kawakami, Susumu Tachi, and Masahiko Inami. Smart-Touch: electric skin to touch the untouchable. *IEEE Computer Graphics and Applications*, 24(1):36–43, jan 2004. pages 142, 163
- [246] Anusha Withana, Daniel Groeger, and Jürgen Steimle. Tacttoo. In *Proceedings of the 31st Annual ACM Symposium on User Interface Software and Technology*, pages 365–378, New York, NY, USA, oct 2018. ACM. pages 142
- [247] Yei Hwan Jung, Jae-Hwan Kim, and John A. Rogers. Skin-Integrated Vibrohaptic Interfaces for Virtual and Augmented Reality. *Advanced Functional Materials*, 2008805:2008805, dec 2020. pages 142
- [248] Alex Chortos and Zhenan Bao. Skin-inspired electronic devices. *Materials Today*, 17(7):321–331, sep 2014. pages 143
- [249] Chuan Wang, David Hwang, Zhibin Yu, Kuniharu Takei, Junwoo Park, Teresa Chen, Biwu Ma, and Ali Javey. User-interactive electronic skin for instantaneous pressure visualization. *Nature Materials*, 12(10):899–904, oct 2013. pages
- [250] Kuniharu Takei, Toshitake Takahashi, Johnny C. Ho, Hyunhyub Ko, Andrew G. Gillies, Paul W. Leu, Ronald S. Fearing, and Ali Javey. Nanowire active-matrix circuitry for low-voltage macroscale artificial skin. *Nature Materials*, 9(10):821–826, oct 2010. pages
- [251] Sangbae Kim, Cecilia Laschi, and Barry Trimmer. Soft robotics: A bioinspired evolution in robotics. *Trends in Biotechnology*, 31(5):287–294, 2013. pages
- [252] Zhenan Bao. Skin-inspired organic electronic materials and devices. *MRS Bulletin*, 41(11):897–904, nov 2016. pages 143
- [253] Daniela Rus and Michael T. Tolley. Design, fabrication and control of soft robots. *Nature*, 521(7553):467–475, may 2015. pages 143
- [254] Aaron P. Gerratt, Hadrien O. Michaud, and Stéphanie P. Lacour. Elastomeric Electronic Skin for Prosthetic Tactile Sensation. *Advanced Functional Materials*, 25(15):2287–2295, apr 2015. pages 143
- [255] Changhyun Pang, Ja Hoon Koo, Amanda Nguyen, Jeffrey M. Caves, Myung-Gil Kim, Alex Chortos, Kwanpyo Kim, Paul J. Wang, Jeffrey B.-H. Tok, and Zhenan Bao. Highly Skin-Conformal Microhairy Sensor for Pulse Signal Amplification. *Advanced Materials*, 27(4):634–640, jan 2015. pages 143
- [256] "TACTILITY – An EU H2020 Research and Innovation Action" [online]. available: <https://tactility-h2020.eu/> [accessed: 2021-08-25. pages 143

- [257] "32-Channel, Current-Input Analog-to-Digital Converter" [online]. available: <https://www.ti.com/lit/ds/symlink/ddc232.pdf> [accessed: 2021-08-28]. pages 147
- [258] "Home | Tecnaia" [online]. available: <https://www.tecnaia.com/en/> [accessed: 2021-03-26]. pages 149
- [259] Vibol Yem and Hiroyuki Kajimoto. Comparative Evaluation of Tactile Sensation by Electrical and Mechanical Stimulation. *IEEE Transactions on Haptics*, 10(1):130–134, jan 2017. pages 163
- [260] Guohong Chai, Dingguo Zhang, and Xiangyang Zhu. Developing Non-Somatotopic Phantom Finger Sensation to Comparable Levels of Somatotopic Sensation through User Training With Electrotactile Stimulation. *IEEE Transactions on Neural Systems and Rehabilitation Engineering*, 25(5):469–480, may 2017. pages 164
- [261] Andreas Geier, Rawleigh Tucker, Sophon Somlor, Hideyuki Sawada, and Shigeki Sugano. End-to-End Tactile Feedback Loop: From Soft Sensor Skin Over Deep GRU-Autoencoders to Tactile Stimulation. *IEEE Robotics and Automation Letters*, 5(4):6467–6474, oct 2020. pages 164
- [262] Lucia Seminara, Paolo Gastaldo, Simon J Watt, Kenneth F Valyear, Fernando Zuher, and Fulvio Mastrogiovanni. Active Haptic Perception in Robots: A Review. *Frontiers in Neurorobotics*, 13(July):1–20, jul 2019. pages
- [263] Zhengkun Yi, Yilei Zhang, and Jan Peters. Bioinspired tactile sensor for surface roughness discrimination. *Sensors and Actuators, A: Physical*, 255:46–53, 2017. pages 164
- [264] Mark Ison, Ivan Vujaklija, Bryan Whitsell, Dario Farina, and Panagiotis Artemiadis. High-Density Electromyography and Motor Skill Learning for Robust Long-Term Control of a 7-DoF Robot Arm. *IEEE Transactions on Neural Systems and Rehabilitation Engineering*, 24(4):424–433, apr 2016. pages 165
- [265] Gordon Cheng, Emmanuel Dean-Leon, Florian Bergner, Julio Rogelio Guadarrama Olvera, Quentin Leboutet, and Philipp Mittendorf. A Comprehensive Realization of Robot Skin: Sensors, Sensing, Control, and Applications. *Proceedings of the IEEE*, 107(10):2034–2051, oct 2019. pages 167, 188
- [266] Ji Young Lee and Franck Deroncourt. Sequential Short-Text Classification with Recurrent and Convolutional Neural Networks. In *Proceedings of the 2016 Conference of the North American Chapter of the Association for Computational Linguistics: Human Language Technologies*, pages 515–520, Stroudsburg, PA, USA, 2016. Association for Computational Linguistics. pages 168
- [267] Wenpeng Yin, Katharina Kann, Mo Yu, and Hinrich Schütze. Comparative Study of CNN and RNN for Natural Language Processing. feb 2017. pages 168
- [268] Sepp Hochreiter and Jürgen Schmidhuber. Long Short-Term Memory. *Neural Computation*, 9(8):1735–1780, nov 1997. pages 168

- [269] Kyunghyun Cho, Bart van Merriënboer, Caglar Gulcehre, Dzmitry Bahdanau, Fethi Bougares, Holger Schwenk, and Yoshua Bengio. Learning Phrase Representations using RNN Encoder–Decoder for Statistical Machine Translation. In *Proceedings of the 2014 Conference on Empirical Methods in Natural Language Processing (EMNLP)*, pages 1724–1734, Stroudsburg, PA, USA, 2014. Association for Computational Linguistics. pages 168, 175
- [270] M. Osta, A. Ibrahim, M. Magno, M. Eggimann, A. Pullini, P. Gastaldo, and M. Valle. An Energy Efficient System for Touch Modality Classification in Electronic Skin Applications. In *2019 IEEE International Symposium on Circuits and Systems (ISCAS)*, volume 2019-May, pages 1–4. IEEE, may 2019. pages 168, 169, 184, 188
- [271] Paolo Gastaldo, Luigi Pinna, Lucia Seminara, Maurizio Valle, and Rodolfo Zunino. Computational intelligence techniques for tactile sensing systems. *Sensors (Switzerland)*, 14(6):10952–10976, 2014. pages 169, 170, 177, 184, 185, 188
- [272] Mohamad Alameh, Yahya Abbass, Ali Ibrahim, and Maurizio Valle. Smart Tactile Sensing Systems Based on Embedded CNN Implementations. *Micromachines*, 11(1):103, 2020. pages 169, 170
- [273] Mohamad Alameh, Yahya Abbass, Ali Ibrahim, Gabriele Moser, and Maurizio Valle. Touch Modality Classification Using Recurrent Neural Networks. *IEEE Sensors Journal*, 21(8):9983–9993, apr 2021. pages 169
- [274] David Silvera Tawil, David Rye, and Mari Velonaki. Interpretation of the modality of touch on an artificial arm covered with an EIT-based sensitive skin. *The International Journal of Robotics Research*, 31(13):1627–1641, nov 2012. pages 169
- [275] Mohsen Kaboli, Alex Long, and Gordon Cheng. Humanoids learn touch modalities identification via multi-modal robotic skin and robust tactile descriptors. *Advanced Robotics*, 29(21):1411–1425, nov 2015. pages 169
- [276] Jerome Friedman, Robert Tibshirani, and Trevor Hastie. Additive logistic regression: a statistical view of boosting (With discussion and a rejoinder by the authors). *The Annals of Statistics*, 28(2):337–407, apr 2000. pages 169
- [277] Juan M. Gandarias, Jesus M. Gomez-de Gabriel, and Alfonso Garcia-Cerezo. Human and object recognition with a high-resolution tactile sensor. In *2017 IEEE SENSORS*, volume 2017-Decem, pages 1–3. IEEE, oct 2017. pages 170
- [278] Herbert Bay, Andreas Ess, Tinne Tuytelaars, and Luc Van Gool. Speeded-Up Robust Features (SURF). *Computer Vision and Image Understanding*, 110(3):346–359, jun 2008. pages 170
- [279] Alex Krizhevsky, Ilya Sutskever, and Geoffrey E. Hinton. ImageNet classification with deep convolutional neural networks. *Communications of the ACM*, 60(6):84–90, may 2017. pages 170

- [280] V.N. Vapnik. An overview of statistical learning theory. *IEEE Transactions on Neural Networks*, 10(5):988–999, 1999. pages 170
- [281] Juan M. Gandarias, Alfonso J. Garcia-Cerezo, and Jesus M. Gomez-de Gabriel. CNN-Based Methods for Object Recognition With High-Resolution Tactile Sensors. *IEEE Sensors Journal*, 19(16):6872–6882, aug 2019. pages 170
- [282] Ghazal Rouhafzay and Ana-Maria Cretu. An Application of Deep Learning to Tactile Data for Object Recognition under Visual Guidance. *Sensors*, 19(7):1534, mar 2019. pages 170
- [283] Zineb Abderrahmane, Gowrishankar Ganesh, Andre Crosnier, and Andrea Cherubini. Visuo-Tactile Recognition of Daily-Life Objects Never Seen or Touched Before. In *2018 15th International Conference on Control, Automation, Robotics and Vision (ICARCV)*, pages 1765–1770. IEEE, nov 2018. pages 170
- [284] Chia Hsien Lin, Todd W. Erickson, Jeremy A. Fishel, Nicholas Wettels, and Gerald E. Loeb. Signal processing and fabrication of a biomimetic tactile sensor array with thermal, force and microvibration modalities. In *2009 IEEE International Conference on Robotics and Biomimetics (ROBIO)*, pages 129–134. IEEE, dec 2009. pages 170
- [285] Mohamad Alameh, Ali Ibrahim, Maurizio Valle, and Gabriele Moser. DCNN for Tactile Sensory Data Classification based on Transfer Learning. In *2019 15th Conference on Ph.D Research in Microelectronics and Electronics (PRIME)*, pages 237–240. IEEE, jul 2019. pages 170, 173, 181, 184, 185, 186, 188
- [286] "imagenet" [online]. available: <http://www.image-net.org> [accessed: 2019-11-20]. pages 170, 171, 181, 186
- [287] Francisco Pastor, Juan M. Gandarias, Alfonso J. García-Cerezo, and Jesús M. Gómez-De-gabriel. Using 3d convolutional neural networks for tactile object recognition with robotic palpation. *Sensors (Switzerland)*, 19(24), 2019. pages 171
- [288] Jianhua Li, Siyuan Dong, and Edward Adelson. Slip Detection with Combined Tactile and Visual Information. In *2018 IEEE International Conference on Robotics and Automation (ICRA)*, pages 7772–7777. IEEE, may 2018. pages 171
- [289] Haoying Wu, Daimin Jiang, and Hao Gao. Tactile motion recognition with convolutional neural networks. In *2017 IEEE/RSJ International Conference on Intelligent Robots and Systems (IROS)*, volume 2017-Septe, pages 1572–1577. IEEE, sep 2017. pages 171
- [290] Jennifer Kwiatkowski, Deen Cockburn, and Vincent Duchaine. Grasp stability assessment through the fusion of proprioception and tactile signals using convolutional neural networks. In *2017 IEEE/RSJ International Conference on Intelligent Robots and Systems (IROS)*, volume 2017-Septe, pages 286–292. IEEE, sep 2017. pages 171

- [291] Wenzhen Yuan, Chenzhuo Zhu, Andrew Owens, Mandayam A. Srinivasan, and Edward H. Adelson. Shape-independent hardness estimation using deep learning and a GelSight tactile sensor. In *2017 IEEE International Conference on Robotics and Automation (ICRA)*, pages 951–958. IEEE, may 2017. pages 171
- [292] Wenzhen Yuan, Yuchen Mo, Shaoxiong Wang, and Edward H. Adelson. Active Clothing Material Perception Using Tactile Sensing and Deep Learning. In *2018 IEEE International Conference on Robotics and Automation (ICRA)*, volume 1, pages 4842–4849. IEEE, may 2018. pages 171
- [293] Karl Van Wyk and Joe Falco. Slip Detection: Analysis and Calibration of Univariate Tactile Signals. jun 2018. pages 171
- [294] Brayan S. Zapata-Impata, Pablo Gil, and Fernando Torres. Tactile-Driven Grasp Stability and Slip Prediction. *Robotics*, 8(4):85, sep 2019. pages 171
- [295] Thomas N. Kipf and Max Welling. Semi-Supervised Classification with Graph Convolutional Networks. *5th International Conference on Learning Representations, ICLR 2017 - Conference Track Proceedings*, pages 1–14, sep 2016. pages 171
- [296] Siyuan Dong and Alberto Rodriguez. Tactile-Based Insertion for Dense Box-Packing. In *2019 IEEE/RSJ International Conference on Intelligent Robots and Systems (IROS)*, pages 7953–7960. IEEE, nov 2019. pages 172
- [297] Vivienne Sze, Yu-Hsin Chen, Joel Emer, Amr Suleiman, and Zhengdong Zhang. Hardware for machine learning: Challenges and opportunities. In *2017 IEEE Custom Integrated Circuits Conference (CICC)*, volume 2017-April, pages 1–8. IEEE, apr 2017. pages 172
- [298] Xingjian Shi, Zhourong Chen, Hao Wang, Dit Yan Yeung, Wai Kin Wong, and Wang Chun Woo. Convolutional LSTM network: A machine learning approach for precipitation nowcasting. *Advances in Neural Information Processing Systems*, 2015-Janua:802–810, 2015. pages 174, 176
- [299] Fazle Karim, Somshubra Majumdar, Houshang Darabi, and Shun Chen. LSTM Fully Convolutional Networks for Time Series Classification. *IEEE Access*, 6:1662–1669, 2018. pages 174
- [300] Martin Sundermeyer, Ralf Schlüter, and Hermann Ney. LSTM neural networks for language processing. *Interspeech 2012*, pages 194–197, 2012. pages 174, 175
- [301] Sreeraj Rajendran, Wannes Meert, Domenico Giustiniano, Vincent Lenders, and Sofie Pollin. Deep Learning Models for Wireless Signal Classification With Distributed Low-Cost Spectrum Sensors. *IEEE Transactions on Cognitive Communications and Networking*, 4(3):433–445, sep 2018. pages 174
- [302] Guangyi Zhang, Vandad Davoodnia, Alireza Sepas-Moghaddam, Yaoxue Zhang, and Ali Etemad. Classification of Hand Movements From EEG Using a Deep Attention-Based LSTM Network. *IEEE Sensors Journal*, 20(6):3113–3122, mar 2020. pages 174, 181

- [303] Kaiming He, Xiangyu Zhang, Shaoqing Ren, and Jian Sun. Deep Residual Learning for Image Recognition. In *2016 IEEE Conference on Computer Vision and Pattern Recognition (CVPR)*, pages 770–778. IEEE, jun 2016. pages 181
- [304] Andrew G. Howard, Menglong Zhu, Bo Chen, Dmitry Kalenichenko, Weijun Wang, Tobias Weyand, Marco Andreetto, and Hartwig Adam. MobileNets: Efficient Convolutional Neural Networks for Mobile Vision Applications. apr 2017. pages 181
- [305] Diederik P. Kingma and Jimmy Ba. Adam: A Method for Stochastic Optimization. *3rd International Conference on Learning Representations, ICLR 2015 - Conference Track Proceedings*, pages 1–15, dec 2014. pages 182
- [306] Ali Ibrahim, Paolo Gastaldo, Hussein Chible, and Maurizio Valle. Real-Time Digital Signal Processing Based on FPGAs for Electronic Skin Implementation †. *Sensors*, 17(3):558, mar 2017. pages 187, 188
- [307] Bart Peerdeman, Daphne Boere, Heidi Witteveen, Rianne Huis in ‘tVeld, Hermie Hermens, Stefano Stramigioli, Hans Rietman, Peter Veltink, and Sarthak Misra. Myoelectric forearm prostheses: State of the art from a user-centered perspective. *The Journal of Rehabilitation Research and Development*, 48(6):719, 2011. pages 191